



**NUMERICAL AND EXPERIMENTAL ANALYSES OF SINGLE AND TWO-
PHASE MICROFLUIDIC FLOWS WITH IMPLICATIONS IN
MICROREACTORS**
Roland Blanch Ojea

Dipòsit Legal: T. 149-2012

ADVERTIMENT. La consulta d'aquesta tesi queda condicionada a l'acceptació de les següents condicions d'ús: La difusió d'aquesta tesi per mitjà del servei TDX (www.tesisenxarxa.net) ha estat autoritzada pels titulars dels drets de propietat intel·lectual únicament per a usos privats emmarcats en activitats d'investigació i docència. No s'autoritza la seva reproducció amb finalitats de lucre ni la seva difusió i posada a disposició des d'un lloc aliè al servei TDX. No s'autoritza la presentació del seu contingut en una finestra o marc aliè a TDX (framing). Aquesta reserva de drets afecta tant al resum de presentació de la tesi com als seus continguts. En la utilització o cita de parts de la tesi és obligat indicar el nom de la persona autora.

ADVERTENCIA. La consulta de esta tesis queda condicionada a la aceptación de las siguientes condiciones de uso: La difusión de esta tesis por medio del servicio TDR (www.tesisenred.net) ha sido autorizada por los titulares de los derechos de propiedad intelectual únicamente para usos privados enmarcados en actividades de investigación y docencia. No se autoriza su reproducción con finalidades de lucro ni su difusión y puesta a disposición desde un sitio ajeno al servicio TDR. No se autoriza la presentación de su contenido en una ventana o marco ajeno a TDR (framing). Esta reserva de derechos afecta tanto al resumen de presentación de la tesis como a sus contenidos. En la utilización o cita de partes de la tesis es obligado indicar el nombre de la persona autora.

WARNING. On having consulted this thesis you're accepting the following use conditions: Spreading this thesis by the TDX (www.tesisenxarxa.net) service has been authorized by the titular of the intellectual property rights only for private uses placed in investigation and teaching activities. Reproduction with lucrative aims is not authorized neither its spreading and availability from a site foreign to the TDX service. Introducing its content in a window or frame foreign to the TDX service is not authorized (framing). This rights affect to the presentation summary of the thesis as well as to its contents. In the using or citation of parts of the thesis it's obliged to indicate the name of the author.

DOCTORAL THESIS

Roland Blanch Ojea

NUMERICAL AND EXPERIMENTAL ANALYSES OF SINGLE AND TWO-PHASE MICROFLUIDIC FLOWS WITH IMPLICATIONS IN MICROREACTORS



Department of Mechanical Engineering

ROVIRA I VIRGILI UNIVERSITY

UNIVERSITAT ROVIRA I VIRGILI

NUMERICAL AND EXPERIMENTAL ANALYSES OF SINGLE AND TWO-PHASE MICROFLUIDIC FLOWS WITH IMPLICATIONS IN MICROREACTORS

Roland Blanch Ojea

DL:T. 149-2012

UNIVERSITAT ROVIRA I VIRGILI

NUMERICAL AND EXPERIMENTAL ANALYSES OF SINGLE AND TWO-PHASE MICROFLUIDIC FLOWS WITH IMPLICATIONS IN MICROREACTORS

Roland Blanch Ojea

DL:T. 149-2012

UNIVERSITAT ROVIRA I VIRGILI

NUMERICAL AND EXPERIMENTAL ANALYSES OF SINGLE AND TWO-PHASE MICROFLUIDIC FLOWS WITH IMPLICATIONS IN MICROREACTORS

Roland Blanch Ojea

DL:T. 149-2012

Roland Blanch Ojea

NUMERICAL AND EXPERIMENTAL ANALYSES OF
SINGLE AND TWO-PHASE MICROFLUIDIC FLOWS
WITH IMPLICATIONS IN MICROREACTORS

DOCTORAL THESIS

Supervised by

Dr. Jordi Pallarès Curto

and

Dr. Francesc Xavier Grau Vidal

Department of Mechanical Engineering
ECoMMFiT Research Group



ROVIRA I VIRGILI UNIVERSITY

Tarragona

2011

UNIVERSITAT ROVIRA I VIRGILI

NUMERICAL AND EXPERIMENTAL ANALYSES OF SINGLE AND TWO-PHASE MICROFLUIDIC FLOWS WITH IMPLICATIONS IN MICROREACTORS

Roland Blanch Ojea

DL:T. 149-2012

Declaració

El catedràtic d'Universitat Francesc Xavier Grau Vidal i el Professor titular d'Universitat Jordi Pallarès Curto, de l'Escola Superior d'Enginyeria Química de la Universitat Rovira i Virgili,

FEM CONSTAR:

Que el present treball, amb títol:

Numerical and Experimental Analyses of Single and Two-phase Microfluidic Flows with Implications in Microreactors

que presenta en Roland Blanch Ojea per optar al grau de doctor en Enginyeria Química ha estat realitzat sota la nostra immediata direcció, i que tots els resultats obtinguts són fruit dels experiments i anàlisis realitzats per l'esmentat doctorand, i que aconsegueix els requeriments per poder optar a Menció Europea.

I, perquè en prengueu coneixement i tingui els efectes que correspongui, signem aquesta certificació.

Tarragona, a 19 de Desembre de 2011

Dr. Francesc Xavier Grau Vidal

Dr. Jordi Pallarès Curto

UNIVERSITAT ROVIRA I VIRGILI

NUMERICAL AND EXPERIMENTAL ANALYSES OF SINGLE AND TWO-PHASE MICROFLUIDIC FLOWS WITH IMPLICATIONS IN MICROREACTORS

Roland Blanch Ojea

DL:T. 149-2012

*A mis padres y hermana,
a Iza y Akún,
y a todas aquellas personas a las que llevo en el corazón*

UNIVERSITAT ROVIRA I VIRGILI

NUMERICAL AND EXPERIMENTAL ANALYSES OF SINGLE AND TWO-PHASE MICROFLUIDIC FLOWS WITH IMPLICATIONS IN MICROREACTORS

Roland Blanch Ojea

DL:T. 149-2012

Agradecimientos

La presente tesis doctoral ha sido llevada a cabo en el grupo de investigación *Experiments, Computation and Modelization in Fluid Mechanics and Turbulence* (ECoMMFiT), de la *Escola Tècnica Superior d'Enginyeria Química*, de la *Universitat Rovira i Virgili* de Tarragona, bajo la dirección conjunta de los Drs. Jordi Pallarès Curto y Francesc Xavier Grau.

Llegar a doctor es un proceso largo, que exige una ingente cantidad de esfuerzo y que conlleva un número demasiado elevado de momentos de frustración y desesperación. Por esta razón le estaré eternamente agradecido a los Drs. Jordi Pallarès Curto y Francesc Xavier Grau, al haber aceptado en su día dirigir mi tesis doctoral. Sin su continuo apoyo, su inagotable paciencia y su inestimable aporte de conocimientos, sé que hoy no tendría la satisfacción de graduarme como doctor.

Pertenecer al grupo de investigación ECoMMFiT ha sido uno de los mayores regalos, por el inmejorable ambiente de trabajo y por la complicidad entre sus miembros, tanto estudiantes como profesores. Por los seminarios de grupo, por las conversaciones y discusiones científicas y laborales, por las comidas, por las sesiones de BZFlag...por demasiadas experiencias vividas. Os echaré de menos a todos y, en especial, a aquellos con los que he compartido la mayor parte de mi tiempo estos años, Manuel Martínez, Guillaume Novelli, Silvana Varela, Àlex Fabregat, Salvatore Cito, Jordi Polo, Elkin Florez y Obai Younis.

Dr. Roald M. Tiggelaar and Prof. Han Gardeniers, at the *Mesoscale Chemical Systems* research group from the *University of Twente* deserve a special word in these acknowledgements. You hosted me in your group and, from the first moment, I felt like home. Trust me when I say I could never anticipate I was going to be treated so generously. My internship with you was a privilege, as it has been your continuous support and friendship ever since.

Deseo expresar mi más sincera gratitud hacia los miembros del PAS de la universidad, en especial a Núria Juanpere, a Samuel Garcia y a Ma. José Duran, por sus valiosas tareas administrativas y por facilitar en un sinfín de ocasiones los trámites más tediosos.

Este doctorado no habría sido posible sin el soporte económico del Proyecto Europeo IMPULSE, de las becas de doctorado FI de la Generalitat de Ca-

talunya, y de las becas de movilidad del Ministerio de Educación y Ciencia del Gobierno de España. Además, agradezco sinceramente al grupo de investigación ECoMMFiT y al Prof. Han Gardeniers por financiar mi asistencia a las conferencias IMRET11 y HPLC2010.

Fuera del ámbito laboral quiero acordarme de mis amigos, a los que considero mi familia, Aitor Bru, Juan José Daniel, Jacob Fibla, Isaac González, Ángel López, Núria Martí, Estefanía Martínez, Sonia Martos, Núria Romero y Elena Valldepérez. Habéis estado a mi lado durante muchos años, incluso en los momentos más duros. Eso es algo que nunca podré recompensaros apropiadamente.

No me olvido de mi familia, primos, tíos y abuelos, siempre me habéis tratado como a un hijo o a un hermano, todos.

Mamá, Papá, he llegado hasta aquí gracias a vosotros, a vuestro cariño y amor desde que nací, y a la educación y valores que supisteis transmitirme, y que nunca olvidaré. Estel, mi hermana, me emociona ver como sonríes y te alegras cada vez que me ves.

Gracias a ti, Iza, mi pareja, por no resignarte a perderme, y porque después de ocho años sigues demostrándome a cada momento que me quieres. De Akún, claro, también me acuerdo, es el mejor recibimiento diario al llegar a casa.

Por último, quiero agradecer a los miembros del tribunal, los Drs. Ildefonso Cuesta Romeo, Roald M. Tiggelaar y Salvatore Cito, por acceder a juzgar y evaluar esta tesis.

Numerical and experimental analyses of single and two-phase microfluidic flows with implications in microreactors

Resumen:

La presente tesis centra sus esfuerzos en el entorno de la microfluídica, un campo dentro de la Mecánica de Fluidos relativamente reciente, y con una prometedora proyección de futuro gracias a las ventajas que es capaz de aportar en comparación con los sistemas macroscópicos convencionales. Básicamente, la microfluídica incluye aquellos sistemas de flujo de dimensiones muy reducidas, con diámetros de canal submilimétricos, y entre sus ventajas destacan, una mayor seguridad en sistemas potencialmente peligrosos, una mayor relación de superficie-volumen o una gran escalabilidad. Sus posibles aplicaciones incluyen, entre otros, análisis y producción química, diagnósticos biomédicos, separación y mezclado de fluidos, producción energética o control térmico de procesos.

En este sentido, la tesis realiza una contribución en dos ámbitos diferentes de la microfluídica. El primero pertenece a la simulación numérica de flujos gaseosos reactivos en microreactores, mientras que el segundo pertenece a la caracterización experimental de flujos bifásicos con fluidos supercríticos, con posibles aplicaciones a reacciones químicas.

En el apartado numérico de la tesis se ha desarrollado un código de simulación propio, 3DINAMICS, capaz de reproducir numéricamente los fenómenos de transporte que ocurren en flujos laminares compresibles a bajo número de Mach, dentro de un reactor en microcanal. Estos flujos de mezclas gaseosas multicomponente experimentan reacciones heterogéneas en las paredes del microreactor. Para la simulación, el código resuelve los campos acoplados de velocidad, temperatura y fracciones másicas de especies químicas.

Una vez desarrollada la herramienta de simulación, ésta se ha aplicado en concreto al estudio de la oxidación catalítica parcial del metano para producir gas de síntesis, en un microreactor. El interés de este estudio viene, por un lado, de la necesidad de evaluar qué impacto tiene el aumento de temperatura asociado a esta reacción en las posibilidades de que se produzcan los peligrosos puntos calientes locales (*hot spot*), y por otro, de identificar bajo qué condiciones se puede mantener una operación auto-mantenida del reactor, sin la necesidad de una aportación energética externa. Este aporte

energético es necesario en aquellos casos en los que la entrada de reactivos fríos en el reactor produce una onda de baja temperatura (*thermal wave*), que extingue el sistema de reacciones. También se ha estudiado la sensibilidad en la estabilidad de operación y en la productividad del microreactor frente a algunos parámetros de operación variables.

La parte experimental de la tesis se centra en la generación y estudio de flujos bifásicos en una microunión en T. Habitualmente, los estudios de microflujos bifásicos trabajan en condiciones adiabáticas con fluidos immiscibles, o con un único fluido al que se lleva a ebullición. En este sentido, el presente estudio aporta la novedad de trabajar con mezclas de fluidos potencialmente miscibles, CO₂-etanol o CO₂-metanol, que experimentan un equilibrio vapor-líquido, con el CO₂ en condiciones gaseosas o supercríticas.

Para las dos mezclas de fluidos se han identificado los diferentes regímenes de flujo obtenidos en un rango de presiones entre 7 MPa y 18 MPa, y de temperaturas entre 294 K y 500 K. Estos regímenes han sido el flujo anular, el flujo Taylor y el flujo wavy, y se han plasmado en unos mapas de flujo basados en condiciones de presión y temperatura. Por otro lado se ha constatado que la presión o el tipo de alcohol utilizado ejercen una influencia insignificante en el comportamiento hidrodinámico o de fracción de vacío de estos sistemas, comparado con la influencia que ejerce la temperatura.

Finalmente, se ha reportado un fenómeno inesperado que consiste en una acumulación continua de líquido en el canal de CO₂. Cada cierto tiempo, esta acumulación acaba bloqueando el canal y el líquido sale eyectado aguas abajo, perturbando momentáneamente el flujo. Esta acumulación supone un serio inconveniente para el uso operativo de este tipo de sistemas puesto que imposibilita una operación estable de los mismos. Un análisis aproximado del fenómeno ha concluido que sus causas más probables son los fenómenos conocidos como capilaridad y *wettability*, debidos a tensiones de Marangoni generadas por gradientes locales de temperatura y concentración en el líquido.

Numerical and experimental analyses of single and two-phase microfluidic flows with implications in microreactors

Abstract:

The PhD thesis here presented focuses on microfluidics, a relatively recent field within Fluid Mechanics, and with a promising future due to its advantages when compared with conventional macroscopic systems. Basically, microfluidics involves those flow systems on the micro-scale dimensions, with sub-millimetre channel diameters, and its proven advantages include, among others, an improved safety for potentially dangerous systems, an increased surface-to-volume ratio or a great capacity for scalability. The potential applications are many, such as analytical chemistry, chemistry production, biomedical diagnosis, separation and mixing of fluids, energy production and thermal management.

In this direction, the thesis contributes on two different topics within microfluidics. First, on the numerical simulation of reactive gas flows inside microreactors, and second, on the experimental characterisation of two-phase microflows with supercritical fluids, with possible application to chemical reactions.

In the numerical part of the thesis, an in-house simulation code, named 3DINAMICS, has been developed, which is able to reproduce numerically the transport phenomena of low-Mach number compressible laminar flows inside a microchannel reactor. These multicomponent gas flows experience heterogeneous reactions on the wall surface of the microreactor. In order to reproduce the phenomena in the microreactor, the code solves the coupled fields of velocity, temperature and mass fraction of chemical species.

Once the simulation tool is ready, it has been used to study the specific case of a microreactor performing the catalytic partial oxidation of methane to produce synthesis gas. The interest of this study relies, on one hand, on the need to evaluate the impact of the heat release associated to this reactive system on the temperature distribution in the reactor, and on the possibility to experience a dangerous *hot spot* and, on the other hand, to identify the proper operating conditions to achieve a self-sustained operation mode of the reactor, in which no external heat source is needed. This external heat supply is necessary when the cold inlet feed gases generate a low temperature *thermal*

wave that propagates from the entrance towards the exit of the reactor, quenching the reactions. Furthermore, the response of the operation stability and of the performance of the reactor to several operation parameters, have also been tested.

In the experimental part of the thesis, the generation and study of two-phase flows in a microfluidic T-junction, have been carried out. Usually, this kind of studies are conducted in adiabatic conditions with non-miscible fluids, or with a single boiling fluid. The novelty of the present work comes from the fact that it uses potentially miscible fluid mixtures, CO₂-ethanol and CO₂-methanol, that are brought to their vapour-liquid equilibrium, with the CO₂ in either gas or supercritical state.

The different two-phase flow regimes obtained for both fluid mixtures in a pressure range from 7 MPa to 18 MPa, and from 294 K to 500 K, have been identified as annular flow, Taylor flow and wavy flow. A series of maps of flow regimes have been generated based on pressure and temperature conditions. Besides, it has been proved that the hydrodynamic behaviour and the void fraction of these flows are barely influenced by the pressure conditions or by the alcohol choice, whereas they show a dramatic dependency on the temperature conditions.

Finally, an unexpected phenomenon has been reported during the two-phase flow experiments. The phenomenon consists of a continuous accumulation of liquid on the CO₂ channel. Periodically, this accumulation ends up blocking the channel, and then a series of liquid plugs are ejected downstream, disturbing temporarily the flow conditions. This accumulation is a serious drawback for the operational use of this type of flow systems since it hinders their stable operation. An approximate analysis pointed as the most probable causes of the phenomenon to capillary and wettability effects due to Marangoni stresses, generated by local temperature and composition gradients in the liquid.

Contents

Contents	xi
List of Publications and Contributions to Conferences	xv
List of Figures	xvii
List of Tables	xxiii
1 Introduction	1
1.1 Aim of the thesis	2
1.2 State-of-the-art	3
1.2.1 Gas-phase microreactors	3
1.2.2 Multiphase flows in microchannels	5
1.3 Outline of the thesis	7
I Numerical simulation of a microreactor performing the catalytic partial oxidation of methane	9
2 The Physical Problem	11
2.1 Physical domain	11
2.2 Reaction mechanism	12
2.3 Flow conditions	13
3 Mathematical Model	17
3.1 Preliminary definitions	18
3.1.1 Notation and relations for mass and molar concentrations	18
3.1.2 Ideal gas law	18
3.2 Physical properties of the gas	18
3.2.1 Density	19
3.2.2 Dynamic viscosity	19
3.2.3 Thermal conductivity	19
3.2.4 Mass diffusivity	20
3.2.5 Heat capacity	21
3.3 Governing equations	22
3.3.1 Overall mass conservation (continuity)	22
3.3.2 Momentum	22
3.3.3 Mass conservation of chemical species	23
3.3.4 Thermal energy in the fluid	24

3.3.5	Thermal energy in the wall	30
3.4	Catalytic fluid-wall interface	30
3.4.1	Reaction kinetics	30
3.4.2	Balances for interface mass and energy transfer	33
3.5	Dimensional analysis	34
3.5.1	Non-dimensional variables and groups	34
3.5.2	Physical properties of the gas	35
3.5.3	Governing equations	35
3.5.4	Catalytic fluid-wall interface	38
4	Numerical resolution	41
4.1	Numerical techniques	41
4.2	Computational domain	42
4.3	Initial and boundary conditions	47
4.3.1	Initial conditions	47
4.3.2	Channel inlet conditions	47
4.3.3	Channel symmetry plane conditions	47
4.3.4	Channel outlet plane conditions	48
4.3.5	Channel catalytic fluid-wall interface conditions	48
4.3.6	Solid wall external boundaries	49
4.4	Convergence criteria, stability and consistency	49
5	Results and discussion	51
5.1	Base case	51
5.1.1	Operating conditions	51
5.1.2	Velocity, temperature and chemical species distribution	53
5.1.3	Performance of the reactor	54
5.1.4	Energetic analysis	57
5.2	Response of the microreactor to the variation of several operating parameters	62
6	Concluding remarks	67
6.1	Overall conclusions	67
6.2	Future directions	69
 II Flow of CO₂-ethanol and CO₂-methanol in a non-adiabatic microfluidic T-junction at high pressures		71
7	Theoretical background	73
7.1	Phase behaviour of Type I binary mixtures	74
7.1.1	Vaporised mass diffusion fraction	75

Contents **xiii**

7.2	Properties of fluids	75
7.2.1	Pseudocritical point of a supercritical fluid	75
7.2.2	Density	76
7.2.3	Dynamic viscosity	76
7.2.4	Interface tension	76
7.3	Two-phase flows	80
7.3.1	Two-phase flow regimes	80
7.3.2	Void fraction	82
7.4	Capillary pumping and wetting processes	85
8	Experimental	89
8.1	Microfluidic chip layout	90
8.2	Experimental setup	90
8.3	Operating conditions	95
8.3.1	Pressure	95
8.3.2	Temperature	95
8.3.3	Flow rate	96
8.3.4	Feed ratio	97
8.3.5	Flow velocity	97
8.4	Issues on experimental procedure	98
8.4.1	Proper cutting of the capillary tubing	98
8.4.2	Use of Rhodamine B for the visualization of flow regimes	99
8.4.3	Operation at high temperatures	103
8.5	Image recording and processing	103
9	Results and discussion	109
9.1	Vapour-Liquid Equilibrium and feed ratio	110
9.1.1	Vapour-Liquid Equilibrium of CO ₂ -EtOH and CO ₂ -MeOH	110
9.1.2	Estimation of the feed ratio of working mixtures	111
9.1.3	Phase behaviour of working mixtures at different pressures	113
9.2	Flow regimes	115
9.2.1	Two-phase flows	116
9.2.2	Single-phase flows	118
9.3	Flow instabilities, and accumulation of liquid in the line of CO ₂	121
9.3.1	Flow instabilities	121
9.3.2	Accumulation of liquid in the line of CO ₂ . Description of the phenomenon	121
9.3.3	Accumulation of liquid in the line of CO ₂ . Analysis of the causes	124
9.4	Two-phase void fraction	131
9.5	Hydrodynamics of Taylor flow	133
9.5.1	Velocity of liquid plugs	134
9.5.2	Elongation rate and frequency of generation of liquid plugs	134

9.5.3	Dimensionless jet entrainment	136
9.5.4	Conclusions	138
10	Concluding remarks	139
10.1	Overall conclusions	139
10.2	Future directions	141
III	Appendices	145
A	Vapor-Liquid Equilibrium data from literature	147
A.1	VLE data for CO ₂ -EtOH	147
A.2	VLE data for CO ₂ -MeOH	152
A.3	Critical locus data for CO ₂ -EtOH and CO ₂ -MeOH	155
B	Velocity of the CO₂ stream in the T-junction	157
	Nomenclature	159
	Bibliography	167

List of Publications and Contributions to Conferences

Journal papers

- Blanch-Ojea R, Tiggelaar RM, Pallares J, Grau FX, Gardeniers JGE, Flow of CO₂-ethanol and of CO₂-methanol in a non-adiabatic microfluidic T-junction at high pressures. *Submitted to Microfluidics and Nanofluidics*
- Blanch-Ojea R, Pallares J, Grau FX, Numerical study of the self-sustained operation and transport phenomena in a microreactor performing the catalytic partial oxidation of methane. *Submitted to Chemical Engineering Journal*

Poster Presentations in International Congresses

- Blanch R, Tiggelaar R, Pallares J, Grau FX, Gardeniers JGE (2010) Flow phenomena and phase behavior of CO₂/alcohol mixtures under near- and supercritical conditions in a microfluidic device, Poster at the 35th International Symposium on High Performance Liquid Phase Separations and Related Techniques (HPLC 2010). Boston. MA. USA. June 19-24
- Blanch R, Pallares J, Grau FX (2010) Numerical study of the self-sustained operation and transport phenomena in a microreactor performing the catalytic partial oxidation of methane, Poster at the 11th International Conference on Microreaction Technology. Kyoto. Japan. March 8-10

UNIVERSITAT ROVIRA I VIRGILI

NUMERICAL AND EXPERIMENTAL ANALYSES OF SINGLE AND TWO-PHASE MICROFLUIDIC FLOWS WITH IMPLICATIONS IN MICROREACTORS

Roland Blanch Ojea

DL:T. 149-2012

List of Figures

2.1	Sketch of the computational domain. The aspect ratio is set to $L_x^* = L_x/L_c = 30$, $L_y^* = L_y/L_c = 1$, $L_{yw}^* = L_{yw}/L_c = 0.6$	12
4.1	Merged grids of the computational domains of the flow channel (301×11) and the conductive wall (301×7). The distribution of the nodes for scalar variables at the initial ($x^* = 0$ to 5) and the final ($x^* = 25$ to 30) sections of the microchannel reactor are depicted.	44
4.2	2D staggered grid. The distribution of the nodes of the scalar variable and its control volume, as well as the location of the u and v velocity components, are indicated.	45
4.3	Profiles of the (a) velocity component in the x -direction, u^* , (b) temperature, T^* , and (c) mass fraction of CH_4 , ω_{CH_4} , along the reactor, x^* , at the fluid-solid interface and the stream-wise symmetry, obtained from the test of grid independence for three different grids, 301×07 , 301×11 and 301×17	46
5.1	Values of the standard equilibrium constants of reaction, $K_{eq,p,REF}^o$ and $K_{eq,p,WGS}^o$, against temperature, T	53
5.2	Fields of (a) velocity, \mathbf{v}^* , (b) temperature, T^* , and (c) mass fraction of CH_4 , ω_{CH_4} , at steady state. The images are scaled to an aspect ratio of $y/x = 0.325$	55
5.3	Velocity field, \mathbf{v}^* , at the entrance of the channel ($x^* = 0$ to $L_x^*/10$).	56
5.4	Mass fraction, ω , of the chemical species along the fluid-solid reactive interface.	56
5.5	Efficiency and performance parameters along the reactor. The parameters include the conversion of CH_4 , η_{CH_4} , the selectivity of H_2 and CO , ξ_{H_2} and ξ_{CO} , and the yield of H_2 and CO , γ_{H_2} and γ_{CO}	58
5.6	Balance of terms of energy along the fluid-solid reactive interface. The profile of the interface temperature, T_{if}^* , is included.	59
5.7	Balance of terms of the energy equation along the reactor at (a) $y^* = 2.36 \times 10^{-2}$ and (b) $y^* = 4.68 \times 10^{-1}$. The temperature profiles, T^* , are included for completeness.	61
5.8	Balance of terms of the energy equation along the span-wise direction of the reactor, $x^* = 7.5$. The temperature profile, T^* , is included for completeness.	62
5.9	Reactor efficiency and performance as function of (a) inlet temperature, T_{inlet}^* , and of (b) thermal conductivity of the wall, κ_s^*	64

5.10	Effect of inlet temperature, T_{inlet}^* , on the evolution along the reactor of (a) interface temperature, T_{if}^* , (b) CH ₄ conversion, η_{CH_4} , (c) H ₂ selectivity, ξ_{H_2} , (d) H ₂ yield, γ_{H_2} , (e) CO selectivity, ξ_{CO} , and (f) CO yield, γ_{CO} . The data points for each T_{inlet}^* where the increment of T_{if}^* stabilizes, $(dT_{if}^*/dx^*) \leq 0.01$, are marked with a cross.	65
5.11	Effect of thermal conductivity of the wall, κ_s^* , on the evolution along the reactor of (a) interface temperature, T_{if}^* , (b) CH ₄ conversion, η_{CH_4} , (c) H ₂ selectivity, ξ_{H_2} , (d) H ₂ yield, γ_{H_2} , (e) CO selectivity, ξ_{CO} , and (f) CO yield, γ_{CO}	66
7.1	Line of pseudocritical point of CO ₂ . The saturation line and the critical point of CO ₂ are included for completeness.	76
7.2	Dependence of density, ρ , on temperature, T , for CO ₂ at 6.89 MPa, 7.87 MPa and 9.81 MPa. T_{pc} and the corresponding density values are indicated.	77
7.3	Dependence of density, ρ , on temperature, T , for EtOH and MeOH at 6.89 MPa, 7.87 MPa and 9.81 MPa.	77
7.4	Dependence of density of saturated liquid in VLE conditions, $\rho_{l,eq}$, on temperature, T , for mixtures of CO ₂ -EtOH and CO ₂ -MeOH at 6.89 MPa, 7.87 MPa and 9.81 MPa.	78
7.5	Dependence of viscosity, μ , on temperature, T , for CO ₂ at 6.89 MPa, 7.87 MPa and 9.81 MPa. T_{pc} and the corresponding viscosity values are indicated.	78
7.6	Dependence of viscosity, μ , on temperature, T , for EtOH and MeOH at 6.89 MPa, 7.87 MPa and 9.81 MPa.	79
7.7	Dependence of viscosity of saturated liquid in VLE conditions, $\mu_{l,eq}$, on temperature, T , for mixtures of CO ₂ -EtOH and CO ₂ -MeOH at 6.89 MPa, 7.87 MPa and 9.81 MPa.	79
7.8	Dependence of interface tension, σ , on temperature, T , for pure CO ₂ , EtOH and MeOH.	80
7.9	Dependence of interface tension of saturated liquid in dynamic conditions, σ_{dyn} , and in equilibrium conditions, σ_{eq} , on temperature, T , for a mixture of CO ₂ -EtOH at 6.89 MPa, 7.87 MPa and 9.81 MPa. Data from Sun and Shekunov (2003)	81
8.1	Pictures and layouts of the glass microfluidic chip with the T-junction in the (a,c) cooled and in the (b,d) heated areas. Layouts legend: [1] Alcohol inlet; [2] CO ₂ inlet; [3] T-junction; [4] Meandering channel; [5] Fluidic resistor; [6] Expansion zone; [7] Outlet; [A-A'] Detail of the cross-section of the microchannel (Fig. 8.2). The areas visualised with the microscope during the experiments, as well as the heated and cooled areas, are indicated. Dimensions: $W_{ch} = 15$ mm; $L_{ch} = 20$ mm; $W_{hca} = 8.2$ mm; $L_{hca} = 7.4$ mm; $W_{va} = 0.325$ mm; $L_{va} = 0.696$ mm.	91

List of Figures

8.2	Geometry and dimensions of the cross-section of the microchannel and the chip. $H_{ch} = 2\text{ mm}$; $H_{mc} = 30\text{ }\mu\text{m}$; $W_{mc} = 70\text{ }\mu\text{m}$	91
8.3	Pictures of the different mechanisms for cooling and heating the chip. (a) Cooling mechanism; (b) Heating mechanism; (c) Heat sink.	92
8.4	Sketch of the experimental setup. Legend: [1] CO ₂ cylinder; [2] Syringe pump; [3] Six-port valves; [4] Syringe; [5] Loop with alcohol sample; [6] Waste collectors; [7] Precolumn filters; [8] Microfluidic chip; [9] Peltier element; [10] Temperature sensor; [11] Heating resistance; [12] Copper blocks; [13] Microscope lens; [14] CCD high speed camera; [15] Computer.	93
8.5	Picture of the experimental setup.	94
8.6	Microfluidic chip placed on the holder.	94
8.7	Picture of the piping system, the precolumn filters and the capillary tubing.	94
8.8	Measurement and linear interpolation of the temperature drop across the chip.	96
8.9	Pictures of two different cuts of the capillary tubing. (a) Dirty cut; (b) Clean cut.	98
8.10	Picture of a fluidic resistor clogged by the debris from a capillary tubing with a dirty cut.	98
8.11	Precipitation of Rhodamine B in CO ₂ -MeOH-RhB mixtures.	99
8.12	Flow visualization of CO ₂ -MeOH-RhB mixtures with Fluorescence and Brightfield contrast techniques. Operating conditions: (a,c) $P = 7.38\text{ MPa}$; $T = 313.2\text{ K}$, and (b,d) $P = 12.2\text{ MPa}$; $T = 352.4\text{ K}$	101
8.13	Degradation of Rhodamine B during experiments of CO ₂ -MeOH-RhB mixtures. Operating conditions: (a,c) $P = 13.2\text{ MPa}$; $T = 360.0\text{ K}$, and (b,d) $P = 13.7\text{ MPa}$; $T = 369.4\text{ K}$	102
8.14	Local transient disappearance of the fluorescence in the heated channel during experiments of CO ₂ -MeOH-RhB at 12.2 MPa and 343.8 K	102
8.15	Effect of high operating temperatures on the T-junction and on the channel.	103
8.16	Image recorded with the CCD high-speed camera attached to the inverted microscope. Taylor flow of CO ₂ -MeOH, at 6.89 MPa and 305.6 K	104
8.17	Two successive frames ($t = 0\text{ ms}$ and $t = 1.96\text{ ms}$) showing the T-junction and the meandering channel, straightened for data analysis. The measurement of Δpx_j , Δpx_{bt} and Δpx_{bn} , are indicated.	104
8.18	Determination of ε_{exp} . The portion of the channel used for the measurement of ε_{exp} is indicated, and the resulting binarized image is shown. The void areas are surrounded by the fluid-fluid and wall-fluid interfaces (in black).	105
8.19	Comparison of the widths and areas of the cross-section of the channel, and of the portion used for the measurement of the void fraction (shaded area), in absolute and percentage values.	105

8.20	Comparison of the different methodologies for calculating ε_{exp} in an (a) idealized smooth flow and in an (b) idealized annular flow. The calculations based on the total channel width and a reduced portion of the channel width are compared, against the exact results based on the area of the cross-section of the channel.	106
9.1	P-xy diagrams from literature data (see Appendix A) of the VLE at different temperatures, for mixtures of (a) CO ₂ -EtOH and (b) CO ₂ -MeOH. The bubble point lines and the dew point lines are indicated.	110
9.2	P-T diagrams, interpolated from Figure 9.1, of the VLE for mixtures of (a) CO ₂ -EtOH and (b) CO ₂ -MeOH, at different x_{eq,CO_2} and y_{eq,CO_2} . The bubble point lines and the dew point lines are indicated. The saturation lines of the pure fluids, and the critical locus of the mixtures, are included for completeness.	111
9.3	Image of the first bubbles appearing when the mixture of CO ₂ -EtOH reaches the bubble point, at 7.87 MPa and 308.7 K. The direction of the flow is indicated.	112
9.4	Comparison of the pressure, P , and temperature, T , conditions of the experimentally observed bubble points in the present work, with the VLE curves from literature data (See Fig. 9.2) at different v_{eq,CO_2} and ω_{eq,CO_2} , for mixtures of (a) CO ₂ -EtOH and (b) CO ₂ -MeOH. The pseudocritical line of CO ₂ is included for completeness.	113
9.5	Phase behaviour at 6.89 MPa, 7.87 MPa and 9.81 MPa, for mixtures of (a) CO ₂ -EtOH at $v_{CO_2} = 0.95$ and (b) CO ₂ -MeOH at $v_{CO_2} = 0.87$	114
9.6	Vaporised mass diffusion fraction, G_d , for mixtures of CO ₂ -EtOH at $v_{CO_2} = 0.95$ and of CO ₂ -MeOH at $v_{CO_2} = 0.87$, at 6.89 MPa, 7.87 MPa and 9.81 MPa, against the temperature, T	115
9.7	Two-phase flow regimes of CO ₂ -MeOH mixture: (a,b) Taylor; (c) Annular; (d) Wavy.	116
9.8	Wavy-Taylor flow regime of CO ₂ -MeOH mixture at $P = 9.81$ MPa and $T = 323.6$ K.	117
9.9	Maps of two-phase flow regimes for mixtures of (a) CO ₂ -EtOH and (b) CO ₂ -MeOH, based on T and P conditions. The boundaries of VLE regions at (a) $v_{CO_2} = 0.95$ and (b) $v_{CO_2} = 0.87$ are indicated. The shadowed areas correspond to the experimental conditions where the liquid accumulation phenomenon was observed (see Sect. 9.3.2).	118
9.10	Single-phase flow, “pseudo” two-phase flow regimes and local phenomena of CO ₂ -MeOH mixture: (a) Standard (Liquid-liquid); (b) Standard (Supercritical-liquid); (c–d) Stratified (Smooth); (e) Taylor; (f) Meniscus; (g) Boiling; (h) Wavy-Boiling; (i) Wavy. The boiling phenomena and the waves are marked for easy identification.	119

List of Figures

9.11	Maps of single-phase flow, “pseudo” two-phase flow regimes and local phenomena for mixtures of (a) CO ₂ -EtOH and (b) CO ₂ -MeOH, based on T and P conditions.	120
9.12	CO ₂ -MeOH at 6.89 MPa and 321.8 K. (a–c) Evolution of the liquid accumulation in the CO ₂ line and (d–f) further generation of a liquid plug. The tiny liquid droplets coalescing with the accumulation are marked for easy identification.	122
9.13	CO ₂ -MeOH at 9.81 MPa and 325.2 K. Appearance and displacement upwards of the accumulation of liquid at the CO ₂ side of the two-phase flow. The accumulation is marked for easy identification.	123
9.14	Dimensionless distance between the T-junction and the liquid accumulation, for CO ₂ -EtOH and CO ₂ -MeOH at 6.89 MPa, 7.87 MPa and 9.81 MPa, against the temperature, T	124
9.15	CO ₂ -EtOH at 9.81 MPa and 340.9 K. Accumulation of liquid during an experiment carried out with the inlet lines inverted. The tiny liquid droplets coalescing with the accumulation, can be easily observed.	125
9.16	Bubbles generated along the mixing layer due to a gradient of temperature. The smallest bubbles are marked for easy identification. Conditions: 6.89 MPa, 300.4 K Boiling temperature of CO ₂ : 301.1 K	126
9.17	Ratios of different properties of EtOH to saturated liquid CO ₂ -EtOH at VLE conditions, at 6.89 MPa, 7.87 MPa and 9.81 MPa, against the temperature, T	127
9.18	Temperature gradient, in a droplet of EtOH, required to overcome the viscous forces, $(\Delta T)_{Ca}$, and the inertial forces, $(\Delta T)_{We}$, at 6.89 MPa, 7.87 MPa and 9.81 MPa, against the temperature, T	129
9.19	Mass fraction gradient of CO ₂ , in a droplet of EtOH, required to overcome the viscous forces, $(\Delta v_{CO_2})_{Ca}$, and the inertial forces, $(\Delta v_{CO_2})_{We}$, at 6.89 MPa, 7.87 MPa and 9.81 MPa, against the temperature, T	129
9.20	Capillary number, Ca , and Weber number, We , values of the accumulation of saturated liquid of CO ₂ -EtOH at 6.89 MPa, 7.87 MPa and 9.81 MPa, against the temperature, T	130
9.21	Comparison of experimental void fraction, ε_{exp} , homogeneous void fraction, ε_{hom} , and the correlation of Xiong and Chung (2007) , ε_{xio} against the relative temperature, at 6.89 MPa, 7.87 MPa and 9.81 MPa. (a) CO ₂ -EtOH at $v_{CO_2} = 0.95$ and (b) CO ₂ -MeOH at $v_{CO_2} = 0.87$	131
9.22	Average velocity of liquid plugs, U_{lp} , of Taylor flow for CO ₂ -EtOH and CO ₂ -MeOH at 6.89 MPa, 7.87 MPa and 9.81 MPa, against the relative temperature, T_{rel}	135
9.23	Rate of elongation, θ , of liquid plugs of Taylor flow for CO ₂ -EtOH and CO ₂ -MeOH at 6.89 MPa, 7.87 MPa and 9.81 MPa, against the relative temperature, T_{rel}	136

9.24	Frequency of generation, f_{lp} , of liquid plugs of Taylor flow for CO ₂ -EtOH and CO ₂ -MeOH at 6.89 MPa, 7.87 MPa and 9.81 MPa, against the relative temperature, T_{rel}	137
9.25	Dimensionless jet entrainment, ι , of Taylor flow for CO ₂ -EtOH and CO ₂ -MeOH at 6.89 MPa, 7.87 MPa and 9.81 MPa, against the relative temperature, T_{rel}	137
B.1	Simplified sketch of the flow line of the setup, from the syringe pump to the T-junction. Legend: [1] Syringe pump with CO ₂ at room temperature; [2] Channel of CO ₂ in the T-junction at experimental temperature; [3] Portion of the sample loop filled with CO ₂ at room temperature; [4] Portion of the sample loop filled with alcohol at room temperature; [5] Channel of alcohol in the T-junction at experimental temperature. The colours indicate which fluid fills each section: blue for CO ₂ , green for alcohol, and red for the mixture of CO ₂ -alcohol.	158

List of Tables

2.1	Reaction mechanism for the catalytic partial oxidation of methane, based on Gosiewski et al (1999) and Kaisare et al (2005a)	13
3.1	Non-dimensional groups	36
4.1	Grid parameters for the computational domains of the flow channel and the conductive wall	43
4.2	CPU times and numerical times elapsed to reach steady state, during the test of grid independence	45
5.1	Operating parameters of the base case	52
5.2	Reaction parameters of the base case	53
5.3	Variable operating parameters and times elapsed to reach steady state	63
8.1	Theoretical and experimental data of the critical point of CO ₂	95
8.2	Approximated average flow rates from the syringe pump, \dot{V}_o , at different pressures, P	97
9.1	Bubble and dew point temperatures for CO ₂ -EtOH at $v_{CO_2} = 0.95$, and for CO ₂ -MeOH at $v_{CO_2} = 0.87$, at different pressures	114
A.1	VLE data for CO ₂ -EtOH from Secuianu et al (2008)	148
A.2	VLE data for CO ₂ -EtOH from Tian et al (2001)	148
A.3	VLE data for CO ₂ -EtOH from Joung et al (2001)	149
A.4	VLE data for CO ₂ -EtOH from Jennings et al (1991)	150
A.5	VLE data for CO ₂ -EtOH from Suzuki et al (1990)	150
A.6	VLE data for CO ₂ -EtOH from Galicia-Luna et al (2000)	150
A.7	VLE data for CO ₂ -EtOH from Mendoza de la Cruz and Galicia-Luna (1999)	151
A.8	VLE data for CO ₂ -MeOH from Ohgaki and Katayama (1976)	152
A.9	VLE data for CO ₂ -MeOH from Leu et al (1991)	152
A.10	VLE data for CO ₂ -MeOH from Bezanehtak et al (2002)	153
A.11	VLE data for CO ₂ -MeOH from Joung et al (2001)	153
A.12	VLE data for CO ₂ -MeOH from Brunner et al (1987)	154
A.13	Critical locus data for CO ₂ -EtOH and CO ₂ -MeOH from Chester (2004)	155

UNIVERSITAT ROVIRA I VIRGILI

NUMERICAL AND EXPERIMENTAL ANALYSES OF SINGLE AND TWO-PHASE MICROFLUIDIC FLOWS WITH IMPLICATIONS IN MICROREACTORS

Roland Blanch Ojea

DL:T. 149-2012

Introduction

Contents

1.1	Aim of the thesis	2
1.2	State-of-the-art	3
1.2.1	Gas-phase microreactors	3
1.2.2	Multiphase flows in microchannels	5
1.3	Outline of the thesis	7

Microfluidics is a relatively recent field within Fluid Mechanics which first appeared about half a century ago, and it has a promising future due to its advantages when compared with the conventional macroscopic systems. Basically, the microfluidic flows involve those flow systems at the micro-scale dimensions, with sub-millimetre channel diameters, and its proven advantages include, among others, an improved safety for potentially dangerous systems, such as those operated at high pressures or in explosive atmospheres; an increased surface-to-volume ratio, enhancing the efficiency of several reactive processes and the thermal transfer; or a great capacity for scalability, which allows flexible production processes or the capacity to integrate all the steps of a complex process within a single device, the so-called 'Lab-on-a-chip' or 'Micro-total-analysis-systems' (μ TAS). The potential applications are many, including analytical chemistry, chemistry production, biomedical diagnosis, separation and mixing of fluids, energy production and thermal management. An extensive source of information about microfluidics, including fundamentals, applications and related technologies, can be found in the literature (e.g. Jensen, 2001; Karniadakis et al, 2005; Nguyen and Wereley, 2002; Squires and Quake, 2005).

As a consequence of the reduced sizes in the microfluidic systems, the forces and phenomena that are usually negligible in conventional macroscopic systems turn to be relevant or even predominant in the microscale. This change in the roles results in potentially unexpected or unknown situations that become a continuous scientific challenge.

On the other hand, the continuous advance in the fabrication technology allows to a progressive miniaturization of the microfluidic devices, and then several restrictions and limitations that are not present in the conventional macroscopic system may arise, such as mechanical restrictions in the systems for pumping fluids, or the existence of flow instabilities in parallel microchannels. With the aim to extend the capabilities of

these microfluidic systems, there is a great interest to overcome these limitations and, hence, the investigations in this field are nowadays highly active and they present a great number of possibilities.

1.1 Aim of the thesis

According to the previous introduction, the present PhD thesis is focused in the area of microfluidic reactors, providing two main contributions. The first contribution is related to the numerical simulations of reactive processes within microreactors, whereas the second contribution is related to the experimental characterization of two-phase flows in microchannels, with potential applications for chemical reactions.

The objectives of the numerical contribution of the thesis are,

- First, it aims to develop a complete numerical tool, a code named 3DINAMICS written in Fortran90 language and solved sequentially, able to simulate in detail the transport phenomena in a rectangular microchannel reactor where a set of heterogeneous reactions occurs on its wall surface. Such reactor is to be fed with a multicomponent gas mixture of reagents at low Reynolds numbers and, therefore, the flow will be laminar. The heterogeneous reactions must be properly represented in a detailed kinetic mode, and the behaviour of energy and mass transport in the reactive area has to be properly represented, as well. Important temperature and composition variations are expected to occur within the reactor due to the reactive process and, accordingly, the code should include the effects of this variation. Therefore, the coupled governing equations of continuity, momentum, energy and mass transport of chemical species, of a low-Mach compressible laminar flow must be solved, in a 2D/3D Cartesian coordinates domain. Besides, the code must take into account some of the particularities of the microfluidic systems, such as including the heat conduction through the surrounding wall.
- Once the simulation code is functional, it will be applied to study the heterogeneous catalytic partial oxidation of methane to produce syngas in a straight microreactor with a high aspect ratio. A proper kinetic model for the catalytic partial oxidation of methane has to be previously chosen. The main aim of the study is to identify the operating conditions under which it is feasible the self-sustained operation of the reactor, without external heat sources. A particular effort must be paid to identify the energetic terms that contribute to sustain the temperature of the system, and the terms that contribute to cool down the system and generate a thermal-wave that quenches the reactions. Evaluating the temperature profile within the reactor and predicting the possibility to experience harmful hot spots, is also an objective. Other interests in the study include the analysis of the performance of the reactor under different operating conditions.

The objectives of the experimental contribution of the thesis are,

- To study the feasibility to generate experimental single and multiphase flows of two sets of potentially miscible fluids, CO₂-ethanol (CO₂-EtOH) and CO₂-methanol (CO₂-MeOH), over a non-adiabatic microfluidic T-junction, in order to gain understanding on the behaviour of these systems at different conditions of temperature and pressure. Within such range of conditions, the alcohols will be in liquid state, the CO₂ will be either in liquid, gas or supercritical state, and their mixtures will experience a fully miscible single phase or a separation of immiscible phases in Vapour-Liquid Equilibrium conditions.
- To identify and characterise the single and multiphase flows obtained experimentally and to compare them with previous literature results with single boiling fluids or with immiscible fluids in adiabatic conditions.
- To characterise several parameters of the obtained multiphase flows, especially for the flows suitable to be used in reactive processes, which are the segmented Taylor flow and the stratified smooth flow.

1.2 State-of-the-art

Based on the objectives of the thesis described in the previous section, here it is presented a brief summary of the state-of-the-art on the research topics regarding gas-phase microreactors and multiphase flows in microchannels.

1.2.1 Gas-phase microreactors

Reaction technology is a field permanently looking for controllable, highly productive, selective and environmentally-friendly production methods, and broad number of authors (Fletcher et al, 2002; Kolb and Hessel, 2004; Walter et al, 2005) recognise the outstanding characteristic of micro-channel reactors as their high transfer rates of reaction heat. According to Fletcher et al (2002), the use of microreactors in chemical industry involves many important advantages. For instance, their high surface-to-volume ratio improves the response time, leads to efficient heat transfer and allows maintaining isothermal conditions. Moreover, microreactors can be designed to provide a rapid mixing and to reach a high degree of chemical selectivity. Micro-reactors consist of a network of micron-sized channels etched into a solid substrate, with a maximum section of 0.5 mm. For solution-based chemistry, the channel network is connected to a series of reservoirs containing chemical reagents, products and/or waste to form the complete device or 'chip' with overall dimensions of few centimetres. Reagents can then be brought together in a specific sequence, mixed and allowed to react in a controlled region of the reactor channel network using electrokinetic and/or hydrodynamic pumping during a specified time.

An issue in micro-channel systems is the necessity to understand the fluid distribution in the parallel micro-channel structures required for chemical production. These parallel micro-channels structures are critical for industrial scale-up, since a single reactor provides only a small volume dedicated to reaction. In this regard, [Commenge et al \(2002\)](#) developed and validated an approximate model, based on pressure drop calculations through a resistive network of ducts, that provides rapid calculation of the fluid distribution, and it offers a qualitative understanding of the influence of geometric parameters, and characteristic dimensions, on the quality of fluid distribution among the channels of a micro-structured plate. In addition, the approximate model can be used to design plate geometries resulting in uniform velocity distributions between the channels.

Regarding the catalytic partial oxidation of methane (CPO), the interest of this reaction comes from the certainty that synthesis gas (syngas), a mixture of CO/H₂ with some CO₂, H₂O and sometimes N₂, is nowadays the only economically available via in the route for the conversion of methane (main component of natural gas) into more valuable chemicals. Production of syngas from natural gas can be realized through three main reactive processes, i.e., steam reforming, dry reforming and partial oxidation. At the present time the only large-scale industrial process for producing syngas is the steam reforming, but apparently CPO tends to become more important in the future due to several thermodynamic advantages. The review of [York et al \(2003\)](#) offers an extended background and explains the basics of the reaction. CPO is a catalyst-driven reaction considered to be heterogeneous, even though several authors have also reported homogeneous models [Quiceno et al \(2006\)](#). It has to be noted that CPO kinetics are not well known yet so, a large number of kinetic models and catalysts is proposed in the literature. Although the overall reaction is only slightly exothermic, one of the partial processes involved in the CPO is the highly exothermic total oxidation of methane, which can lead to the appearance of hot-spots in the catalyst wall. This is the main drawback of the CPO and, hence, the possibility to use microreactors, with their improved heat transfer efficiency, turns to be a great advantage.

[Younes-Metzler et al \(2005\)](#) developed a relatively simple and flexible high-temperature experimental set-up using micro-fabricated silicon reactors for the CPO. [Tiggelaar et al \(2004\)](#) designed a microreactor for the rhodium-catalysed investigation of the CPO, which achieved response times of 1 ms for heating up and cooling down the reactive gas, and that was stable for temperatures of at least 700 °C. [Kikas et al \(2003\)](#) built an experimental reverse-flow reactor and reported one of the first preliminary evidences of the significant performance improvement when operating the reactor in auto-thermal reverse-flow conditions, compared to the operation in the usual unidirectional conditions. They also discussed the critical issues in the design of portable catalytic microreactors for small-scale power generation, and proposed a novel, highly integrated planar reactor design, which aimed at optimal functionality, manufacturability, and low cost.

Some work has been recently presented regarding the numerical simulation of CPO

on microreactors. [Kaisare et al \(2005a,b,c\)](#) proposed the design of a device to be used in unidirectional or reverse-flow modes of operation, and studied their pros and cons through an operability analysis. They found that the reverse-flow operation was significantly more robust and gave higher hydrogen yield than the unidirectional operation. Although the system of the present study is not going to be used in reverse-flow operation, some of their conclusions might be useful such as the proven sensitivity of the reactor to the thermal diffusivity of the walls, and to the rate constants of oxidation and reforming reactions.

[Gervais and Jensen \(2006\)](#) studied the so-called Graetz problem, the steady-state diffusion-limited transport to a surface in a pressure-driven flow, and performed an analytical and a numerical simulation analysis for different regimes of diffusion and laminar flow convection, combined with bi-molecular surface reactions relevant to biochemical essays performed in micro-fluid devices. As a result, they characterized the transport to the surfaces in the absence of a boundary layer, proposed a simple approach to obtain the Damköhler number and established the intervals of validity of the entrance region models, developed for surface-based detection systems, that can also be considered as microreactors.

[Raja et al \(2000\)](#) developed, evaluated and established the ranges of validity of three different formulations, for simulating the steady-state flow and the chemistry in a honeycomb channel with similar conditions to the ones of CPO. As expected, Navier-Stokes formulation turned to be suitable for the most general settings but it was computationally expensive. On the other hand, the boundary-layer models provided accurate results for moderate to high Reynolds numbers, at a much lower computational cost. Plug-flow models were computationally inexpensive, but their range of validity was very limited.

1.2.2 Multiphase flows in microchannels

Provided that gas-liquid and liquid-liquid multiphase flows, in both adiabatic and non-adiabatic microchannels, have been proven to differ to their veteran macroscopic counterparts ([Kandlikar, 2002](#); [Thome, 2006](#); [Shao et al, 2009](#)), the study of these microfluidic systems has become nowadays a topic of great interest and, therefore, extensive information can be found in recent publications. In their series of reviews, Shui and her co-workers ([Shui et al, 2007a,b](#)) addressed the different phenomena, the actuation and manipulation methods and the applications of multiphase flows of immiscible fluids in micro- and nanochannels. Their reviewed applications included emulsification, encapsulation, microreaction, chemical synthesis, mixing, bioassay, biological enzymatic degradation, extraction, separation and kinetic studies. The available experimental data dealing with adiabatic gas-liquid flows in microchannels, the existing flow regimes, the influence of different parameters in their transitions and the broad range of flow regime maps previously presented in literature were included in the reviews of [Akbar et al \(2003\)](#) and [Shao et al \(2009\)](#). [Thome \(2006\)](#) and [Kandlikar \(2002\)](#) focused their overviews on flow boiling in single- and multi-microchannels. They summarised the existing two-phase

flow regimes, their corresponding maps and the flow prediction methods, they also discussed about critical heat fluxes, flow instabilities and pressure drops. In their review of the physics behind microfluidics, [Squires and Quake \(2005\)](#) devoted a section to the existing phenomena and available techniques for manipulating and controlling solid-liquid and multiphase fluid systems. [Guido and Preziosi \(2010\)](#) presented a review on experimental and numerical literature concerning the physics of droplet flow behaviour in microchannels, such as deformation and breakup, and the effect of surfactants on the aforementioned behaviour. A recent report of current experimental techniques, methods and limitations for characterizing mixing and flow phenomena of miscible and immiscible fluids has been recently presented by [Aubin et al \(2010\)](#).

One of the main characteristics of multiphase flow in microchannels as compared to macrochannels is a shift in the balance of forces acting on the system: surface tension forces turn to be predominant over others such as viscous, inertial and drag forces, while gravitational forces become negligible ([Garstecki et al, 2006](#); [Günther and Jensen, 2006](#)). Both the respectively high and low values of Confinement number, Co , and its related Eötvös number, $Eö$ (Eq. (1.1)), illustrate the negligible effect of gravitational forces when compared to surface tension forces, and are the basis of some of the main established criteria for differentiating macro- to microchannels, formulated by several researchers ([Brauner and Maron, 1992](#); [Kew and Cornwell, 1997](#); [Triplett et al, 1999](#); [Akbar et al, 2003](#)).

$$Co = Eö^{-1/2} = \left(\frac{\sigma}{g(\rho_l - \rho_v)d_h^2} \right)^{1/2} \quad (1.1)$$

These differences in the balance of forces between micro- and macrochannels lead to discrepancies in the observed flow regimes and in their available prediction methods.

Although most of the work on multiphase flow in microchannels so far has been devoted either to boiling flows of single fluids in non-adiabatic conditions (e.g. [Revellin et al, 2006](#); [Agostini et al, 2008](#); [Revellin et al, 2008](#)), or to flows of immiscible fluids in adiabatic conditions, with each fluid present exclusively in one of the phases (e.g. [Kawahara et al, 2002](#); [Chung and Kawaji, 2004](#); [Guillot and Colin, 2005](#); [Garstecki et al, 2006](#); [de Loos et al, 2010](#)), the use of potentially miscible fluids is also feasible. A two-phase flow of two potentially miscible fluids can be achieved if the mixture, originally in a miscible single phase, is taken to certain temperature and pressure conditions where its thermodynamic phase equilibrium, also known as Vapour-Liquid Equilibrium (VLE), occurs ([Smith et al, 2000](#)). In VLE, the mixture splits into two coexisting, separated, immiscible liquid and vapour phases. However, unlike the usual flows of immiscible fluids in adiabatic conditions, here there is a mass transport of each fluid to both immiscible phases, in a proportion specific to the temperature and pressure conditions.

Two-phase flow systems of fluids experiencing VLE can be applied to generate fluid micromixers or microreactors. These benefit from the control of the composition of liquid and vapour phases by selecting the appropriate temperature and/or pressure conditions. The possibility to manipulate the surface tension forces, which are important in the

dynamics of flows in microfluidic channels, is another interesting feature. On the other hand, the unique properties of supercritical fluids, i.e. their easily tunable physical properties, their high diffusivity and their zero surface tension, make them very attractive for a number of applications not only at macro- but also at micro- and nanoscales (Chehroudi, 2006). CO₂ has gained special attention among these supercritical fluids. It is cheap, non-flammable, non-toxic, environmentally friendly, with a moderate critical point (7.37 MPa and 304.2 K), and it is advantageous in a broad range of applications such as extraction processes, cooling in microchannels (e.g. Cheng et al, 2008), or as reaction solvent in microreactors (e.g. Trachsel et al, 2009).

Few related studies with fluids experiencing VLE (e.g. Hwang et al, 2005; Weinmueller et al, 2009) or with supercritical fluids (e.g. Dang et al, 2008; Marre et al, 2009) are available in the two-phase flow literature. However, at the studied experimental conditions their equilibrium compositions are as in the usual immiscible fluids without mass transport between phases, with each phase composed exclusively by a single fluid.

1.3 Outline of the thesis

The thesis is composed by three main parts. Part I includes the numerical study of microreactors performing the catalytic partial oxidation of methane. Part II includes the experimental study of two-phase flows of CO₂ and alcohols in a non-adiabatic microfluidic T-junction at high pressures. Finally, Part III includes the Appendices.

Part I comprises Chapters 2 until 6. Chapter 2 introduces the physical problem to be studied in the numerical analysis of microreactors, including the physical domain of the reactor, the kinetic mechanism of the catalytic partial oxidation of methane, and the characteristics of the gas flow. Chapter 3 develops the mathematical model used for the resolution of the physical problem, including the governing equations, the properties of the gas, the mathematical formulation of the kinetic mechanism, and a dimensional analysis of the equations. Chapter 4 describes the numerical methodology applied in the simulation code to solve the mathematical model of the microreactor, including the numerical techniques, the grid choice for the computational domain, the applicable boundary conditions and some stability concepts. Chapter 5 presents the results of the simulation code applied to the study of the microreactor performing the catalytic partial oxidation of methane, including the distribution of the relevant variables, the performance of the reactor and the energetic analysis of a base case, and the analysis of the response of the reactor to the variation of different operating parameters. Finally, Chapter 6 includes the concluding remarks of Part I of the thesis.

Part II comprises Chapters 7 until 10. Chapter 7 provides theoretical knowledge of several concepts useful for Part II, including the phase behaviour of Type I binary mixtures, the properties of the fluids involved in the study, the two-phase flows, the capillary pumping and the wetting processes. Chapter 8 describes the methodology of the experiments, including the experimental facilities, the operating conditions, several

issues encountered during the experiments, and the procedure for processing the data obtained during the experiments. Chapter 9 presents the results of the study, including the flow regimes obtained, the maps of these regimes, the analysis of the void fraction of the flows, the characterisation of several hydrodynamic parameters of Taylor flow, and the report of an unexpected phenomenon of accumulation of liquid in the vapour channel. Finally, Chapter 10 includes the concluding remarks of Part II of the thesis.

The Appendices in Part III include literature data of the phase behaviour of the mixtures of CO₂-ethanol and CO₂-methanol (Part II), and the description of the development of the equation for the approximate estimation of the velocity of CO₂ in the T-junction (Part II).

Part I

Numerical simulation of a microreactor performing the catalytic partial oxidation of methane

UNIVERSITAT ROVIRA I VIRGILI

NUMERICAL AND EXPERIMENTAL ANALYSES OF SINGLE AND TWO-PHASE MICROFLUIDIC FLOWS WITH IMPLICATIONS IN MICROREACTORS

Roland Blanch Ojea

DL:T. 149-2012

The Physical Problem

Contents

2.1	Physical domain	11
2.2	Reaction mechanism	12
2.3	Flow conditions	13

This first chapter of Part I introduces the physical problem to be studied in the numerical analysis of microreactors. The chapter comprises the description of the geometry, the boundaries and the different elements of the physical domain of the reactor (Sect. 2.1); the description of the nature of the reaction of CPO and its kinetic mechanism (Sect. 2.2); and the description of the nature and the characteristics of the gas flow within the microchannel reactor (Sect. 2.3).

2.1 Physical domain

A straight rectangular microchannel reactor, where the catalytic partial oxidation of methane (CPO) is performed heterogeneously to produce synthesis gas, is under consideration here. The CPO occurs as a gas phase reaction in a layer of catalyst loaded in the walls of the channel, and its reaction mechanism is presented later in Section 2.2. In the channel there is a constant inlet flow containing a homogeneous gas mixture of reagents and an outlet flow of products, remaining reagents and intermediate species. This flow is coupled with the processes of multicomponent mass and heat transfer, and it is to be studied numerically together with the reactive processes in the catalytic layer. The heat conduction through the solid walls surrounding microreactor channels has been proven to be of importance in many occasions (Stutz and Poulikakos, 2005; Grimm and Mazumder, 2008) and, therefore, the conductive wall is included in the physical domain of the study. Accordingly, the fluid-solid interface between the wall and the channel is where the catalyst is loaded and where the reaction is to occur. For sake of simplicity, this catalyst layer is assumed to have no physical thickness and then, it has no significance to the dimensions of the domain. This situation, in which the heat distribution through the surroundings of the channel and its interaction with the flow is taken into account, is commonly known as *conjugate heat transfer*, and it has been widely considered in many situations besides microreactors, for instance in microchannels (Maranzana

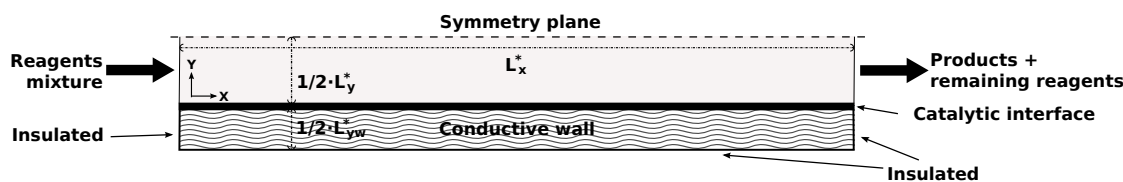


Figure 2.1: Sketch of the computational domain. The aspect ratio is set to $L_x^* = L_x/L_c = 30$, $L_y^* = L_y/L_c = 1$, $L_{yw}^* = L_{yw}/L_c = 0.6$.

et al, 2004) and in microchannel heat sinks (Li and Peterson, 2007).

For the purposes of the numerical study, a two-dimensional (2D) simulation will be performed and, therefore, only a sliced portion of the reactor is considered as computational domain, assuming symmetry in the direction of the neglected dimension. The portion of the reactor considered is shown in the sketch of Figure 2.1. The sketch includes the different elements of the microchannel reactor, i.e. the channel itself, the conductive wall and the catalytic interface, as well as the boundary conditions and the relevant dimensions of the domain. The presence of a symmetry plane in the stream-wise direction, i.e. the direction parallel to the wall, allows to exclude half of the total 2D physical domain. The external parts of the conductive wall are supposed to be insulated. This assumption would be particularly valid with a bunch of reactors placed in parallel, side-by-side. As already mentioned, there is a continuous feed of reagents mixture with uniform conditions along the entrance. On the other hand, the outlet of the reactor will hardly present fully developed conditions, due to the reactive process all along the channel. The channel width is chosen as the characteristic length of the system, $L_c = L_y$, and thus, the corresponding aspect ratios of channel length, channel width and wall width are $L_x^* = L_x/L_c = 30$, $L_y^* = L_y/L_c = 1$, $L_{yw}^* = L_{yw}/L_c = 0.6$, respectively. Please note that the computational domain only includes $1/2 \cdot L_y^*$ and $1/2 \cdot L_{yw}^*$ according to the selected configuration of the cross-section of the channel.

2.2 Reaction mechanism

Nowadays there is no full knowledge, yet, of the detailed reaction mechanism for the conversion of methane to synthesis gas via the catalytic partial oxidation, which can be formulated as an overall reaction with the form of $\text{CH}_4 + 0.5\text{O}_2 \rightarrow \text{CO} + 2\text{H}_2$. Nevertheless, several general mechanisms have been proposed and the theory of an indirect reaction occurring in several steps, with an initial exothermic phase followed by endothermic processes, is widely accepted (Gosiewski et al, 1999; York et al, 2003).

Accordingly, the kinetic reaction mechanism proposed by Gosiewski et al (1999) and subsequently adapted and used by Kaisare et al (2005a,b,c), is adopted here. This mechanism was tested in Kaisare et al (2005a) against other proposed mechanisms, and it proved to be suitable for a wider range of operating conditions and to be able to reproduce the experimental results of Kikas et al (2003). The mechanism consists of a

2.3. Flow conditions

13

Table 2.1: Reaction mechanism for the catalytic partial oxidation of methane, based on Gosiewski et al (1999) and Kaisare et al (2005a)

Overall reaction	Formulation	$\Delta\bar{H}_{298}^o/\text{J kmol}^{-1}$
Partial oxidation	$\text{CH}_4 + 0.5\text{O}_2 \rightarrow \text{CO} + 2\text{H}_2,$	-3.75×10^7
Partial reactions	Formulation	$\Delta\bar{H}_{298}^o/\text{J kmol}^{-1}$
Total oxidation	$\text{CH}_4 + 2\text{O}_2 \rightarrow \text{CO}_2 + 2\text{H}_2\text{O}_g,$	-8.020×10^8
Steam reforming	$\text{CH}_4 + \text{H}_2\text{O}_g \leftrightarrow \text{CO} + 3\text{H}_2,$	$+2.061 \times 10^8$
Water-gas shift	$\text{CO} + \text{H}_2\text{O}_g \leftrightarrow \text{CO}_2 + \text{H}_2,$	-4.115×10^7

set of three linearly independent reactions involved in the overall CPO, i.e. the total oxidation of methane (OXI), a reversible steam reforming reaction (REF) and a reversible water-gas shift reaction (WGS). The reaction mechanism with the overall reaction, the set of partial reactions and their corresponding standard heats of reaction, is indicated in Table 2.1, while the kinetic equations of reaction rates, r , for the partial reactions are as follows,

$$r_{OXI} = 2.306 \times 10^4 e^{-1.00320 \times 10^8/(\mathcal{R}T)} C_{CH_4} C_{O_2} \quad (2.1)$$

$$r_{REF} = 7.616 \times 10^4 e^{-1.14120 \times 10^8/(\mathcal{R}T)} C_{CH_4} C_{H_2O} \left(1 - \frac{\prod_{\alpha} p_{\alpha}^{st_{\alpha,REF}}}{K_{eq,p,REF}} \right) \quad (2.2)$$

$$r_{WGS} = 4.12 \times 10^2 e^{-3.8130 \times 10^7/(\mathcal{R}T)} C_{CO} C_{H_2O} \left(1 - \frac{\prod_{\alpha} p_{\alpha}^{st_{\alpha,WGS}}}{K_{eq,p,WGS}} \right) \quad (2.3)$$

where the different terms within these equations will be defined later in Chapter 3.

As shown in Table 2.1, the overall enthalpy balance of the reaction is slightly exothermic, although the presence of the highly exothermic OXI reaction is a potential source of large temperature gradients and of hot spots. In fact, the OXI reaction is expected to provide the heat necessary to sustain the endothermic REF reaction, which is in turn the main source of synthesis gas.

2.3 Flow conditions

According to the reaction mechanism already presented, the multicomponent gas flow in the channel is composed of up to six different chemical species ($N = 6$), CH_4 and O_2 as reagents, CO and H_2 as products, and CO_2 and H_2O_g (steam) as intermediate species. The gas mixture is assumed to follow the ideal gas law of thermodynamics. Due to the nature of the reactive system, a broad range of temperatures and important variations in the gas composition are expected to occur in time and within the physical domain, and these will lead to remarkable variations in the transport and thermodynamic properties

of the gas mixture. Therefore, the properties of the gas including density, dynamic viscosity, thermal conductivity, mass diffusivity and heat capacity are considered to be dependent on temperature and mixture composition. On the other hand, the physical properties of the conductive wall, i.e. density, thermal conductivity and heat capacity, are assumed to be constant.

The flow in the channel is pressure driven and, according to the typical low Reynolds numbers of microfluidic flows, it is assumed to be laminar and it will thus be correspondingly modelled. However, the density variations within the flow are large enough as to be considered as low-Mach number compressible flow. The absolute pressure in the reactor is assumed to be constant at atmospheric value inasmuch as it is an open, gas-phase system. Besides, the buoyancy/gravitational forces, the viscous dissipation effect and the radiation effect in the flow are neglected. It is well known that buoyancy/gravitational forces play a negligible role in microfluidic systems due to the reduced sizes of these systems. Regarding the viscous dissipation effect, although it has been demonstrated to be of importance for liquid flows in microchannels with $d_h < 100 \mu\text{m}$ (Morini, 2005), the viscous heating can still be usually neglected in gas-phase systems. As for radiation, despite the high temperatures that can be reached by the solid wall in the present work, it has been already proven that radiation effects can be neglected in microchannels, especially in those with high length/width aspect ratio (Kaisare et al, 2005a; Schneider et al, 2006). Finally, the possible effects of the catalyst to the flow, such as those related to roughness and to adsorption/desorption phenomena, are also not taken into account here.

The nature of the reaction mechanism is intimately linked to the thermal conditions of the flow, and therefore several considerations must be clear for the operation of the system. First, a continuous source of heat is necessary to satisfy the energetic requirements and to sustain the overall system of reactions. Usually, there are no external heat sources during the operation, and the highly exothermic reaction of total oxidation of methane is the main provider of this required heat. However, this system of reactions is not viable at atmospheric pressures and low temperatures, it needs a high initial temperature to overcome the kinetic barrier (to reach its ignition point) and to be initiated. Depending on the mixture composition of the inlet feed, in the present case the ignition temperatures of the total oxidation of methane are in the range of 1000 K to 1200 K, in agreement with Kikas et al (2003) and Kaisare et al (2005a). On the other hand, a broad range of ignition temperatures for different kinetic models of CPO have been reported, from 500 K to 1120 K (York et al, 2003; Schwiedernoch et al, 2003; Hannemann et al, 2007; Stutz and Poulikakos, 2005). This initial temperature required to initiate the reaction is usually achieved preheating the whole reactor in a furnace (Schwiedernoch et al, 2003) or with heating elements placed on one side of the channel (Tiggelaar et al, 2004; Srinivasan et al, 1997). Also, sometimes the temperature in the reactor is gradually ramped during operation until the reaction ignites (Younes-Metzler et al, 2005). In the present case, the whole reactor, including the surrounding wall, is assumed to be

preheated, and this will be reflected in the initial conditions of temperature during the simulations.

Usually, after the reactive system is initiated the gas mixture of reagents is fed into the reactor at lower, near-room temperatures. This is also the operating method selected for the present work. As a result, it arises the risk to generate a low temperature thermal wave that will propagate with time from the entrance towards the exit of the reactor, inducing a decrease in the temperature of the channel and eventually quenching the reactions. Several types of reactors have been designed to take profit of these thermal waves, such as the reverse-flow reactors where the flow direction is reversed before the thermal wave quenches completely the reactions (Kikas *et al*, 2003). However, the present work aims to find the operating conditions at which the system can operate in thermally self-sustained mode without external support, thus avoiding the appearance of these thermal waves.

UNIVERSITAT ROVIRA I VIRGILI

NUMERICAL AND EXPERIMENTAL ANALYSES OF SINGLE AND TWO-PHASE MICROFLUIDIC FLOWS WITH IMPLICATIONS IN MICROREACTORS

Roland Blanch Ojea

DL:T. 149-2012

Mathematical Model

Contents

3.1 Preliminary definitions	18
3.1.1 Notation and relations for mass and molar concentrations	18
3.1.2 Ideal gas law	18
3.2 Physical properties of the gas	18
3.2.1 Density	19
3.2.2 Dynamic viscosity	19
3.2.3 Thermal conductivity	19
3.2.4 Mass diffusivity	20
3.2.5 Heat capacity	21
3.3 Governing equations	22
3.3.1 Overall mass conservation (continuity)	22
3.3.2 Momentum	22
3.3.3 Mass conservation of chemical species	23
3.3.4 Thermal energy in the fluid	24
3.3.5 Thermal energy in the wall	30
3.4 Catalytic fluid-wall interface	30
3.4.1 Reaction kinetics	30
3.4.2 Balances for interface mass and energy transfer	33
3.5 Dimensional analysis	34
3.5.1 Non-dimensional variables and groups	34
3.5.2 Physical properties of the gas	35
3.5.3 Governing equations	35
3.5.4 Catalytic fluid-wall interface	38

The following mathematical model is formulated to solve the physical model described in Chapter 2.

3.1 Preliminary definitions

This section presents a set of preliminary definitions related to concentrations and thermodynamics of multicomponent solutions, and to the law of thermodynamics for ideal gases. These definitions are of use in the present mathematical model.

3.1.1 Notation and relations for mass and molar concentrations

The definitions and several useful relations for mass and mole fraction of chemical species α , ω_α and y_α , for mass density and molar concentration of chemical species α , ρ_α and C_α , for mass density and molar concentration of the gas mixture, ρ and C , for the molecular weight of chemical species α , M_α , and for the molar mean molecular weight of the gas mixture, \bar{M} , are presented here (Bird et al, 2001),

$$\omega_\alpha = \frac{\rho_\alpha}{\rho} \quad (3.1)$$

$$y_\alpha = \frac{C_\alpha}{C} = \omega_\alpha \frac{\bar{M}}{M_\alpha} \quad (3.2)$$

$$C_\alpha = \rho_\alpha / M_\alpha \quad (3.3)$$

$$\bar{M} = \frac{\rho}{C} = \frac{1}{\sum_\alpha (\omega_\alpha / M_\alpha)} \quad (3.4)$$

3.1.2 Ideal gas law

According to the law of thermodynamics for ideal gases,

$$p = \rho RT \quad (3.5)$$

$$p_\alpha = y_\alpha p = C_\alpha \mathfrak{R} T \quad (3.6)$$

where p_α is the partial pressure of chemical species α , $\mathfrak{R} = 8314 \text{ J kmol}^{-1} \text{ K}^{-1}$ is the universal gas constant and R is the gas constant, defined as,

$$R = \frac{\mathfrak{R}}{\bar{M}} \quad (3.7)$$

3.2 Physical properties of the gas

As mentioned in Section 2.3, the properties of the gas mixture including density, ρ , dynamic viscosity, μ , thermal conductivity, κ , mass diffusivity, D , and heat capacity, c_p , are considered to be dependent on temperature and mixture composition, and they are properly calculated as described herein. The use of the database of fluid thermodynamic and transport properties from the National Institute of Standards and Technology (NIST), the software package REFPROP v8.0 (Lemmon et al, 2007), has been discarded for the calculation of the properties due to limitations of the package with the present working gas mixture. A detailed description for most of the theories, formulas and relationships

3.2. Physical properties of the gas

19

applied in the calculation of these properties, as well as their authorship, can be found in [White \(1991\)](#) and [Bird et al \(2001\)](#).

3.2.1 Density

The density of the gas mixture is calculated using the law of thermodynamics for ideal gases formulated in Equation (3.5).

3.2.2 Dynamic viscosity

The dynamic viscosity of a single specie α in the mixture, μ_α , is calculated using the Chapman-Enskog kinetic theory of nonpolar monoatomic gases at low density. Note that, although this theory is valid for monoatomic gases, it has been found to be remarkably accurate for polyatomic gases as well ([Bird et al, 2001](#)). The formula is therefore as follows,

$$\mu_\alpha = 2.6693 \times 10^{-6} \frac{\sqrt{M_\alpha T}}{\sigma_\alpha^2 \Omega_{\mu,\alpha}} \quad (3.8)$$

where $\Omega_{\mu,\alpha}$ is the collision integral for viscosity,

$$\Omega_{\mu,\alpha} = \frac{1.16145}{T''^{0.14874}} + \frac{0.52487}{\exp(0.77320 \cdot T'')} + \frac{2.16178}{\exp(2.43787 \cdot T'')} \quad (3.9)$$

$$T'' = T \left/ \frac{\varepsilon_\alpha}{K} \right. \quad (3.10)$$

where T'' is a dimensionless temperature parameter and ε_α/K is the Lennard-Jones intermolecular potential of species α .

The dynamic viscosity of the gas mixture, μ , is calculated with the semiempirical formula developed by C. R. Wilke,

$$\mu = \sum_\alpha \frac{y_\alpha \mu_\alpha}{\sum_\beta y_\beta \Theta_{\alpha\beta}} \quad (3.11)$$

where α and β are the species of the multicomponent gas mixture and $\Theta_{\alpha\beta}$ is a dimensionless parameter,

$$\Theta_{\alpha\beta} = \frac{1}{\sqrt{8}} \left(1 + \frac{M_\alpha}{M_\beta} \right)^{-1/2} \left[1 + \left(\frac{\mu_\alpha}{\mu_\beta} \right)^{1/2} \left(\frac{M_\beta}{M_\alpha} \right)^{1/4} \right]^2 \quad (3.12)$$

3.2.3 Thermal conductivity

The Chapman-Enskog kinetic theory used to calculate μ_α is not valid for calculating the thermal conductivity of polyatomic gases. Therefore, the formula developed by Eucken

for polyatomic gases is used, instead, for calculating the thermal conductivity of a single specie α in the mixture, κ_α . The formula is as follows,

$$\kappa_\alpha = \left(c_{p,\alpha} + \frac{5}{4} \frac{\mathfrak{R}}{M_\alpha} \right) \mu_\alpha \quad (3.13)$$

The thermal conductivity of the gas mixture, κ , is calculated using the equation developed by E. A. Mason and S. C. Saxena and modified by Bird et al (2001). This equation and its development method are analogous to Eq. (3.11),

$$\kappa = \sum_\alpha \frac{y_\alpha \kappa_\alpha}{\sum_\beta y_\beta \Theta_{\alpha\beta}} \quad (3.14)$$

where $\Theta_{\alpha\beta}$ is already defined in Eq. (3.12).

3.2.4 Mass diffusivity

Molecular diffusion in multicomponent systems is an extremely complex topic. Two main theories have been formulated which describe accurately this phenomena, the Maxwell-Stefan relations and equations, and the generalized Fick's Law for multicomponent systems. Unfortunately, these are complex theories and, when implemented in numerical methods, they are highly demanding of computing resources. For this reason, a simpler approach called effective diffusivity has been successfully implemented and widely used in the past for solving multicomponent diffusion problems (e.g. Deutschmann et al, 2007; Stutz and Poulikakos, 2005). This is, thus, the approach used in the present work. Nevertheless, it must be kept in mind that this approach is based on several fundamental idealizations and simplifications and, then, it presents many limitations. These limitations have been usually neglected in previous studies, though. A complete discussion and analysis of this topic is beyond the scope of the present study, and the book of Taylor and Krishna (1993) is highly recommended for the interested reader.

According to the previous hypotheses, the Chapman-Enskog kinetic theory is again used to obtain the product of density and mass binary diffusivity of a pair of chemical species (Bird et al, 2001),

$$\rho D_{\alpha,\beta} = C' \frac{\bar{M} \sqrt{T (1/M_\alpha + 1/M_\beta)}}{\sigma_{\alpha\beta}^2 \Omega_{D,\alpha\beta}} \quad (3.15)$$

$$C' = \frac{3 \times 10^{20}}{16} \frac{\sqrt{2\mathfrak{R}/\pi}}{\tilde{N}} = 2.2651 \times 10^{-6}$$

where $\tilde{N} = 6.022 14 \times 10^{26}$ molecules kmol⁻¹ is the Avogadro's number, $\sigma_{\alpha\beta}$ is a function of the Lennard-Jones collision diameters of species α and β , σ_α and σ_β , and $\Omega_{D,\alpha\beta}$ is

3.2. Physical properties of the gas

21

the collision integral for diffusion,

$$\sigma_{\alpha\beta} = \frac{1}{2}(\sigma_{\alpha} + \sigma_{\beta}) \quad (3.16)$$

$$\Omega_{D,\alpha\beta} = \frac{1.06036}{T''^{0.15610}} + \frac{0.19300}{\exp(0.47635 \cdot T'')} + \frac{1.03587}{\exp(1.52996 \cdot T'')} + \frac{1.76474}{\exp(3.89411 \cdot T'')} \quad (3.17)$$

$$T'' = T \left/ \sqrt{\frac{\varepsilon_{\alpha}}{K} \frac{\varepsilon_{\beta}}{K}} \right. \quad (3.18)$$

The product of density and mass effective diffusivity of a specie is calculated using the formula developed by C. R. Wilke (Taylor and Krishna, 1993),

$$\rho D_{eff,\alpha} = \left[(1 - y_{\alpha}) \left/ \sum_{\substack{\beta \\ \beta \neq \alpha}} \frac{y_{\beta}}{\rho D_{\alpha,\beta}} \right. \right] \quad (3.19)$$

Please note that, as already mentioned, this formula gives accurate results in very few situations.

The Equations (3.15) and (3.19) for the mass diffusivity have been formulated as a product with ρ , for practical reasons related with the formulation of the governing equations for the chemical species (See Sect. 3.3.3).

3.2.5 Heat capacity

The standard heat capacity at constant pressure of a specie α , $c_{p,\alpha}^o$, is calculated by the Shomate equation of gas phase proposed in the NIST Chemistry WebBook (NIST, 2009),

$$\frac{c_{p,\alpha}^o \cdot M_{\alpha}}{10^3} = A_{sh,\alpha} + B_{sh,\alpha} \cdot T_{sh} + C_{sh,\alpha} \cdot T_{sh}^2 + D_{sh,\alpha} \cdot T_{sh}^3 + E_{sh,\alpha}/T_{sh}^2 \quad (3.20)$$

where $A_{sh,\alpha}$ to $E_{sh,\alpha}$ are the coefficients of specie α for the Shomate equation, and T_{sh} is the dimensionless temperature for the Shomate equation,

$$T_{sh} = T/10^3 \quad (3.21)$$

The thermodynamic summability relation (Eq. (3.47)) described in Section 3.3.4.2 is used to calculate the heat capacity of the mixture, c_p ,

$$c_p = \sum_{\alpha} \omega_{\alpha} c_{p,\alpha} \quad (3.22)$$

where the next equality is assumed: $c_{p,\alpha} = c_{p,\alpha}^o$.

3.3 Governing equations

As mentioned in Section 2.3 a set of low-Mach number compressible transient governing equations of a multicomponent Newtonian fluid flow, where density changes due to temperature and composition variations, is formulated in Cartesian coordinates. These are the equations of overall mass conservation (continuity), momentum, mass conservation for each chemical specie, thermal energy in the fluid and thermal energy in the conductive solid wall. Note that, for compactness reasons, the equations are presented in vector and tensor notation whenever possible. This section does not, either, engage in detail the formulation and development of these governing equations, but rather presents them in a way as direct as possible, for practical reasons. The only exception to this is the equation for thermal energy in the fluid, which requires a special treatment due to its complexity, and it is therefore developed in detail. The books of Bird et al (2001) and Kays et al (2004), which offer detailed information on this topic, are recommended for the interested reader.

3.3.1 Overall mass conservation (continuity)

The governing equation for overall mass conservation, also known as equation of continuity, is formulated as,

$$\frac{\partial}{\partial t}\rho + (\nabla \cdot \rho\mathbf{v}) = 0 \quad (3.23)$$

where the first term in the left hand side of the equation is the temporal variation of ρ , and \mathbf{v} is the velocity vector.

3.3.2 Momentum

The governing equation for momentum in the x , y and z directions is expressed in its general form as,

$$\frac{\partial}{\partial t}\rho\mathbf{v} + [\nabla \cdot \rho\mathbf{v}\mathbf{v}] = -[\nabla p] - [\nabla \cdot \boldsymbol{\tau}] \quad (3.24)$$

where the viscous stress tensor, $\boldsymbol{\tau}$, is,

$$\boldsymbol{\tau} = -\mu(\nabla\mathbf{v} + (\nabla\mathbf{v})^\dagger) + \frac{2}{3}\mu(\nabla \cdot \mathbf{v})\boldsymbol{\delta} \quad (3.25)$$

The different components of $\boldsymbol{\tau}$ in the i^{th} and j^{th} directions are,

$$\tau_{ij} = -\mu\left(\frac{\partial v_j}{\partial x_i} + \frac{\partial v_i}{\partial x_j}\right) + \frac{2}{3}\mu(\nabla \cdot \mathbf{v})\delta_{ij} \quad (3.26)$$

where v_i and v_j are the components of \mathbf{v} in the i^{th} and j^{th} directions, x_i and x_j are the length steps in the i^{th} and j^{th} directions, and δ_{ij} is known as the Kronecker delta,

$$\delta_{ij} = \begin{cases} 1, & \text{if } i = j, \\ 0, & \text{if } i \neq j \end{cases}$$

Developing $-\nabla \cdot \boldsymbol{\tau}$ in each direction it gives,

$$\begin{aligned} & -[\nabla \cdot \boldsymbol{\tau}]_x \\ &= -\left[\frac{\partial}{\partial x} \tau_{xx} + \frac{\partial}{\partial y} \tau_{yx} + \frac{\partial}{\partial z} \tau_{zx} \right] \\ &= \nabla \cdot (\mu \nabla u) + \frac{\partial}{\partial x} \left(\mu \frac{\partial u}{\partial x} \right) + \frac{\partial}{\partial y} \left(\mu \frac{\partial v}{\partial x} \right) + \frac{\partial}{\partial z} \left(\mu \frac{\partial w}{\partial x} \right) - \frac{2}{3} \left(\frac{\partial}{\partial x} \mu \nabla \cdot \mathbf{v} \right) \end{aligned} \quad (3.27)$$

$$\begin{aligned} & -[\nabla \cdot \boldsymbol{\tau}]_y \\ &= -\left[\frac{\partial}{\partial x} \tau_{xy} + \frac{\partial}{\partial y} \tau_{yy} + \frac{\partial}{\partial z} \tau_{zy} \right] \\ &= \nabla \cdot (\mu \nabla v) + \frac{\partial}{\partial x} \left(\mu \frac{\partial u}{\partial y} \right) + \frac{\partial}{\partial y} \left(\mu \frac{\partial v}{\partial y} \right) + \frac{\partial}{\partial z} \left(\mu \frac{\partial w}{\partial y} \right) - \frac{2}{3} \left(\frac{\partial}{\partial y} \mu \nabla \cdot \mathbf{v} \right) \end{aligned} \quad (3.28)$$

$$\begin{aligned} & -[\nabla \cdot \boldsymbol{\tau}]_z \\ &= -\left[\frac{\partial}{\partial x} \tau_{xz} + \frac{\partial}{\partial y} \tau_{yz} + \frac{\partial}{\partial z} \tau_{zz} \right] \\ &= \nabla \cdot (\mu \nabla w) + \frac{\partial}{\partial x} \left(\mu \frac{\partial u}{\partial z} \right) + \frac{\partial}{\partial y} \left(\mu \frac{\partial v}{\partial z} \right) + \frac{\partial}{\partial z} \left(\mu \frac{\partial w}{\partial z} \right) - \frac{2}{3} \left(\frac{\partial}{\partial z} \mu \nabla \cdot \mathbf{v} \right) \end{aligned} \quad (3.29)$$

where u , v and w are the different velocity components in each direction and x , y and z are the length steps in each direction.

3.3.3 Mass conservation of chemical species

The governing equation for the mass conservation of a specie α is formulated as,

$$\frac{\partial}{\partial t} \rho_\alpha = -(\nabla \cdot \mathbf{n}_\alpha) + Sp_\alpha \quad (3.30)$$

where Sp_α is the production source term of specie α , and the combined mass flux vector of a specie α , \mathbf{n}_α , is,

$$\mathbf{n}_\alpha = \mathbf{j}_\alpha + \rho_\alpha \mathbf{v} \quad (3.31)$$

where \mathbf{j}_α is the molecular mass flux vector of a specie α . Then, applying Eq. (3.1),

$$\frac{\partial}{\partial t} \rho \omega_\alpha + (\nabla \cdot \rho \omega_\alpha \mathbf{v}) = -(\nabla \cdot \mathbf{j}_\alpha) + Sp_\alpha \quad (3.32)$$

Also, since there is no homogeneous reaction within the fluid, the associated production term of species in the fluid disappears, $Sp_\alpha = 0$, and,

$$\frac{\partial}{\partial t} \rho \omega_\alpha + (\nabla \cdot \rho \omega_\alpha \mathbf{v}) = -(\nabla \cdot \mathbf{j}_\alpha) \quad (3.33)$$

where \mathbf{j}_α is,

$$\mathbf{j}_\alpha = -\rho D_{eff,\alpha} \nabla \omega_\alpha \quad (3.34)$$

One of the main advantages of the effective diffusivity approach, presented in Section 3.2.4, is its simplicity because, as it can be observed, it allows to formulate \mathbf{j}_α in a very similar way to the Fick's first diffusion law for binary mixtures. On the other hand, other components contributing to \mathbf{j}_α such as the thermal diffusion, also known as Soret effect, are not taken into account here (Bird et al, 2001; Taylor and Krishna, 1993).

Finally, due to the relation between the overall mass conservation and the mass conservation of chemical species, the next two equalities must be always accomplished,

$$\sum_{\alpha} \omega_\alpha = 1 \quad (3.35)$$

$$\sum_{\alpha} \mathbf{j}_\alpha = 0 \quad (3.36)$$

3.3.4 Thermal energy in the fluid

The formulation of the governing equation for thermal energy in multicomponent fluids is not straightforward and, therefore, the equation is developed step-by-step here, from its rather fundamental form to a temperature based form suitable to be used in the simulation code. A bunch of preliminary equations and a brief summary about thermodynamics of multicomponent solutions, which will result in several useful equalities to be used in the development of the governing equation, are presented in first place in Sections 3.3.4.1 and 3.3.4.2.

3.3.4.1 Preliminary equations

First, for any scalar property, ϕ , e.g. enthalpy, temperature or mass fraction, the next function applies,

$$\frac{\partial}{\partial t} \rho \phi + (\nabla \cdot \rho \phi \mathbf{v}) = \rho \frac{D\phi}{Dt} + \phi \left(\frac{\partial \rho}{\partial t} + (\nabla \cdot \rho \mathbf{v}) \right) \quad (3.37)$$

where $\frac{D\phi}{Dt}$ is known as the substantial derivative of ϕ ,

$$\frac{D\phi}{Dt} = \frac{\partial \phi}{\partial t} + (\mathbf{v} \cdot \nabla \phi) \quad (3.38)$$

Although the last term in the right hand side of Eq. (3.37) could be eliminated right away according to the equation of continuity (Eq. (3.23)), it is rather kept in the equation and in this way it will usefully appear in the development of the energy equation.

Second, the energy transport due to molecular mass fluxes can be formulated as follows,

$$\begin{aligned} \left(\nabla \cdot \sum_{\alpha} \mathbf{j}_{\alpha} H_{\alpha} \right) &= \sum_{\alpha} (\nabla \cdot \mathbf{j}_{\alpha} H_{\alpha}) \\ &= \sum_{\alpha} (H_{\alpha} (\nabla \cdot \mathbf{j}_{\alpha})) + \sum_{\alpha} ((\mathbf{j}_{\alpha} \cdot \nabla H_{\alpha})) \end{aligned} \quad (3.39)$$

3.3.4.2 Thermodynamics of multicomponent solutions

The simplified summary about thermodynamics of multicomponent solutions presented here has been extracted from [Smith et al \(2000\)](#), and there the interested reader can find an extended and detailed discussion on the topic. Note that, although the summary is focused on enthalpy, it could be also applied to any other thermodynamic property such as internal energy, Gibbs energy and others.

Given an intensive thermodynamic property of a multicomponent solution such as the enthalpy, which is function of temperature, pressure and composition, $H(T, p, \omega_1, \omega_2, \dots, \omega_N)$. The extensive form of this property is still function of temperature, pressure and composition, $mH(T, p, m_1, m_2, \dots, m_N)$, where m is the total mass. Then, the derivative of mH is formulated as follows,

$$d(mH) = \left(\frac{\partial mH}{\partial T} \right)_{p,m} dT + \left(\frac{\partial mH}{\partial p} \right)_{T,m} dp + \sum_{\alpha} \left(\frac{\partial mH}{\partial m_{\alpha}} \right)_{p,T,m_{\beta}} dm_{\alpha} \quad (3.40)$$

where the variables included in the subscript of each derivative term indicate that they have been kept constant. Then, developing the derivative it gives,

$$\begin{aligned} &m dH + H dm \\ &= m \left(\frac{\partial H}{\partial T} \right)_{p,\omega} dT + m \left(\frac{\partial H}{\partial p} \right)_{T,\omega} dp + \sum_{\alpha} \hat{H}_{\alpha} (\omega_{\alpha} dm + m d\omega_{\alpha}) \end{aligned} \quad (3.41)$$

Where \hat{H}_{α} is defined as the partial mass enthalpy of species α in the mixture,

$$\hat{H}_{\alpha} \equiv \left(\frac{\partial mH}{\partial m_{\alpha}} \right)_{p,T,m_{\beta}} \quad (3.42)$$

A partial mass property of a specie α in the mixture represents the variation of the total mixture property due to the addition, at constant T and p , a differential amount of this specie α in the mixture. It is important to note that, by definition, the partial mass property is different than the property of the pure specie α , i.e. $\hat{H}_{\alpha} \neq H_{\alpha}$.

Equation (3.41) results in the following two important equalities, the second one being known as the summability relation,

$$dH = \left(\frac{\partial H}{\partial T} \right)_{p,\omega} dT + \left(\frac{\partial H}{\partial p} \right)_{T,\omega} dp + \sum_{\alpha} \hat{H}_{\alpha} d\omega_{\alpha} \quad (3.43)$$

$$H = \sum_{\alpha} \omega_{\alpha} \hat{H}_{\alpha} \quad (3.44)$$

When an ideal gas is considered, the Gibbs's theorem can be applied. This theorem states that a partial property of a specie α in an ideal gas mixture at T and p , is equal to the property of this pure specie at T and p_{α} . The Gibbs's theorem together with the fact that the enthalpy of an ideal gas can be considered to be independent of pressure, leads to the next equality,

$$\hat{H}_{\alpha}(T, p) = H_{\alpha}(T, p_{\alpha}) = H_{\alpha}(T, p) \quad (3.45)$$

Then, the equalities in Eqs. (3.43) and (3.44) turn into,

$$dH = \left(\frac{\partial H}{\partial T} \right)_{p,\omega} dT + \left(\frac{\partial H}{\partial p} \right)_{T,\omega} dp + \sum_{\alpha} H_{\alpha} d\omega_{\alpha} \quad (3.46)$$

$$H = \sum_{\alpha} \omega_{\alpha} H_{\alpha} \quad (3.47)$$

This form of the summability relation (Eq. (3.47)) is also applicable to c_p (See Sect. 3.2.5).

Eq. (3.46) can be further developed with the fundamental thermodynamic dependence of H with T and p ,

$$\left(\frac{\partial H}{\partial T} \right)_{p,\omega} = c_p \quad (3.48)$$

$$\left(\frac{\partial H}{\partial p} \right)_{T,\omega} = \varrho - T \left(\frac{\partial \varrho}{\partial T} \right)_{p,\omega} \quad (3.49)$$

which results in,

$$dH = c_p dT + \left(\varrho - T \left(\frac{\partial \varrho}{\partial T} \right)_{p,\omega} \right) dp + \sum_{\alpha} H_{\alpha} d\omega_{\alpha} \quad (3.50)$$

where ϱ is the specific volume,

$$\varrho = 1/\rho \quad (3.51)$$

Note that the equalities in Eqs. (3.48) and (3.49) must be accomplished not only at constant T and p , but also at constant ω . Eq. (3.50) is especially meaningful in the sense that it shows that for multicomponent mixtures, $c_p \neq dH/dT$ unless the composition of the mixture is uniform or all the $c_{p,\alpha}$'s are equal and there is no chemical reaction (**Kays**

et al, 2004) (it is already assumed that the gas is ideal and the pressure-related term can be eliminated). For this reason, the enthalpy of a mixture can be rarely obtained exclusively from its heat capacity. What is still valid, though, is the definition of $c_{p,\alpha}$,

$$c_{p,\alpha} = \left(\frac{\partial H_\alpha}{\partial T} \right)_{p,\omega} \quad (3.52)$$

Finally, when a number of pure species are mixed at constant T and p there is always a property change of mixing defined for H as,

$$\Delta H_{mix} = H - \sum_{\alpha} \omega_{\alpha} H_{\alpha} \quad (3.53)$$

Then, if the previous assumptions for ideal gases apply (Eqs. (3.45) and (3.47)), the enthalpy change of mixing can be eliminated,

$$\Delta H_{mix} = 0 \quad (3.54)$$

This is the condition assumed in the present work.

3.3.4.3 Development of the energy equation

The equation of change for enthalpy in a multicomponent mixture can be formulated as (Taylor and Krishna, 1993),

$$\frac{\partial}{\partial t} \sum_{\alpha} \rho_{\alpha} \hat{H}_{\alpha} + \left(\nabla \cdot \sum_{\alpha} \mathbf{n}_{\alpha} \hat{H}_{\alpha} \right) = -(\nabla \cdot \mathbf{q}) + \frac{Dp}{Dt} + \mu\Phi \quad (3.55)$$

where \mathbf{q} is the heat flux vector of the multicomponent mixture and Φ is the viscous dissipation function.

Developing the left hand side of the equation with Eqs. (3.31), (3.37), (3.44) and (3.45),

$$\begin{aligned} & \frac{\partial}{\partial t} \sum_{\alpha} \rho_{\alpha} \hat{H}_{\alpha} + \left(\nabla \cdot \sum_{\alpha} \mathbf{n}_{\alpha} \hat{H}_{\alpha} \right) \\ &= \frac{\partial}{\partial t} \sum_{\alpha} \rho_{\alpha} \hat{H}_{\alpha} + \left(\nabla \cdot \sum_{\alpha} (\rho_{\alpha} \hat{H}_{\alpha}) \mathbf{v} \right) + \left(\nabla \cdot \sum_{\alpha} \mathbf{j}_{\alpha} \hat{H}_{\alpha} \right) \\ &= \frac{\partial}{\partial t} \rho H + (\nabla \cdot \rho H \mathbf{v}) + \left(\nabla \cdot \sum_{\alpha} \mathbf{j}_{\alpha} H_{\alpha} \right) \\ &= \rho \frac{DH}{Dt} + H \left(\frac{\partial \rho}{\partial t} + (\nabla \cdot \rho \mathbf{v}) \right) + \left(\nabla \cdot \sum_{\alpha} \mathbf{j}_{\alpha} H_{\alpha} \right) \end{aligned} \quad (3.56)$$

and then reformulating Eq. (3.55) accordingly, it gets,

$$\rho \frac{DH}{Dt} + H \left(\frac{\partial \rho}{\partial t} + (\nabla \cdot \rho \mathbf{v}) \right) = -(\nabla \cdot \mathbf{q}) + \frac{Dp}{Dt} + \mu\Phi - \left(\nabla \cdot \sum_{\alpha} \mathbf{j}_{\alpha} H_{\alpha} \right) \quad (3.57)$$

Now, the first component on the left hand side of the equation can be combined with Eq. (3.50), and result in,

$$\rho \frac{DH}{Dt} = \rho c_p \frac{DT}{Dt} + \left(1 + \frac{\partial \ln \rho}{\partial \ln T}\right) \frac{Dp}{Dt} + \sum_{\alpha} H_{\alpha} \rho \frac{D\omega_{\alpha}}{Dt} \quad (3.58)$$

Then, Eqs. (3.57) and (3.58) give,

$$\begin{aligned} \rho c_p \frac{DT}{Dt} = & -(\nabla \cdot \mathbf{q}) - \left(\frac{\partial \ln \rho}{\partial \ln T}\right) \frac{Dp}{Dt} + \mu \Phi \\ & - \left(\nabla \cdot \sum_{\alpha} \mathbf{j}_{\alpha} H_{\alpha}\right) - \sum_{\alpha} H_{\alpha} \rho \frac{D\omega_{\alpha}}{Dt} - H \left(\frac{\partial \rho}{\partial t} + (\nabla \cdot \rho \mathbf{v})\right) \end{aligned} \quad (3.59)$$

Developing the substantial derivative of mass fractions with Eq. (3.37), the energy transport due to mass fluxes with Eq. (3.39), and using the thermodynamic relationship of Eq. (3.47), it finally gives the general developed form of the energy equation,

$$\begin{aligned} \rho c_p \frac{DT}{Dt} = & -(\nabla \cdot \mathbf{q}) - \left(\frac{\partial \ln \rho}{\partial \ln T}\right) \frac{Dp}{Dt} + \mu \Phi \\ & - \sum_{\alpha} \left[H_{\alpha} \left((\nabla \cdot \mathbf{j}_{\alpha}) + \frac{\partial \rho \omega_{\alpha}}{\partial t} + (\nabla \cdot \rho \omega_{\alpha} \mathbf{v}) \right) + (\mathbf{j}_{\alpha} \cdot \nabla H_{\alpha}) \right] \end{aligned} \quad (3.60)$$

where,

$$\mathbf{q} = -\kappa \nabla T \quad (3.61)$$

$$\Phi = \frac{1}{2} \sum_i \sum_j \left[\left(\frac{\partial v_i}{\partial x_j} + \frac{\partial v_j}{\partial x_i} \right) - \frac{2}{3} (\nabla \cdot \mathbf{v}) \delta_{ij} \right]^2 \quad (3.62)$$

Analogous to the case of \mathbf{j}_{α} (See Sect. 3.3.3), here the component in \mathbf{q} that accounts for the heat transfer due to concentration gradients, known as diffusion-thermo or Dufour effect, is not taken into account (Bird et al, 2001; Taylor and Krishna, 1993). As for the viscous dissipation function, Φ , its development gives different results for two than for three dimensions,

$$\Phi_{2D} = 2 \left[\left(\frac{\partial u}{\partial x} \right)^2 + \left(\frac{\partial v}{\partial y} \right)^2 \right] + \left[\frac{\partial u}{\partial y} + \frac{\partial v}{\partial x} \right]^2 - \frac{8}{9} (\nabla \cdot \mathbf{v})^2 \quad (3.63)$$

$$\begin{aligned} \Phi_{3D} = & 2 \left[\left(\frac{\partial u}{\partial x} \right)^2 + \left(\frac{\partial v}{\partial y} \right)^2 + \left(\frac{\partial w}{\partial z} \right)^2 \right] \\ & + \left[\frac{\partial u}{\partial y} + \frac{\partial v}{\partial x} \right]^2 + \left[\frac{\partial v}{\partial z} + \frac{\partial w}{\partial y} \right]^2 + \left[\frac{\partial w}{\partial x} + \frac{\partial u}{\partial z} \right]^2 - \frac{2}{3} (\nabla \cdot \mathbf{v})^2 \end{aligned} \quad (3.64)$$

3.3.4.4 Forms of the energy equation

Equation (3.60) is the most general formulation of the governing equation of thermal energy based on temperature in a multicomponent fluid, and it can still be further reformulated developing the substantial derivative of the temperature with Eq. (3.37),

$$\begin{aligned}
 & c_p \left(\frac{\partial}{\partial t} \rho T + (\nabla \cdot \rho T \mathbf{v}) \right) \\
 = & -(\nabla \cdot \mathbf{q}) - \left(\frac{\partial \ln \rho}{\partial \ln T} \right) \frac{Dp}{Dt} + \mu \Phi \\
 & - \sum_{\alpha} \left[H_{\alpha} \left((\nabla \cdot \mathbf{j}_{\alpha}) + \frac{\partial \rho \omega_{\alpha}}{\partial t} + (\nabla \cdot \rho \omega_{\alpha} \mathbf{v}) \right) + (\mathbf{j}_{\alpha} \cdot \nabla H_{\alpha}) \right] \\
 & + c_p T \left(\frac{\partial \rho}{\partial t} + (\nabla \cdot \rho \mathbf{v}) \right) \tag{3.65}
 \end{aligned}$$

Now, if the equations of overall mass conservation and of mass conservation of every chemical species (Eqs. (3.23) and (3.32)) are satisfied, the Equations (3.60) and (3.65) result in a simplified form,

$$\begin{aligned}
 & \rho c_p \frac{DT}{Dt} \\
 = & -(\nabla \cdot \mathbf{q}) - \left(\frac{\partial \ln \rho}{\partial \ln T} \right) \frac{Dp}{Dt} + \mu \Phi - \sum_{\alpha} (H_{\alpha} S p_{\alpha} + (\mathbf{j}_{\alpha} \cdot \nabla H_{\alpha})) \tag{3.66}
 \end{aligned}$$

$$\begin{aligned}
 & c_p \left(\frac{\partial}{\partial t} \rho T + (\nabla \cdot \rho T \mathbf{v}) \right) \\
 = & -(\nabla \cdot \mathbf{q}) - \left(\frac{\partial \ln \rho}{\partial \ln T} \right) \frac{Dp}{Dt} + \mu \Phi - \sum_{\alpha} (H_{\alpha} S p_{\alpha} + (\mathbf{j}_{\alpha} \cdot \nabla H_{\alpha})) \tag{3.67}
 \end{aligned}$$

Finally, in the limiting case where there is a single chemical specie, $\omega_{\alpha} = 1$, the next conditions are satisfied,

$$\mathbf{j}_{\alpha} = 0 \tag{3.68}$$

$$\frac{\partial \rho \omega_{\alpha}}{\partial t} + (\nabla \cdot \rho \omega_{\alpha} \mathbf{v}) = \frac{\partial \rho}{\partial t} + (\nabla \cdot \rho \mathbf{v}) = 0 \tag{3.69}$$

and then, Eqs. (3.60) and (3.65) result in the well known energy equations for pure fluids,

$$\rho c_p \frac{DT}{Dt} = -(\nabla \cdot \mathbf{q}) - \left(\frac{\partial \ln \rho}{\partial \ln T} \right) \frac{Dp}{Dt} + \mu \Phi \tag{3.70}$$

$$c_p \left(\frac{\partial}{\partial t} \rho T + (\nabla \cdot \rho T \mathbf{v}) \right) = -(\nabla \cdot \mathbf{q}) - \left(\frac{\partial \ln \rho}{\partial \ln T} \right) \frac{Dp}{Dt} + \mu \Phi \tag{3.71}$$

Remark on the numerical application of the energy equation The Equations (3.60), (3.65), (3.66) and (3.67) are all fundamentally valid to be chosen as the governing energy equation in the fluid for the numerical analysis of the problem. Nevertheless, it is very important to realize that the numerically discretized formulation of the equations based on the substantial derivative of T (Eqs. (3.60) and (3.66)) is highly sensitive to large temperature gradients and, in such cases, they can lead to inaccurate results. In the present system, the use of these equations resulted in overall temperature imbalance errors of three to four orders of magnitude larger than in the use of Equations (3.65) or (3.67). Besides, although the numerical resolution of the equations based on the substantial derivative is noticeably faster, this improvement in computing time is hardly appreciable when the momentum and continuity fields are also solved, because these equations are the most demanding on computing resources.

3.3.5 Thermal energy in the wall

Heat conduction is considered as the governing equation for thermal energy in the conductive solid wall, because radiation heat transfer is neglected,

$$\frac{\partial}{\partial t} c_{p,s} \rho_s T_s = -(\nabla \cdot \mathbf{q}_s) \quad (3.72)$$

where,

$$\mathbf{q}_s = -\kappa_s \nabla T_s \quad (3.73)$$

3.4 Catalytic fluid-wall interface

As described in Chapter 2, the CPO in the microreactor takes place heterogeneously in a layer of catalyst loaded on the wall. The reactive process has been simplified significantly and most of the possible factors of importance in the process have been neglected, including those related to adsorption/desorption phenomena such as the Stefan velocities (Ertl et al, 2008), the loading and thickness of the catalyst, and those related to the nature of the catalyst such as the deactivation time and the active sites. Therefore, a simple model is here formulated, where the reaction mechanism takes place as the reactants reach the interface between the conductive wall and the channel by diffusion, and the corresponding energy and mass balances in the interface are formulated, assuming the interface to be infinitesimal with zero thickness. These balances will be used later on as boundary conditions between the channel and the wall.

3.4.1 Reaction kinetics

Based on the kinetic reaction mechanism proposed in Section 2.2, the kinetic equations of reaction rates for the OXI, REF and WGS partial reactions (Eqs. (2.1), (2.2) and (2.3)) are reformulated here to suitable form for the simulation code. Prior to reformulating the

equations, though, a brief background review on enthalpies and equilibrium constants of reactions is necessary. Extended information about this background can be found elsewhere (Felder and Rousseau, 1999; Fogler, 2005; Levine, 2008).

3.4.1.1 Standard enthalpies and equilibrium constants of reactions

For a given reaction of ideal gases, the standard molar enthalpy of reaction, $\Delta\bar{H}_{rx}^o$, and the standard molar Gibbs free energy of reaction, $\Delta\bar{G}_{rx}^o$, are formulated as a sum of the contribution of the enthalpies and the Gibbs free energies of each chemical specie involved in the reaction,

$$\Delta\bar{H}_{rx}^o = \sum_{\alpha} st_{\alpha,rx} M_{\alpha} H_{\alpha}^o \quad (3.74)$$

$$\Delta\bar{G}_{rx}^o = \sum_{\alpha} st_{\alpha,rx} M_{\alpha} G_{\alpha}^o \quad (3.75)$$

where $st_{\alpha,rx}$ is the stoichiometric coefficient of the chemical specie α in the reaction rx , and the standard enthalpy and Gibbs free energy of a single specie, H_{α}^o and G_{α}^o , are obtained as,

$$H_{\alpha}^o = \Delta_{298}^T H_{\alpha}^o + H_{f,298,\alpha}^o \quad (3.76)$$

$$G_{\alpha}^o = H_{\alpha}^o - T S_{\alpha}^o \quad (3.77)$$

where $H_{f,298,\alpha}^o$ is the standard enthalpy of formation of the specie α at 298 K, $\Delta_{298}^T H_{\alpha}^o$ is the variation in the standard enthalpy of the specie α from 298 K to T , and S_{α}^o is the standard entropy of the specie α .

Bear in mind that the sign of $st_{\alpha,rx}$ depends on whether the specie α is a reagent or a product in the reaction rx . Similarly, the sign of $\Delta\bar{H}_{rx}^o$ depends on whether the reaction rx is exothermic or endothermic. Accordingly,

$$\Delta\bar{H}_{rx}^o \begin{cases} (+), & \text{if endothermic,} \\ (-), & \text{if exothermic} \end{cases} \quad st_{\alpha,rx} \begin{cases} (+), & \text{if product,} \\ (-), & \text{if reagent} \end{cases}$$

$\Delta_{298}^T H_{\alpha}^o$ and S_{α}^o can be obtained with Shomate equations similar to the one used for calculating $c_{p,\alpha}^o$ (Eq. (3.20)),

$$\begin{aligned} \frac{\Delta_{298}^T H_{\alpha}^o \cdot M_{\alpha}}{10^6} &= A_{sh,\alpha} \cdot T_{sh} + B_{sh,\alpha} \cdot T_{sh}^2/2 + C_{sh,\alpha} \cdot T_{sh}^3/3 \\ &+ D_{sh,\alpha} \cdot T_{sh}^4/4 - E_{sh,\alpha}/T_{sh} + F_{sh} - H_{sh} \end{aligned} \quad (3.78)$$

$$\begin{aligned} \frac{S_{\alpha}^o \cdot M_{\alpha}}{10^3} &= A_{sh,\alpha} \cdot \ln(T_{sh}) + B_{sh,\alpha} \cdot T_{sh} + C_{sh,\alpha} \cdot T_{sh}^2/2 \\ &+ D_{sh,\alpha} \cdot T_{sh}^3/3 - E_{sh,\alpha}/(2 \cdot T_{sh}^2) + G_{sh,\alpha} \end{aligned} \quad (3.79)$$

The coefficients $A_{sh,\alpha}$ to $H_{sh,\alpha}$ are those of Eq. (3.20), and T_{sh} is defined in Eq. (3.21).

Finally, the standard pressure equilibrium constant of reaction, $K_{eq,p,rx}^o$, and the pressure equilibrium constant of reaction, $K_{eq,p,rx}$, are formulated as follows,

$$K_{eq,p,rx}^o = \prod_{\alpha} \left(\frac{p_{\alpha,eq}}{p^o} \right)^{st_{\alpha,rx}} = \exp \left(- \frac{\Delta \bar{G}_{rx}^o}{\mathfrak{R}T} \right) \quad (3.80)$$

$$K_{eq,p,rx} = \prod_{\alpha} (p_{\alpha,eq})^{st_{\alpha,rx}} = K_{eq,p,rx}^o \cdot (p^o)^{\sum_{\alpha} st_{\alpha,rx}} \quad (3.81)$$

3.4.1.2 Kinetic reaction rates

The kinetic equations of reaction rates for the partial reactions presented in Section 2.2, are reformulated here to a form suitable for the simulation code. Therefore, Eqs. (2.1), (2.2) and (2.3), together with the relations defined in Sections 3.1.1 and 3.4.1.1, are rewritten as follows,

$$r_{OXI} = k_{OXI}'' C_{CH_4} C_{O_2} = k_{OXI}'' \frac{\rho_{CH_4}}{M_{CH_4}} \frac{\rho_{O_2}}{M_{O_2}} = k_{OXI}'' \rho^2 \frac{\omega_{CH_4}}{M_{CH_4}} \frac{\omega_{O_2}}{M_{O_2}} \quad (3.82)$$

$$\begin{aligned} r_{REF} &= k_{REF}'' C_{CH_4} C_{H_2O} \left(1 - \frac{p_{CO}^1 p_{H_2}^3 p_{CH_4}^{-1} p_{H_2O}^{-1}}{K_{eq,p,REF}} \right) \\ &= k_{REF}'' \left(C_{CH_4} C_{H_2O} - \frac{C_{CO} C_{H_2}^3}{K_{eq,p,REF}} \left(\frac{\mathfrak{R}T}{p^o} \right)^2 \right) \\ &= k_{REF}'' \rho^2 \left(\frac{\omega_{CH_4}}{M_{CH_4}} \frac{\omega_{H_2O}}{M_{H_2O}} - \frac{(\omega_{CO}/M_{CO})(\omega_{H_2}/M_{H_2})^3}{K_{eq,p,REF}} \left(\frac{\rho \mathfrak{R}T}{p^o} \right)^2 \right) \end{aligned} \quad (3.83)$$

$$\begin{aligned} r_{WGS} &= k_{WGS}'' C_{CO} C_{H_2O} \left(1 - \frac{p_{CO_2}^1 p_{H_2}^1 p_{CO}^{-1} p_{H_2O}^{-1}}{K_{eq,p,WGS}} \right) \\ &= k_{WGS}'' \left(C_{CO} C_{H_2O} - \frac{C_{CO_2} C_{H_2}}{K_{eq,p,WGS}} \right) \\ &= k_{WGS}'' \rho^2 \left(\frac{\omega_{CO}}{M_{CO}} \frac{\omega_{H_2O}}{M_{H_2O}} - \frac{(\omega_{CO_2}/M_{CO_2})(\omega_{H_2}/M_{H_2})}{K_{eq,p,WGS}} \right) \end{aligned} \quad (3.84)$$

where,

$$k_{rx}'' = a_{rx} \exp \left(\frac{Ea_{rx}}{\mathfrak{R}T} \right) \quad (3.85)$$

where k_{rx}'' is the specific rate constant for the reaction rx , a_{rx} is the Arrhenius pre-exponential factor of reaction rx , and Ea_{rx} is the activation energy of the reaction rx .

The reversibility of the REF and WGS reactions is represented by the presence of a negative term in these kinetic equations of reaction rates.

3.4.2 Balances for interface mass and energy transfer

A mass balance in the catalytic interface is formulated for every chemical specie, and it is the result of the transport to/from the interface by mass effective diffusion and the amount of production/consumption by the chemical reactions. It is an instantaneous balance without temporal term, and in the direction normal to the interface. The balance for a chemical specie α is as follows (Taylor and Krishna, 1993),

$$M_\alpha \sum_{rx} st_{\alpha,rx} r_{rx} = n_{\alpha,if} = j_{\alpha,if} \quad (3.86)$$

Note that only the components of the mass flux vectors \mathbf{n}_α and \mathbf{j}_α in the direction normal to the interface, l_{if} , are used here. Then, Eq. (3.34) can be used to obtain the expression for the derivative of the mass fraction of species α in the direction normal to the interface, and evaluated at the interface,

$$\left. \frac{d\omega_\alpha}{dl_{if}} \right|_{if} = -\frac{1}{\rho D_{eff,\alpha}} M_\alpha \sum_{rx} (st_{\alpha,rx} r_{rx}) \quad (3.87)$$

The energy balance is based on the continuity of an energy flux across an interface. Then, the energy fluxes across the interface in the channel side, e_{if} , and in the solid wall side, $e_{s,if}$, are equivalent (Taylor and Krishna, 1993),

$$e_{if} = e_{s,if} \quad (3.88)$$

$$-\left[q_{if} + \sum_{\alpha} (n_{\alpha} H_{\alpha})_{if} \right] = q_{s,if} + \sum_{\alpha} (n_{\alpha} H_{\alpha})_{s,if} \quad (3.89)$$

Analogous to the mass balance, the only component of the heat flux vector, \mathbf{q} , used here is the one in the direction normal to the interface, l_{if} .

Since the flux of species across the solid wall is zero, the last term in the right hand side disappears,

$$-\left[q_{if} + \sum_{\alpha} (n_{\alpha} H_{\alpha})_{if} \right] = q_{s,if} \quad (3.90)$$

and assuming $H_{\alpha} = H_{\alpha}^o$, the component of enthalpies in the left hand side can be developed with Eqs. (3.74) and (3.86), thus giving,

$$\begin{aligned} \sum_{\alpha} (n_{\alpha} H_{\alpha})_{if} &= \sum_{\alpha} \left(M_{\alpha} \sum_{rx} (st_{\alpha,rx} r_{rx}) H_{\alpha}^o \right)_{if} \\ &= \sum_{rx} \left(r_{rx} \sum_{\alpha} (st_{\alpha,rx} M_{\alpha} H_{\alpha}^o) \right)_{if} = \sum_{rx} \left(r_{rx} \Delta \bar{H}_{rx}^o \right) \end{aligned} \quad (3.91)$$

Finally, for a temperature range from 500 K to 2000 K, the enthalpies of the reactions can be fairly assumed constant, thus Eqs. (3.90) and (3.91) can be combined,

$$q_{s,if} = - \left[q_{if} + \sum_{rx} r_{rx} \Delta \bar{H}_{rx}^o \right] \quad (3.92)$$

and developed with Eqs. (3.61) and (3.73),

$$\left. \frac{dT_s}{dl_{if}} \right|_{if} = \frac{1}{\kappa_s} \left[-\kappa \left. \frac{dT}{dl_{if}} \right|_{if} + \sum_{rx} \left(r_{rx} \Delta \bar{H}_{rx}^o \right) \right] \quad (3.93)$$

Besides the useful Eq. (3.93) resulting from the energy balance at the interface, another relation arises when considering the catalytic interface with zero thickness. This relation is the zero temperature jump, which results in equivalent solid and fluid temperatures at the interface,

$$T_{if} = T_{s,if} \quad (3.94)$$

Finally, in the special case of a non-conductive solid wall, i.e. adiabatic, then $q_{s,if} = 0$ and Eq. (3.93) would turn into,

$$\left. \frac{dT}{dl_{if}} \right|_{if} = \frac{1}{\kappa} \sum_{rx} \left(r_{rx} \Delta \bar{H}_{rx}^o \right) \quad (3.95)$$

3.5 Dimensional analysis

As a matter of versatility, the mathematical model used in the present work is to be solved in its non-dimensional form by the numerical simulation code. Accordingly, the equations of the mathematical model already presented in the previous sections will be reformulated to their non-dimensional form, based on a set of relevant non-dimensional variables and groups. This process and the resulting equations are presented here.

3.5.1 Non-dimensional variables and groups

The relevant variables of the model are normalized with the corresponding appropriate characteristic scales to obtain the non-dimensional variables. These are,

$$u_i^* = \frac{u_i}{U_c} \quad T^* = \frac{T}{T_c} \quad T_s^* = \frac{T_s}{T_c} \quad (3.96a)$$

$$t^* = \frac{tU_c}{L_c} \quad x_i^* = \frac{x_i}{L_c} \quad p^* = \frac{p}{\rho_c U_c^2} \quad \check{\nabla} = L_c \nabla \quad (3.96b)$$

$$\mu^* = \frac{\mu}{\mu_c} \quad c_p^* = \frac{c_p}{c_{p,c}} \quad \kappa^* = \frac{\kappa}{\kappa_c} \quad D_{eff,\alpha}^* = \frac{D_{eff,\alpha}}{D_c} \quad (3.96c)$$

$$\rho^* = \frac{\rho}{\rho_c} \quad \bar{M}^* = \frac{\bar{M}}{M_c} \quad \kappa_s^* = \frac{\kappa_s}{\kappa_c} \quad \alpha_s^* = \frac{\kappa_s / \rho_s / c_{p,s}}{\kappa_c / \rho_c / c_{p,c}} \quad (3.96d)$$

Note that the fundamental formulation of ω_α is already non-dimensional and, therefore, it does not need to be normalized.

Besides the non-dimensional variables, the non-dimensional groups relevant in the present work are presented in Table 3.1 together with their interpretation. These non-dimensional groups are formulated with the corresponding characteristic scales as components, and they are accordingly denoted with the 'c' subscript.

3.5.2 Physical properties of the gas

The non-dimensional properties of the gas are already defined in Eq. (3.96d), including ρ^* , μ^* , c_p^* , κ^* and $D_{eff,\alpha}^*$. Unlike the main variables in the system such as velocities, temperature and mass fractions, which can be directly calculated in their non-dimensional form with the governing equations, the complex formulation of the dimensional form of the properties of the gas (See Sect. 3.2) precludes their formulation directly in non-dimensional form. For this reason, these properties must be continuously calculated in their dimensional form and then normalized with the characteristic scale. The only exception to this restriction is the density, which can be directly formulated as function of T^* and \bar{M}^* with the law of ideal gases and assuming constant pressure throughout the system,

$$\rho^* = \frac{\rho}{\rho_c} = \frac{R_c T_c}{RT} = \frac{\bar{M}^*}{T^*} \quad (3.97)$$

3.5.3 Governing equations

Based on the non-dimensional variables and groups already formulated, the governing equations of the system for continuity (Eq. (3.23)), momentum (Eq. (3.24)), mass conservation for chemical species (Eq. (3.33)), thermal energy in the fluid (Eq. (3.67)) and thermal energy in the wall (Eq. (3.72)), are rewritten in their non-dimensional forms as follows,

Overall mass conservation (continuity)

$$\frac{\partial}{\partial t^*} \rho^* + (\check{\nabla} \cdot \rho^* \mathbf{v}^*) = 0 \quad (3.98)$$

Momentum

$$\frac{\partial}{\partial t^*} \rho^* \mathbf{v}^* + [\check{\nabla} \cdot \rho^* \mathbf{v}^* \mathbf{v}^*] = - [\check{\nabla} p^*] - \frac{1}{Re_{L,c}} [\check{\nabla} \cdot \boldsymbol{\tau}^*] \quad (3.99)$$

where,

$$\boldsymbol{\tau}^* = \frac{L_c}{\mu_c U_c} \boldsymbol{\tau} = -\mu^* (\check{\nabla} \mathbf{v}^* + (\check{\nabla} \mathbf{v}^*)^\dagger) + \frac{2}{3} \mu^* (\check{\nabla} \cdot \mathbf{v}^*) \boldsymbol{\delta} \quad (3.100)$$

Table 3.1: Non-dimensional groups

Group	Definition	Interpretation
Arrhenius nr. ($Ar_{rx,c}$)	$\frac{E_{rx}^{act}}{RT_c}$	Ratio of activation energy of a reaction to thermal energy.
Prandtl nr. (Pr_c)	$\frac{c_p c_l \mu_c}{\kappa_c} = \frac{\nu_c}{\alpha_c}$	Ratio of momentum to thermal diffusivities.
Reynolds nr. ($Re_{L,c}$)	$\frac{U_c L_c}{\nu_c}$	Ratio of inertia to viscous forces.
$Rh_{rx,c}$	$\frac{\Delta \bar{H}_{rx}^o k_{rx,c}^{\prime\prime} \rho_c^2}{(\prod_{rg} M_{rg,rx}) \kappa_c T_c / L_c}$	Ratio of reaction to diffusion heat rates.
Schmidt nr. (Sc_c)	$\frac{\nu_c}{D_c}$	Ratio of momentum to mass diffusivities.
Second Danköbler nr. ($Da_{CH_4,rx,c}$)	$\frac{M_{CH_4} L_c^2 / D_c}{(\prod_{rg} M_{rg,rx}) L_c / k_{rx,c}^{\prime\prime} / \rho_c}$	Ratio of diffusion to reaction characteristic times.

Mass conservation for chemical species

$$\frac{\partial}{\partial t^*} \rho^* \omega_\alpha + \left(\check{\nabla} \cdot \rho^* \omega_\alpha \mathbf{v}^* \right) = - \frac{1}{Re_{L,c} Sc_c} \left(\check{\nabla} \cdot \mathbf{j}_\alpha^* \right) \quad (3.101)$$

where,

$$\mathbf{j}_\alpha^* = \frac{L_c}{\rho_c D_c} \mathbf{j}_\alpha = -\rho^* D_{eff,\alpha}^* \check{\nabla} \omega_\alpha \quad (3.102)$$

and,

$$\sum_{\alpha} \omega_\alpha = 1 \quad (3.103)$$

$$\sum_{\alpha} \mathbf{j}_\alpha^* = 0 \quad (3.104)$$

The mass fraction fields of all chemical species could be solved using Eq. (3.101) a number of $N - 1$ times, for $\alpha = 1, 2, \dots, N - 1$, and then obtain the mass fraction field of the last chemical specie, $\alpha = N$ with Eq. (3.103). This strategy would ensure the conservation of the condition in Eq. (3.103). Nevertheless, this would also mask any possible physical inconsistencies or errors in the methodology for calculating the mass fractions of the chemical species, such as in the accuracy of the effective diffusion model or in the time step chosen during the numerical resolution. Besides, should this be the case, the influence of the N^{th} specie in the flow and in the reaction system would also be lowered in comparison with the other chemical species, as a result of forcing explicitly the condition of balance of chemical species. Consequently, the policy in the present simulation code is to solve Eq. (3.101) for all N chemical species and then, as it will be explained later in Section (4.4), to check the fulfilment of the condition of balance of chemical species with Eq. (3.103).

Thermal energy in the fluid With the next conditions accomplished in the system,

$$Sp_\alpha = 0 \quad (\text{No homogeneous reaction}) \quad (3.105)$$

$$\left(\frac{\partial \ln \rho}{\partial \ln T} \right) = -1 (\text{Ideal gas}) \quad (3.106)$$

$$\frac{Dp}{Dt} = 0 \quad (\text{Open system at constant pressure}) \quad (3.107)$$

$$\Phi = 0 \quad (\text{Gas flow at low Mach number}) \quad (3.108)$$

and with the formulation of $c_{p,\alpha}$ in Eq. (3.52), the energy equation in the fluid results in,

$$\begin{aligned} & \frac{\partial}{\partial t^*} \rho^* T^* + \left(\check{\nabla} \cdot \rho^* T^* \mathbf{v}^* \right) \\ &= \frac{1}{c_p^*} \left[- \frac{1}{Re_{L,c} Pr_c} \left(\check{\nabla} \cdot \mathbf{q}^* \right) - \frac{1}{Re_{L,c} Sc_c} \sum_{\alpha} \left(\mathbf{j}_\alpha^* \cdot \left(c_{p,\alpha}^* \check{\nabla} T^* \right) \right) \right] \end{aligned} \quad (3.109)$$

where,

$$\mathbf{q}^* = \frac{L_c}{\kappa_c T_c} \mathbf{q} = -\kappa^* \check{\nabla} T^* \quad (3.110)$$

$$(3.111)$$

Thermal energy in the wall The equation for heat conduction through the solid wall, with the properties of the solid assumed to be constant, results in,

$$\frac{\partial}{\partial t^*} T_s^* = \frac{\alpha_s^*}{Re_{L,c} Pr_c} \check{\nabla}^2 T_s^* \quad (3.112)$$

3.5.4 Catalytic fluid-wall interface

3.5.4.1 Reaction kinetics

With the proper substitution of the variables involved, the non-dimensional form of the kinetic equations of reaction rates for the OXI, REF and WGS partial reactions (Eqs. (3.82), (3.83) and (3.84)) result in,

$$r_{OXI}^* = \frac{M_{CH_4} M_{O_2}}{k_{OXI,c}'' \rho_c^2} r_{OXI} = k_{OXI}''^* \omega_{CH_4} \omega_{O_2} \quad (3.113)$$

$$r_{REF}^* = \frac{M_{CH_4} M_{H_2O}}{k_{REF,c}'' \rho_c^2} r_{REF} = k_{REF}''^* \left(\omega_{CH_4} \omega_{H_2O} - \Upsilon_{REF} \frac{(\rho^* T^*)^2 \omega_{CO} \omega_{H_2}^3}{K_{eq,p,REF}^o} \right) \quad (3.114)$$

$$r_{WGS}^* = \frac{M_{CO} M_{H_2O}}{k_{WGS,c}'' \rho_c^2} r_{WGS} = k_{WGS}''^* \left(\omega_{CO} \omega_{H_2O} - \Upsilon_{WGS} \frac{\omega_{CO_2} \omega_{H_2}}{K_{eq,p,WGS}^o} \right) \quad (3.115)$$

where,

$$k_{rx}''^* = \frac{k_{rx}''}{k_{rx,c}''} = \frac{a_{rx} \exp(Ea_{rx}/\mathcal{R}T)}{a_{rx} \exp(Ea_{rx}/\mathcal{R}T_c)} = \exp(Ar_{rx,c}((1/T^*) - 1)) \quad (3.116)$$

and Υ_{rx} is the dimensionless ratio of forward to backward velocities for a reversible reaction, rx ,

$$\Upsilon_{REF} = \frac{M_{CH_4} M_{H_2O} / (M_{CO} M_{H_2}^3)}{(p^o / (\rho_c \mathcal{R} T_c))^2} \quad (3.117)$$

$$\Upsilon_{WGS} = \frac{M_{CO} M_{H_2O}}{M_{CO_2} M_{H_2}} \quad (3.118)$$

3.5.4.2 Balances for interface mass and energy transfer

With the proper use of the non-dimensional variables, groups and equations of reaction rates previously formulated, the mass and energy balances in the catalytic interface

3.5. Dimensional analysis

39

formulated in Eqs. (3.87), (3.93) and (3.94), can be rewritten in their non-dimensional form as follows,

$$\begin{aligned} \left. \frac{d\omega_\alpha}{dl_{if}^*} \right|_{if} &= -\frac{L_c}{\rho_c D_c} \frac{M_\alpha}{\rho^* D_{eff,\alpha}^*} \left(st_{\alpha,OXI} \frac{k''_{OXI,c} \rho_c^2}{M_{CH_4} M_{O_2}} r_{OXI}^* \right. \\ &\quad \left. + st_{\alpha,REF} \frac{k''_{REF,c} \rho_c^2}{M_{CH_4} M_{H_2O}} r_{REF}^* + st_{\alpha,WGS} \frac{k''_{WGS,c} \rho_c^2}{M_{CO} M_{H_2O}} r_{WGS}^* \right) \\ &= -\frac{1}{\rho^* D_{eff,\alpha}^*} \frac{M_\alpha}{M_{CH_4}} \sum_{rx} (st_{\alpha,rx} Da_{CH_4,rx,c} r_{rx}^*) \end{aligned} \quad (3.119)$$

$$\begin{aligned} \left. \frac{\partial T_s^*}{\partial l_{if}^*} \right|_{if} &= \frac{1}{\kappa_s^*} \left[-\kappa^* \left. \frac{dT^*}{dl_{if}^*} \right|_{if} + \frac{L_c}{\kappa_c T_c} \left(\Delta \bar{H}_{OXI}^o \frac{k''_{OXI,c} \rho_c^2}{M_{CH_4} M_{O_2}} r_{OXI}^* \right. \right. \\ &\quad \left. \left. + \Delta \bar{H}_{REF}^o \frac{k''_{REF,c} \rho_c^2}{M_{CH_4} M_{H_2O}} r_{REF}^* + \Delta \bar{H}_{WGS}^o \frac{k''_{WGS,c} \rho_c^2}{M_{CO} M_{H_2O}} r_{WGS}^* \right) \right] \\ &= \frac{1}{\kappa_s^*} \left(-\kappa^* \left. \frac{\partial T^*}{\partial l_{if}^*} \right|_{if} - \sum_{rx} (Rh_{rx,c} r_{rx}^*) \right) \end{aligned} \quad (3.120)$$

$$T_{if}^* = T_{s,if}^* \quad (3.121)$$

UNIVERSITAT ROVIRA I VIRGILI

NUMERICAL AND EXPERIMENTAL ANALYSES OF SINGLE AND TWO-PHASE MICROFLUIDIC FLOWS WITH IMPLICATIONS IN MICROREACTORS

Roland Blanch Ojea

DL:T. 149-2012

Numerical resolution

Contents

4.1	Numerical techniques	41
4.2	Computational domain	42
4.3	Initial and boundary conditions	47
4.3.1	Initial conditions	47
4.3.2	Channel inlet conditions	47
4.3.3	Channel symmetry plane conditions	47
4.3.4	Channel outlet plane conditions	48
4.3.5	Channel catalytic fluid-wall interface conditions	48
4.3.6	Solid wall external boundaries	49
4.4	Convergence criteria, stability and consistency	49

The mathematical model formulated in Chapter 3 includes all the processes occurring in the microchannel reactor that have been taken into account and, therefore, the resolution of this model is the key for unveiling the behaviour of the studied system and its posterior analysis. The complexity of the mathematical model, increased by the strong coupling of most of the processes involved, precludes an analytical solution of the physical system. Thus, a proper choice and use of the available numerical techniques is the only suitable possibility for solving the mathematical model. Accordingly, the in-house three-dimensional simulation code 3DINAMICS, developed originally at the Fluid Mechanics research group (ECoMMFiT) of the Mechanical Engineering Department of the Rovira i Virgili University, has been chosen for this purpose.

The present chapter describes briefly the background and the numerical techniques used in the 3DINAMICS code in Section 4.1, the choice of the grid for the computational domain in Section 4.2, the applicable initial and boundary conditions in Section 4.3, and some stability concepts in Section 4.4.

4.1 Numerical techniques

The in-house finite volume simulation code 3DINAMICS was developed originally by Cuesta (1993), and ever since it has been further developed and applied in a wide range

of studies, including either laminar and turbulent flows, natural and Rayleigh Bénard convection, dispersion of buoyant plumes, mass transport, homogeneous reactions, and others (e.g. Pallares et al, 1999; Jiménez, 2003; Valencia, 2006; Fabregat, 2007; Younis, 2010). The version of 3DINAMICS used in the present study is a serial second order finite volume code written in FORTRAN 90, that works in Cartesian domains.

The spatial terms of the governing equations are discretised with the second-order central differencing scheme, whereas the second-order Crank-Nicholson semi-implicit scheme is used for their time marching integration. The multi-dimensional Tri-Diagonal Matrix Algorithm is used to solve the resulting system of linearised algebraic equations. The coupling between the pressure and the velocity fields is solved with a Fractional Step Method, and the resulting Poisson equation for pressure correction is solved by a variant of the Biconjugate Gradient Method, the BI-CGSTAB. The physical properties of the fluid are calculated at the beginning of each time step, and then they are applied to the corresponding governing equations and balances in the interface.

A complete description of the fundamentals of 3DINAMICS can be found in Cuesta (1993) and Fabregat (2007). Besides, the numerical techniques used in 3DINAMICS, and just enumerated here, are described in detail in Versteeg and Malalasekera (1996) and Ferziger and Perić (2001). For the Biconjugate Gradient Method, van der Vorst (1992) and Shewchuk (1994) are also suggested.

4.2 Computational domain

The numerical techniques of 3DINAMICS to solve the governing equations of the system, require the computational domain to be divided into discrete control volumes forming a grid. However, the overall computational domain is fundamentally divided into two clearly identified sub-domains due to the conjugate heat transfer problem between the flow channel, where all governing equations are applied, and the solid conductive wall where only the heat conduction needs to be solved.

So far, there exist a number of several methods to handle the sub-domains of the conjugate heat transfer, including meshless boundary element methods (He et al, 1995) and boundary-domain integral methods (Hriberšek and Kuhn, 2000). The methods with a single grid that comprises both the flow and the solid domains are quite popular (e.g. Patankar, 1980; Sugavanam et al, 1995; Fedorov and Viskanta, 1999; Wanker et al, 2000; Toh et al, 2002). In these unitary grid methods, the velocities in the solid domain are artificially set to zero, usually by imposing a very high viscosity term, and then the general heat equation becomes valid for both domains. The fluid-solid interface boundary conditions are automatically included in the discretised terms of the equation. These methods are appropriated for complex geometries, but they are expensive in computing resources. Moreover, special attention has to be paid when calculating the physical properties, to ensure physical consistency of the heat equation in the interface (Chen and Han, 2000). Another popular method consists of using separated grids, and solving

Table 4.1: *Grid parameters for the computational domains of the flow channel and the conductive wall*

	Flow channel	Conductive wall
Grid resolution (Total nodes)	301 x 11 (3311)	301 x 7 (2107)
$(\Delta x^*)_{min}$	2.997×10^{-2}	2.997×10^{-2}
$(\Delta x^*)_{max}$	1.320×10^{-1}	1.320×10^{-1}
$(\Delta y^*)_{min}$	4.725×10^{-2}	5.520×10^{-2}
$(\Delta y^*)_{max}$	6.466×10^{-2}	6.500×10^{-2}

the corresponding equations in each grid, i.e. all governing equations in the fluid grid and only the conductive heat equation in the solid grid. In this case, appropriated for simpler geometries, both grids are linked by the boundary interface, where the conditions previously formulated in Section 3.5.4.2 are applied as boundary conditions. This method of separated grid domains, applied by a broad number of researchers (e.g. [Jahn et al, 1997](#); [Tischer et al, 2001](#); [Stutz and Poulikakos, 2005](#); [Schwiedernoch et al, 2003](#)), is adopted in the present work.

Both domains are discretised with non-uniform 2D Cartesian grids, with a higher density of grid nodes at two critical regions, the entrance of the channel where the inlet fields develop, and the fluid-solid interface, where the reactions take place and highest property gradients occur. The resolution of the grids and the minimum and maximum distances between nodes in the grids, $(\Delta x^*)_{min}$, $(\Delta x^*)_{max}$, $(\Delta y^*)_{min}$ and $(\Delta y^*)_{max}$, are indicated in Table 4.1 for the fluid and the solid domains. A merged image of the grids of both domains for scalar variables, i.e temperature and mass species, is shown in Figure 4.1. The image depicts the initial and final sections of the microchannel reactor, and the non-uniform distribution of the nodes can be noted, especially in the stream-wise direction.

A staggered arrangement is also used in the fluid grid, with the scalar variables evaluated at ordinary nodal points and the velocity components centred on the faces of the scalar control volumes. Staggered grids, first introduced by [Harlow and Welch \(1965\)](#), are basically used to avoid the non-physical results of non-staggered grids, where the influence of pressure is not properly represented in the discretised momentum equations ([Versteeg and Malalasekera, 1996](#)). A sketch of a 2D staggered grid is shown in Figure 4.2, where the control volume of the scalar and the u and v velocity components, located in the faces of the scalar control volumes, are indicated .

Although the expected laminar profiles in the flow anticipate the possibility to use relatively coarse grids without a decrease in the accuracy of the results, a preliminary test of grid independence in the span-wise direction, i.e. the direction normal to the interface, has been carried out to assess the suitability of the grid selected for the fluid domain. A reactive case similar to the ones studied later in the Results chapter (Chapter 5) has

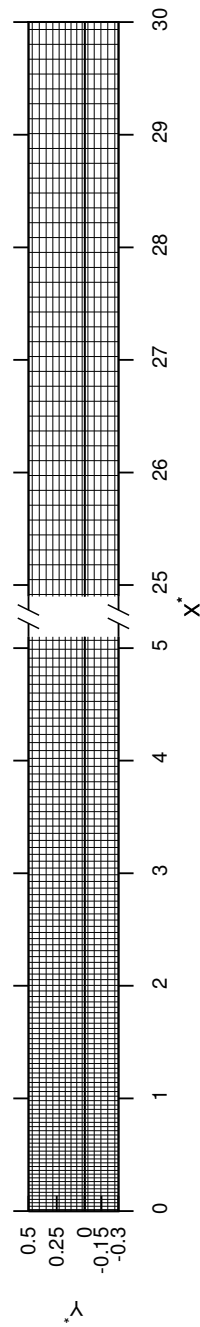


Figure 4.1: Merged grids of the computational domains of the flow channel (301×11) and the conductive wall (301×7). The distribution of the nodes for scalar variables at the initial ($x^* = 0$ to 5) and the final ($x^* = 25$ to 30) sections of the microchannel reactor are depicted.

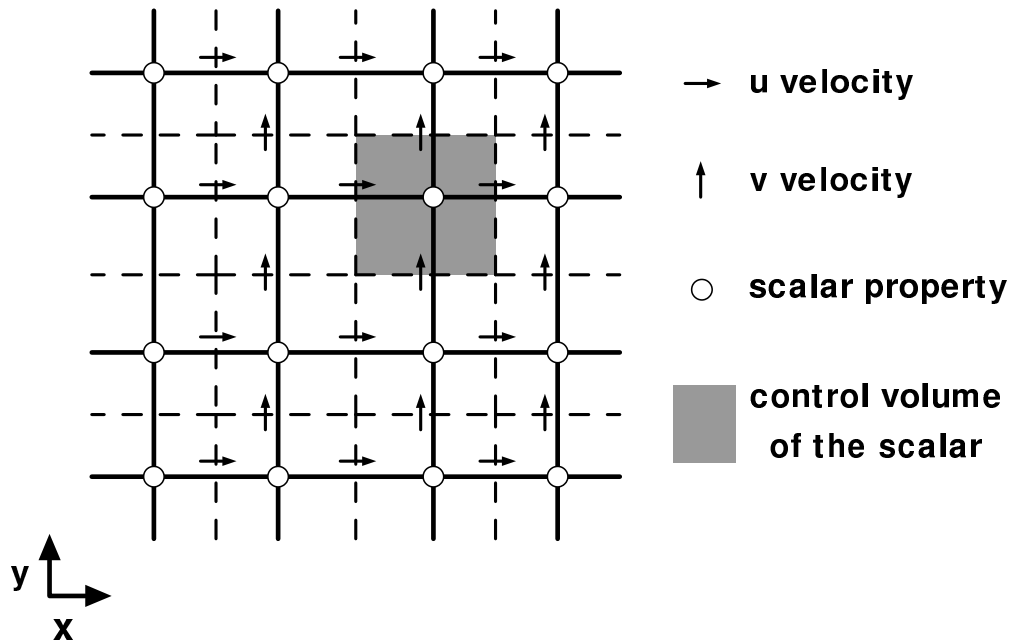


Figure 4.2: 2D staggered grid. The distribution of the nodes of the scalar variable and its control volume, as well as the location of the u and v velocity components, are indicated.

Table 4.2: CPU times and numerical times elapsed to reach steady state, during the test of grid independence

Grid resolution (Total nodes)	CPU time	t^*
301x07 (2107)	9h 12min	1446
301x11 (3311)	15h 55min	1385
301x17 (5117)	27h 20min	1362

been solved for three grids of the fluid domain with a different number of grid points in the span-wise direction, 301×07 , 301×11 and 301×17 , whereas the grid of the conductive wall has been left unchanged. The resulting profiles of u^* , T^* and ω_{CH_4} at the fluid-solid interface and the stream-wise symmetry along x^* are shown in Figure 4.3. A complete agreement can be observed in all of these profiles for the three different grids, thus proving the suitability of the chosen grid.

The required CPU times and the elapsed times required to reach steady state, t^* , during the test of grid independence are also listed in Table 4.2 for orientation purposes. The long CPU times required, compared to the low amount of total number of grid nodes in the domain, give an idea of the costs of the present system in terms of computational resources. The large values of t^* also give an idea of the slow temporary evolution of the overall simulated process.

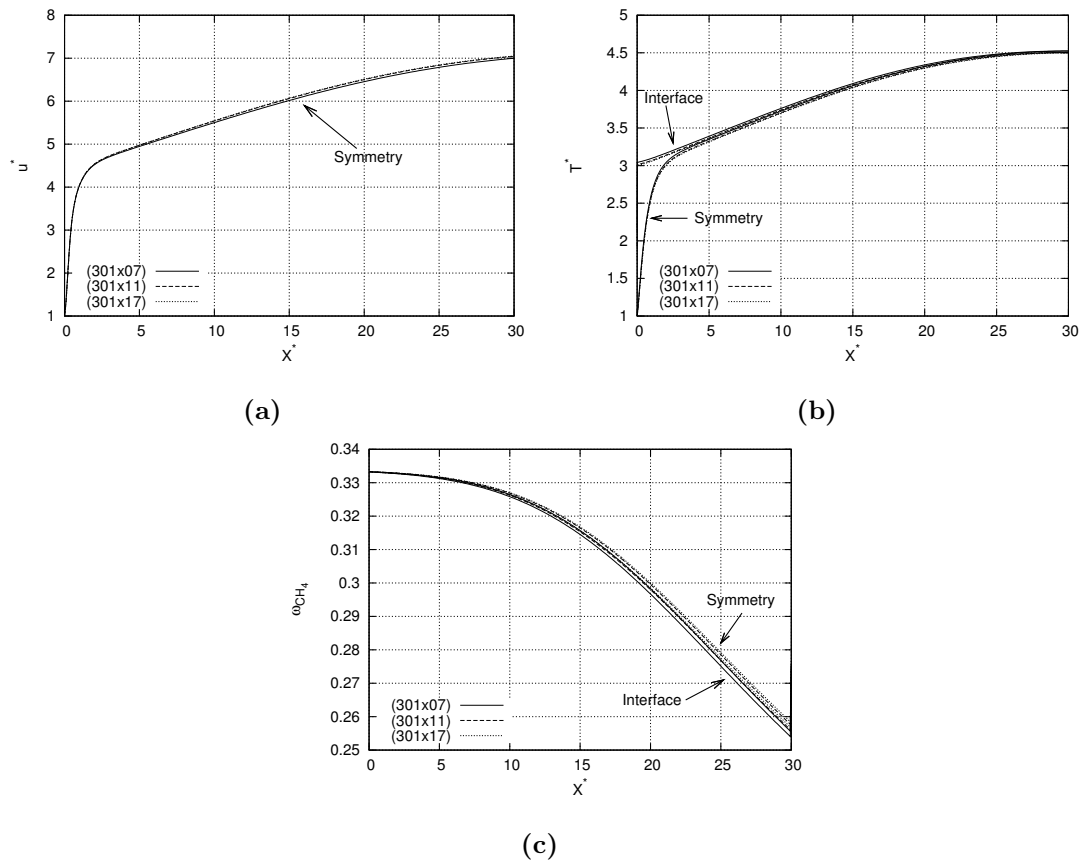


Figure 4.3: Profiles of the (a) velocity component in the x -direction, u^* , (b) temperature, T^* , and (c) mass fraction of CH_4 , ω_{CH_4} , along the reactor, x^* , at the fluid-solid interface and the stream-wise symmetry, obtained from the test of grid independence for three different grids, 301×07 , 301×11 and 301×17 .

4.3 Initial and boundary conditions

The initial and boundary conditions of the computational domain were physically enumerated and described in Chapter 2. Here, these conditions are formulated numerically in order to be implemented in the simulation code.

4.3.1 Initial conditions

As initial conditions for the calculations ($t^* = 0$), the velocities and the mass fractions of chemical species throughout the whole domain are set equal to the inlet values of the corresponding variables. On the other hand, the fluid and solid domains are initially preheated to a certain temperature in order to ignite the OXI reaction, which will initiate the overall reaction system. These momentum, chemical species and energy conditions are formulated numerically as follows,

$$u^*|_{(x^*,y^*,0)} = u^*|_{(0,y^*,t^*)} \quad v^*|_{(x^*,y^*,0)} = v^*|_{(0,y^*,t^*)} \quad (4.1)$$

$$\omega_\alpha|_{(x^*,y^*,0)} = \omega_\alpha|_{(0,y^*,t^*)} \quad (4.2)$$

$$T^*|_{(x^*,y^*,0)} = T_s^*|_{(x^*,y^*,0)} = T_{preheated}^* \quad (4.3)$$

4.3.2 Channel inlet conditions

The constant feed flow in the channel ($x^* = 0$), with a flat inlet velocity profile, containing a homogeneous gas mixture of reagents is expressed in the form of specified boundary values for all variables, also known as *Dirichlet* boundary condition (Hoffman and Frankel, 2001). The characteristic velocity, U_c , is specified as the inlet velocity.

$$u^*|_{(0,y^*,t^*)} = 1 \quad v^*|_{(0,y^*,t^*)} = 0 \quad (4.4)$$

$$\omega_\alpha|_{(0,y^*,t^*)} = \omega_{\alpha,inlet} \quad (4.5)$$

$$T^*|_{(0,y^*,t^*)} = T_{inlet}^* \quad (4.6)$$

4.3.3 Channel symmetry plane conditions

The axial symmetry along the channel ($y^* = 1/2 \cdot L_y^*$) is equivalent to the absence of momentum, mass or energy transfer across the plane. This is expressed by a derivative of the scalars and the u velocity component specified to 0, also known as *Neumann* boundary condition (Hoffman and Frankel, 2001), while the v velocity component vanishes,

$$\frac{du^*}{dy^*} \Big|_{(x^*,1/2L_y^*,t^*)} = 0 \quad v^*|_{(x^*,1/2L_y^*,t^*)} = 0 \quad (4.7)$$

$$\frac{d\omega_\alpha}{dy^*} \Big|_{(x^*,1/2L_y^*,t^*)} = 0 \quad (4.8)$$

$$\frac{dT^*}{dy^*} \Big|_{(x^*,1/2L_y^*,t^*)} = 0 \quad (4.9)$$

4.3.4 Channel outlet plane conditions

Unlike the other boundary conditions, the flow conditions at the outlet of the channel are now known a priori. Yet, due to the configuration of the reactor in which the reactive interface reaches the end of the channel, the flow is not expected to achieve fully developed conditions before the outlet ($x^* = L_x^*$). In this case, several possible boundary conditions can be applied. For the u component of the velocity, the possibilities include constant gradient condition, unsteady convective condition for momentum (Ferziger and Perić, 2001) and overall mass conservation condition. The constant gradient condition is already discarded, while the unsteady convective condition and overall mass conservation condition are formulated respectively as follows,

$$\left(\frac{\partial \rho^* u^*}{\partial t^*} + U^* \frac{\partial \rho^* u^*}{\partial x^*} \right) \Big|_{(L_x^*, y^*, t^*)} = 0 \quad (4.10)$$

$$\left(\frac{\partial \rho^*}{\partial t^*} + \frac{\partial \rho^* u^*}{\partial x^*} + \frac{\partial \rho^* v^*}{\partial y^*} \right) \Big|_{(L_x^*, y^*, t^*)} = 0 \quad (4.11)$$

In Eq. (4.10), U^* is an independent velocity value that is usually chosen so that mass flux conservation is accomplished.

Several tests have been performed to choose the most suitable outlet boundary condition for the present system. From these tests it can be observed that the system turns out to be more robust, in convergence terms, when Eq. (4.11) is used, whereas it usually experiences instabilities near the outlet and divergence issues when Eq. (4.10) is used.

Accordingly, overall mass conservation condition (Eq. (4.11)) is used for the u component of the velocity. As for the v component of the velocity and the scalar variables, a constant gradient in their values along the axial direction has been imposed. This is expressed in the form of a *second-order Neumann* boundary condition, which specifies the second derivative of the scalar, in this case with a null value,

$$\frac{d}{dx^*} \left(\frac{dv^*}{dx^*} \right) \Big|_{(L_x^*, y^*, t^*)} = 0 \quad (4.12)$$

$$\frac{d}{dx^*} \left(\frac{d\omega_\alpha^*}{dx^*} \right) \Big|_{(L_x^*, y^*, t^*)} = 0 \quad (4.13)$$

$$\frac{d}{dx^*} \left(\frac{dT^*}{dx^*} \right) \Big|_{(L_x^*, y^*, t^*)} = 0 \quad (4.14)$$

4.3.5 Channel catalytic fluid-wall interface conditions

In the catalytic fluid-wall interface ($y^* = 0$), the no-slip velocity condition applies,

$$u^* \Big|_{(x^*, 0, t^*)} = v^* \Big|_{(x^*, 0, t^*)} = 0 \quad (4.15)$$

On the other hand, the mass and energy balances previously formulated in Section 3.5.4.2 lead to Eq. (3.119) being applicable for $\omega_\alpha|_{(x^*,0,t^*)}$, Eq. (3.120) being applicable for $T_s^*|_{(x^*,0,t^*)}$, and Eq. (3.121) being applicable for $T^*|_{(x^*,0,t^*)}$.

4.3.6 Solid wall external boundaries

The external boundaries ($x^* = 0, x^* = L_x^*, y^* = -1/2 \cdot L_{yw}^*$) of the solid conductive wall are insulated and, thus, there is no energy transfer across the boundaries,

$$\left. \frac{dT_s^*}{dx^*} \right|_{(0,y^*,t^*)} = \left. \frac{dT_s^*}{dx^*} \right|_{(L_x^*,y^*,t^*)} = \left. \frac{dT_s^*}{dy^*} \right|_{(x^*,-1/2 \cdot L_{yw}^*,t^*)} = 0 \quad (4.16)$$

4.4 Convergence criteria, stability and consistency

For the time marching resolution of the transient governing equations of the system, a time step of $dt^* = 5 \times 10^{-3}$ has been imposed, with a maximum number of time steps of 600 000. This choice ensured convergence for all cases calculated and the accomplishment of the conservation requirements. The convergence criteria has been set to 1×10^{-6} for the time evolution of overall momentum, chemical species and both energy equations. The tolerance to the residuals of momentum, chemical species and both energy equations is set to 1×10^{-3} , with a maximum number of inner iterative steps of 10. On the other hand, the tolerance to the pressure correction equation is 1×10^{-2} . Finally, the tolerance to the total imbalance in the interface between the solid and the fluid temperatures is set to 1×10^{-4} .

The numerical stability of the code has been monitored during the calculations by measuring the values of the Courant-Friedrichs-Lewy stability criterion, also known as Courant number (Cu), and the cell Péclet number (Pe_{cell}), for the momentum equation in each grid cell of the fluid domain. Cu is the ratio of the time step to the characteristic convection time, and it can be understood as the time required for a disturbance to be convected a certain distance, whereas Pe_{cell} is the ratio of the convective term to the diffusive term of the transport equation (Ferziger and Perić, 2001). Both Cu and Pe_{cell} are direction sensitive and, as such, they are measured for both the x and y directions of the grid cells,

$$Cu_x = \frac{u^* \Delta t^*}{\Delta x^*} \quad Cu_y = \frac{v^* \Delta t^*}{\Delta y^*} \quad (4.17)$$

$$Pe_{cell,x} = Re_{L,c} \frac{\rho^* u^* \Delta x^*}{\mu^*} \quad Pe_{cell,y} = Re_{L,c} \frac{\rho^* v^* \Delta y^*}{\mu^*} \quad (4.18)$$

The limiting values for Cu and Pe_{cell} depend on the numerical scheme chosen to discretise the transport equations, but an approximate limiting value of 2 is usually accepted. This limit has been effectively accomplished by $Cu_x, Cu_y, Pe_{cell,x}$ and $Pe_{cell,y}$ during the calculations.

The preservation of the physical consistency of the system during the calculations has been monitored checking the accomplishment of two conditions during these calculations. The conditions to be accomplished are, the overall mass conservation (Eq. (3.98)) throughout the whole fluid domain, and the balance of chemical species (Eq. (3.103)) in each grid point of the fluid domain. The residual of the overall mass conservation has ranged from values below 1×10^{-1} in the initial time steps, to values below 1×10^{-9} in the steady state, whereas the maximum local imbalance of the chemical species has been below 5×10^{-2} for all the studied cases. According to these values, the two conditions have been fairly accomplished during the calculations.

Finally, the consistency of the steady state results of the calculations have been checked with the accomplishment of the shell balances of mass conservation, momentum, chemical species and fluid energy (Eqs. (3.98), (3.99), (3.101) and (3.109)). These shell balances are based on the Gauss-Ostrogradskii divergence theorem, Eq. (4.19), and its related theorems, Eqs. (4.20) and (4.21), (Bird et al, 2001),

$$\int_V (\nabla \cdot \mathbf{v}) dV = \int_A (\boldsymbol{\delta}_A \cdot \mathbf{v}) dA \quad (4.19)$$

$$\int_V \nabla \phi dV = \int_A \boldsymbol{\delta}_A \phi dA \quad (4.20)$$

$$\int_V [\nabla \cdot \boldsymbol{\tau}] dV = \int_A [\boldsymbol{\delta}_A \cdot \boldsymbol{\tau}] dA \quad (4.21)$$

The maximum deviations of these shell balances have been on the order of $1 \times 10^{-4} \%$ for mass conservation, $5 \times 10^{-2} \%$ for the x component of momentum, $1 \times 10^{-6} \%$ for the y component of momentum, $5 \times 10^{-1} \%$ for the chemical species, and $5 \times 10^{-2} \%$ for the fluid energy. In most of the cases, all chemical species have shown similar maximum deviations, without significant differences between them. These percentage deviations for all shell balances are satisfactory and, therefore, consistency of the steady state results is ensured.

Results and discussion

Contents

5.1 Base case	51
5.1.1 Operating conditions	51
5.1.2 Velocity, temperature and chemical species distribution	53
5.1.3 Performance of the reactor	54
5.1.4 Energetic analysis	57
5.2 Response of the microreactor to the variation of several operating parameters	62

Once developed with the mathematical model formulated in Chapter 3 and the numerical methodology described in Chapter 4, the simulation code 3DINAMICS has been applied to analyse the physical problem exposed in Chapter 2. The analysis consists of two main studies. In Section 5.1 a case where the microreactor operates in self-sustained mode is first studied, including the analysis of the resulting fields of velocity, mass fractions and temperature, the analysis of the efficiency and performance of the reactor, and the analysis of the relevance of the different terms of the energy equations. Then, in Section 5.2 the response of the reactor to the variation of different operating parameters is tested, with focus on the temperature and performance distribution in the reactor.

5.1 Base case

A base case has been chosen in which the self-sustained reaction occurs, without the appearance of a thermal wave that quenches the reactive system. In this conditions, from the aforementioned initial state the reactor reaches a steady-state suitable for study. This study includes the analyses of the distribution of the main variables within the reactor, of the performance of the reactor and the reactive mechanism, and of the energy balances at the interface and in the channel.

5.1.1 Operating conditions

The operating conditions of the base case are presented in Table 5.1. The inlet velocities were already specified in Section 4.3.2. To ensure the initiation of the reactions, a

Table 5.1: *Operating parameters of the base case*

$(u^*, v^*)_{inlet}$	(1,0)
$T_{preheated}^*$	4
T_{inlet}^*	1.6
$\omega_{CH_4 inlet}$	1/3
$\omega_{O_2 inlet}$	2/3
$Re_{L,c}$	10
α_s^*	1
κ_s^*	30

$T_{preheated}^*$ similar to the one specified in Kaisare et al (2005a) has been chosen, with the characteristic temperature, T_c , set first to 300 K. As it will be discussed in forthcoming sections, to avoid the appearance of a thermal wave with the present conditions, a T_{inlet}^* higher than the room temperature is necessary, and it has been set to 1.6. The mass composition of the inlet gas feed corresponds to a molar ratio of $y_{CH_4}/y_{O_2} = 1$. This ratio is a balance between the stoichiometric ratios of the CPO reaction, $(y_{CH_4}/y_{O_2})_{stoich} = 2$, and of the OXI reaction, $(y_{CH_4}/y_{O_2})_{stoich} = 0.5$. Considering the set of partial reactions, the feed is a rich fuel mixture for the OXI reaction and the limited amount of O_2 , which on the other hand is only present in this reaction, should restrain the oxidation of CH_4 and the increase of temperature. The remaining CH_4 from the OXI reaction is then intended to feed the REF reaction, the main source of production of synthesis gas. A low value of $Re_{L,c}$ has been chosen, again to avoid the inlet feed to generate a cold convective flow that quenches the reactions. The characteristic scales of the physical properties of the gas, used in $Re_{L,c}$ as well as in other non-dimensional groups, are chosen to be those of pure CH_4 at T_c . For this reason, Pr_c and Sc_c cannot be set here, and their values are obtained from these characteristic scales. Finally, κ_s^* is similar to ceramic materials at high temperatures such as silicon dioxide (Stutz and Poulikakos, 2005; Incropera et al, 2006), whereas α_s^* has been chosen based on numerical criteria, which required a reasonable velocity of the transient evolution of T_s^* .

The reaction parameters of the base case are presented in Table 5.2. $Ar_{rx,c}$, Υ_{rx} , $Rh_{rx,c}$ and $Da_{CH_4,rx,c}$ have constant values by definition (See Secs. 3.5.1 and 3.5.4.1), and they have been obtained from the selected reaction mechanism (See Sect. 2.2) and the characteristic scales. On the other hand, $K_{eq,p,rx}^o$ are temperature dependent (See Sect. 3.4.1) and, as such, they should be continuously recalculated during the transient simulation. The dependence of $K_{eq,p,REF}^o$ and $K_{eq,p,WGS}^o$ on temperature is illustrated in the plots in logarithmic scale of Figure 5.1. However, for simplicity, both $K_{eq,p,rx}^o$ have been considered to be constant in the present work with a value equal to their average value from 1000 K to 2000 K. With the extremely high value of $K_{eq,p,REF}^o$ and the moderate value of Υ_{REF} , the REF reaction can be fairly considered a priori as

Table 5.2: Reaction parameters of the base case

	OXI	REF	WGS
Ar_c	-4.022×10^1	-4.575×10^1	-1.529×10^1
Υ	–	3.323×10^2	5.683
$K_{eq,p}^o$	–	3.735×10^6	2.595
Rh_c	-2.778×10^{-12}	1.821×10^{-14}	-1.283×10^{-4}
$Da_{CH_4,c}$	3.644×10^{-14}	8.464×10^{-16}	4.461×10^{-5}

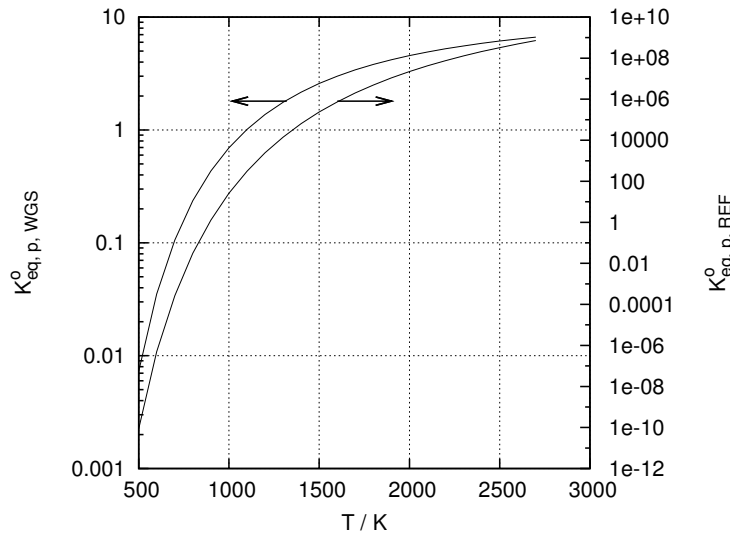


Figure 5.1: Values of the standard equilibrium constants of reaction, $K_{eq,p,REF}^o$ and $K_{eq,p,WGS}^o$, against temperature, T .

irreversible, always with consumption of CH_4 and H_2O and generation of CO and H_2 .

5.1.2 Velocity, temperature and chemical species distribution

The fields with the distribution of velocity, temperatures and mass fraction of CH_4 within the 2D domain once the system reaches the steady state, can be found in Figure 5.2. The velocity field in Figure 5.2a, which also includes its absolute value, shows a typical parabolic laminar profile in the span-wise direction of the channel with a vanished v component. Unlike the usual fields of laminar incompressible flows, here the velocity increases continuously its magnitude in the stream-wise direction, reaching values of $u \approx 11$, mostly due to an important decrease in the gas density resulting from the high temperatures reached towards the outlet. A detailed view of the development of the velocity field in the entry region of the reactor ($x^* = 0$ to 3) is shown in Figure 5.3.

There it can be observed how the adjustment of the velocity profile due to the entrance discontinuity is completed near the entrance ($x^* < 1$).

The more remarkable details extracted from the fields of T^* , T_s^* and ω_{CH_4} (Figs. 5.2b and 5.2c) are the appearance of sudden gradients in the stream-wise direction at locations between $x^* = 5$ to 10, which indicates the initiation of the reactions, and an almost flat profile in span-wise direction throughout the whole reactor length, especially for T_s^* . This flat profile, which is also the case for the other chemical species, indicates instantaneous diffusion from/to the catalytic wall and that the system must be reaction limited and not diffusion limited.

The profile of the complete set of ω_α along the reactive interface ($y^* = 0$) is illustrated in Figure 5.4, which also includes the T_{if}^* for reference purposes. The consumption of CH_4 and O_2 , and therefore the initiation of the reactions, begins at $x^* \approx 5$ to 6 when the temperature reaches values of around $T_{if}^* \approx 3.5$ to 4.5, proving that the choice of $T_{preheated}^*$ was accurate for the studied case. The sharp consumption of CH_4 and O_2 is followed by the generation of the products of the OXI reaction, the intermediate species CO_2 and H_2O . A bit afterwards ($x^* \approx 8$) the components of the synthesis gas, CO and H_2 , appear due to the start of the REF reaction, which also moderates the increase of T_{if}^* . It is noticeable the different behaviour of the intermediate species and the components of the synthesis gas. While ω_{CO_2} and ω_{H_2O} are stabilized after $x^* \approx 20$, ω_{CO} and ω_{H_2} continuously increase along the reactor. Contrary to what was expected, CH_4 is the limiting reagent and it is consumed almost completely, while O_2 is in excess. This is caused by, as it will be observed later, the REF reaction being initiated before the OXI reaction consumes completely the O_2 .

5.1.3 Performance of the reactor

One of the main interests of the study is the analysis of the performance of the reactor with the selected operating conditions. The performance of a reactor is usually characterised by means of three different parameters, the conversion of the reagents, and the selectivity and yield of the desired products. The conversion, η , is defined as the ratio of number of reagent moles that have reacted to the moles of reagent fed to the system, whereas the yield, γ , is defined as the ratio of moles of product formed to the maximum theoretical moles of product, i.e. those that would have been formed if there were no side reactions and the conversion of the reagent was complete (Felder and Rousseau, 1999; Fogler, 2005). The selectivity, ξ , accepts several definitions (Felder and Rousseau, 1999; Fogler, 2005; Schneider et al, 2006), and the one used here is based on Kikas et al (2003) and Stutz and Poulikakos (2005), which define ξ as the ratio of the moles of desired product formed to the total moles of desired and undesired products. One of the advantages of this definition is that ξ becomes a bounded parameter with values that range from 0 to 1.

The relevant performance parameters here are, hence, the conversion of CH_4 , η_{CH_4} , the selectivity of the components of the synthesis gas, ξ_{H_2} and ξ_{CO} , and the yield of

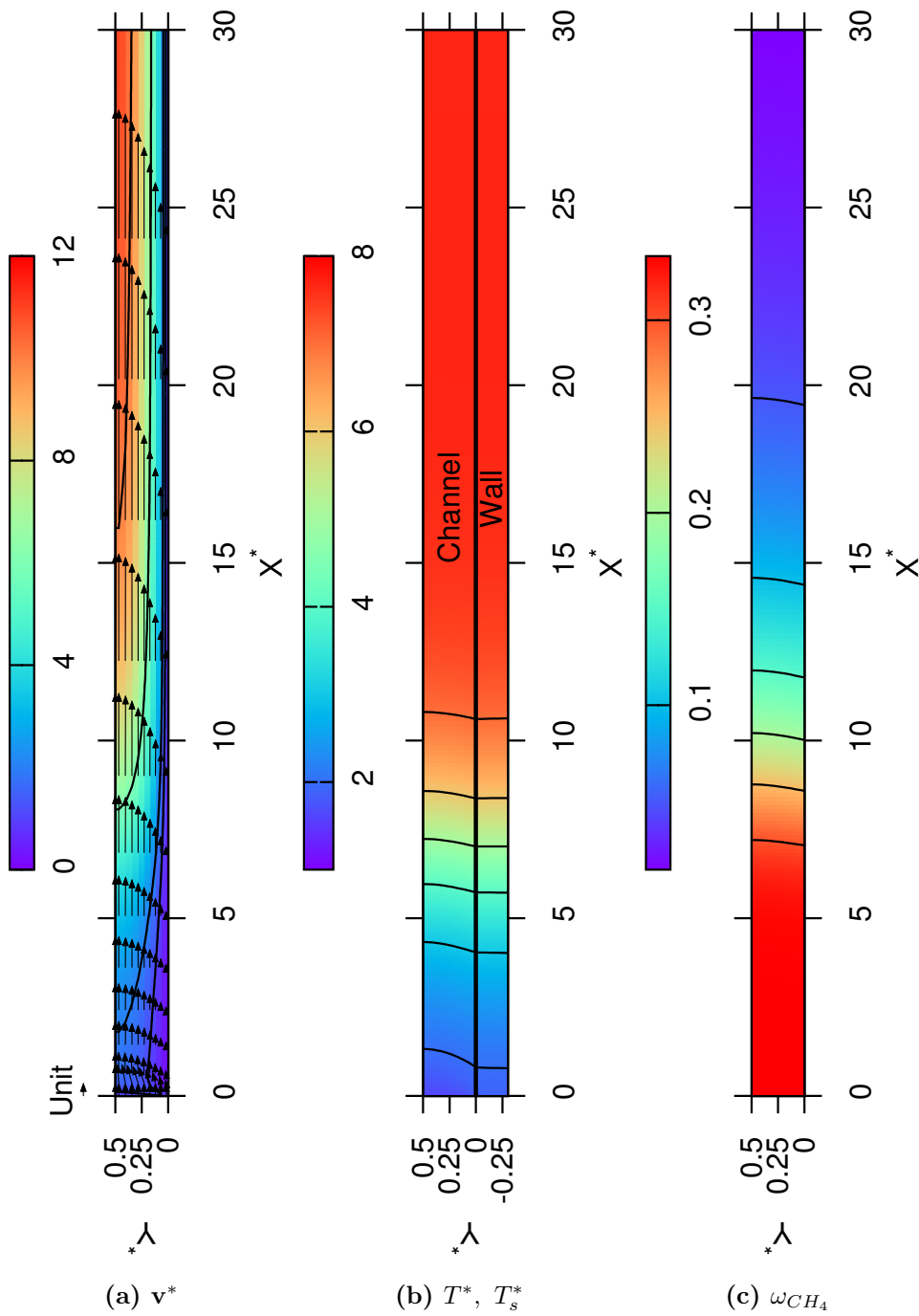


Figure 5.2: Fields of (a) velocity, \mathbf{v}^* , (b) temperature, T^* , and (c) mass fraction of CH_4 , ω_{CH_4} , at steady state. The images are scaled to an aspect ratio of $y/x = 0.325$.

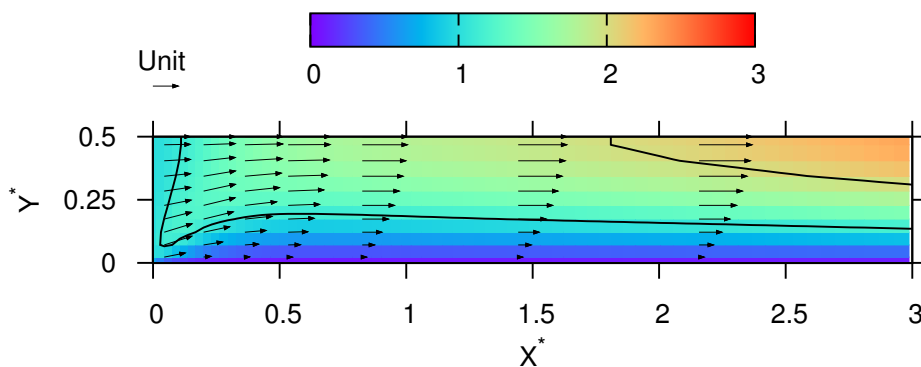


Figure 5.3: Velocity field, \mathbf{v}^* , at the entrance of the channel ($x^* = 0$ to $L_x^*/10$).

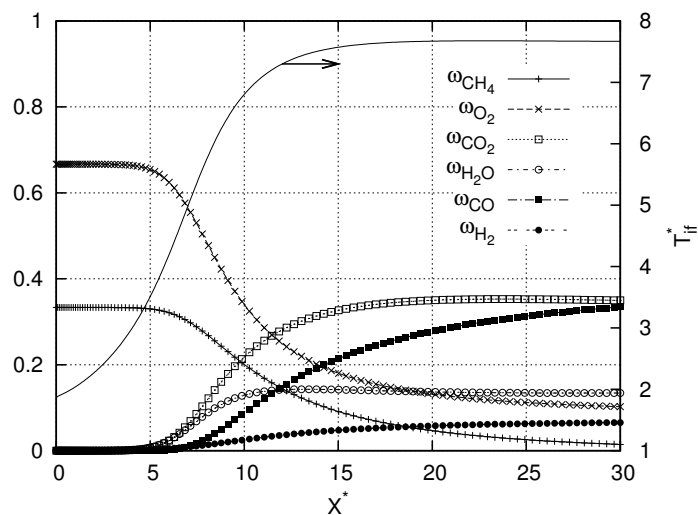


Figure 5.4: Mass fraction, ω , of the chemical species along the fluid-solid reactive interface.

the components of the synthesis gas, γ_{H_2} and γ_{CO} . These parameters are formulated in Equations (5.1), (5.2) and (5.3),

$$\eta_{CH_4} = \frac{\dot{m}_{CH_4,inlet} - \dot{m}_{CH_4}}{\dot{m}_{CH_4,inlet}} \quad (5.1)$$

$$\xi_{H_2} = \frac{\dot{m}_{H_2}/M_{H_2}}{\dot{m}_{H_2}/M_{H_2} + \dot{m}_{H_2O}/M_{H_2O}} \quad \gamma_{H_2} = \eta_{CH_4} \cdot \xi_{H_2} \quad (5.2)$$

$$\xi_{CO} = \frac{\dot{m}_{CO}/M_{CO}}{\dot{m}_{CO}/M_{CO} + \dot{m}_{CO_2}/M_{CO_2}} \quad \gamma_{CO} = \eta_{CH_4} \cdot \xi_{CO} \quad (5.3)$$

where,

$$\dot{m}_\alpha = \int_{A_x} \rho_\alpha u dA_x \quad (5.4)$$

\dot{m}_α is understood as the total mass flow rate of a specie α through the cross-sectional area of the channel, A_x .

The efficiency and performance results along the reactor are plotted in Figure 5.5. In accordance with ω_{CH_4} in Figure 5.4, the conversion of CH_4 begins at $x^* \approx 5$ and it reaches a satisfactory value of $\eta_{CH_4} \approx 0.95$ at the reactor outlet. The evolution of the profile of η_{CH_4} , though, is not yet asymptotic at the outlet, meaning that there is still a reactive process that would increase η_{CH_4} in a longer reactor. ξ_{H_2} experiences an initial decrease when H_2O is first generated in the OXI reaction ($x^* \approx 8$), but this trend is quickly reverted and the $\xi_{H_2} \approx 0.8$ at the outlet is also a satisfactory result. On the other hand, ξ_{CO} only achieves a 0.6 due, most probably, to the fact that the CO_2 generated in the OXI reaction is hardly or none consumed by the WGS reaction. Both ξ_{H_2} and ξ_{CO} almost reach their asymptotic values at $x^* \approx 25$, which means that the efficiency of the reactor will not be enhanced if its length is increased.

Together with the behaviour of η_{CH_4} these asymptotic selectivities set a dilemma, to which a decision should be taken according to the specific needs of an hypothetical industrial operation of this reactor. The dilemma comes from the fact that the performance of the reactor could be enhanced increasing η_{CH_4} and, hence, γ_{H_2} and γ_{CO} , with a longer reactor. However, since ξ_{H_2} and ξ_{CO} have already reached their maxima, the enlargement of the reactor would also result in a higher production of the undesired products, CO_2 and H_2O . An alternative to enlarging the reactor might be a subsequent recovery of the remaining CH_4 in the outlet flow, in order to add it again to the feed flow.

5.1.4 Energetic analysis

A key in the CPO microchannel reactor is the feasibility to achieve a self-sustained situation, in which the reactor can operate continuously without external support. The energetic balance between the cold inlet reagents, the energy generated or consumed by the reactions and transferred to the flow, and the energy storage source which is the conductive wall, determines whether the temperature in the domain is enough as to

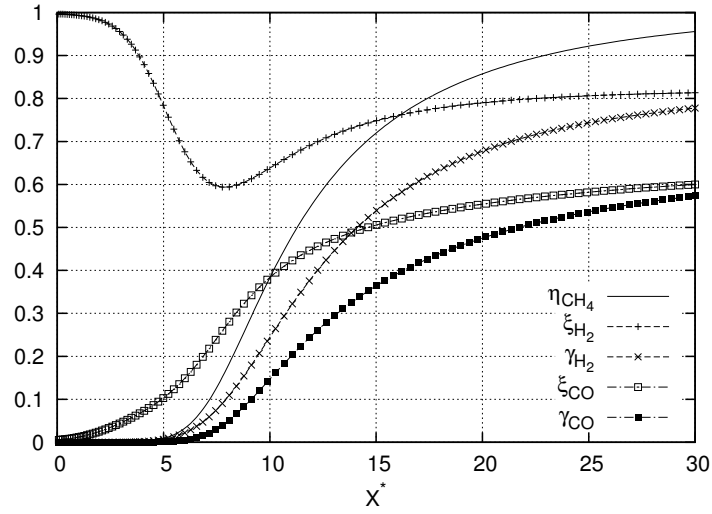


Figure 5.5: Efficiency and performance parameters along the reactor. The parameters include the conversion of CH_4 , η_{CH_4} , the selectivity of H_2 and CO , ξ_{H_2} and ξ_{CO} , and the yield of H_2 and CO , γ_{H_2} and γ_{CO} .

allow the desired self-sustained operation of the reactor. Hence, identifying which are the energetic components that play a major role in the system is of utmost importance to predict the appearance of a thermal wave under different operating conditions. With this aim, several analysis of the energy balance in the system were conducted.

Recalling the Equations (3.92) and (3.120), the energy balance at the catalytic interface can be reformulated to evaluate the contribution of the different terms to the increase/decrease of T_{if}^* . The balance is reformulated in Eq. (5.5), and the different terms include the energy produced/consumed by the three reactions, and the heat fluxes from/to the fluid in the channel and the solid wall. All the terms have been placed on the right hand side of the equation, in a way that they can be understood as contributors to the increment of T_{if}^* when they are positive, and to the decrease of T_{if}^* when they are negative.

$$0 = \underbrace{-q_{if}^*}_{(1)} - \underbrace{q_{s,if}^*}_{(2)} - \underbrace{(Rh_{OXI,c}r_{OXI}^*)}_{(3)} - \underbrace{(Rh_{REF,c}r_{REF}^*)}_{(4)} - \underbrace{(Rh_{WGS,c}r_{WGS}^*)}_{(5)} \quad (5.5)$$

Terms

- (1), Heat flux from/to fluid,
- (2), Heat flux from/to solid,
- (3), OXI reaction energy,
- (4), REF reaction energy,
- (5), WGS reaction energy

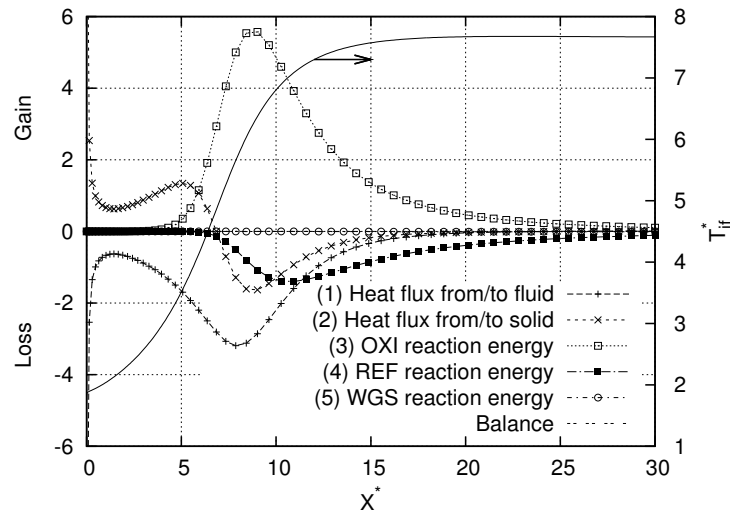


Figure 5.6: Balance of terms of energy along the fluid-solid reactive interface. The profile of the interface temperature, T_{if}^* , is included.

As it can be observed in Figure 5.6, the most relevant region with the highest energy transport at the interface is located at $x^* \approx 5$ to 20. The main term in the balance of Eq. (5.5) is, by far, the energy released by the OXI reaction. As previously anticipated, the OXI reaction is ignited at $x^* \approx 5$ and it reaches a peak at $x^* \approx 8$. In its peak, the heat is transported mostly to the fluid in the channel, followed by the solid wall. The peak also sets the inflection point on the behaviour of increasing T_{if}^* along the interface, also included in Figure 5.6. The REF reaction initiates and reaches its maximum energy consumption both after the OXI reaction, at $x^* \approx 7$ and 11 respectively. In the first half of the reactor its magnitude is significantly smaller than the OXI energy, but in the second half of the reactor it becomes the only active term together with the OXI energy. As expected, the negative value of REF energy throughout the domain indicates that the reaction occurs only in the forward direction, always consuming CH_4 and H_2O and producing CO and H_2 . As for the WGS reaction, its energetic contribution is none.

The importance of the conductive solid wall is evident in the first half of the reactor, $x^* \approx 0$ to 15, where the energy stored in the wall from the OXI reaction at $x^* \approx 7$ to 15, is diffused towards the entrance and, once there, it is transported to the fluid at $x^* \approx 0$ to 5. This results in the gradual heating of the interface, which is crucial for T_{if}^* to reach the threshold where the OXI reaction is ignited. Finally, the fluid is obviously a continuous receiver of energy from the interface.

In the same way as with the catalytic interface, the energy equation in the fluid (Eq. (3.109)) can be reformulated in steady state to evaluate the contribution of its different terms to the increase/decrease of T^* . The balance is reformulated in Eq. (5.6), and it includes the stream-wise and span-wise terms of convection, diffusion and en-

ergy associated to the transport of chemical species. Note that the temporal term has disappeared in steady state.

$$0 = \underbrace{\frac{\partial \rho^* T^* u^*}{\partial x^*}}_{(1)} - \underbrace{\frac{\partial \rho^* T^* v^*}{\partial y^*}}_{(2)} + \underbrace{\frac{1}{Re_{L,c} Pr_c} \frac{1}{c_p^*} \frac{\partial}{\partial x^*} \left(\kappa^* \frac{\partial T^*}{\partial x^*} \right)}_{(3)} + \underbrace{\frac{1}{Re_{L,c} Pr_c} \frac{1}{c_p^*} \frac{\partial}{\partial y^*} \left(\kappa^* \frac{\partial T^*}{\partial y^*} \right)}_{(4)} + \underbrace{\frac{1}{Re_{L,c} Sc_c} \sum_{\alpha} \left(\rho^* D_{eff,\alpha}^* \frac{c_{p,\alpha}^*}{c_p^*} \frac{\partial \omega_{\alpha}}{\partial x^*} \right) \frac{\partial T^*}{\partial x^*}}_{(5)} + \underbrace{\frac{1}{Re_{L,c} Sc_c} \sum_{\alpha} \left(\rho^* D_{eff,\alpha}^* \frac{c_{p,\alpha}^*}{c_p^*} \frac{\partial \omega_{\alpha}}{\partial y^*} \right) \frac{\partial T^*}{\partial y^*}}_{(6)} \quad (5.6)$$

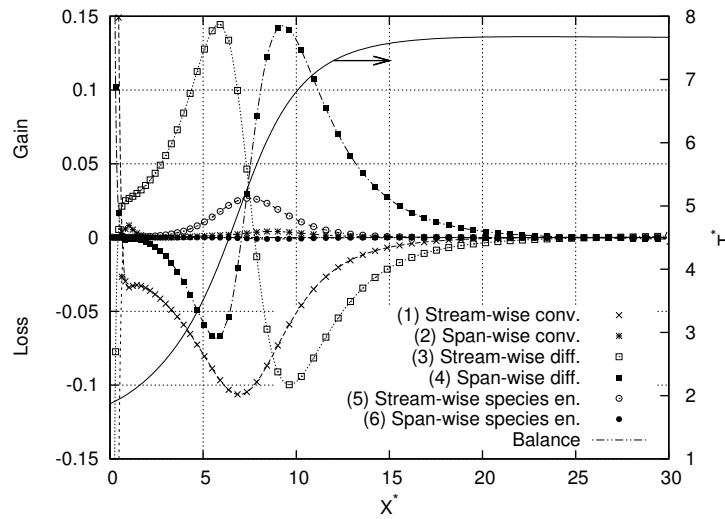
- Terms
- (1), Stream-wise convection,
 - (2), Span-wise convection,
 - (3), Stream-wise diffusion,
 - (4), Span-wise diffusion,
 - (5), Stream-wise species transport energy,
 - (6), Span-wise species transport energy

The contribution of the energy terms has been evaluated along the stream-wise direction of the reactor at $y^* = 0.0236$ and $y^* = 0.468$, and along the span-wise direction of the reactor at $x^* = 7.5$. These y^* locations correspond to the closest grid points to the interface and to the symmetry plane, the two most meaningful regions of the channel. Due to numerical limitations, it is not possible to evaluate the energy terms beyond the location of these grid points. The results of the balance of energy terms are plotted in Figure 5.7 for the stream-wise direction, and in Figure 5.8 for the span-wise direction.

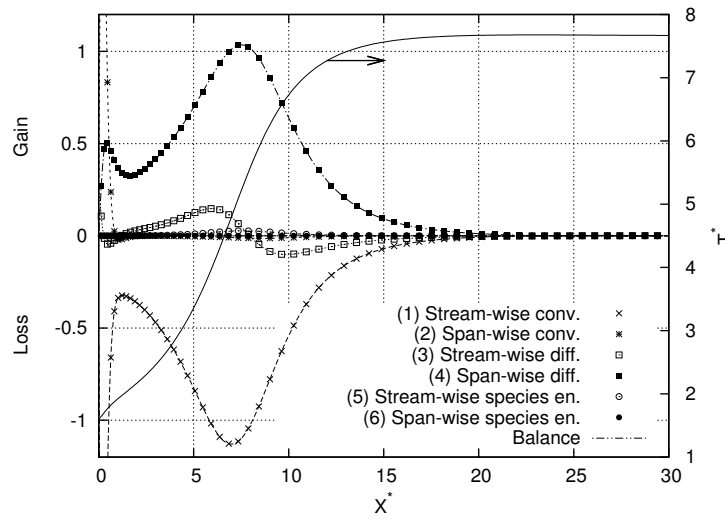
Again, the first half of the reactor length is the region with the highest energetic activity. Obviously, the main contribution to the decrease of T^* throughout the entire domain comes from the convection, in stream-wise direction, of the cold inlet feed, whereas the span-wise convection term is non-existent due to the null v component of velocity in the channel, with the only exception of the narrow entrance region (See Fig. 5.3).

The behaviour of the diffusion terms is somewhat interesting. Near the interface, both the stream-wise and the span-wise terms are relevant, and they show a reverse trend with each other. They shift their contribution at the region where the peak of the OXI reaction occurs and there is an inflection point in the positive gradient of temperature. On the other hand, near the symmetry, the span-wise diffusion becomes predominant, with a positive contribution to T^* .

Remarkably, the contribution of the energy associated to the transport of the chemical species is non-existent throughout the entire domain, with the only exception of a narrow region near the interface at $x^* \approx 5$ to 10. Specifically, at $x^* \approx 7.5$ the stream-wise component reaches its highest magnitude, and there it is of relative relevance compared



(a)



(b)

Figure 5.7: Balance of terms of the energy equation along the reactor at (a) $y^* = 2.36 \times 10^{-2}$ and (b) $y^* = 4.68 \times 10^{-1}$. The temperature profiles, T^* , are included for completeness.

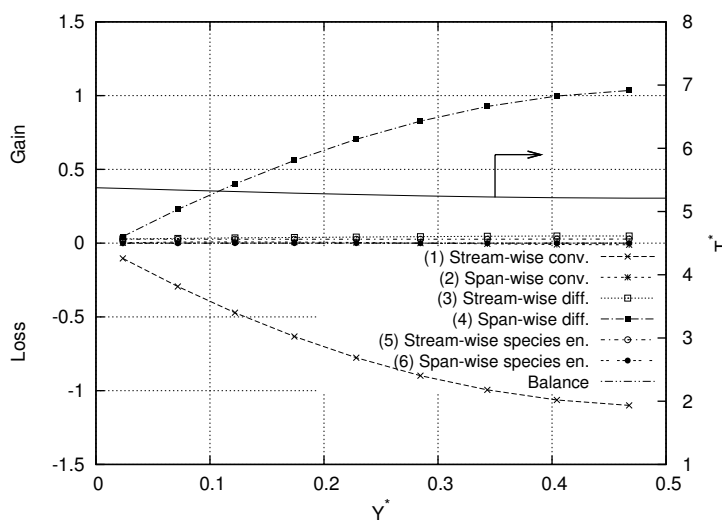


Figure 5.8: Balance of terms of the energy equation along the span-wise direction of the reactor, $x^* = 7.5$. The temperature profile, T^* , is included for completeness.

to the other terms. Comparing the profile of the stream-wise component of the species energy with the balance of terms in the interface (See Fig. 5.6), it is found that this profile is qualitatively identical to the sum of the energies of reactions, and it is slightly displaced towards the inlet. Therefore, it can be assumed that the energy generated by the heterogeneous reactions is exclusively transmitted to the fluid by means of the transport of species in the stream-wise direction.

From the balance along the span-wise direction in Figure 5.8, it can be observed that, while the stream-wise components of diffusion and species energy remain almost constant along y^* , the stream-wise convection and the span-wise diffusion terms increase significantly with y^* . These trends along the span-wise direction are observed throughout the entire reactor length.

5.2 Response of the microreactor to the variation of several operating parameters

Based on the results of the base case, the response of the microreactor to the variation of an operating parameter has also been investigated. The variable parameters in this study have been selected to be the inlet temperature in the reactor, T_{inlet}^* , and the thermal conductivity of the surrounding wall, κ_s^* , which reflect two common cases in the operation of microreactors, i.e. reactors fabricated in different materials and variations in the feed temperature either pointedly or by external causes. Besides, the present mathematical model assumes constant physical properties of the surrounding wall which, according to

5.2. Response of the microreactor to the variation of several operating parameters

Table 5.3: Variable operating parameters and times elapsed to reach steady state

T_{inlet}^*	t^*	κ_s^*	t^*
1.52	816.0	26	755.7
1.60	2006	30	2006
2.00	1232	100	2742
3.00	1748	1000	845.3

the wide temperature range experienced within the wall in the base case, it is definitely not the real situation. The results of the investigation on the effect of varying κ_s^* can give a hint on the inaccuracy of this assumption.

Four different tests of each of the variable operating parameters have been performed, and their selected values are shown in Table 5.3. During each test the corresponding parameter adopted the selected value from this table, whereas the rest of the operating conditions remained with the values of the base case (See Table 5.1). The test with $\kappa_s^* = 1000$ is a rather extreme case of hypothetical variation of κ_s^* from its base case value to this test value, and it is not expected to occur for any material. However, this κ_s^* is typical of some metallic materials at 300 K such as platinum or titanium (Incropera et al, 2006). The lower parameters tested, $T_{inlet}^* = 1.52$ and $\kappa_s^* = 26$, are the limiting operating values for the self-sustained operation of the reactor, and below these conditions the previously mentioned thermal wave appeared and quenched the system. Table 5.3 also includes the elapsed times needed to reach steady state, t^* , for every case analysed. Contrary to what was initially expected, there is not a direct relationship between the increment of T_{inlet}^* or κ_s^* and the resulting t^* .

The effect of T_{inlet}^* and κ_s^* on the efficiency and performance of the reactor is depicted in Figure 5.9, which shows the values of the performance parameters at the reactor outlet. From this figure it is clear that T_{inlet}^* has a negligible effect on the performance of the reactor, while κ_s^* does influence the results of the performance parameters. Despite the few data points available in Figure 5.9b, it seems that there is a nearly inverse linear relationship between the variation of κ_s^* and the resulting η_{CH_4} , ξ_{H_2} and ξ_{CO} , with average values of $(d\eta_{CH_4}/d\kappa_s^*) \approx -6.89 \times 10^{-2}$, $(d\xi_{H_2}/d\kappa_s^*) \approx -4.89 \times 10^{-2}$ and $(d\xi_{CO}/d\kappa_s^*) \approx -4.15 \times 10^{-2}$. There is also a slight decrease in $(d\eta_{CH_4}/d\kappa_s^*)$ and $(d\xi_{CO}/d\kappa_s^*)$, and a slight increase in $(d\xi_{H_2}/d\kappa_s^*)$ as the thermal conductivity of the wall increases.

From the analysis of the evolution of T_{if}^* , η_{CH_4} , ξ_{H_2} , γ_{H_2} , ξ_{CO} and γ_{CO} along the reactor at the different values of T_{inlet}^* , shown in the series of images in Figure 5.10, several observations can be made. Probably the most important implication from Figure 5.10a is that an increment in T_{inlet}^* causes a noticeable reduction in the maximum T_{if}^* reached in the reactor, which is beneficial for the energetic stability and for the

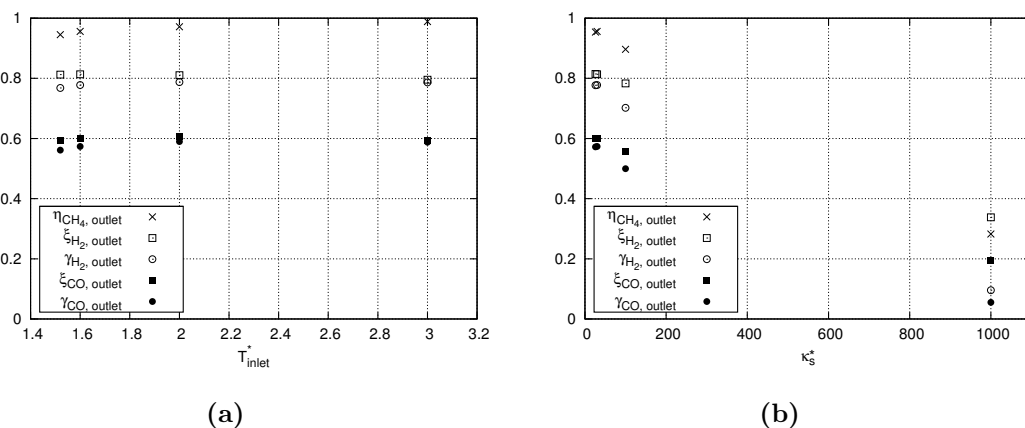


Figure 5.9: Reactor efficiency and performance as function of (a) inlet temperature, T_{inlet}^* , and of (b) thermal conductivity of the wall, κ_s^* .

mechanical preservation of the reactor. Although the qualitative profile of T_{if}^* is similar for all the analysed T_{inlet}^* , without the appearance of hot-spots, T_{if}^* reaches its maxima at shorter distances from the inlet as T_{inlet}^* increases, probably because a higher T_{inlet}^* contributes to a faster initiation of the system of reactions.

The differences in the profiles of the performance parameters along the reactor, shown in Figures 5.10b to 5.10f, can also be explained as a result of the distributions of T_{if}^* . In these figures the data points for each T_{inlet}^* where the increment of T_{if}^* stabilizes, $(dT_{if}^*/dx^*) \leq 0.01$, which is assumed to be the location where the system of reactions is almost exhausted (See Fig. 5.6), are indicated. An agreement can be observed, for each performance parameter, among the values of every data point. This agreement demonstrates that the displacement of the profile of T_{if}^* causes a mere displacement on the profiles of the performance parameters, while they are not qualitatively affected. This agreement also supports the previous observation in Figure 5.9a that T_{inlet}^* does not affect the performance of the reactor. Given these results, an energetic analysis of the different cases would be desirable to elucidate the causes of the decrease of T_{if}^* .

The effect of κ_s^* on the evolution of T_{if}^* , η_{CH_4} , ξ_{H_2} , γ_{H_2} , ξ_{CO} and γ_{CO} along the reactor is shown in Figure 5.11. Here, an increment of κ_s^* leads to a damping in the gradients of T_{if}^* , towards isothermal conditions, with lower overall temperatures. Although a reduction in the temperature of the walls is always beneficial, unlike in the case of different T_{inlet}^* this damping reduces dramatically the performance of the reactor (Figs. 5.11b to 5.11f). η_{CH_4} , and hence also γ_{H_2} and γ_{CO} , is especially sensitive to κ_s^* , and its positive gradient along the reactor at the highest values of κ_s^* suggests that an enlargement of the reactor would be desirable.

5.2. Response of the microreactor to the variation of several operating parameters

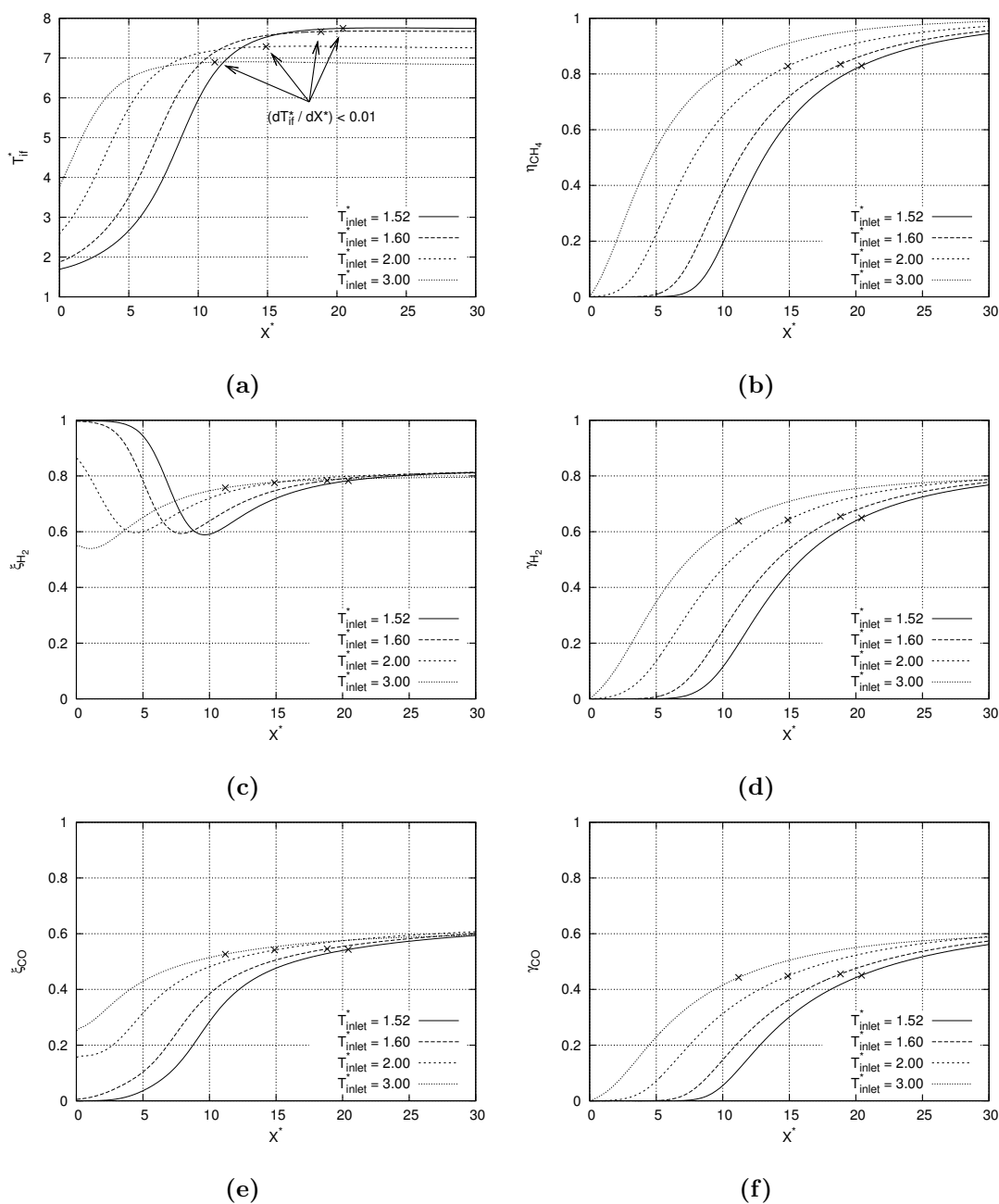


Figure 5.10: Effect of inlet temperature, T_{inlet}^* , on the evolution along the reactor of (a) interface temperature, T_{if}^* , (b) CH_4 conversion, η_{CH_4} , (c) H_2 selectivity, ξ_{H_2} , (d) H_2 yield, γ_{H_2} , (e) CO selectivity, ξ_{CO} , and (f) CO yield, γ_{CO} . The data points for each T_{inlet}^* where the increment of T_{if}^* stabilizes, $(dT_{if}^*/dx^*) \leq 0.01$, are marked with a cross.

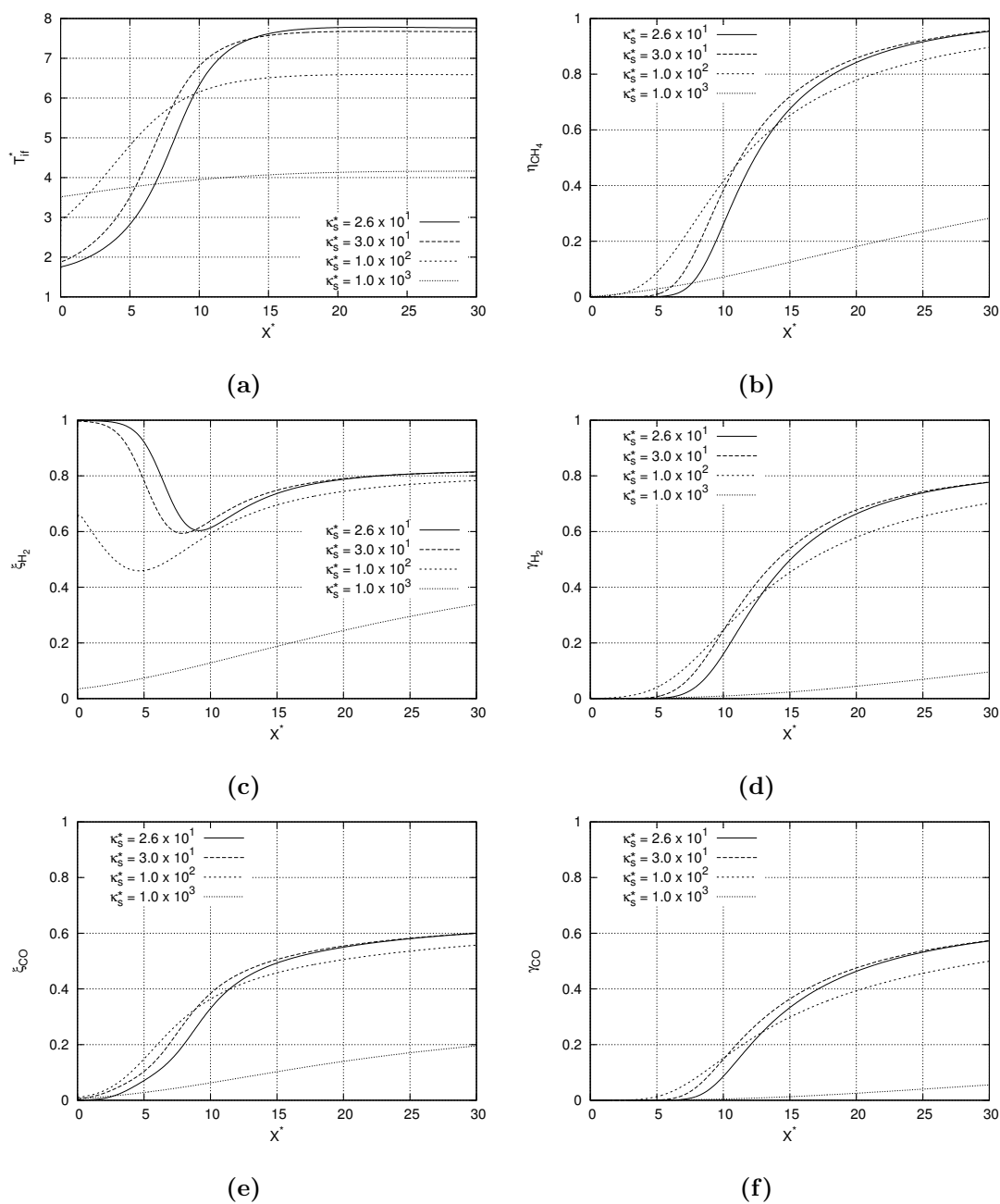


Figure 5.11: Effect of thermal conductivity of the wall, κ_s^* , on the evolution along the reactor of (a) interface temperature, T_{if}^* , (b) CH_4 conversion, η_{CH_4} , (c) H_2 selectivity, ξ_{H_2} , (d) H_2 yield, γ_{H_2} , (e) CO selectivity, ξ_{CO} , and (f) CO yield, γ_{CO} .

Concluding remarks

Contents

6.1 Overall conclusions	67
6.2 Future directions	69

This final chapter of Part I gathers the overall conclusions that can be extracted from the study conducted in this part of the thesis (Sect. 6.1), taking into account the main objectives that were proposed initially. Finally, the suggestions for future work directions are listed in Section 6.2.

6.1 Overall conclusions

The two main objectives of this numerical part of the thesis have been accomplished.

First, the in-house simulation code developed, 3DINAMICS, is functional and it is able to represent, with physically meaningful results, the transport phenomena and the coupled fields of velocity, temperature and mass fraction of chemical species of 2D microchannel reactors where sets of heterogeneous reactions occur along the wall surface. The code is able to deal with the low Mach number compressible laminar flow, and it allows to include detailed kinetic models for the reactive system, which are properly integrated in the governing equations. The physical properties of the fluid are calculated as function of temperature and composition. The surrounding wall of the channel is considered to be conductive and the conjugate heat transfer problem between the solid and the fluid is accordingly solved.

Then, the following can be concluded after applying 3DINAMICS to the study of the catalytic partial oxidation of methane (CPO) to produce synthesis gas in a straight 2D microchannel reactor, via a kinetic model that involves three partial reactions, the total oxidation of methane (OXI), the steam reforming (REF) and the water-gas shift (WGS).

The self-sustained operation of the reaction is feasible in a reactor with relatively high aspect ratio $L_x^*/L_y^* = 30$, with properties of the wall of $\alpha_s^* = 1$ and $\kappa_s^* = 30$, at low Reynolds number, $Re_{L,c} = 10$, and with an inlet feed ratio of reagents below the stoichiometric value, $y_{CH_4}/y_{O_2} = 1$, and at moderate temperatures, $T_{inlet}^* = 1.6$. Nevertheless, the whole system needs to be preheated to a certain temperature, $T_{preheated}^* = 4$ in order

to initiate the reaction mechanism of the CPO. Under these conditions, three regions can be differentiated along the domain. An initial region near the inlet, $x^* \approx 0$ to 5, where the cold gas feed is heated until it reaches the ignition temperature, $T^* \approx 3.5$. An intermediate region, $x^* \approx 5$ to 20, where the reactions occur, especially the OXI and the REF reactions. A final region, $x^* \approx 20$ to 30, where the reagents are almost exhausted, especially the CH_4 , and the reactions stop. The temperature profile along the reactor experiences a steep increment in the reacting region, quickly reaching very high temperatures once the OXI reaction is ignited, $T^* \approx 8 \rightarrow T \approx 2400$ K. These temperatures, though, are not reached locally in the form of a hot spot as it was expected, but they are maintained almost constant all along the final exhausted region. The enhanced diffusions of heat and of chemical species due to the high temperatures result in a reaction limited (not diffusion limited) system and in flat profiles of temperature and chemical species in the span-wise direction of the channel.

The conversion of CH_4 along the reactor increases continuously, even in the exhausted region, reaching almost 100% of conversion. However the selectivity of H_2 and of CO are almost constant after the reacting region. As a result, the choice of the length of the reactor must be a balance of interests, between the performance of a longer reactor with higher yields but also more undesired products (CO_2 and H_2O), and the lower yields of a shorter reactor but with less CH_4 wasted in undesired products.

Obviously, the OXI reaction is the only energy provider during the operation of the system. The energy released by the OXI reaction in the channel-wall interface is mainly transported to the fluid, followed by its consumption by the REF reaction and the transport to the conductive wall. In this sense, the reactive wall proves its role as energy storage, transporting the heat absorbed from the OXI reaction towards the inlet of the channel, where it is released to the cold feed gases, increasing their temperature. The energetic contribution of the WGS reaction and of the energy associated to the transport of chemical species within the fluid, are both negligible. The main contributor to maintain the high temperatures in the fluid is the span-wise diffusion whereas, as expected, the stream wise convection continuously cools down the flow.

The stability of the microreactor has been tested against variations on the inlet temperature of the feed gas, T_{inlet}^* , and on the thermal conductivity of the reactor walls, κ_s^* , and the limiting values of these parameters under which it appears a cold thermal wave that quenches the reactive system, have been identified. It has been demonstrated that the performance of the reactor is mostly insensitive to changes in T_{inlet}^* , while the maximum temperature of the reactor is noticeably reduced at the higher T_{inlet}^* . It is therefore recommendable to allow the inlet feed gases to be preheated before entering the microchannel reactor, in order to benefit from reduced temperatures which are less aggressive, in terms of thermal stress, to the reactor. On the other hand, an increment in κ_s^* leads to homogenized, lower temperatures in the conductive wall, at the cost of significantly reduced performance of the reactor. In this case, increasing the length/width aspect ratio of the microreactor might be desirable.

6.2 Future directions

With the basis of the present work, several forthcoming directions can be followed in this numerical analysis of gas microreactors. These directions can be sorted into two groups, the directions focused on the development of the code and the directions to extend the knowledge of the present reactive system.

A list of possibilities on the development of the code includes,

- The simulation of this physical system is computationally expensive. This is due to the coupling between the different governing equations, the amount of variable properties involved, and the presence of the conductive wall which leads to a slow temporary evolution of the system. Accordingly, to extend the possibilities of the present code, the potential ways to accelerate its computation speed should be first considered. An obvious step is to implement OpenMP or MPI libraries for parallel resolution of the code. Also, alternative solutions can be found, such as using a pseudo-1D flow model or solving the steady-state form of the governing equations in the fluid domain and the transient form of the heat conduction in the solid, according to the different time scales of energy transfer in both media (Tischer and Deutschmann, 2005).
- Once the speed performance of the code is enhanced, actions that require higher computing resources can be undertaken. These include enlarging the 2D domain, solving a 3D version of the domain, which allows to study the stagnant areas generated in the corners of the channel, or substituting the poorly reliable effective diffusion model for multicomponent diffusion by a model based on the matrix-system of Maxwell-Stefan equations or Fick's generalized law equations.
- A number of several improvements might be also applied to the code without the need to enhance its speed performance. Taking into account the Soret/Dufour effects that have been neglected in the present work (See Sect. 3.3) is an interesting possibility. This would, probably, increase the coupling level between the governing equations for energy and mass conservation of species, though. Also, the broad temperature range within the domain must certainly affect the physical properties of the conductive wall so, considering these solid variables as temperature-dependent would result in an enhancement of the physical coherency of the model. Finally, a deeper insight on the fundamentals and relevance of the reactive process can be achieved by including several details in the code, such as the Stefan velocity or the process of adsorption/desorption of chemical species along the reactive surface (Schwiedernoch et al, 2003).

As for the further analysis of the present CPO microreactor, the possibilities include,

- The immediate choice is to analyse the effect of a broader number of different operating parameters, such as the inlet feed ratio. Increasing the ratio of CH_4 to

reach stoichiometric conditions would allow consuming totally the O_2 feed, and it would increase the rate of REF reaction as well. Using an alternate kinetic model for the reactions is another interesting possibility.

- The temperatures reached in the microreactor are high enough as to take into account the radiation heat transfer within the system, in order to assess whether its effects are really negligible, as it has been concluded in previous works (Schneider et al, 2006).
- It is worth considering the reacting area to occupy only a portion of the total length of the channel, i.e. to leave a certain inert length after the inlet and before the outlet of the reactor. In this way, the reagents would be preheated before reaching the reacting area, and the flow would be stabilized at the outlet. Both situations are physically more realistic than the present one. Furthermore, the aspect ratio could be varied in order to check the consistency of the results of a particular case, or to study the cases with a lower reacting performance and which require a longer channel to achieve proper reaction conditions.

Part II

Flow of CO₂-ethanol and CO₂-methanol in a non-adiabatic microfluidic T-junction at high pressures

UNIVERSITAT ROVIRA I VIRGILI

NUMERICAL AND EXPERIMENTAL ANALYSES OF SINGLE AND TWO-PHASE MICROFLUIDIC FLOWS WITH IMPLICATIONS IN MICROREACTORS

Roland Blanch Ojea

DL:T. 149-2012

Theoretical background

Contents

7.1	Phase behaviour of Type I binary mixtures	74
7.1.1	Vaporised mass diffusion fraction	75
7.2	Properties of fluids	75
7.2.1	Pseudocritical point of a supercritical fluid	75
7.2.2	Density	76
7.2.3	Dynamic viscosity	76
7.2.4	Interface tension	76
7.3	Two-phase flows	80
7.3.1	Two-phase flow regimes	80
7.3.2	Void fraction	82
7.4	Capillary pumping and wetting processes	85

This chapter provides fundamental knowledge of several useful concepts for the Part II of the thesis. Here is presented a qualitative description of the phase behaviour of both sets of fluids, CO₂-EtOH and CO₂-MeOH, which belong to the Type I binary mixtures (Sect. 7.1). This description focuses on the behaviour of the mixtures during Vapour-Liquid Equilibrium conditions, the different phase diagrams used to illustrate VLE, and on the vaporised mass diffusion fraction, a parameter that quantifies the vapourisation conditions of a mixture during VLE, and which will be important for the forthcoming calculations of void fraction. The broad range of experimental operating pressures and temperatures, and the different compositions of the fluids during VLE, lead to important variations in the physical and transport properties of these fluids. The values of the most relevant of these properties, as well as the identification of the pseudocritical point of supercritical CO₂ are included in Section 7.2. Section 7.3 provides descriptions of the most common two-phase flows in microchannels, as well as fundamental definitions and relationships related to the void fraction of two-phase flows. Finally, a brief introduction on capillary pumping and wetting processes is included Section 7.4.

7.1 Phase behaviour of Type I binary mixtures

Both sets of fluids, CO₂-EtOH and CO₂-MeOH, belong to the so called Type I binary mixtures. These binary mixtures are characterised by the complete miscibility of both fluids when they are in liquid state, and by the simplest fluid phase behaviour of the mixture. When a binary mixture experiences the thermodynamic phase equilibrium, also known as Vapour-Liquid Equilibrium (VLE), two separated immiscible phases, liquid and vapour, coexist in equilibrium. The fluid compositions in both phases in equilibrium, x_{eq} and y_{eq} , are determined by the temperature and pressure conditions. If this equilibrium of immiscible phases happens in a fluidic system, two-phase flows are expected.

In Type I binary mixtures, VLE always occurs at temperatures enclosed between those of the saturation lines of both pure fluids, i.e. with one fluid in liquid state and the other in gas or supercritical state. The VLE region is a volume in a three-dimensional P-T-xy phase diagram. Outside this VLE region only single-phase can exist, either in liquid-liquid, vapour-vapour or supercritical-liquid form.

Together with the saturation lines of both pure fluids, the VLE region is enclosed by the bubble point surface and by the dew point surface. Basically, when a mixture, initially in single-phase liquid conditions (a.k.a. subcooled liquid), experiences a temperature increase or pressure decrease, it will eventually reach a point where a first vapour bubble appears. This is a bubble point of the mixture, and here the liquid is saturated. After the bubble point, the mixture enters the VLE region, with the two separated immiscible phases in equilibrium. As the change in temperature or pressure continues, the mixture will reach a point where the last liquid droplet disappears and the mixture turns to single-phase vapour. This is a dew point of the mixture, and here the vapour is saturated. After the dew point, the mixture is in superheated vapour conditions. The bubble point surface is formed by all the bubble points of the mixture, whereas the dew point surface is formed by all the dew points of the mixture.

The VLE of mixtures is commonly illustrated by two-dimensional T-xy, P-xy and P-T diagrams, rather than by the more complex P-T-xy phase diagram. In two-dimensional phase diagrams, the bubble point and dew point surfaces turn to bubble point lines and dew point lines. In T-xy and P-xy phase diagrams, besides, these lines indicate the composition of the liquid and vapour phases inside VLE. Given a point with known pressure and temperature conditions, an horizontal line connects that point with the bubble point line and with the dew point line. The composition in these points correspond to the saturated liquid and saturated vapour phases in equilibrium, x_{eq} and y_{eq} , respectively. The horizontal line connecting the points is tie line.

The boundaries of the VLE region are also fixed by the critical locus of the mixture. The critical locus is the line formed by all the possible critical points of the mixture, and it connects the critical points of both pure fluids. A critical point of the mixture is the highest pressure at which VLE can exist at a specified temperature, depending on the

composition of the mixture. In a P-T diagram, VLE is only feasible below the critical locus.

Much more detailed and concise description of the phase behaviour of binary mixtures can be found in [Chester \(2004\)](#) and [Smith et al \(2000\)](#).

7.1.1 Vaporised mass diffusion fraction

An important parameter in VLE is the vaporised mass diffusion fraction, G_d . In binary mixtures, G_d is the analogous to the vapour quality of single boiling fluids χ (see Sect. 7.3.2.1), i.e. the fraction of the mixture, in mass terms, that is already vaporised at the specified conditions ([Collier and Thome, 1996](#)). In a mixture of CO₂-alcohol, G_d is defined as,

$$G_d = \frac{m_v}{m_v + m_l} = \frac{v_{CO_2} - v_{eq,CO_2}}{\omega_{eq,CO_2} - v_{eq,CO_2}} \quad (7.1)$$

where v_{CO_2} is the mass fraction of CO₂ in the mixture in single phase (outside VLE), and ω_{eq,CO_2} and v_{eq,CO_2} are the mass fractions of CO₂ in the saturated liquid and vapour in VLE, respectively.

7.2 Properties of fluids

The dependency of relevant fluid properties on temperature, at different pressures, is included here. These properties are, density (Sect. 7.2.2), viscosity (Sect. 7.2.3), and interface tension (Sect. 7.2.4) of pure CO₂, EtOH and MeOH, and of the saturated liquids in VLE conditions for mixtures of CO₂-EtOH and CO₂-MeOH. All the properties have been obtained at 6.89 MPa, 7.87 MPa and 9.81 MPa. Besides, the pseudocritical point of supercritical fluids is introduced in Section 7.2.1.

7.2.1 Pseudocritical point of a supercritical fluid

The pseudocritical point of a supercritical fluid is the temperature, at a specified pressure, where the specific heat of the fluid reaches a peak, and the variation of its physical and transport properties with temperature is maximum. These temperature and pressure conditions are known as pseudocritical temperature, T_{pc} , and pseudocritical pressure, P_{pc} . This dramatic behaviour of the properties of the fluid is maximum in the vicinity of the critical point, and it decreases as pressure increases far above the critical point of the fluid ([Cheng et al, 2008](#); [Liao and Zhao, 2002](#)).

The T_{pc} of supercritical CO₂, given a value of P_{pc} , can be estimated with the next equation based on the algebraic equation by [Liao and Zhao \(2002\)](#),

$$T_{pc} = 150.55 + 61.24 \cdot P_{pc} - 16.57 \cdot P_{pc}^2 + 5.6067 \cdot P_{pc}^{2.5} - 0.5608 \cdot P_{pc}^3 \quad (7.2)$$

The resulting line of the pseudocritical point of CO₂ is shown in Figure 7.1.

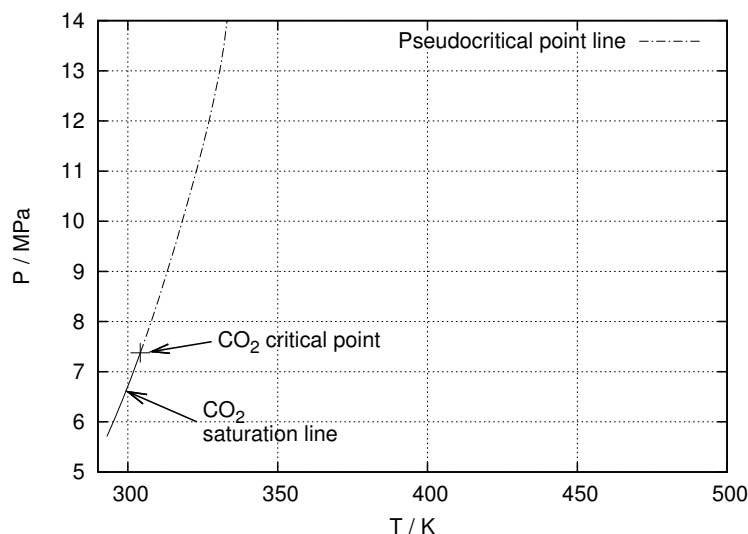


Figure 7.1: Line of pseudocritical point of CO_2 . The saturation line and the critical point of CO_2 are included for completeness.

7.2.2 Density

The densities for CO_2 , EtOH and MeOH, calculated with the software package REFPROP v8.0 (Lemmon et al, 2007), are shown in Figures 7.2 and 7.3. The density values of supercritical CO_2 at T_{pc} (Eq. (7.2)), are also indicated in Figure 7.2.

The density of the saturated liquid phase in VLE conditions for mixtures of CO_2 -EtOH and CO_2 -MeOH, calculated with Eq. (7.3) from Bird et al (2001), is shown in Figure 7.4.

$$\rho_{l,eq} = 1 / \sum_{\alpha} \frac{v_{eq,\alpha}}{\rho_{\alpha}} \quad (7.3)$$

7.2.3 Dynamic viscosity

The dynamic viscosities for CO_2 , EtOH and MeOH, calculated with the software package REFPROP v8.0 (Lemmon et al, 2007), are shown in Figures 7.5 and 7.6. The viscosity values of supercritical CO_2 at T_{pc} (Eq. (7.2)), are also indicated in Figure 7.5.

The viscosity of the saturated liquid phase in VLE conditions, $\mu_{l,eq}$, for mixtures of CO_2 -EtOH and CO_2 -MeOH, calculated with the method proposed in Bird et al (2001) for rough estimation of viscosities of mixtures, is shown in Figure 7.7.

7.2.4 Interface tension

The interface tensions for pure CO_2 , EtOH and MeOH in saturation conditions, calculated with the software package REFPROP v8.0 (Lemmon et al, 2007), are shown in

7.2. Properties of fluids

77

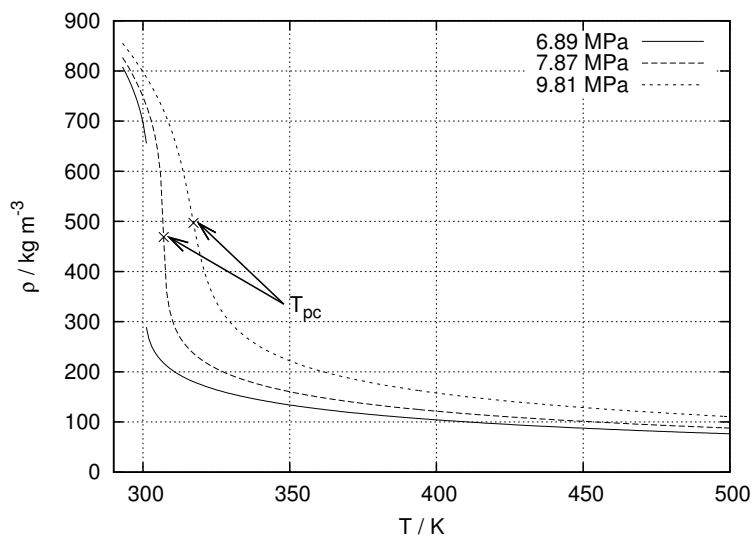


Figure 7.2: Dependence of density, ρ , on temperature, T , for CO_2 at 6.89 MPa, 7.87 MPa and 9.81 MPa. T_{pc} and the corresponding density values are indicated.

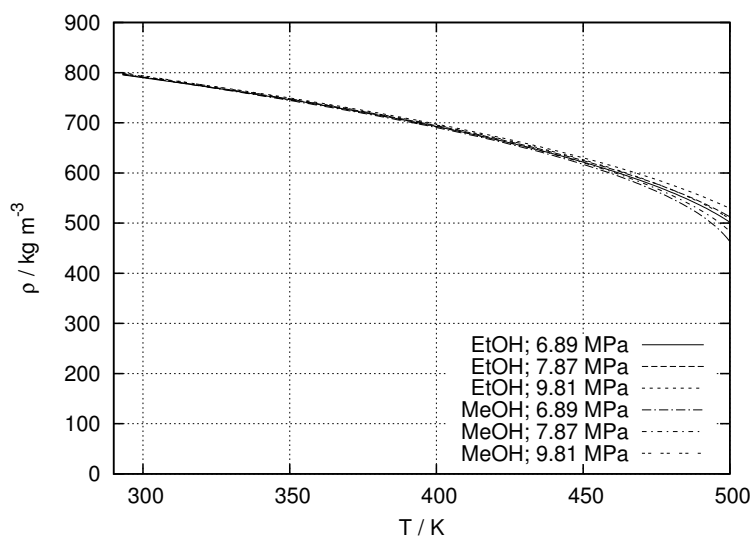


Figure 7.3: Dependence of density, ρ , on temperature, T , for EtOH and MeOH at 6.89 MPa, 7.87 MPa and 9.81 MPa.

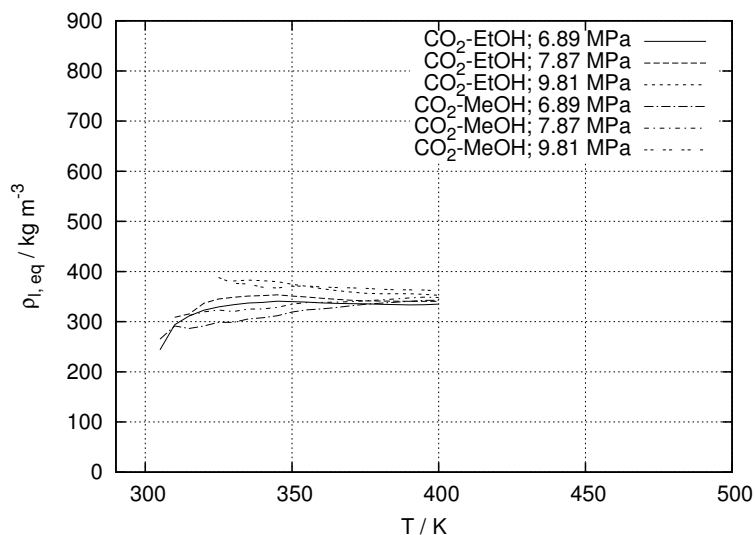


Figure 7.4: Dependence of density of saturated liquid in VLE conditions, $\rho_{l,eq}$, on temperature, T , for mixtures of CO₂-EtOH and CO₂-MeOH at 6.89 MPa, 7.87 MPa and 9.81 MPa.

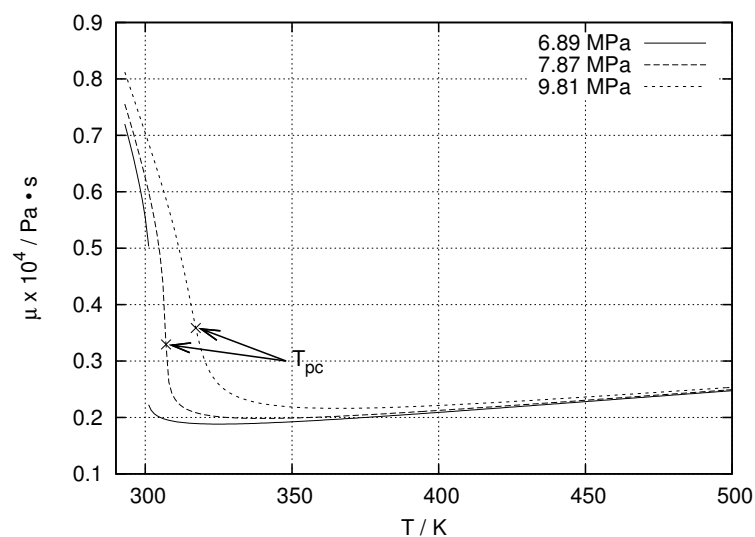


Figure 7.5: Dependence of viscosity, μ , on temperature, T , for CO₂ at 6.89 MPa, 7.87 MPa and 9.81 MPa. T_{pc} and the corresponding viscosity values are indicated.

7.2. Properties of fluids

79

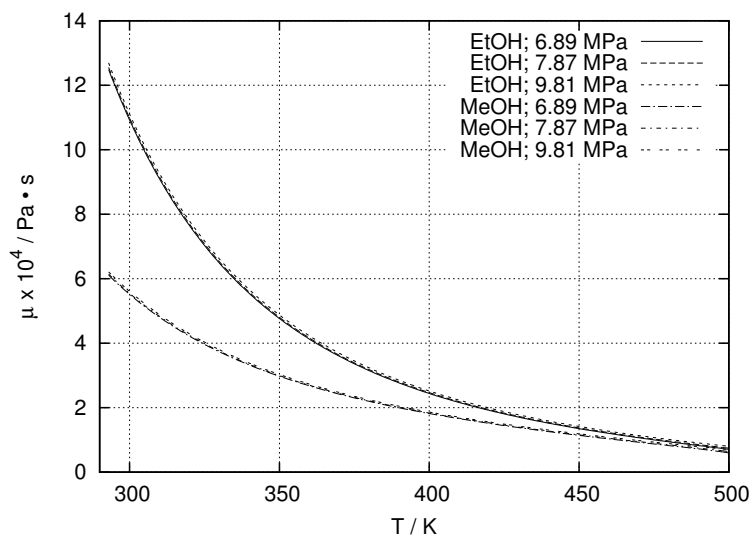


Figure 7.6: Dependence of viscosity, μ , on temperature, T , for EtOH and MeOH at 6.89 MPa, 7.87 MPa and 9.81 MPa.

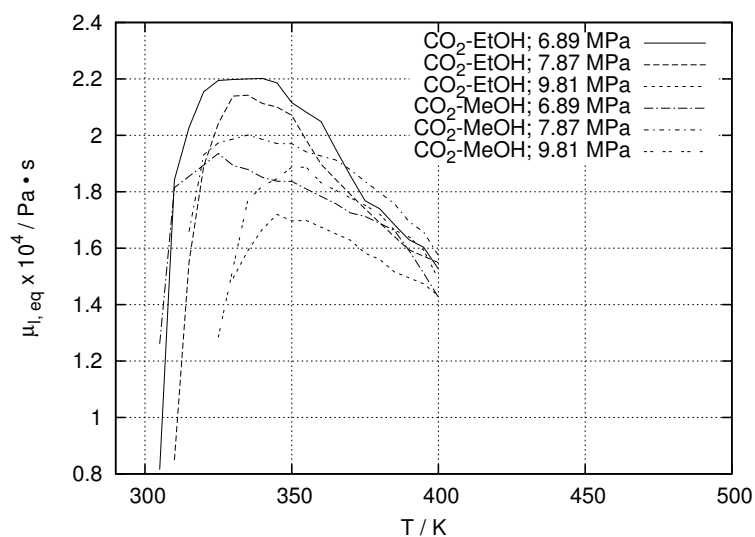


Figure 7.7: Dependence of viscosity of saturated liquid in VLE conditions, $\mu_{l,eq}$, on temperature, T , for mixtures of CO_2 -EtOH and CO_2 -MeOH at 6.89 MPa, 7.87 MPa and 9.81 MPa.

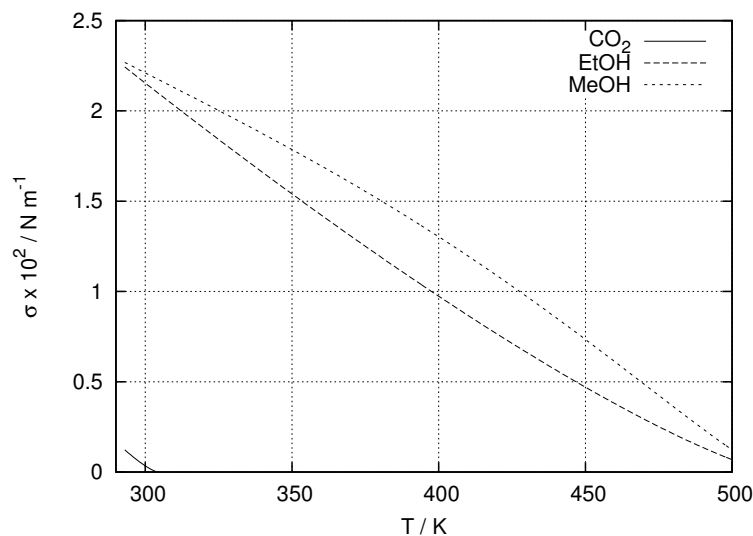


Figure 7.8: Dependence of interface tension, σ , on temperature, T , for pure CO_2 , EtOH and MeOH .

Figure 7.8.

The interface tension for the saturated liquid of CO_2 - EtOH , obtained from the data of Sun and Shekunov (2003), is shown in Figure 7.9. This figure includes the interface tension in dynamic conditions, σ_{dyn} , i.e. the saturated liquid in an atmosphere of pure CO_2 , and in equilibrium conditions, σ_{eq} , i.e. both the liquid and the vapour phases saturated at VLE conditions.

Currently, no data for the interface tension for mixtures of CO_2 - MeOH has been found.

7.3 Two-phase flows

This section describes the most remarkable theoretical concepts of two-phase flows in microchannels. A summary and a brief description of the regimes already identified in the literature are presented first (Sect. 7.3.1). Then, the void fraction and its related parameters, as well as their relationships, are presented in Sect. 7.3.2.

7.3.1 Two-phase flow regimes

As accurately stated by Shao et al (2009), the two-phase flow regimes in microchannels have been revealed to be morphologically similar to those observed in conventional channels and thus the same terminology can be adopted. However, a major problem in studying these two-phase flows is the lack of uniformity in their terminology, mostly due to the difficulty in categorising and analysing the different flows, and to different

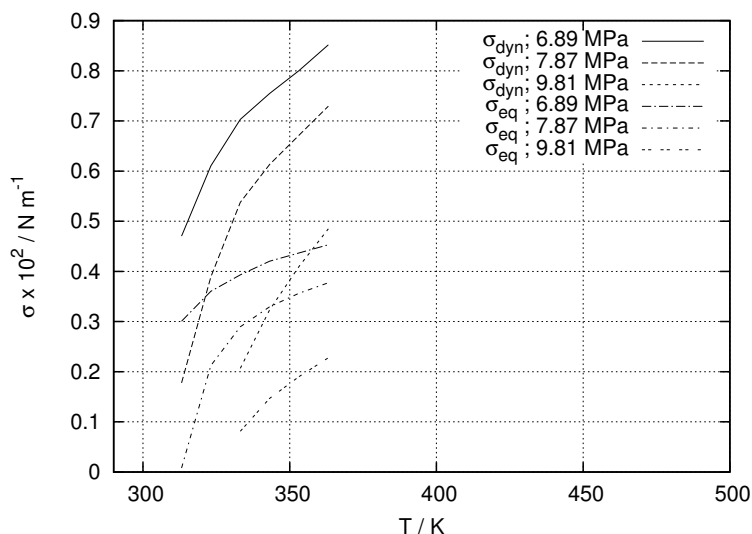


Figure 7.9: Dependence of interface tension of saturated liquid in dynamic conditions, σ_{dyn} , and in equilibrium conditions, σ_{eq} , on temperature, T , for a mixture of CO_2 -EtOH at 6.89 MPa, 7.87 MPa and 9.81 MPa. Data from *Sun and Shekunov (2003)*.

subjective criteria of the researchers.

With this issue in mind, an approximated list of the main two-phase flow regimes obtained in microchannels is presented here. The descriptions of most of these regimes have been obtained from *Shao et al (2009)*; *Revellin et al (2006)*; *Serizawa et al (2002)*.

Bubbly flow This flow is characterised by the presence of dispersed vapour bubbles inside the continuous liquid phase. The bubbles are considerably smaller than the channel diameter and can have various shapes. This flow is typical of the lowest vapour phase flow rates and of the lowest vaporised mixtures.

Taylor flow Also known as segmented, slug, plug, elongated bubble or intermittent flow, Taylor flow is characterised by a continuous succession of vapour bubbles and liquid plugs. The bubbles tend to be elongated and with approximately the diameter of the channel. Sometimes, there is a liquid layer between the bubbles and the walls of the channel, especially depending on the wettability properties of channel. This flow regime is characteristic of higher vapour velocities than bubbly flow. The length of the bubbles can vary considerably, and some authors (e.g. *Kew and Cornwell, 1997*; *Yang and Shieh, 2001*; *Yue et al, 2008*) divided the flows with such different bubble lengths into two flow sub-types, i.e. plug / Taylor flow with shorter bubbles, and slug / unstable slug / annular slug flow with longer bubbles. In some cases, a “train” of several bubbles have been observed flowing together, separated only by a thin liquid interface. This has been called bubble-train slug flow (*Chen et al, 2002*).

Annular flow Annular flow is formed by a continuous vapour core surrounded by a liquid film attached to the walls. This flow is obtained at the highest vapour phase flow rates and the mixtures with higher vaporisations. Several variants of this flow have been described in the literature, and they are listed afterwards in the *Other flows* category.

Taylor-annular flow Also known as slug-annular (Triplett et al, 1999), liquid ring or skewed flow (Serizawa et al, 2002), Taylor-annular flow is similar to annular flow in the sense that a gas core is surrounded by a liquid film. However, here the liquid film shows a low frequency of large-amplitude solitary waves which do not block the channel.

Churn flow Also known as semi-annular flow, churn flow is similar to Taylor flow. Nevertheless, here the liquid plugs are replaced by churning liquid zones, due to the disruption of the bubbles and the entrainment of the vapour into the liquid, or to the disturbance of the liquid film attached to the wall.

Dispersed flow Also known as mist flow, is typical of the highest liquid and vapour velocities. In dispersed flow, the liquid is entrained in the form of tiny dispersed droplets into the gas core. Sometimes, there is a remaining thin liquid layer flowing along the walls of the channel.

Other flows Besides these flows described, the list of identified two-phase microfluidic flows is large. Some of them require particular conditions and are less commonly obtained, some others are subjected to a more subjective criteria. Rivulet, liquid droplets, frothy(wispy) and dry flows such as liquid lump, can be considered special variations of annular flow. Other transition flows between regimes have also been identified, such as bubbly/slug or slug/semi-annular. Due to the suppression of buoyancy effect by surface tension, stratified flows including smooth and wavy have been reported to be non-existent in microchannels. Wavy flow has been observed in few occasions, though (Lee and Lee, 2008).

7.3.2 Void fraction

The comparison between the experimental void fraction, ε_{exp} , and the homogeneous void fraction, ε_{hom} , is one of the main parameters when characterizing two-phase flows in microchannels. The experimental void fraction of a two-phase flow, ε_{exp} , represents the fraction of volume within the channel occupied by the vapour phase and, when compared to the homogeneous void fraction, ε_{hom} , it gives information on the slip between the average velocities of the vapour and the liquid phases. ε_{hom} is the ratio of vapour volumetric flow rate to total volumetric flow rate, and it can be understood as the resulting void fraction if both phases would flow with the same actual velocities, i.e no slip between the velocities of both phases. Then, ε_{exp} would be equal to ε_{hom} . However,

this is not the case for most of the two-phase flows, where the vapour phase flows with higher velocity than the liquid phase. This results in lower ε_{exp} than ε_{hom} .

Most of the definitions and relationships presented in this section have been extracted from Revellin (2005), and there can be found extended information about void fraction in two-phase flows.

7.3.2.1 Definitions

The definition of the basic parameters related with void fraction are presented here.

Volumetric flow rate The volumetric rate of a flow inside a channel, \dot{V} , is calculated as,

$$\dot{V} = A \cdot U \quad (7.4)$$

Mass flow rate The mass rate of a flow inside a channel, \dot{m} , is calculated as,

$$\dot{m} = \dot{V} \cdot \rho = A \cdot U \cdot \rho \quad (7.5)$$

Superficial velocity When there is more than one fluid phase flowing along the channel, the superficial velocity is the average velocity of the fluid phase in case it would occupy the whole area of the channel. It is commonly known simply as velocity. The superficial velocities of the liquid and the vapour phases, U_l and U_v , are calculated as,

$$U_l = \frac{\dot{V}_l}{A} \quad (7.6)$$

$$U_v = \frac{\dot{V}_v}{A} \quad (7.7)$$

Actual velocity When there is more than one fluid phase flowing along the channel, the actual velocity is the real average velocity at which the fluid phase flows in the fraction of the area of the channel occupied by this phase. The actual velocities of the liquid and the vapour phases, $U_{a,l}$ and $U_{a,v}$, are calculated as,

$$U_{a,l} = \frac{\dot{V}_l}{A_l} \quad (7.8)$$

$$U_{a,v} = \frac{\dot{V}_v}{A_v} \quad (7.9)$$

where A_l and A_v are the areas occupied by each phase inside the channel.

Vapour quality The vapour quality, a.k.a mass quality, χ , is the ratio of vapour mass flow rate to total mass flow rate, and is calculated as,

$$\chi = \frac{\dot{m}_v}{\dot{m}_v + \dot{m}_l} = \frac{\dot{m}_v}{\dot{m}} \quad (7.10)$$

In single boiling fluids, χ , indicates the fraction of the mixture that is already vaporised at the specified conditions.

Homogeneous void fraction The homogeneous void fraction, a.k.a homogeneous volumetric quality, ε_{hom} , is the ratio of vapour volumetric flow rate to total volumetric flow rate, and is calculated as,

$$\varepsilon_{hom} = \frac{\dot{V}_v}{\dot{V}_v + \dot{V}_l} = \frac{\dot{V}_v}{\dot{V}} \quad (7.11)$$

Experimental void fraction The experimental void fraction, ε_{exp} , represents the fraction of volume within the channel occupied by the vapour phase. It can be calculated by means of the cross-sectional areas as,

$$\varepsilon_{exp} = \frac{A_v}{A_v + A_l} = \frac{A_v}{A} \quad (7.12)$$

7.3.2.2 Relationships

Based on the already defined parameters, the next important relationships arise.

Homogeneous void fraction ε_{hom} can be calculated by means of the superficial velocities (Eq. (7.13)), by means of the vapour quality and the densities of both fluid phases (Eq. (7.14)), or by means of the experimental void fraction and the actual velocities of both fluid phases (Eq. (7.15)).

$$\varepsilon_{hom} = \frac{U_v}{U_v + U_l} \quad (7.13)$$

$$= \frac{1}{1 + (1/\chi - 1)\rho_v/\rho_l} \quad (7.14)$$

$$= \frac{1}{1 + (1/\varepsilon_{exp} - 1)U_{a,l}/U_{a,v}} \quad (7.15)$$

Also, as described in Section 7.1, the vaporised mass diffusion fraction, G_d , is analogous to χ . Therefore, in VLE conditions, ε_{hom} can be calculated by means of G_d , $\rho_{v,eq}$ and $\rho_{l,eq}$ when they are included in Eq. (7.14) replacing χ , ρ_v and ρ_l ,

$$\varepsilon_{hom} = \frac{1}{1 + (1/G_d - 1)\rho_{v,eq}/\rho_{l,eq}} \quad (7.16)$$

7.4. Capillary pumping and wetting processes

85

Besides, when there is no slip between the actual velocities of both phases, $U_{a,l} = U_{a,v}$, the equality between ε_{hom} and ε_{exp} is demonstrated in the next equation,

$$\varepsilon_{hom} = \frac{\dot{V}_v}{\dot{V}_v + \dot{V}_l} = \frac{U_{a,v} \cdot A_v}{U_{a,v} \cdot A_v + U_{a,l} \cdot A_l} = \frac{A_v}{A_v + A_l} = \varepsilon_{exp} \quad (7.17)$$

Vapour quality χ can be calculated by means of the superficial velocities and the densities of both fluid phases (Eq. (7.18)), by means of the homogeneous void fraction and the densities of both fluid phases (Eq. (7.19)), or by means of the experimental void fraction, and the actual velocities and densities of both fluid phases (Eq. (7.20)).

$$\chi = \frac{U_v}{U_v + U_l \cdot (\rho_l / \rho_v)} \quad (7.18)$$

$$= \frac{1}{1 + (1/\varepsilon_{hom} - 1)\rho_l / \rho_v} \quad (7.19)$$

$$= \frac{1}{1 + (1/\varepsilon_{exp} - 1)(U_{a,l}/U_{a,v})(\rho_l / \rho_v)} \quad (7.20)$$

Velocity slip The slip between the velocities of both fluid phases, expressed in form of the ratio between actual velocities, $U_{a,l}/U_{a,v}$, can be calculated by means of the homogeneous and the experimental void fractions (Eq. (7.21)), or by means of the vapour quality, the experimental void fraction and the densities of both fluid phases (Eq. (7.22)).

$$\frac{U_{a,l}}{U_{a,v}} = \frac{(1/\varepsilon_{hom}) - 1}{(1/\varepsilon_{exp}) - 1} \quad (7.21)$$

$$= \frac{(1/\chi) - 1}{(1/\varepsilon_{exp}) - 1} \cdot \frac{\rho_v}{\rho_l} \quad (7.22)$$

7.4 Capillary pumping and wetting processes

As previously mentioned, the important role of the capillary forces in confined microfluidics has been already identified. Their prevalence over other forces can be noted in the typically low values of Capillary and Weber numbers (Eqs. (7.23)–(7.24)), which represent the ratio of viscous forces to interface tension forces and of inertia forces to interface tension forces, respectively.

$$Ca = \frac{\mu U}{\sigma} \quad (7.23)$$

$$We = \frac{\rho U^2 d_h}{\sigma} \quad (7.24)$$

According to their predominance, these capillary forces have been extensively manipulated for non-mechanical transport of fluids, either by modifying the fluid-fluid interface tension, i.e. generating Marangoni stresses, of isolated droplets or bubbles inside another fluid (Lajeunesse and Homsy, 2003), or by modifying the solid-liquid interface tension,

i.e. the wettability properties, of liquid plugs (Sammarco and Burns, 1999; Nguyen and Huang, 2005). These interface tensions are dependent of a broad number of factors such as temperature, concentration of fluids, electrostatic potential, light intensity and others. Thus, generating a gradient of one or more of these conditions along a surface or between the two extremes of a liquid plug will lead to a gradient of any of the interface tensions and, consequently, it will induce the displacement of the liquid. Among these, the most common techniques are the thermal modification of fluid-fluid interface tension, known as thermocapillary pumping, and the electrostatic modification of solid-liquid interface tension, also known as electrowetting. Detailed descriptions of this topic can be found in Squires and Quake (2005) and in Shui et al (2007a).

The Capillary and Weber numbers (Eqs. (7.23)–(7.24)) can be used for determining the capillary motion of an isolated droplet or bubble inside another fluid (Squires and Quake, 2005). To do so, one has to find the conditions at which the capillary forces balance the viscous forces, $Ca \approx 1$, and the inertial forces, $We \approx 1$, when a gradient in the interface tension is induced. At these conditions, and assuming similar length-scales for the different forces, the equations (7.23) and (7.24) can be reformulated to obtain the following relations,

$$(\Delta v_{CO_2})_{Ca} \approx -\frac{\mu U}{\partial \sigma / \partial v_{CO_2}} \quad (7.25)$$

$$(\Delta v_{CO_2})_{We} \approx -\frac{\rho U^2 d_h}{\partial \sigma / \partial v_{CO_2}} \quad (7.26)$$

These relations can be understood as the mass fraction difference along the fluid-fluid interface required to generate a Marangoni stress enough as to overcome the viscous forces (Eq. (7.25)) and inertial forces (Eq. (7.26)) of a droplet or a bubble that tends to flow with velocity U . Analogous relations can be also developed for other factors, such $(\Delta T)_{Ca}$ and $(\Delta T)_{We}$,

$$(\Delta T)_{Ca} \approx -\frac{\mu U}{\partial \sigma / \partial T} \quad (7.27)$$

$$(\Delta T)_{We} \approx -\frac{\rho U^2 d_h}{\partial \sigma / \partial T} \quad (7.28)$$

Wetting is a highly complex process involving the interaction of two different fluids (usually a liquid and a gas) and a solid, that depends on many parameters including the properties of fluids such as viscosity and density; the characteristics of the solid such as roughness, heterogeneity and cleanliness; the three interface (one fluid-fluid and two fluid-solid) tensions; and others. In the simplest case of the process, these three interface tensions determine the contact angle among the fluids and the solid by the so-called Young's equation. The manuscript of Kumar and Prabhu (2007) offers a complete information on this topic.

The atmospheres of CO_2 at high pressure have been proven to increase the hydrophobicity of glass substrates (Dickson et al, 2006). The high pressure atmosphere reduces

7.4. Capillary pumping and wetting processes

87

the solid-gas and the liquid-gas interface tensions, and increases the solid-liquid interface tension. Besides, opposite to the behaviour predicted by Young's equation, the decreased liquid-gas interface tension leads to an increment in the solid-liquid contact angle, i.e. a higher hydrophobic nature. It remains to be identified how this behaviour might affect the present studied system, at high pressures, with supercritical CO₂ and with variable compositions in the liquid.

UNIVERSITAT ROVIRA I VIRGILI

NUMERICAL AND EXPERIMENTAL ANALYSES OF SINGLE AND TWO-PHASE MICROFLUIDIC FLOWS WITH IMPLICATIONS IN MICROREACTORS

Roland Blanch Ojea

DL:T. 149-2012

Experimental¹

Contents

8.1	Microfluidic chip layout	90
8.2	Experimental setup	90
8.3	Operating conditions	95
8.3.1	Pressure	95
8.3.2	Temperature	95
8.3.3	Flow rate	96
8.3.4	Feed ratio	97
8.3.5	Flow velocity	97
8.4	Issues on experimental procedure	98
8.4.1	Proper cutting of the capillary tubing	98
8.4.2	Use of Rhodamine B for the visualization of flow regimes	99
8.4.3	Operation at high temperatures	103
8.5	Image recording and processing	103

The description of the experiments conducted to study the two-phase flows in the non-adiabatic T-junction is depicted in this chapter. First, the experimental facility is presented, with focus on the design of the glass microfluidic chip that contains the T-junction and other fluidic elements (Sect. 8.1), and on the description of the auxiliary experimental setup (Sect. 8.2). The encompassed range of values of the relevant operating conditions appear in Section 8.3, together with their control, monitoring and/or estimation techniques used. Section 8.4 includes some of the issues encountered during the experimental procedure, and the way how these were solved. Finally, the procedure of recording the images from the microscope and their subsequent processing for extracting the relevant data is presented in Section 8.5.

¹The present experiments were carried out at the *Mesoscale Chemical Systems* research group from the *University of Twente*, in Enschede, The Netherlands.

8.1 Microfluidic chip layout

A microfluidic chip made of Borofloat glass (wide (W_{ch}) x long (L_{ch}) x high (H_{ch}) = 15 mm x 20 mm x 2 mm) was used in this work. Figure 8.1 shows pictures and layouts of two versions of the chip. The chip consists of: two independent in-plane inlets for CO₂ and alcohol feeds; the T-junction where both fluids join; a meandering channel after the T-junction; a fluidic resistor; an expansion channel where the fluid mixture gradually expands to atmospheric conditions before finally reaching the outlet. The cross-sectional geometry of the main channels is semicircular ($W_{mc} \times H_{mc} = 70 \mu\text{m} \times 30 \mu\text{m}$; $d_{h,mc} = 39.3 \mu\text{m}$), as shown in Figure 8.2. The microfluidic resistor ($W_{fr} \times H_{fr} = 20 \mu\text{m} \times 5 \mu\text{m}$) maintains constant the upwards pressure in the meandering channel of the chip. Fused silica capillaries with standard polyimide coating (Polymicro Technologies TSP040105; $d_{in} = 41 \mu\text{m}$; $d_{out} = 108 \mu\text{m}$) were glued (Araldite Rapid) to the inlets and to the outlet of the chip for withstanding high operating pressures. Details of the glued capillaries can be observed in Fig. 8.1a and Fig. 8.1b. Further details of the design, fabrication and testing of the microfluidic chip can be found elsewhere (Tiggelaar et al, 2007; Benito-López, 2007).

As shown in Figures 8.1c and 8.1d, two areas ($W_{hca} \times L_{hca} = 8.2 \text{ mm} \times 7.4 \text{ mm}$) were cooled and heated by placing on top of the glass chip, respectively, a thermoelectric Peltier element (Melcor CP0.8-7-06) glued to a copper block, and an electric resistor on top of a second copper block. Heat sink silicone compound (Dow Corning 340) was used for improving contact between the copper blocks and the chip, and between the electric resistor and the copper block. A Pt100 sensor connected to a temperature controller (CAL3300), measured the temperatures on top of each copper block. A heat sink was used for removing the excess heat generated by the peltier element. Figure 8.3 shows pictures of both cooling and heating mechanisms. The different elements of the mechanisms can be observed.

The cooled area nearby the inlets kept both fluids in liquid state at temperatures around 283 K to 288 K as they entered the chip. The heated area, on the other hand, included the meandering channel and the area visualised with the microscope ($W_{va} \times L_{va} = 0.325 \text{ mm} \times 0.696 \text{ mm}$). In the first version of the chip (Figs. 8.1a and 8.1c) the T-junction was placed in the cooled area. In this way, the liquid fluids were allowed to mix completely before reaching the visualized meandering channel, at the experimental temperature. In the chip with the T-junction in the heated area (Figs. 8.1b and 8.1d), the fluids reach separately the T-junction already at the experimental temperature and state.

8.2 Experimental setup

A sketch of the experimental setup used in this work, similar to the one in Tiggelaar et al (2007), is shown in Figure 8.4. Figure 8.5 also shows a picture of the experimental

8.2. Experimental setup

91

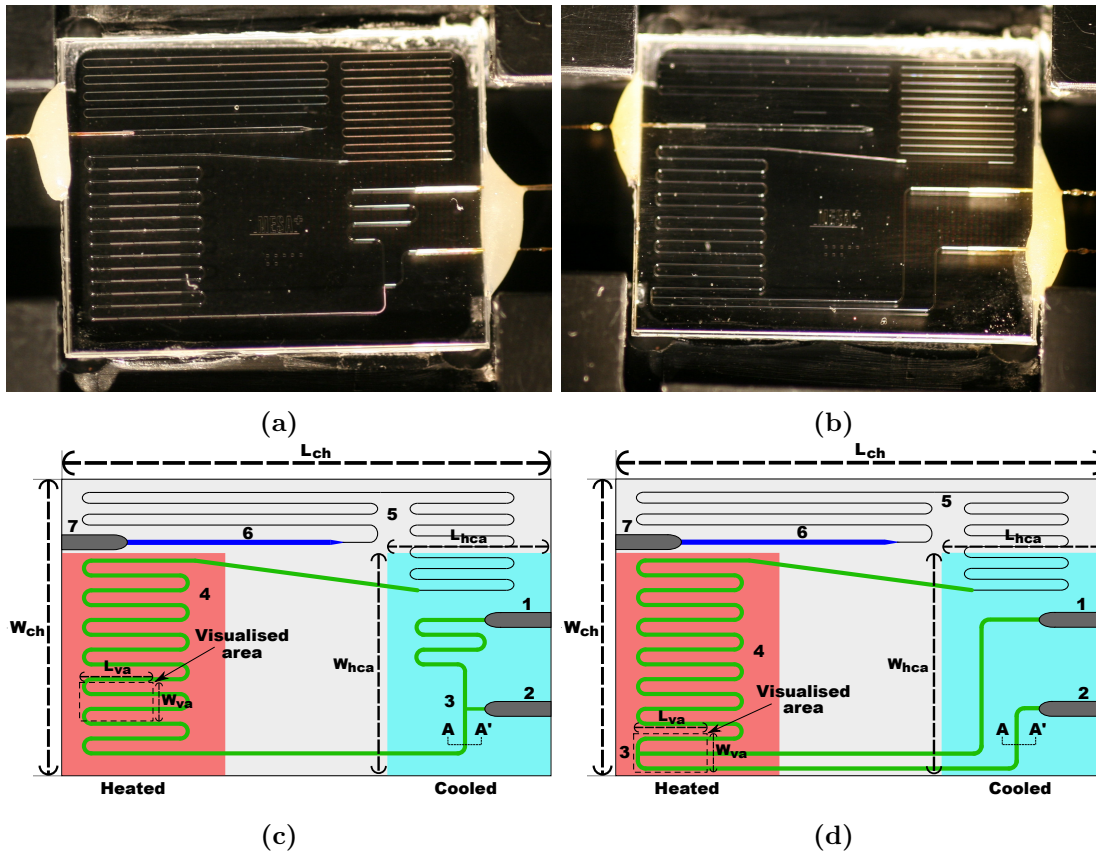


Figure 8.1: Pictures and layouts of the glass microfluidic chip with the T-junction in the (a,c) cooled and in the (b,d) heated areas. Layouts legend: [1] Alcohol inlet; [2] CO₂ inlet; [3] T-junction; [4] Meandering channel; [5] Fluidic resistor; [6] Expansion zone; [7] Outlet; [A-A'] Detail of the cross-section of the microchannel (Fig. 8.2). The areas visualised with the microscope during the experiments, as well as the heated and cooled areas, are indicated. Dimensions: $W_{ch} = 15$ mm; $L_{ch} = 20$ mm; $W_{hca} = 8.2$ mm; $L_{hca} = 7.4$ mm; $W_{va} = 0.325$ mm; $L_{va} = 0.696$ mm.

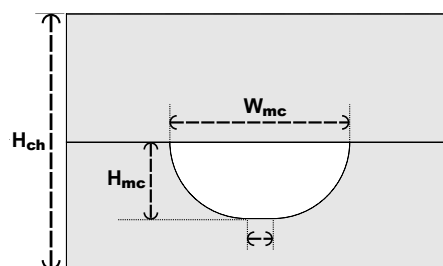


Figure 8.2: Geometry and dimensions of the cross-section of the microchannel and the chip. $H_{ch} = 2$ mm; $H_{mc} = 30$ μ m; $W_{mc} = 70$ μ m.

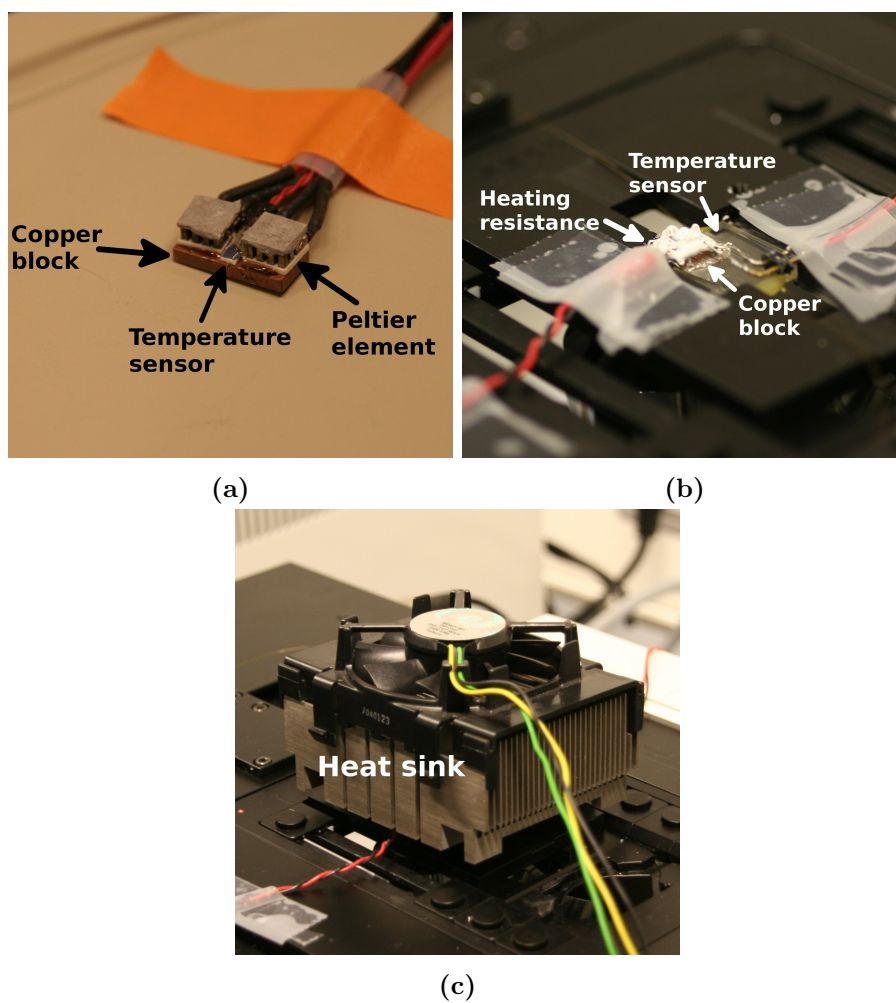


Figure 8.3: Pictures of the different mechanisms for cooling and heating the chip. (a) Cooling mechanism; (b) Heating mechanism; (c) Heat sink.

8.2. Experimental setup

93

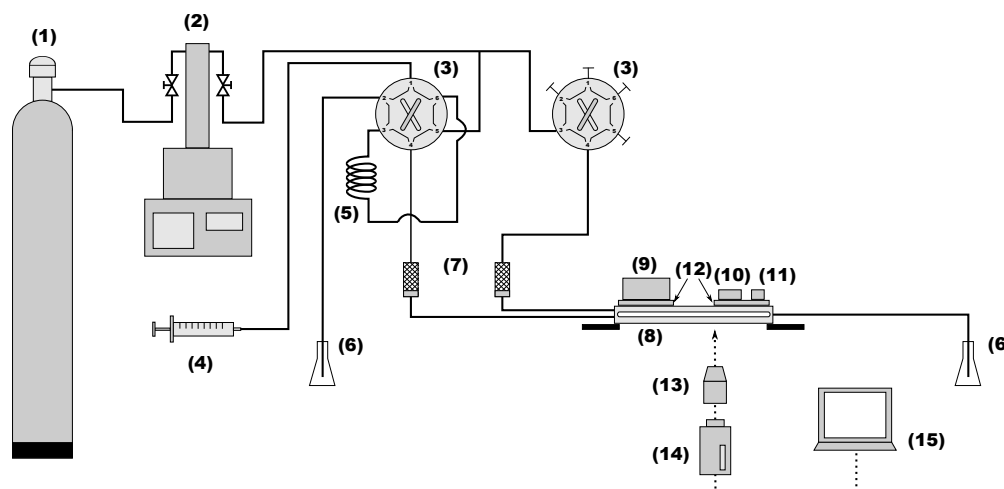


Figure 8.4: Sketch of the experimental setup. Legend: [1] CO₂ cylinder; [2] Syringe pump; [3] Six-port valves; [4] Syringe; [5] Loop with alcohol sample; [6] Waste collectors; [7] Precolumn filters; [8] Microfluidic chip; [9] Peltier element; [10] Temperature sensor; [11] Heating resistance; [12] Copper blocks; [13] Microscope lens; [14] CCD high speed camera; [15] Computer.

setup.

A pulseless syringe pump (ISCO Syringe Pump Model 100DM; ISCO Pump Controller Series D) was used for pumping the liquid CO₂ stored in a pressurised cylinder. The CO₂ was then split into two streams, the first one flowed directly to the chip whereas the second was used to pump the liquid alcohol previously loaded in a loop with a capacity of 400 μl. Two six-port valves (Rheodyne C6W, Valco Instruments Co. Inc.) kept the alcohol inside the loop and distributed the CO₂ flow. Two precolumn filters (Upchurch Scientific A-316; Upchurch Scientific A-102X frit SS Blk 0.5 μm) were used to prevent any particle to clog the channels. The piping system was made of stainless steel (Upchurch Scientific). The microfluidic chip together with a chip holder (Fig. 8.6), were placed on an inverted microscope (LEICA DMI5000M) and illuminated with a mercury bulb (LEICA EL6000) for optical recording. Figure 8.7 shows in detail the connection between the piping system, the precolumn filters and the capillary tubing.

The possible pressure imbalances and fluctuations in the flow line, were minimised using a single pressure source to pump both fluids into the chip. However, doing so the CO₂ used for pumping the alcohol into the chip gradually contaminated the sample. In order to avoid this contaminated alcohol to reach the experimental section and to induce an error in the results, only half of the loaded sample was used in the experiment. Assuming a maximum volumetric flow rate from the pump² of $\dot{V}_o \approx 13 \mu\text{l min}^{-1}$ at 18 MPa, and a volumetric ratio of CO₂-alcohol flowing into the chip of $\%v/v_{o,CO_2} \approx 0.5$, the system could be run for about 60 min before replacing completely the alcohol sample.

²Note that, from now on, the subscript 'o' means that the variable is evaluated at pressure and temperature conditions of the CO₂ syringe pump.

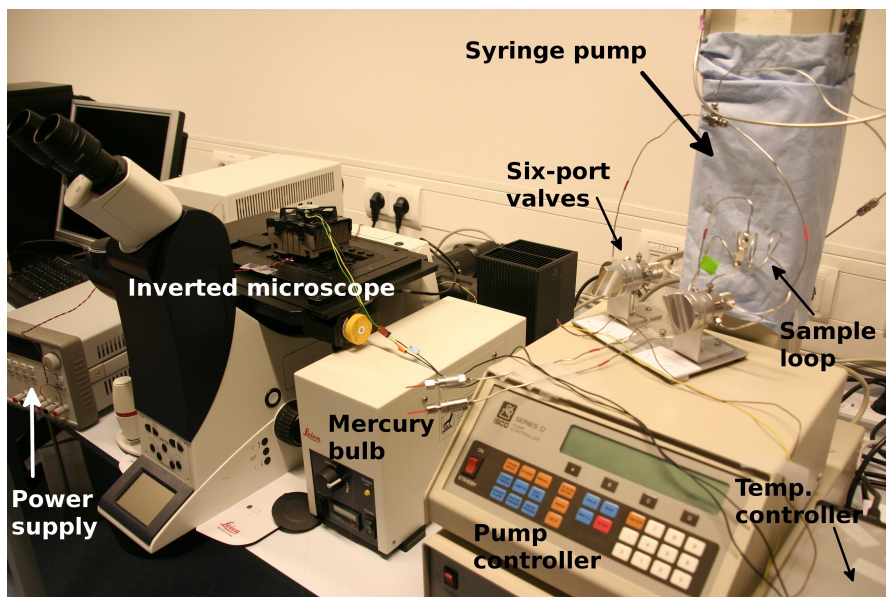


Figure 8.5: *Picture of the experimental setup.*

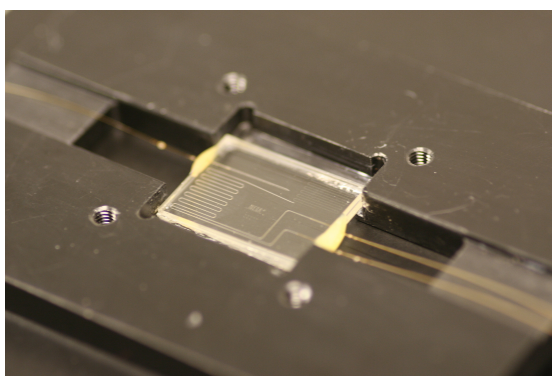


Figure 8.6: *Microfluidic chip placed on the holder.*

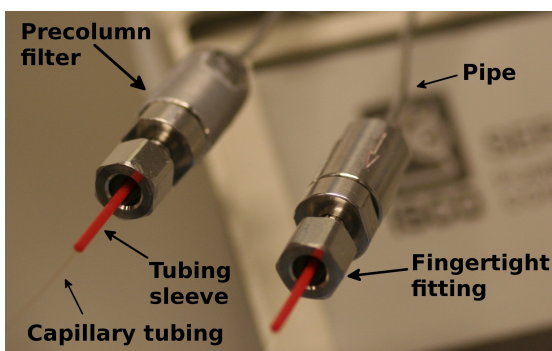


Figure 8.7: *Picture of the piping system, the precolumn filters and the capillary tubing.*

Table 8.1: *Theoretical and experimental data of the critical point of CO₂*

	T/K	P/MPa
Theoretical	304.2	7.37
Experimental	303.70	7.59
	305.23	7.61

CO₂ was purchased from Linde, ethanol from Merck (Merck KGcA proanalysis; > 99.9% purity) and methanol from Sigma-Aldrich/Riedel de Haën (> 99.9% purity).

8.3 Operating conditions

Pressure, temperature, flow rate, feed ratio of the fluids and flow velocity were the most significant operating conditions in the present work.

8.3.1 Pressure

The system pressure ranged from 6 MPa to 18 MPa, and it was set and monitored by means of the syringe pump. Although the fluidic resistor (see Fig. 8.1) minimised the pressure losses within the chip channels, a slight pressure drop of around 3% from the pump to the T-junction was estimated for every experiment in the present work. The estimated pressure drop was obtained comparing present experimental results of the critical point of CO₂ with theoretical data (See Table 8.1).

8.3.2 Temperature

The experimental temperature of the copper block on top of the glass chip was measured with a Pt100 sensor (See Sect. 8.1), whereas the temperature of the bottom of the glass chip was measured with an auxiliary sensor. The ratio of thermal conductivity, κ , of copper ($401 \text{ W m}^{-1} \text{ K}^{-1}$) to that of borofloat glass ($1.2 \text{ W m}^{-1} \text{ K}^{-1}$), is significantly high. Furthermore, the copper block (wide x long x high = $8.2 \text{ mm} \times 7.4 \text{ mm} \times 2.0 \text{ mm}$) heated a surface much larger than the observed area in the microscope ($W_{va} \times L_{va} = 0.325 \text{ mm} \times 0.696 \text{ mm}$). Altogether, this allowed to neglect any temperature gradients within the copper block and in both horizontal directions of the glass chip, and to assume a one dimensional heat conduction across the chip in the vertical direction. In this way, the effective temperature in the channel and in the T-junction was estimated by measuring the linear vertical temperature gradient across the chip, at different temperatures of the copper block, from 294 K to 500 K. The results of the measurement of the temperature drop are shown in Figure 8.8, in the form of the temperature difference

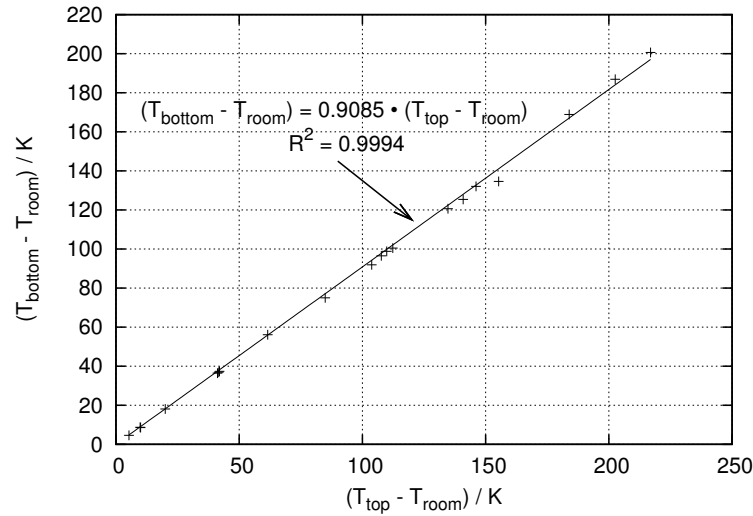


Figure 8.8: Measurement and linear interpolation of the temperature drop across the chip.

between the top of the chip and the room conditions, $T_{top} - T_{room}$, against the temperature difference between the bottom of the chip and the room conditions, $T_{bottom} - T_{room}$. Here, T_{top} was assumed to be the same as the temperature of the copper block. The linear interpolation of these results resulted in the next ratio,

$$\frac{T_{bottom} - T_{room}}{T_{top} - T_{room}} = 0.9085 \quad (8.1)$$

with a coefficient of determination, R^2 , of 0.9994. With the Equation (8.1), and assuming that the channels are located in the mid-height of the chip, the next equation was developed to estimate the effective temperature in the channel,

$$T = T_{top} - 0.5 \cdot (1 - 0.9085) \cdot (T_{top} - T_{room}) \quad (8.2)$$

It must be remarked that, during the experiments, the light from the mercury bulb that illuminated the bottom of the glass chip heated that side of the chip, thus certainly increasing the effective temperature in the channel and in the T-junction. Unfortunately, the effect of the illumination on the effective temperature could not be evaluated and, therefore, it had to be neglected.

8.3.3 Flow rate

The total feed flow rate was monitored with the flow meter included in the syringe pump (but could not be controlled, due to pressure-mode operation of the pump). Nevertheless, a continuous oscillation in the readings during the experiments precluded an accurate monitoring. Therefore, only approximate values could be estimated at different

Table 8.2: *Approximated average flow rates from the syringe pump, \dot{V}_o , at different pressures, P*

P/MPa	$\dot{V}_o/\mu\text{l min}^{-1}$
7	3
8	5
10	7
18	13

pressures, and these are listed in Table 8.2. Possible causes of these oscillations are discussed in Section 9.3.1.

8.3.4 Feed ratio

The feed ratio of fluids could not be monitored or controlled during the experiments. This ratio was estimated by comparing present experimental visualisations of the bubble point of the mixtures at different pressures, with the available data of VLE from literature. The comparison allowed to accurately estimate the mass fractions in the mixtures, which were $v_{o,CO_2} = v_{CO_2} \approx 0.95$ ($\%v/v_{o,CO_2} \approx 0.949$) for CO_2 -EtOH and $v_{o,CO_2} = v_{CO_2} \approx 0.87$ ($\%v/v_{o,CO_2} \approx 0.869$) for CO_2 -MeOH. Unlike previous works, here the feed ratio of fluids was assumed constant throughout the study, whereas the composition of the separated vapour and liquid phases during VLE, as well as the vaporisation of the mixture, varied depending on temperature and pressure conditions. The procedure and results of this comparison are presented in detail in Section 9.1.2.

8.3.5 Flow velocity

The velocity of the flows of CO_2 and alcohol reaching the T-junction could not be monitored or controlled during the experiments and, therefore, there is no available data of these velocities in the present work. Nevertheless, where strictly necessary, the velocity of the stream of CO_2 right before the T-junction at the experimental P and T conditions, U_{CO_2} , was roughly calculated with the next equation obtained by mass and volumetric flows balance between the syringe pump and the T-junction,

$$U_{CO_2} = \frac{\rho_{o,CO_2}}{[1 + \rho_{o,CO_2}/\rho_{o,alc} \cdot (1/v_{o,CO_2} - 1)] \rho_{CO_2}} \frac{\dot{V}_o}{A} \quad (8.3)$$

The estimated average flow rate values from the syringe pump, \dot{V}_o , were obtained from Table 8.2. The formulation of Eq. (8.3) is described in Appendix B. Let's remark that this equation and the \dot{V}_o values used here are both roughly approximated and, thus, the resulting U_{CO_2} are not expected to be accurate.

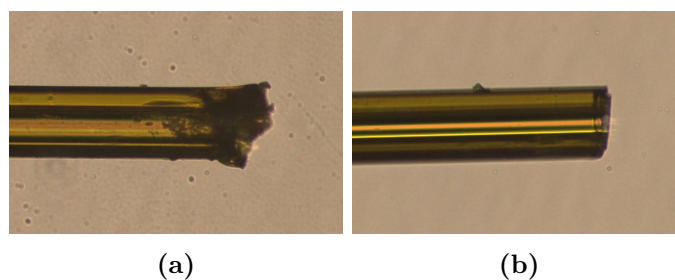


Figure 8.9: Pictures of two different cuts of the capillary tubing. (a) Dirty cut; (b) Clean cut.

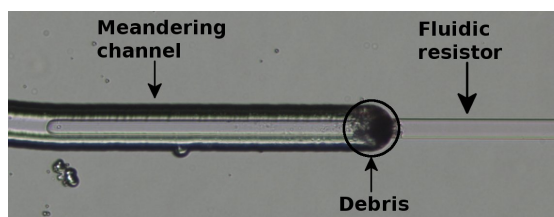


Figure 8.10: Picture of a fluidic resistor clogged by the debris from a capillary tubing with a dirty cut.

8.4 Issues on experimental procedure

Several issues were experienced during the procedure of the experiments. These are described here.

8.4.1 Proper cutting of the capillary tubing

The fused silica capillaries used to connect the precolumn filters and the microfluidic chip were previously cut to a certain length. The diameter of these capillaries, $d_{out} = 108 \mu\text{m}$, was too small and none of the available tools for the precision cutting of capillaries, such as ShortixTM Fused Silica Tubing Cutter, could be used. Hence, the capillaries were cut manually by rolling the edge of a ceramic disc around the capillary. This is a rough method for cutting the capillaries, and special care had to be paid to achieve relatively clean cuts.

Clean cuts in capillaries are crucial because, in a dirty cut, the capillary gets partially smashed and the polyimide coating cracks. The dirty cuts can lead to many problems and complications. The difference between a clean cut and a dirty cut can be clearly observed in the two images in Figure 8.9. In the present experimental setup the higher risk with the dirty cuts was a release of the cracked coating in the form of debris inside the channels of the microfluidic chip. This debris eventually clogged chip when it got stacked in the transition between the meandering channel and the fluidic resistor, as it can be observed in Figure 8.10.

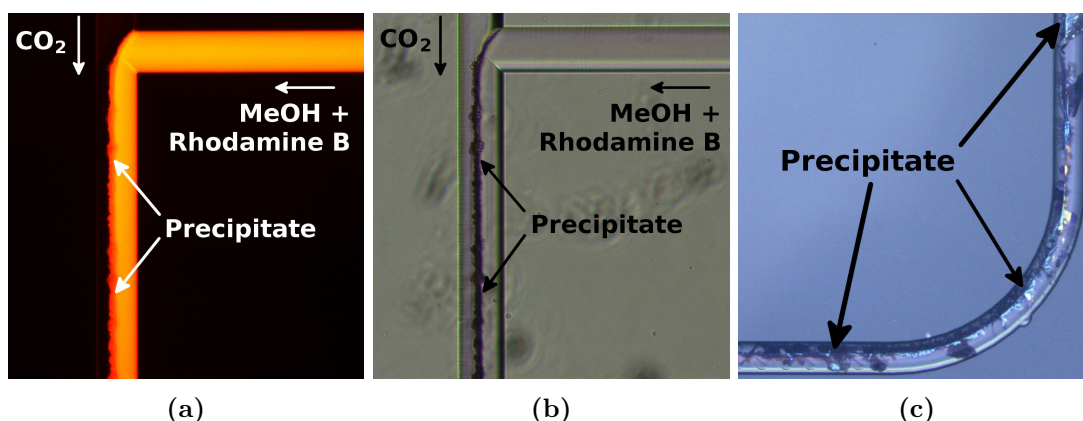


Figure 8.11: Precipitation of Rhodamine B in CO_2 -MeOH-RhB mixtures.

8.4.2 Use of Rhodamine B for the visualization of flow regimes

Initially, the method selected for visualizing the flow regimes was the Fluorescence contrast technique, which has been used previously for CO_2 and aqueous MeOH mixtures in adiabatic microchannels (Weinmueller et al, 2009), and is available in the selected model of inverted microscope (LEICA DMI5000M). With this technique, the fluorescent liquid phase would be visualized in the microscope, in contrast with the non-fluorescent gas phase which would remain non-illuminated in the image. Since both EtOH and MeOH are non-fluorescent, Rhodamine B (RhB), a fluorescent dye, was purchased from Sigma-Aldrich in powder form and it was added to the alcohols to induce their fluorescence. Solutions of alcohol/Rhodamine B were prepared with molar concentrations of Rhodamine B from 10^{-3} M to 10^{-5} M. Below this concentration values, the fluorescence in the liquid could be barely observed in the microscope.

The suitability of the Fluorescence contrast technique was tested in a series of preliminary experiments. However, several important problems arise from these tests. The problems encountered were, precipitation of Rhodamine B, low quality of visualization of the flows, and degradation of Rhodamine B under certain conditions. Besides, the effect of the Rhodamine B on the miscibility of CO_2 and alcohols and on their VLE conditions, was unknown and it was not taken into account. Consequently, the use of Fluorescence contrast technique had to be discarded and substituted with the common and widely used Brightfield contrast technique.

Precipitation of Rhodamine B This process was instantaneous when both fluids in liquid state, the CO_2 and the alcohol/Rhodamine B, met in the T-junction, as it can be observed in the series of images in Figure 8.11. The precipitation began in the interface or the mixing layer of both fluids (Figs. 8.11a and 8.11b), and soon spread throughout all the channel (Fig. 8.11c). This behaviour indicates that the precipitation occurred in the mixing region of the fluids.

Several simple tests were made trying to gain some understanding on the causes of the precipitation. Firstly, CO₂ was substituted by water. No precipitation was observed then, and both fluids mixed completely. Secondly, a small amount of Rhodamine B was placed in the liquid CO₂ line, but when the CO₂ stream reached the visualized area, no fluorescence was observed.

From the behaviour of the process and from the tests carried out, it can be assumed that the precipitation is the result of the low solubility of Rhodamine B in CO₂, or of some unidentified interaction between Rhodamine B and CO₂. Let's remark that the amount of precipitate was higher when EtOH was used. Compared with [Weinmueller et al \(2009\)](#), the possible reason why they did not suffer from this issue when using Rhodamine B with CO₂ and aqueous MeOH, comes from the fact that they worked with CO₂ in gas state at ambient temperatures. Under this conditions, both fluids are already in VLE and their miscibility is minimum. The liquid phase is almost exclusively composed by aqueous MeOH, whereas the gas phase is mostly CO₂.

Low quality of visualization To minimise the precipitation of Rhodamine B, alcohol mixtures with very low content of Rhodamine were used. Thus, the fluorescence of the liquid phase was also low, and it was necessary to increase the exposure time of the camera to reach a sensitivity enough as to be able to capture the fluorescent signal. This high exposure times resulted in a poor definition of the fluid-fluid interfaces, in low quality of the images, and in a very hard identification of the flow regimes. Figure 8.12 shows the difference between the quality of the recorded images with Fluorescence contrast and Brightfield contrast techniques. The pairs of images in Figures 8.12a-8.12c, and in Figures 8.12b-8.12d, respectively, correspond to the same experiment recorded with the two different techniques.

Degradation of Rhodamine B When the experiments of both alcohols with Rhodamine B were conducted above certain pressure and temperature conditions, the flow showed an unexpected and interesting behaviour. During the operation, some droplets with high content in Rhodamine B gradually appeared and began moving with a slower velocity than the typical flow velocity. These droplets also left a trace along the channel. Furthermore, sometimes a transient disappearance of the fluorescence in the heated channel, combined with sudden fluorescent sparkles in some points of the channel, were also observed. The droplets and their trace are clearly shown in Figure 8.13, especially in the images recorded with Fluorescence contrast, and the local transient disappearance of the fluorescence in the channel is shown in Figure 8.14.

The stability conditions for Rhodamine B, and its chemical nature, are beyond the knowledge of the author. Nevertheless, the observed behaviour points at a possible degradation of the Rhodamine B. The threshold pressure and temperature conditions above which this behaviour occurred, were also not studied in detail, but it could be observed starting from 9 MPa and 318 K.

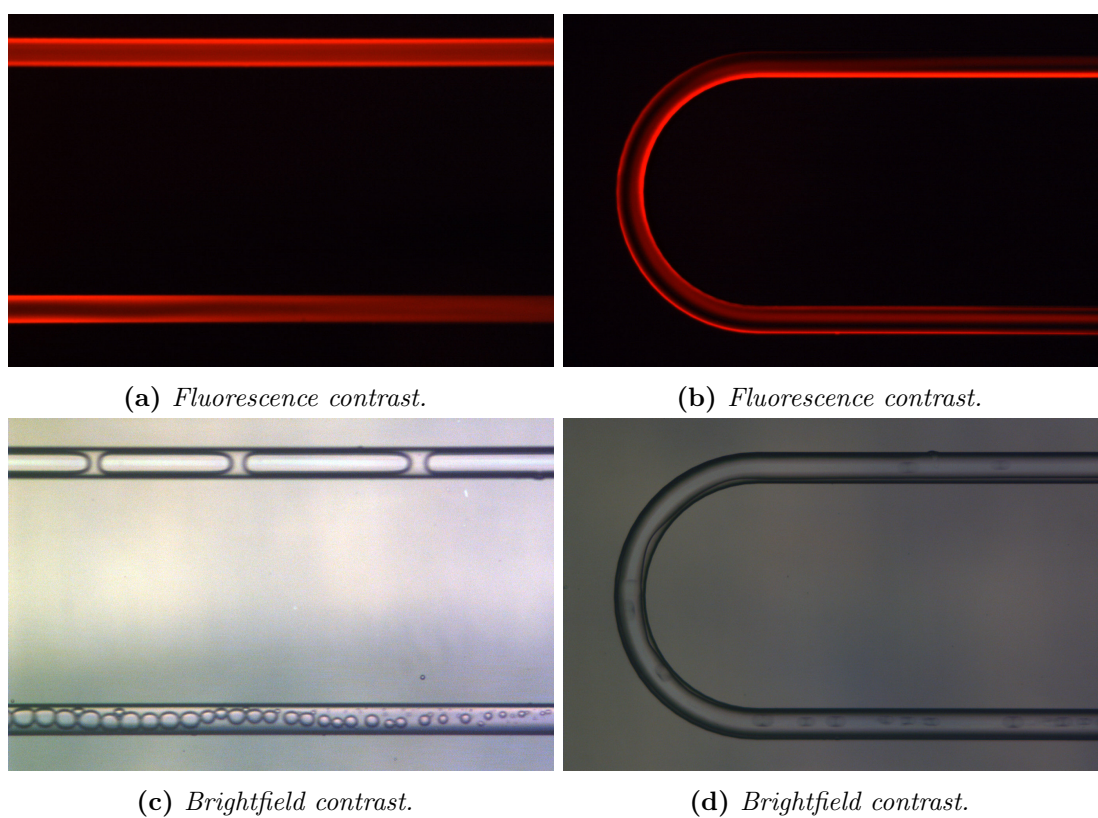


Figure 8.12: Flow visualization of CO_2 -MeOH-RhB mixtures with Fluorescence and Brightfield contrast techniques. Operating conditions: (a,c) $P = 7.38$ MPa; $T = 313.2$ K, and (b,d) $P = 12.2$ MPa; $T = 352.4$ K.

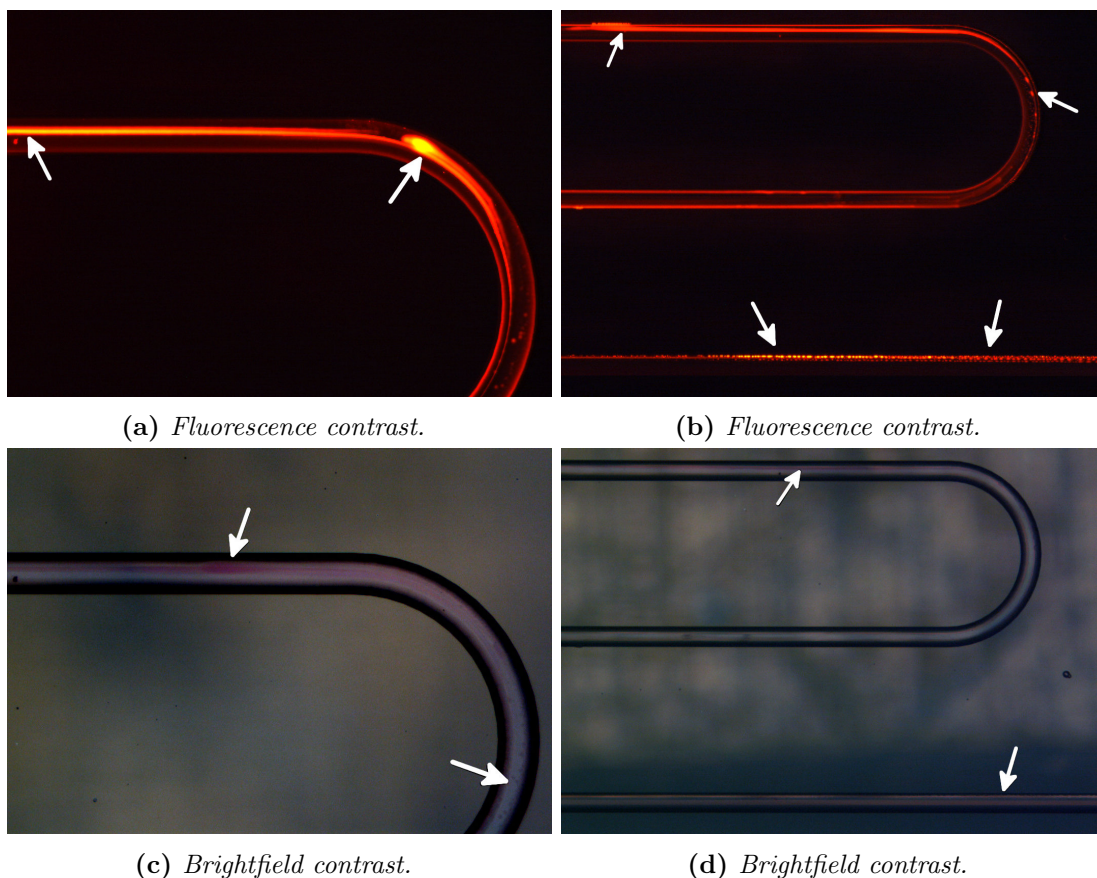


Figure 8.13: Degradation of Rhodamine B during experiments of $\text{CO}_2\text{-MeOH-RhB}$ mixtures. Operating conditions: (a,c) $P = 13.2$ MPa; $T = 360.0$ K, and (b,d) $P = 13.7$ MPa; $T = 369.4$ K.



Figure 8.14: Local transient disappearance of the fluorescence in the heated channel during experiments of $\text{CO}_2\text{-MeOH-RhB}$ at 12.2 MPa and 343.8 K.

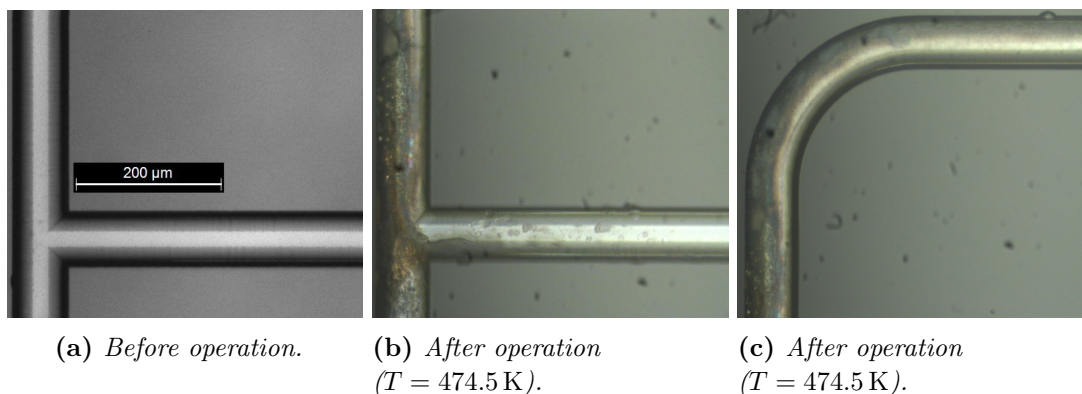


Figure 8.15: Effect of high operating temperatures on the T-junction and on the channel.

8.4.3 Operation at high temperatures

The experiments could be typically carried out at all pressures and at low temperatures, for as long as there was enough alcohol in the sample loop, and the chip could be reused afterwards as many times as necessary. However, this was not the case at the highest temperatures. When the system was operated above 470 K, the area near the T-junction turned gradually dirty and unclear, and the experiments could not be carried out more than a few minutes. The microfluidic chip became, then, useless and had to be replaced after the experiment.

Figure 8.15 shows images of the empty, clean T-junction before being used (Fig. 8.15a), and of the empty, dirty T-junction and the following elbow after the system was operated at 474.5 K (Figs. 8.15b and 8.15c). At a first sight, the dirtiness in the images has bronze or golden colour, and is deposited in the walls of the channel, especially in the side of the channel occupied by the CO₂. Unfortunately, the images offer few information other than visual evidence of the phenomenon, and no further effort was made trying to identify the nature or the causes of the dirtiness. Briefly, the dirtiness might be the resulting substance from an unexpected reaction. It could also be an erosion in the wall due, again, to an unknown interaction between the fluids and the Borofloat glass material of the chip (let's remind that other fluids in supercritical conditions, such as water, are well known for their aggressiveness (Kritzer, 2004)).

8.5 Image recording and processing

During each experiment, 50 to 450 images were recorded with a CCD high-speed camera (PCO 1200s) attached to an inverted microscope (LEICA DMI5000M), at exposure times of 20 μs to 30 μs and maximum frame rates, fr , of 940 Hz with a size of 541 × 1160 pixels per frame. The pixel resolution, b , of the images was 0.600 pixel μm⁻¹. See Figure 8.16 for a sample of the recorded images.

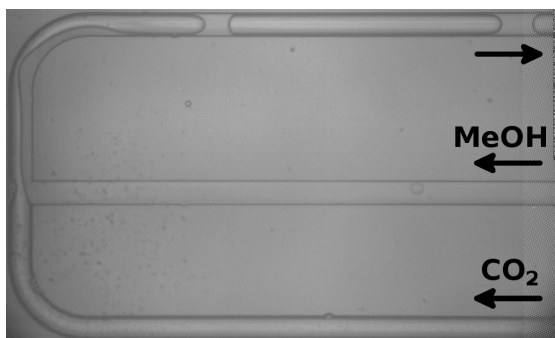


Figure 8.16: Image recorded with the CCD high-speed camera attached to the inverted microscope. Taylor flow of CO_2 -MeOH, at 6.89 MPa and 305.6 K.

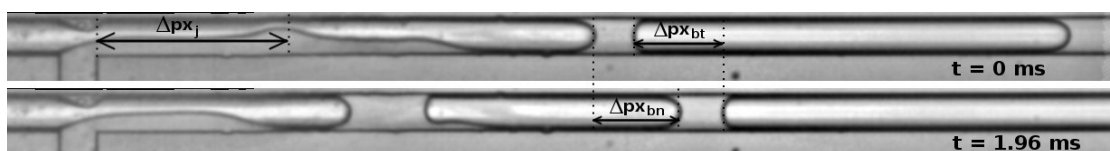


Figure 8.17: Two successive frames ($t = 0$ ms and $t = 1.96$ ms) showing the T-junction and the meandering channel, straightened for data analysis. The measurement of Δpx_j , Δpx_{bt} and Δpx_{bn} , are indicated.

Each stack of images was processed with “ImageJ Image Processing Software” (Rasband, 1997–2011) for the analysis of two-phase flows. The void fraction of the experiments, ε_{exp} , and the liquid-vapour interfaces were determined and identified, respectively, in a similar way to the one of Agostini et al (2008). The image of the channel after the T-junction was straightened, and the liquid-vapour interfaces were identified by increasing the contrast ratio. Figure 8.17 shows two successive frames, $\Delta t = 1.96$ ms, from the experiment in Figure 8.16. In this figure one can observe the measurement of the difference in position between both frames, in pixel units, of the liquid-vapour interfaces of the nose, Δpx_{bn} , and the tail, Δpx_{bt} , of a bubble of Taylor flow. The measurement of the distance, again in pixel units, between the T-junction and the position where the liquid plugs of Taylor flow are generated, Δpx_j , can also be observed.

To determine ε_{exp} , a threshold was applied to the image, which was then binarized and, finally, the Area Measurement feature from ImageJ was used. In this procedure, the thin liquid layers on top and bottom of the channel were neglected. The non-uniform distribution of the area-to-volume fraction associated with the cross-sectional geometry of the channel (See Fig. 8.2) was not taken into account. Figure 8.18 shows the procedure for determining ε_{exp} in a section of the channel from Figure 8.16.

Neglecting the non-uniform distribution of the cross-sectional geometry of the channel would result in erroneous values of ε_{exp} , due to the overestimation of the volume corresponding to the sides of the channel, and to the underestimation of the volume



Figure 8.18: Determination of ε_{exp} . The portion of the channel used for the measurement of ε_{exp} is indicated, and the resulting binarized image is shown. The void areas are surrounded by the fluid-fluid and wall-fluid interfaces (in black).

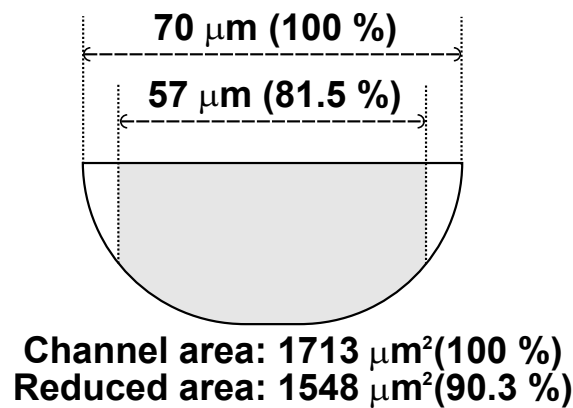


Figure 8.19: Comparison of the widths and areas of the cross-section of the channel, and of the portion used for the measurement of the void fraction (shadowed area), in absolute and percentage values.

corresponding to the centre of the channel. This situation would be specially important in the case of stratified flow regimes, such as annular and wavy flows, where the liquid occupied the sides of the channel while the vapour flowed through the core of the channel. On the other hand, segmented flows, including Taylor flow, would be less affected by this error. In order to minimise this inaccuracy in the results of ε_{exp} , both sides of the channel (6.5 μm in width, each) were excluded from the determination of ε_{exp} , as it can be observed in Figure 8.18. The remaining width (57 μm) and cross-sectional geometry are shown in Figure 8.19. It can be observed that the removed sides of the channel were highly overestimated, with the 18.5 % of the width of the channel, and only the 9.7 % of its area.

Two examples with idealised stratified flows demonstrate the improved accuracy when using only a reduced portion of the total width of the channel, in the determination of ε_{exp} . The first example considers a smooth flow, with a single liquid layer attached to one side of the channel. The second example considers an annular flow, with two liquid layers attached to both sides of the channel. In both examples, the fluid-fluid interfaces are ideally vertical. Figure 8.20 compares the resulting ε_{exp} when using three different methods: calculations based on the total width of the channel; calculations based on the reduced portion of the width of the channel; and calculations based on the area of the

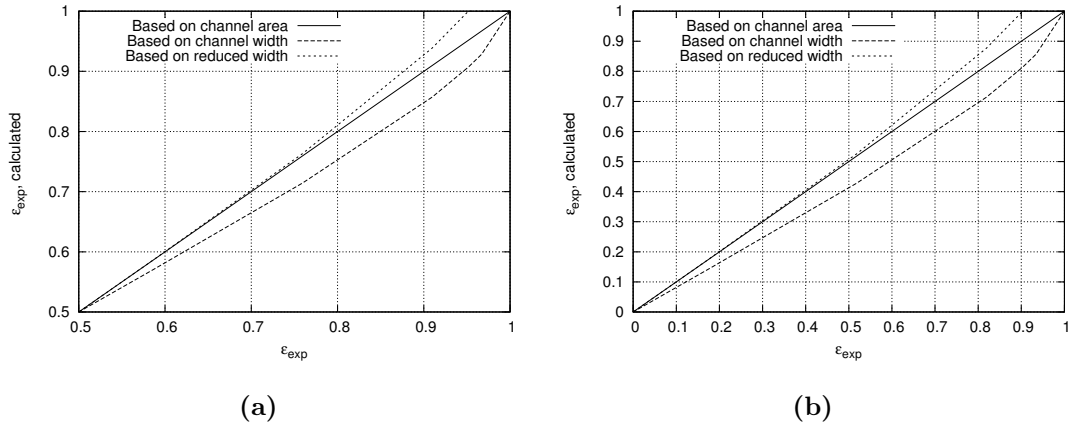


Figure 8.20: Comparison of the different methodologies for calculating ε_{exp} in an (a) idealized smooth flow and in an (b) idealized annular flow. The calculations based on the total channel width and a reduced portion of the channel width are compared, against the exact results based on the area of the cross-section of the channel.

cross-section of the channel. Determining ε_{exp} based on the area of the cross-section of the channel gives the exact values of ε_{exp} , as in Eq. (7.12). It can be observed that the results of ε_{exp} when using the total width of the channel clearly underestimate the exact ε_{exp} . On the other hand, using the reduced portion of the width of the channel is much more accurate, and it just gives overestimated results at the higher values, especially around $\varepsilon_{exp} \approx 0.9$.

Once the images were already processed, the velocity of liquid plugs, U_{lp} , was determined as,

$$U_{lp} = 0.5 \cdot (U_{bt} + U_{bn}) \quad (8.4)$$

Both the bubble tail and nose velocities, U_{bt} and U_{bn} , were calculated as,

$$U = \frac{fr \cdot \Delta px}{b} \quad (8.5)$$

The elongation rate, θ , measured by means of the ratio of elongation of a plug to the distance it travelled along the channel, was defined as,

$$\theta = \frac{U_{bt} - U_{bn}}{U_{lp}} \quad (8.6)$$

The frequency of liquid plugs during a video sequence was determined as,

$$f_{lp} = \frac{N - 1}{\Delta t} \quad (8.7)$$

where N is the number of plugs and Δt is the elapsed time between the first and the last liquid plug observed in the video sequence.

8.5. Image recording and processing

107

Finally, the dimensionless jet entrainment, ι , measured by means of the distance between the T-junction and the position where the liquid plugs of Taylor flow were generated, scaled with the hydraulic diameter of the channel, was defined as,

$$\iota = \frac{\Delta p x_j}{b \cdot d_h} \quad (8.8)$$

UNIVERSITAT ROVIRA I VIRGILI

NUMERICAL AND EXPERIMENTAL ANALYSES OF SINGLE AND TWO-PHASE MICROFLUIDIC FLOWS WITH IMPLICATIONS IN MICROREACTORS

Roland Blanch Ojea

DL:T. 149-2012

Results and discussion

Contents

9.1	Vapour-Liquid Equilibrium and feed ratio	110
9.1.1	Vapour-Liquid Equilibrium of CO ₂ -EtOH and CO ₂ -MeOH	110
9.1.2	Estimation of the feed ratio of working mixtures	111
9.1.3	Phase behaviour of working mixtures at different pressures	113
9.2	Flow regimes	115
9.2.1	Two-phase flows	116
9.2.2	Single-phase flows	118
9.3	Flow instabilities, and accumulation of liquid in the line of CO₂	121
9.3.1	Flow instabilities	121
9.3.2	Accumulation of liquid in the line of CO ₂ . Description of the phenomenon	121
9.3.3	Accumulation of liquid in the line of CO ₂ . Analysis of the causes	124
9.4	Two-phase void fraction	131
9.5	Hydrodynamics of Taylor flow	133
9.5.1	Velocity of liquid plugs	134
9.5.2	Elongation rate and frequency of generation of liquid plugs	134
9.5.3	Dimensionless jet entrainment	136
9.5.4	Conclusions	138

The different results obtained after the analysis of the data gathered from the experiments conducted are presented and discussed in this Chapter. These results include the preliminary identification of the quantitative behaviour of the VLE of both sets of fluids with experimental data from the literature, and the estimation of the feed ratio during the experiments (Sect. 9.1). The identification of the different flow regimes observed during the experiments is presented afterwards in Section 9.2. These flow regimes have been sorted into two groups, the two-phase flows and the single phase flows, and the corresponding flow regime maps based on pressure and temperature have been generated. An unexpected phenomenon consisting in the accumulation of liquid in the line of CO₂ is reported in Section 9.3. Here are provided a detailed description of the phenomenon and an approximate identification and analysis of its causes. Section 9.4 presents the

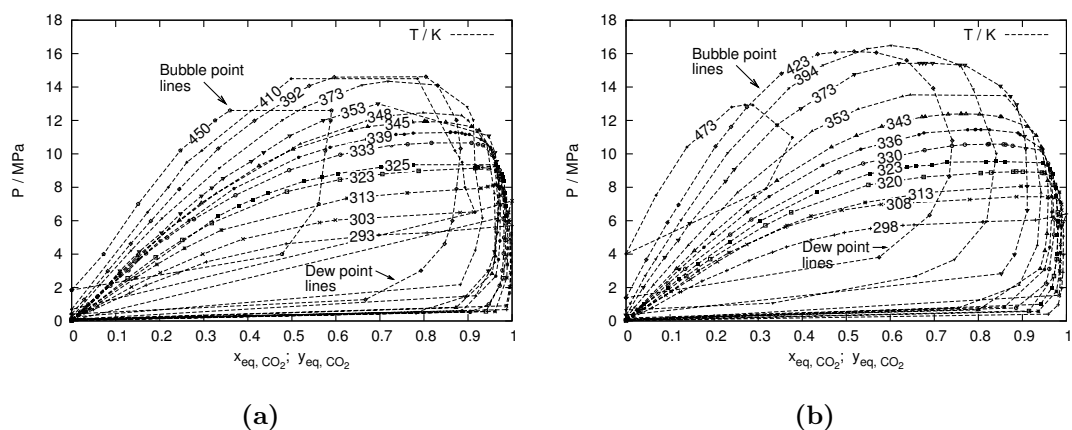


Figure 9.1: P - xy diagrams from literature data (see Appendix A) of the VLE at different temperatures, for mixtures of (a) CO_2 -EtOH and (b) CO_2 -MeOH. The bubble point lines and the dew point lines are indicated.

results of the experimental void fraction obtained during the two-phase flows, and their comparison with the homogeneous void fraction, with the initial volumetric fraction and with the void fraction predicted by the literature. The final Section 9.5, analyses several hydrodynamic parameters of Taylor flow at the different operating conditions for both sets of fluids.

9.1 Vapour-Liquid Equilibrium and feed ratio

9.1.1 Vapour-Liquid Equilibrium of CO_2 -EtOH and CO_2 -MeOH

P-T- xy experimental data of VLE for both sets of fluids has been obtained from several authors (Secuianu et al, 2008; Joung et al, 2001; Jennings et al, 1991; Suzuki et al, 1990; Galicia-Luna et al, 2000; Brunner et al, 1987; Ohgaki and Katayama, 1976; Bezahehtak et al, 2002; Leu et al, 1991; Mendoza de la Cruz and Galicia-Luna, 1999; Tian et al, 2001). The use of any of the available equations of state has been rejected. A complete list of these literature data is included in Appendix A, and is gathered in the form of P- xy phase diagrams for CO_2 -EtOH and for CO_2 -MeOH in Figure 9.1. CO_2 is the primary component in both mixtures and, thus, the mole fractions of CO_2 , x_{eq,CO_2} and y_{eq,CO_2} , are used in the diagrams. It can be observed that, at P and T conditions below the critical point of CO_2 , the diagram reaches $x_{eq,\text{CO}_2} = 1$. On the other hand, P and T conditions are always below the critical point of the alcohols and, therefore, the diagrams always reach $x_{eq,\text{CO}_2} = 0$. The bubble point lines and the dew point lines are indicated in the diagrams.

The forthcoming phase diagrams are the result of the interpolation of the literature data from Figure 9.1. An example is the P-T diagram shown in Figure 9.2, with the

9.1. Vapour-Liquid Equilibrium and feed ratio

111

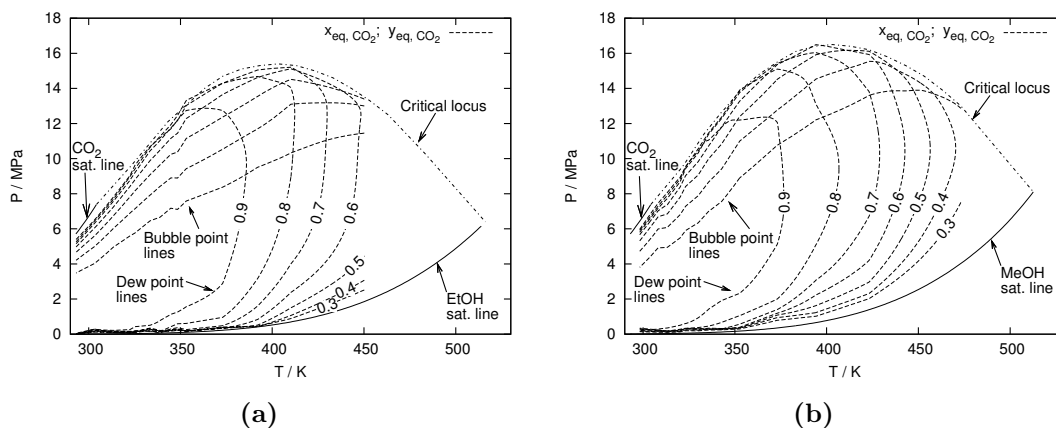


Figure 9.2: *P-T diagrams, interpolated from Figure 9.1, of the VLE for mixtures of (a) CO₂-EtOH and (b) CO₂-MeOH, at different x_{eq,CO_2} and y_{eq,CO_2} . The bubble point lines and the dew point lines are indicated. The saturation lines of the pure fluids, and the critical locus of the mixtures, are included for completeness.*

VLE at x_{eq,CO_2} , y_{eq,CO_2} from 0.3 to 0.9. The critical locus of the mixtures, connecting the critical points of both pure fluids, is included in this diagram. The data for the critical locus was obtained experimentally by Chester (2004), and is also included in Appendix A. Finally, the saturation lines of CO₂, EtOH and MeOH are also included, and the bubble point and dew point lines are indicated.

9.1.2 Estimation of the feed ratio of working mixtures

As explained in Section 8.3.4, due to setup limitations, the feed ratio of the fluids could not be monitored or controlled during the experiments. Therefore, a series of preliminary experiments were conducted to estimate this feed ratio.

9.1.2.1 Description of the procedure

The feed ratio of the fluids was estimated by comparing present experimental visualisations of the bubble point of the mixtures at different pressures, with the available data of VLE from literature. The glass microfluidic chip with the T-junction in the cooled area (Figs. 8.1a and 8.1c) was used to this purpose. In this way, the syringe pump operated at a fixed pressure. Then, both fluids mixed, with unknown feed ratio, in the cooled area of the chip before flowing towards the heated meandering channel. The temperature of the meandering channel, initially at room temperature, was gradually increased until the first bubbles appeared. The experiments were repeated at higher pressures, until no phase change on the mixture was observed at any temperature. Figure 9.3 shows an example of an image recorded when the mixture of CO₂-EtOH reached the bubble point, at 7.87 MPa and 308.7 K. The visualized area is a section of the meandering channel, as

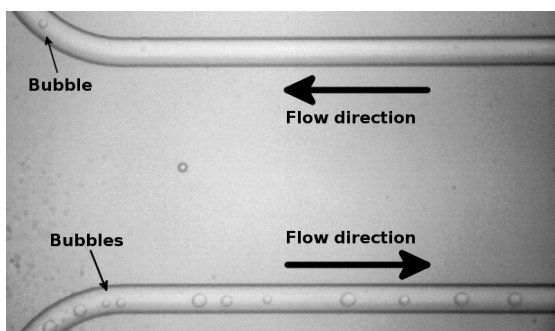


Figure 9.3: Image of the first bubbles appearing when the mixture of CO_2 -EtOH reaches the bubble point, at 7.87 MPa and 308.7 K. The direction of the flow is indicated.

indicated in Figure 8.1c.

Several assumptions were made when estimating the feed ratio of the fluids:

- The feed ratio did not vary with pressure conditions.
- The variation with time in the content of CO_2 inside the loop with alcohol sample, did not affect the feed ratio during the experiments.
- Heating the fluids before reaching the T-junction in the chip of Figures 8.1b and 8.1d, had a negligible effect on variations in the feed ratio. This assumption is reasonable, since the portion of the channels that is heated is very small compared to the total distance between the split of the CO_2 line and the T-junction.

These assumptions lead to the following suppositions:

- The results of the estimation of the feed ratio of fluids with the chip with the T-junction in the cooled area, are valid for the main experiments with the chip with the T-junction in the heated area.
- The feed ratio of fluids was constant throughout the study.

9.1.2.2 Results

The resulting bubble point line from the experiments is plotted in the P-T phase diagram shown in Figure 9.4, for both sets of fluids. The bubble point line reaches P values of 11.3 MPa and 15.0 MPa for CO_2 -EtOH and for CO_2 -MeOH, respectively. Above these P , phase changes in the mixtures were observed no more.

The experimental bubble point lines are compared in Figure 9.4 with the bubble point lines from literature data at different mixture compositions, to estimate the feed ratio of the mixtures during the experiments. Let's remark that, according to the needs of the present study, from now on the curves from literature data will be based on mass fractions, v and ω , instead of on molar fractions, x and y . Both experimental bubble

9.1. Vapour-Liquid Equilibrium and feed ratio

113

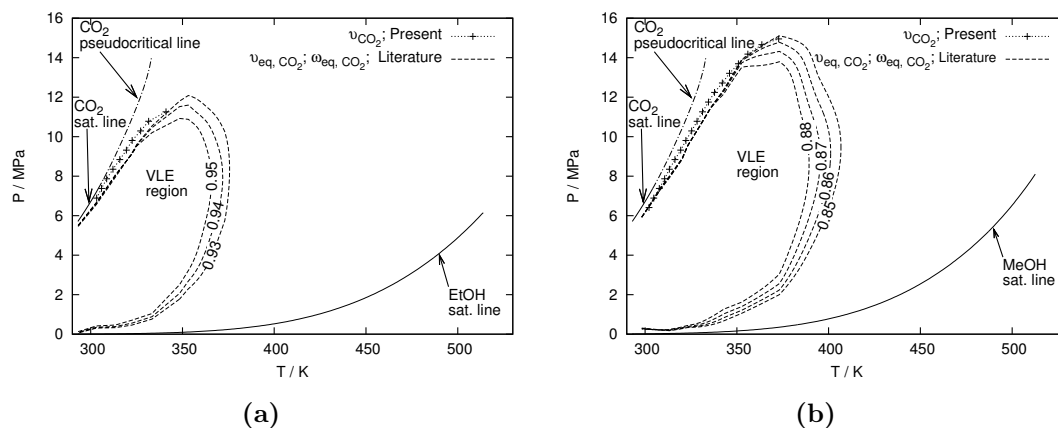


Figure 9.4: Comparison of the pressure, P , and temperature, T , conditions of the experimentally observed bubble points in the present work, with the VLE curves from literature data (See Fig. 9.2) at different v_{eq,CO_2} and ω_{eq,CO_2} , for mixtures of (a) CO₂-EtOH and (b) CO₂-MeOH. The pseudocritical line of CO₂ is included for completeness.

point lines fall slightly above the literature data. This was already expected due to the assumption of a constant experimental pressure drop of 3% (see Sect. 8.3.1), which leads to an underestimation of the pressure drop at the highest pumping pressures. Yet, the comparison allows to accurately predict feed ratios of $v_{o,CO_2} = v_{CO_2} \approx 0.95$ ($\%v/v_{o,CO_2} \approx 0.949$) for CO₂-EtOH and $v_{o,CO_2} = v_{CO_2} \approx 0.87$ ($\%v/v_{o,CO_2} \approx 0.869$) for CO₂-MeOH.

The pseudocritical line of CO₂ is included in Figure 9.4 to illustrate the proximity of this line to the experimental bubble point line of both sets of fluids. This proximity may have important implications in the forthcoming results near the bubble point line, due to the high sensitivity of the properties of CO₂ with temperature, in the vicinity of the pseudocritical points (See Sect. 7.2).

9.1.3 Phase behaviour of working mixtures at different pressures

The T-xy phase diagrams in Figure 9.5 show the phase behaviour for CO₂-EtOH at $v_{CO_2} = 0.95$, and for CO₂-MeOH at $v_{CO_2} = 0.87$ at three different pressures, 6.89 MPa, 7.87 MPa and 9.81 MPa. These mixtures increase their temperature under isobaric conditions, from an initial single-phase point at low temperature, until a final single-phase point at high temperature and $\omega_{CO_2} = v_{CO_2}$. Between the initial and the final points, the mixtures reach: the bubble point; the VLE region with different compositions of the saturated liquid, v_{eq,CO_2} , and vapour phases, ω_{eq,CO_2} , depending on temperature; and the dew point. The VLE regions, the bubble point and dew point lines at the different P , and several tie lines are indicated in the phase diagrams. The bubble point temperatures, T_{bub} , and dew point temperatures, T_{dew} for both sets of fluids at 6.89 MPa, 7.87 MPa and 9.81 MPa, extracted from Figure 9.5, are listed in Table 9.1.

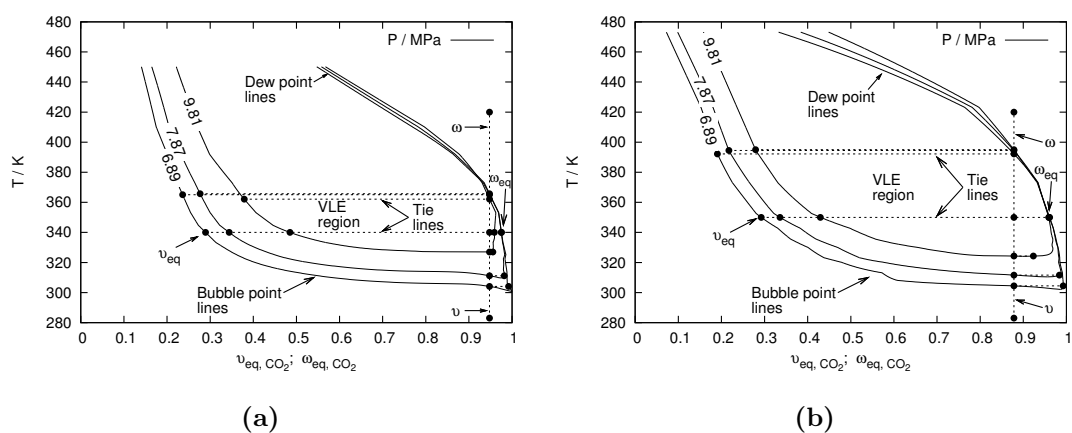


Figure 9.5: Phase behaviour at 6.89 MPa, 7.87 MPa and 9.81 MPa, for mixtures of (a) CO_2 - $EtOH$ at $v_{CO_2} = 0.95$ and (b) CO_2 - $MeOH$ at $v_{CO_2} = 0.87$.

Table 9.1: Bubble and dew point temperatures for CO_2 - $EtOH$ at $v_{CO_2} = 0.95$, and for CO_2 - $MeOH$ at $v_{CO_2} = 0.87$, at different pressures

P/MPa	CO_2 - $EtOH$		CO_2 - $MeOH$	
	T_{bub}/K	T_{dew}/K	T_{bub}/K	T_{dew}/K
6.89	304.1	365.1	304.4	392.2
7.87	311.1	365.7	311.6	394.5
9.81	327.0	362.1	324.3	395.0

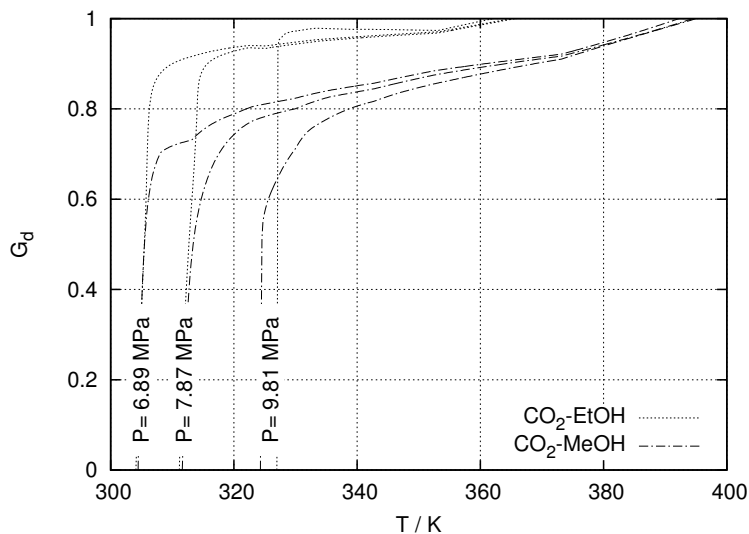


Figure 9.6: Vaporised mass diffusion fraction, G_d , for mixtures of CO_2 -EtOH at $v_{\text{CO}_2} = 0.95$ and of CO_2 -MeOH at $v_{\text{CO}_2} = 0.87$, at 6.89 MPa, 7.87 MPa and 9.81 MPa, against the temperature, T .

In Figure 9.5, a steep gradient in v_{eq,CO_2} can be seen for all VLE cases at temperatures close to the bubble point, which gradually decreases as temperature approaches the dew point. The steep variation in v_{eq,CO_2} can lead to important changes in some properties of the saturated liquid phase (see, for instance, $\mu_{l,eq}$ in Fig. 7.7), as well as in the vaporisation of the mixture and in the flow conditions. On the other hand, ω_{eq,CO_2} remains relatively constant at all VLE temperatures, especially in the case of CO_2 -EtOH mixture.

The vaporised mass diffusion fraction, G_d , has been calculated with Eq. (7.1), based on the results in Figure 9.5. The resulting values of G_d are shown in Figure 9.6. Obviously, $G_d = 0$ at T_{bub} , and $G_d = 1$ at T_{dew} . As it can be observed, extremely high vaporisations are reached at few temperature degrees above the bubble point at all pressures, with values of $G_d > 0.9$ for CO_2 -EtOH and of $G_d > 0.7$ for CO_2 -MeOH. These values are the result of the mentioned steep gradient in v_{eq,CO_2} near the bubble point. This behaviour is quite important because it implies very high vaporisation of the mixtures at most of the VLE conditions, and a region close to the bubble point where the mixtures are very sensitive to temperature. On the other hand, the pressure plays a minor role in the distribution of the vaporisation of the mixtures.

9.2 Flow regimes

Two independent scenarios were identified for the study of flow behaviour of the two sets of fluids, CO_2 -EtOH and CO_2 -MeOH, over a T-junction. The first, at the operating

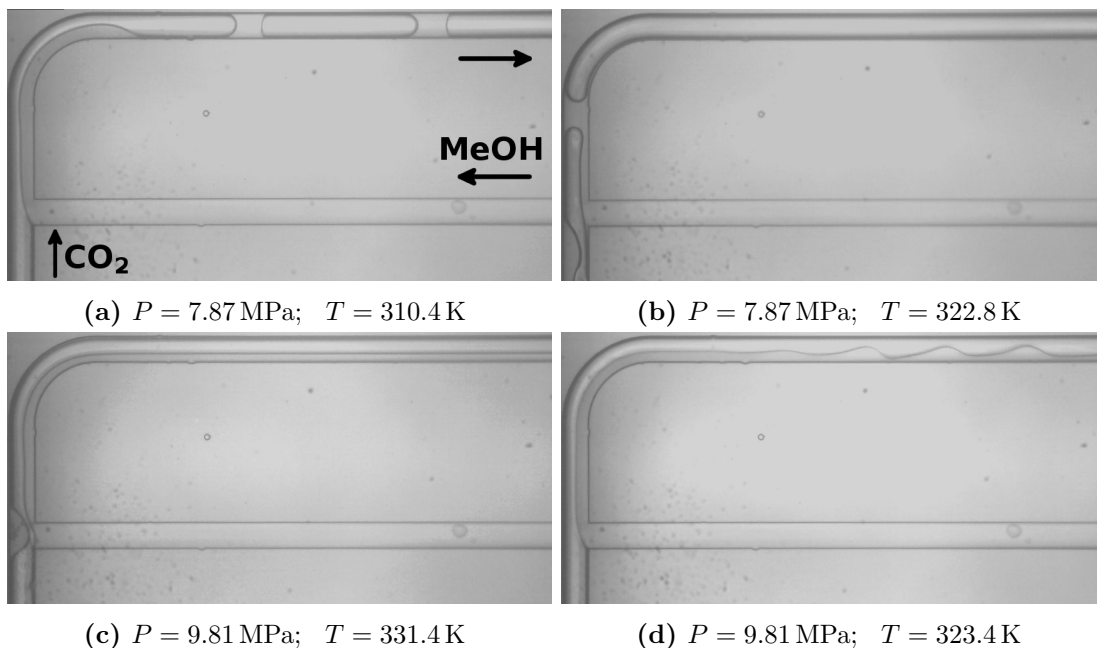


Figure 9.7: Two-phase flow regimes of CO_2 -MeOH mixture: (a,b) Taylor; (c) Annular; (d) Wavy.

conditions under which the mixture experienced VLE and two-phase flows occurred; and the second, with single-phase mixtures and single-phase flows.

Unlike previous literature, in the present work the liquid alcohols, also known as continuous phase, were fed from the side channel of the T-junction, whereas the gas CO_2 or supercritical CO_2 , also known as disperse phase, were fed from the main channel of the T-junction (Fig. 8.1). The centrifugal forces generated in the curvature of the channel after the T-junction did not affect the observed flow regimes and, therefore, the associated Dean effects can be considered negligible.

9.2.1 Two-phase flows

In the two-phase flows scenario three pressures were tested, 6.89 MPa, 7.87 MPa and 9.81 MPa. According to the definitions presented in Section 7.3.1, Taylor and annular were the main observed two-phase flow regimes for both mixtures in VLE conditions. The flow regimes are shown in Figure 9.7 for CO_2 -MeOH. Surprisingly, wavy flow was also observed under certain conditions, whereas bubbly, churn, Taylor-annular, dispersed or rivulet flows did not appear. No different regimes other than those already reported in gas-liquid systems were found in the experiments with supercritical CO_2 .

Figures 9.7a and 9.7b, both at 7.87 MPa and with a temperature difference of 12.8 K, show Taylor flow with an extreme difference in the length of vapour bubbles. As mentioned in Section 7.3.1, sometimes these Taylor flows with such different bubble lengths

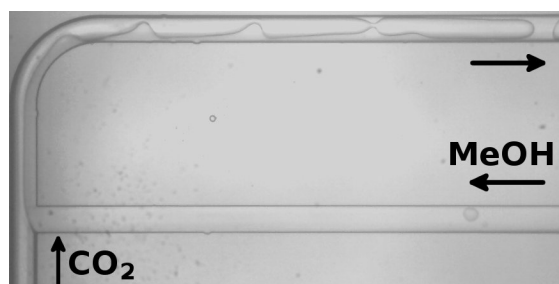


Figure 9.8: *Wavy-Taylor flow regime of CO₂-MeOH mixture at $P = 9.81$ MPa and $T = 323.6$ K.*

have been differentiated into different flow sub-types. For the sake of simplicity and practicality, this differentiation is discarded here, and all such cases were considered Taylor flow.

Besides the flow regimes shown in Figure 9.7, a rather different regime was also observed in both mixtures. Figure 9.8 shows what could be called a wavy-taylor flow regime, due to its wavy profile after the T-junction, that turns to Taylor type after a certain distance in the channel. Two kinds of transitions from liquid waves to plugs were observed: one was with the liquid wave stretching towards the opposite wall as it flowed along the channel, until it turned to a plug; the second way was in the form of a secondary, smaller wave appearing at the dry opposite wall, then both waves merged and generated the liquid plug. The latter way was only observed in CO₂-MeOH mixtures. A flow behaviour similar to the first kind of transition was reported as slug flow by [Damianides and Westwater \(1988\)](#) and [Barajas and Panton \(1993\)](#). This kind of flow regime was obtained in very few occasions, thus it is only shown here for completeness, and it has not been considered anywhere in the analysis of the results.

Figure 9.9 shows the maps of two-phase flow regimes inside the VLE regions based on temperature and on the three pressures tested. The boundaries of VLE regions for CO₂-EtOH at $v_{CO_2} = 0.95$ and for CO₂-MeOH at $v_{CO_2} = 0.87$ are obtained from Figure 9.4. The saturation line of CO₂ is included in the maps for completeness. In both cases annular flow was obtained almost throughout the entire regions analysed, in particular for CO₂-EtOH. Taylor flow was typical of lower pressures and low-medium temperatures, being more common in the CO₂-MeOH system where it was obtained at 6.89 MPa and 7.87 MPa.

The predominance of annular flow is usually favoured by significant inertial forces and by high gas-to-liquid rates ([Shao et al, 2009](#)). This is consistent with the very high vaporised fractions obtained in the present work in most of the experimental conditions (Fig. 9.6). It also agrees with the high contents of CO₂ in the liquid phases (Fig. 9.5) which decrease the interface tension. The increased velocities of the vapour phase, a result of increased feed rates at higher pressures and temperatures, also supports the predominance of annular flows. Taylor flow is more common for CO₂-MeOH than for CO₂-EtOH, which is probably due to lower vaporised fractions shown in the first mixture.

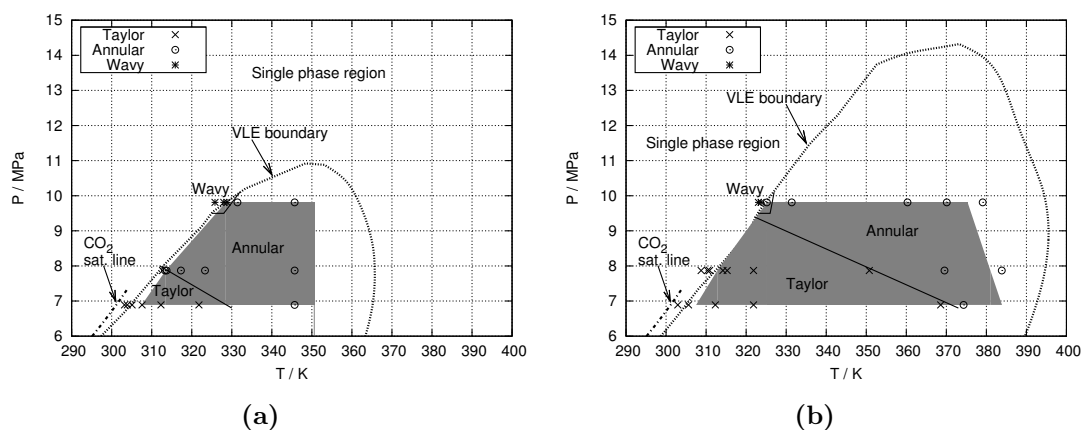


Figure 9.9: Maps of two-phase flow regimes for mixtures of (a) $\text{CO}_2\text{-EtOH}$ and (b) $\text{CO}_2\text{-MeOH}$, based on T and P conditions. The boundaries of VLE regions at (a) $v_{\text{CO}_2} = 0.95$ and (b) $v_{\text{CO}_2} = 0.87$ are indicated. The shadowed areas correspond to the experimental conditions where the liquid accumulation phenomenon was observed (see Sect. 9.3.2).

The effect of different fluid properties should be minor because the large content of CO_2 in both liquid phases should balance their properties. Note that methanol is less viscous and it has higher surface tension than ethanol. Wavy flow was obtained in a few occasions, always in the bubble point limits of the VLE regions at the highest pressure tested. The failure to maintain the wavy flow over a wider range of temperatures might be due to the sharp gradients of the CO_2 content in liquid phases (Fig. 9.5) and of the vaporised fractions in these regions (Fig. 9.6), together with the proximity of the pseudocritical point of CO_2 (Fig. 9.4) which leads to important variations in the density and viscosity of CO_2 with temperature.

9.2.2 Single-phase flows

A series of different flow regimes were observed outside the VLE region, including the expected standard single-phase flows as well as a variety of “pseudo” two-phase flows and two local phenomena in the T-junction. Examples of the listed regimes and phenomena can be observed in Figure 9.10 for $\text{CO}_2\text{-MeOH}$, and the corresponding regime maps for $\text{CO}_2\text{-EtOH}$ and $\text{CO}_2\text{-MeOH}$ based on temperature and pressure conditions are included in Figure 9.11.

The standard single-phase flows were mostly found at low temperature, in the form of either liquid CO_2 -liquid alcohol (Fig. 9.10a) or supercritical CO_2 -liquid alcohol (Fig. 9.10b). Characteristic of these flows was a mixing layer after the T-junction, without a clearly recognisable interface between both fluids.

At certain pressure and temperature conditions, the mixing layer turned into a clear interface between both phases, resulting in a “pseudo” two-phase flow along the mixing distance after the T-junction, just to disappear as both fluids reached a homogeneous

9.2. Flow regimes

119

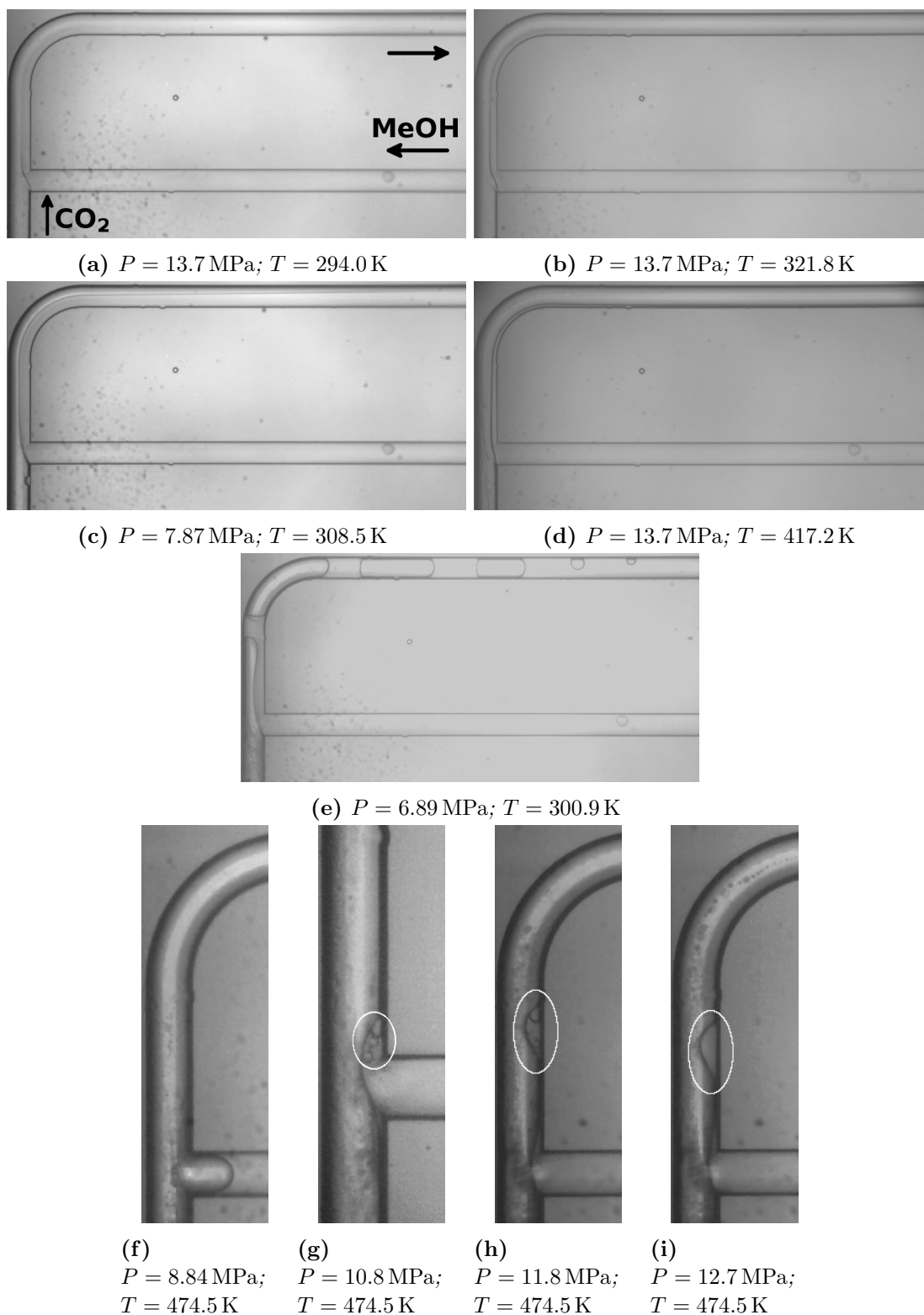


Figure 9.10: Single-phase flow, “pseudo” two-phase flow regimes and local phenomena of CO_2 -MeOH mixture: (a) Standard (Liquid-liquid); (b) Standard (Supercritical-liquid); (c-d) Stratified (Smooth); (e) Taylor; (f) Meniscus; (g) Boiling; (h) Wavy-Boiling; (i) Wavy. The boiling phenomena and the waves are marked for easy identification.

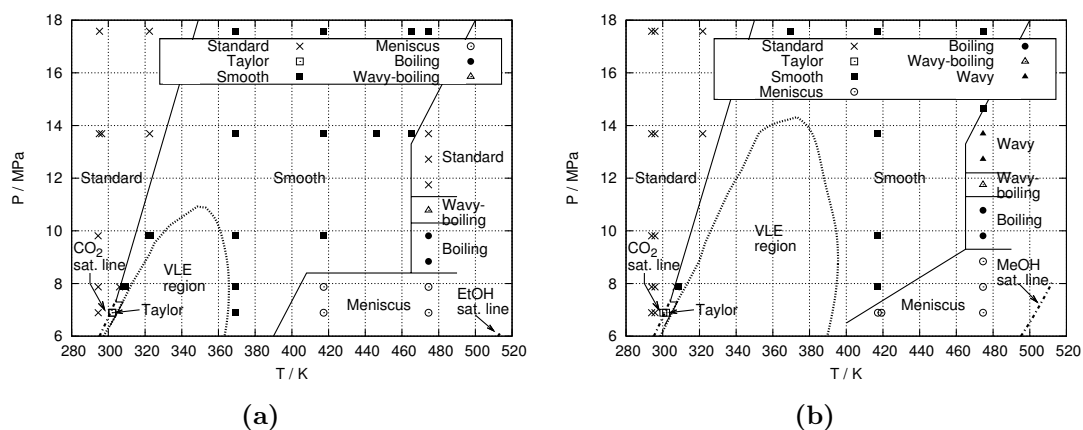


Figure 9.11: Maps of single-phase flow, “pseudo” two-phase flow regimes and local phenomena for mixtures of (a) CO_2 -EtOH and (b) CO_2 -MeOH, based on T and P conditions.

mixing and became single-phase flow. The downstream extension of the “pseudo” two-phase flows, measured from the T-junction, always increased with pressure. The flow regimes in the “pseudo” two-phase flow were: stratified (smooth) (Figs. 9.10c–9.10d), Taylor (Fig. 9.10e) and wavy (Fig. 9.10i). The main observed regime was “pseudo” stratified flow which, especially at higher pressures and at temperatures above the VLE region, decreased its extension as temperature increased (Figs. 9.10c–9.10d). In fact, the VLE regions were surrounded by this “pseudo” stratified flow, with the exception of a small region between the saturation line of CO_2 and the bubble point line, of around 2 K to 3 K, where “pseudo” Taylor flow was observed. The extension of the “pseudo” Taylor flow increased as temperature approached the bubble point of the mixture.

Determining visually the transition between single phase and VLE regions was somehow difficult when the flow regimes in the boundaries of both regions were similar. This is the case of “pseudo” Taylor and Taylor flows below supercritical conditions of CO_2 , and in particular of “pseudo” stratified and annular flows in the dew point line. As an approximate criteria, the regime was considered to be in the VLE region when it exceeded the visualization area of the images. For that reason, several data in Figure 9.9 lay beyond the theoretical VLE boundaries.

The “pseudo” wavy flow and the two local phenomena, namely meniscus and boiling, were only observed at higher temperatures. For both phenomena the liquid alcohol was quickly absorbed by the CO_2 stream in the T-junction, and therefore no liquid flow reached the main channel (Figs. 9.10f and 9.10g). Meniscus (Fig. 9.10f) was observed at lower pressures, both below and above supercritical CO_2 conditions, and oscillated along the alcohol channel with a frequency of a few Hertz. This is a similar phenomenon to that already studied by Ody et al (2007), who identified a threshold pressure below which a liquid plug gets blocked at the entrance of a bifurcating T-junction. Accordingly, as the pressure increased, the meniscus turned into a liquid tip in the T-junction with

9.3. Flow instabilities, and accumulation of liquid in the line of CO₂ 121

a boiling phenomenon inside (Fig. 9.10g). By further increasing the pressure, the tip turned to “pseudo” wavy flow with boiling inside the waves (Fig. 9.10h) until the boiling disappeared above certain pressure (Fig. 9.10i).

9.3 Flow instabilities, and accumulation of liquid in the line of CO₂

9.3.1 Flow instabilities

Dynamic instabilities are a common issue in flow of boiling fluids in microchannels. These have been identified as pressure, mass and temperature fluctuations, sometimes inducing periodic changes in the flow regimes and flow reversal (Thome, 2006; Kandlikar, 2002). Recently, also density wave and Ledinegg phenomena instabilities have been demonstrated in supercritical fluid systems (Ambrosini, 2007).

None of the present experiments seemed to suffer from any of these dynamic instabilities. Nevertheless, the continuous oscillation that affected the flow meter of the syringe pump (see Sect. 8.3.3) could be indicative of the system suffering from a density wave phenomenon or mass fluctuations. Unfortunately, this cannot be asserted with the available experimental data.

9.3.2 Accumulation of liquid in the line of CO₂. Description of the phenomenon

Besides the discussed issues of flow instabilities, another unexpected phenomenon was observed during the experiments which deserves special attention. The phenomenon consists in a continuous accumulation of liquid, either in the CO₂ channel before the T-junction or at the side of the channel occupied by the CO₂ after the T-junction. The accumulation occurred only at VLE conditions for both mixtures, starting at temperatures slightly above the bubble point until temperatures of 10 K to 20 K below the dew point. It was present at all pressure conditions, with the CO₂ in gas and supercritical state. The shadowed areas in the maps of two-phase flow regimes (Fig. 9.9) highlight the conditions at which this liquid accumulation was observed.

The overall process of this phenomenon can be divided into four different stages, as illustrated in the series of images of Figure 9.12, corresponding to a mixture of CO₂-MeOH at 6.89 MPa and 321.8 K, with a Taylor flow regime. The first stage, which could not be observed in the experiments, consists in the splitting of a small amount of liquid from the bulk flow of alcohol in the T-junction. The second stage is the displacement of the liquid upwards the CO₂ channel in form of tiny droplets, of sizes up to 10 μm to 15 μm, or a thin film attached to the wall. In the third stage these droplets reach a position where they tend to coalesce and generate one or more accumulations of liquid that increase their size with time (Figs. 9.12a–9.12c). The accumulation was not always static, as it experienced a random displacement over a narrow distance along

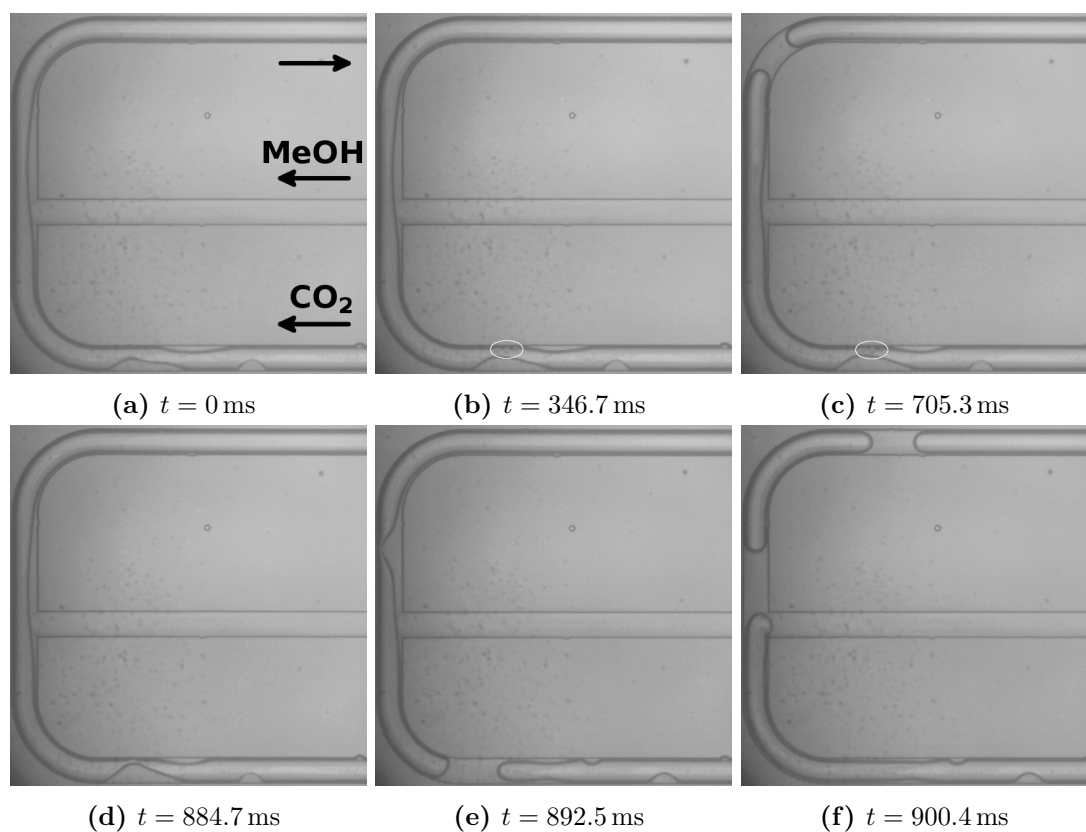


Figure 9.12: CO_2 -MeOH at 6.89 MPa and 321.8 K. (a-c) Evolution of the liquid accumulation in the CO_2 line and (d-f) further generation of a liquid plug. The tiny liquid droplets coalescing with the accumulation are marked for easy identification.

the channel, but without being dragged by the CO_2 stream. Finally in the fourth stage, depending on pressure and temperature conditions, the accumulation of liquid gradually grows up (Fig. 9.12d) until the channel gets completely blocked (Fig. 9.12e) and then one or more plugs of liquid are ejected downwards the channel, disturbing the whole two-phase flow regime (Fig. 9.12f). The blocking of the CO_2 channel and the subsequent formation of one or more liquid plugs occurred up to a region of 10 K to 20 K below the high temperature limits of the phenomenon. At these high temperatures, the amount of liquid accumulated was not enough to block the channel. Finally, further above these temperatures the accumulation of liquid disappeared completely.

At higher experimental pressures (9.81 MPa) and within a narrow temperature range close to the bubble temperature (328.8 K to 331.4 K for CO_2 -EtOH; 325.2 K to 328.7 K for CO_2 -MeOH), the accumulation appeared first after the T-junction, at the CO_2 side wall of the two-phase flow. In this case it showed a slow, periodic movement towards the T-junction as depicted in the images of Figure 9.13, corresponding to a mixture of CO_2 -MeOH with an annular flow regime. In these images the liquid is initially accumulated

9.3. Flow instabilities, and accumulation of liquid in the line of CO₂ 123

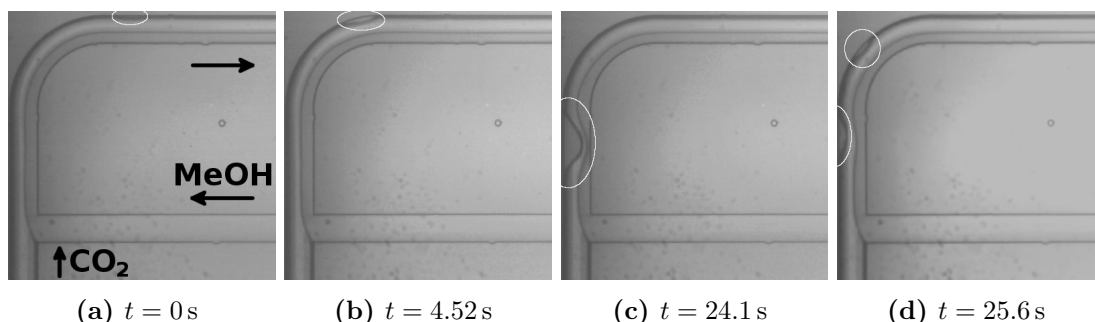


Figure 9.13: *CO₂-MeOH at 9.81 MPa and 325.2 K. Appearance and displacement upwards of the accumulation of liquid at the CO₂ side of the two-phase flow. The accumulation is marked for easy identification.*

somewhere after the T-junction (Fig. 9.13a), then it slowly moves upwards (Fig. 9.13b) until it reaches a position (Fig. 9.13c) where it disappears while the process starts again with a new accumulation appearing downwards the channel (Fig. 9.13d). In this way, no liquid plugs were generated because the accumulation disappeared periodically. The behaviour was also different than in the previous example (Fig. 9.12) in the sense that no tiny liquid droplets could be observed coalescing in the accumulation. As the temperature of the system was increased several degrees, the liquid accumulation reached the position of the T-junction and surpassed it upwards, leading to the phenomenon shown in Figure 9.12.

As it can be noticed from the timestamps of the images of Figures 9.12 and 9.13, this phenomenon was a slow and random process in comparison with the usual time-scale of the two-phase flows. Compared to the average generation period of Taylor plugs in the present work, of the order of 5 ms to 200 ms, the period of the plugs from the accumulation, could be from 300 ms up to several seconds. In some occasions, a continuous bunch of liquid plugs appeared and lasted up to 0.5 s before the system stabilised and the accumulation started again. As mentioned, the time-scales and frequencies of this phenomenon showed an apparently random behaviour, thus their dependency on temperature and pressure conditions could not be properly identified. On the other hand, the experimental conditions clearly affected the average distance between the liquid accumulation and the T-junction. The distance increased with temperature and decreased with pressure, as it can be observed in Figure 9.14. This figure shows the distance from the T-junction to the place where the plugs from the accumulation were generated, normalized with the d_h , at different temperatures and pressures. The negative distances in the figure correspond to the accumulation placed before the T-junction, in the CO₂ channel.

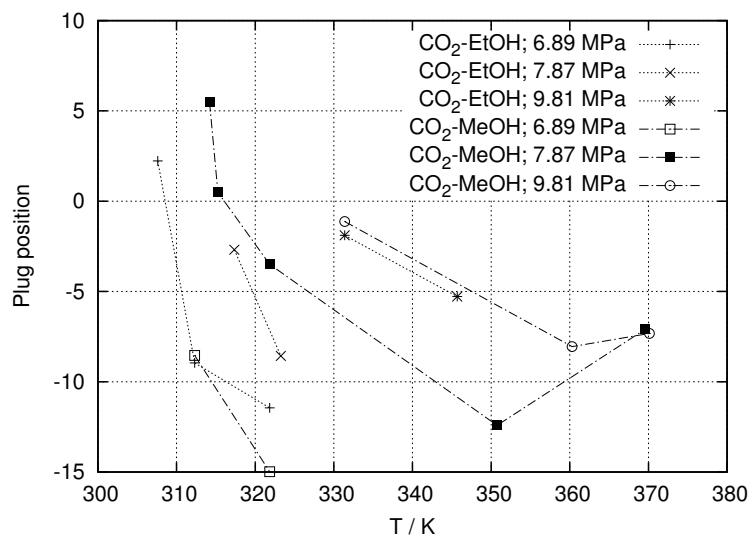


Figure 9.14: Dimensionless distance between the T-junction and the liquid accumulation, for CO_2 -EtOH and CO_2 -MeOH at 6.89 MPa, 7.87 MPa and 9.81 MPa, against the temperature, T .

9.3.3 Accumulation of liquid in the line of CO_2 . Analysis of the causes

The phenomenon of accumulation of liquid in the CO_2 channel was fully reproducible, and the continuous generation of plugs disturbed the two-phase flow regimes throughout most of the VLE conditions. Overall, this can be a drawback for the use of miscible two-phase flow systems. Therefore, its causes should be analysed aiming for a further prevention.

The mechanisms of the phenomenon were not clear a priori, and several efforts were made trying to elucidate its causes. In order to discard the possible interactions with the curvature of the channels before and after the T-junction as a cause for the phenomenon, a preliminary test was performed with the inlet lines inverted, i.e. the CO_2 flowing through the straight side channel and the alcohols through the curved main channel. Accumulation of both alcohols before and after the T-junction could be observed with this configuration as well, as shown in Figure 9.15 The result of a sudden pressure adjustment between both inlet lines in the T-junction can be also ruled out. In this case, one would expect evidences of liquid accumulation not only in VLE conditions but also during “pseudo” two-phase flows, at least at temperatures slightly below the bubble line. This, certainly, did not occur.

So far, capillary and wettability effects, are most likely to be responsible for the phenomenon of the accumulation of liquid. A thorough identification and analysis on these effects would be desirable, however this is beyond the possibilities of the present work, according to the available experimental data. Yet, a brief discussion to shed some light on their possible role in the phenomenon is presented here, with focus in the

9.3. Flow instabilities, and accumulation of liquid in the line of CO₂ 125

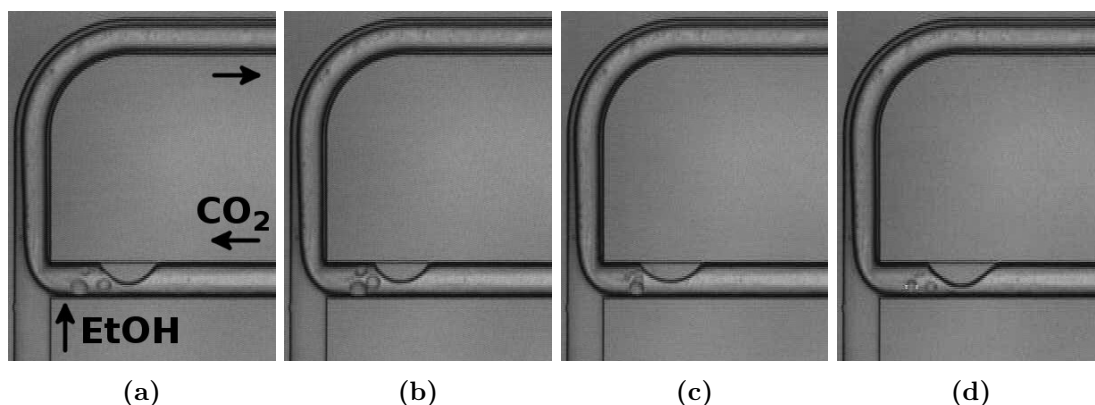


Figure 9.15: *CO₂-EtOH at 9.81 MPa and 340.9 K. Accumulation of liquid during an experiment carried out with the inlet lines inverted. The tiny liquid droplets coalescing with the accumulation, can be easily observed.*

experiments with CO₂-EtOH.

9.3.3.1 Identification of the local gradients and their effect on the properties of fluids

During the experiments, local gradients of temperature and of mass fractions were likely to occur. On one hand, regarding temperature, the heated area of the chip was large enough as to assume an isothermal distribution along the channels where the accumulation of liquid occurred (Sect. 8.3.2). Besides, the vertical temperature gradient between the top and the bottom walls of the channels is not likely to have a pronounced effect on the horizontal displacement of the liquid. However, there were local gradients of temperature due to the exothermic mixing of both fluids, roughly quantified as $\Delta T \approx 0.5 \text{ K}$ to 1 K . These gradients of temperature were identified with the generation of small bubbles along the mixing layer of both fluids after the T-junction, at temperatures slightly below the evaporation point of CO₂, when both fluids were in liquid state (See an example in Figure 9.16).

On the other hand, regarding the mass fraction, the mixing of both fluids after they came in contact in the T-junction might be an important factor in the displacement of the liquid. If the absorption of CO₂ into an isolated liquid droplet was not instantaneously homogeneous, the temporary heterogeneous distribution of composition, Δv_{CO_2} , across the droplet before reaching equilibrium compositions, would lead to gradients of several properties such as the interface tension, the density and the viscosity. Meanwhile, the CO₂ atmosphere around the droplet would never reach an equilibrium composition, because a continuous stream of pure CO₂ flowed over the isolated liquid. As a result, there would be a continuous transport of alcohol from the droplet to the stream, thus reducing the size of the droplet. With the present experimental data, it is not possible to

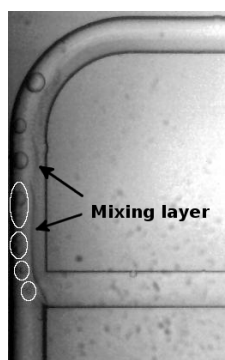


Figure 9.16: Bubbles generated along the mixing layer due to a gradient of temperature. The smallest bubbles are marked for easy identification. Conditions: 6.89 MPa, 300.4 K Boiling temperature of CO_2 : 301.1 K

determine whether this transient heterogeneous distribution of composition in the liquid is feasible or not, but many related studies with droplets in supercritical environments can be found elsewhere (e.g. Meng et al, 2005).

The relevant properties (including density, viscosity and interface tension) for CO_2 , EtOH and saturated liquid CO_2 -EtOH at VLE conditions, at different temperatures and pressures have been already presented in Section 7.2. Let's note, however, that the interface tension of EtOH presented there corresponds to a system of pure EtOH, not to a system of pure liquid EtOH in a CO_2 atmosphere. The corresponding v_{eq,CO_2} of the saturated CO_2 -EtOH have been also already presented in Figure 9.5a. From the values in Section 7.2 and in Figure 9.5a, it can be deduced that ΔT has a negligible effect on the properties of both liquids, compared to the effect of Δv_{CO_2} from pure EtOH to saturated CO_2 -EtOH. Assuming a linear dependency of the properties with the composition, a $\Delta v_{CO_2} \approx 0.1$ causes gradients of one order of magnitude larger in interface tension, and one to three orders of magnitude larger in viscosity and density, than those caused in both liquids by the $\Delta T \approx 1$ K experienced in the system.

Figure 9.17 shows the ratios of density (Fig. 9.17a), viscosity (Fig. 9.17b) and interface tension (Fig. 9.17c) of pure EtOH to saturated liquid CO_2 -EtOH at VLE conditions. The ratios are especially high at lower temperatures, and they decrease when temperature increases. The ratios decrease when temperature increases, mostly due to lower v_{eq,CO_2} in the CO_2 -EtOH at higher temperatures. In the range of temperatures where the phenomenon was observed, 308 K to 350 K, these ratios are large enough as to have important effects on the wetting properties of the liquid, as well as on the viscous and inertial forces acting on the liquid.

9.3.3.2 Mechanisms of the different stages of the phenomenon

As mentioned in Section 9.3.2, the phenomenon can be divided into four different stages. Whereas the first stage could not be visualised, and the fourth one was simply the

9.3. Flow instabilities, and accumulation of liquid in the line of CO₂ 127

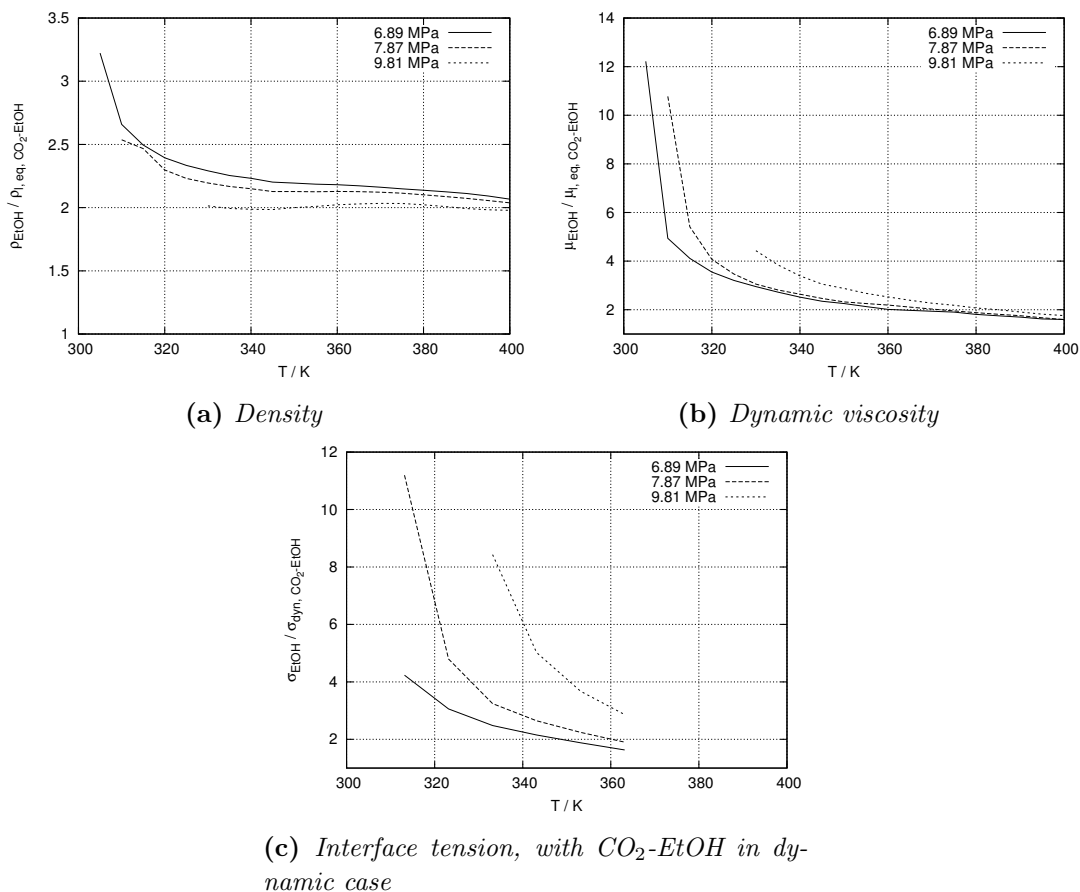


Figure 9.17: Ratios of different properties of EtOH to saturated liquid CO₂-EtOH at VLE conditions, at 6.89 MPa, 7.87 MPa and 9.81 MPa, against the temperature, T.

formation of a liquid plug due to a continuous accumulation of liquid, the second and the third stages, i.e. the displacement of small amounts of liquid upwards the channel and their subsequent accumulation, are apt to be analysed in order to identify their mechanisms.

Second stage of the phenomenon Once the possible local gradients along the channel have been identified (Sect. 9.3.3.1), and according to the processes described Section 7.4, it can be stated that the second stage of the phenomenon might be the consequence of thermo- and solutocapillary and of thermo- and solutowetting processes, in dynamic conditions with a continuous flow of fluid. All these processes together become a complex system, that cannot be characterised by separated analysis of single factors. Yet, here I attempt to illustrate the importance of these hypothetical temperature and composition gradients in the displacement of small amounts of liquid upwards the channel, by analysing their effect on the capillary pumping process.

According to Equations (7.25), (7.26), (7.27) and (7.28), Figures 9.18 and 9.19 show the approximated temperature and composition gradients, necessary to produce a Marangoni stress enough as to overcome the viscous and inertial forces, exerted by the stream of CO₂, acting upon a liquid droplet of EtOH attached to the channel walls. Any (ΔT) or (Δv_{CO_2}) exceeding these values, will result in an offset on the tendency of the droplet to be drag by the stream of CO₂, and in the observed displacement of the liquid upwards the channel. These temperature and composition gradients were calculated with Equations (7.25), (7.26), (7.27) and (7.28), using in the equations the velocity of the stream of CO₂, U_{CO_2} , calculated with Equation (8.3).

The positive sign of the results in the figures means that the gradients along the surface of the droplet must follow the direction of the flow. Let's note, however, that the results in Figure 9.18 correspond to a droplet of pure EtOH. If a saturated droplet of CO₂-EtOH would have been considered, instead, the results would have been similar but with opposite sign, due to the opposite behaviour of $\partial\sigma/\partial T$ for EtOH and for saturated CO₂-EtOH (See Sect. 7.2.4). The direction of (ΔT) would have to be also opposite to the flow, then.

As expected, higher (ΔT) and (Δv_{CO_2}) are required for overcoming the inertial forces, than for overcoming the viscous forces. The differences are about one order of magnitude for both cases. Besides, (ΔT)_{Ca} and (Δv_{CO_2})_{Ca} remain almost constant throughout all conditions, whereas (ΔT)_{We} and (Δv_{CO_2})_{We} are significantly dependent on pressure and, especially, temperature. Let's remark, however, that the results in Figures 9.18 and 9.19 might be overestimated, because they were calculated assuming the tendency of the liquid to flow with the same average velocity as the CO₂ stream. In fact, the droplets or the thin film were attached to the wall, where the effective velocity is lower.

As it happens with the properties of fluids (See Sect. 9.3.3.1), the effect of (Δv_{CO_2}) seems to be much more important than the effect of (ΔT), in the second stage of the phe-

9.3. Flow instabilities, and accumulation of liquid in the line of CO₂ 129

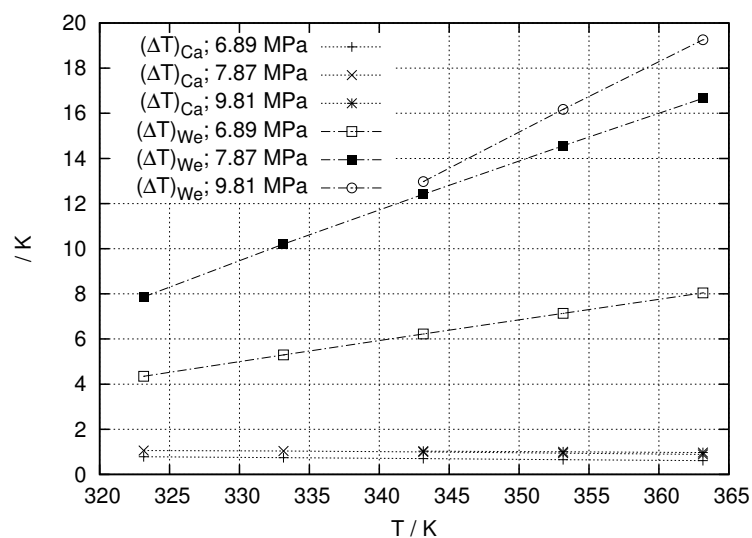


Figure 9.18: Temperature gradient, in a droplet of EtOH, required to overcome the viscous forces, $(\Delta T)_{Ca}$, and the inertial forces, $(\Delta T)_{We}$, at 6.89 MPa, 7.87 MPa and 9.81 MPa, against the temperature, T .

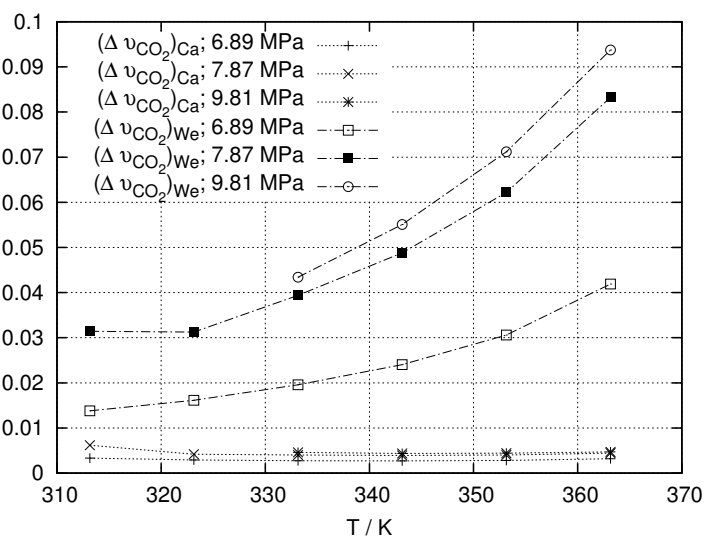


Figure 9.19: Mass fraction gradient of CO₂, in a droplet of EtOH, required to overcome the viscous forces, $(\Delta v_{CO_2})_{Ca}$, and the inertial forces, $(\Delta v_{CO_2})_{We}$, at 6.89 MPa, 7.87 MPa and 9.81 MPa, against the temperature, T .

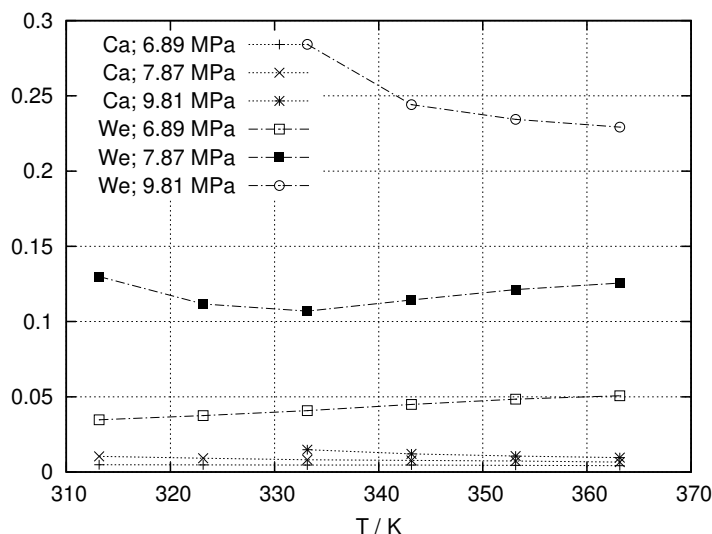


Figure 9.20: Capillary number, Ca , and Weber number, We , values of the accumulation of saturated liquid of CO_2 - $EtOH$ at 6.89 MPa, 7.87 MPa and 9.81 MPa, against the temperature, T .

nomenon. According to Figures 9.18 and 9.19, even in the worst experimental conditions, at higher temperatures, a $(\Delta v_{CO_2}) \geq 0.08$ would ensure a solutocapillary displacement of the liquid. This is feasible with the expected gradients in mass composition during the experiments. On the other hand, a thermocapillary displacement of the liquid would require values of (ΔT) up to 16 K, which is above the assumed temperature gradients in the present experiments.

Third stage of the phenomenon In the third stage, the tiny droplets reach a position where they stop their displacement and they begin to coalesce. This might be caused by the disappearance of (ΔT) and (Δv_{CO_2}) when the liquid reaches equilibrium compositions. The coalescence generates the liquid accumulation, which gets stacked to the wall without being flushed by the CO_2 stream, again by the predominance of interface tension forces. This is consistent with the values of $Ca < 1$ and $We < 1$ (See Eqs. (7.23) and (7.24)) of the accumulation of saturated liquid CO_2 - $EtOH$, shown in Figure 9.20. Besides, the increased contact surface between the accumulation and the wall due to the specific cross-section of the channel, further enhances the predominance of the interface tension forces.

A balance between the amount of liquid coalescing into the accumulation and its continuous dissolution into the pure CO_2 stream (explained in Sect. 9.3.3.1), might explain why no more liquid plugs were generated (the fourth stage) at the higher temperatures, even though the accumulation was still present.

Surprisingly, the observed increment in the distance between the liquid accumulation and the T-junction with the temperature (Fig. 9.14) did not agree with the calculations,

9.4. Two-phase void fraction

131

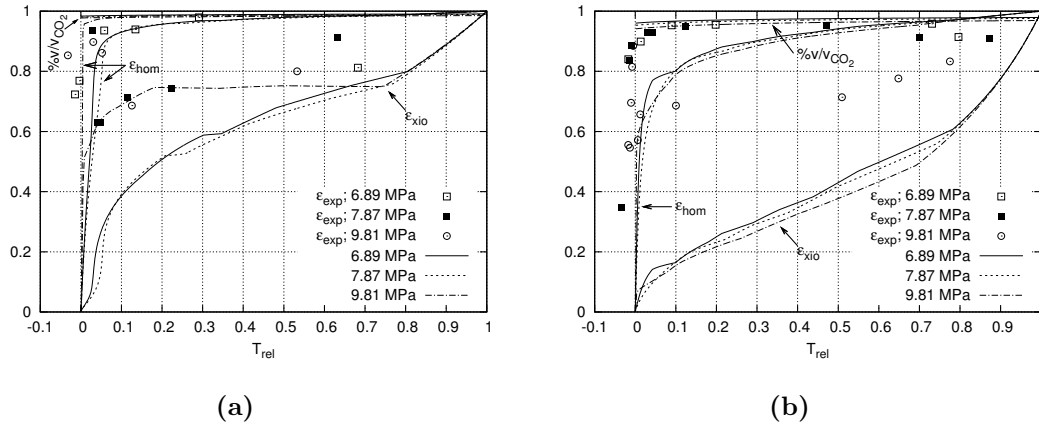


Figure 9.21: Comparison of experimental void fraction, ϵ_{exp} , homogeneous void fraction, ϵ_{hom} , and the correlation of Xiong and Chung (2007), ϵ_{xio} against the relative temperature, at 6.89 MPa, 7.87 MPa and 9.81 MPa. (a) CO_2 -EtOH at $v_{CO_2} = 0.95$ and (b) CO_2 -MeOH at $v_{CO_2} = 0.87$.

which predicted the opposite behaviour. First, because although $\partial\sigma/\partial v_{CO_2}$ is barely sensitive to temperature, a temperature increment lowers the possible gradients in composition, and therefore in Marangoni stresses, due to a lower saturation content of CO_2 in the liquid phase (Fig. 9.5). Second, because at higher temperatures, the composition and temperature gradients required to overcome the increased inertial forces of the CO_2 stream, are also higher (Figs. 9.18 and 9.19).

9.4 Two-phase void fraction

The experimental and homogeneous void fractions, ϵ_{exp} and ϵ_{hom} , are plotted against the relative temperature, T_{rel} , in Figure 9.21 for both sets of fluids at the three experimental pressures. ϵ_{exp} in the microchannel after the T-junction was obtained as described in Sect. 8.5, whereas ϵ_{hom} was calculated with Equation 7.16. Pure CO_2 was assumed when calculating $\rho_{v,eq}$ for Eq. 7.16, according to the high content of CO_2 in vapour phase throughout all VLE conditions.

T_{rel} is a normalised dimensionless temperature that relates the actual temperature to the bubble and dew temperatures of the mixture. T_{rel} is defined as,

$$T_{rel} = \frac{T - T_{bub}}{T_{dew} - T_{bub}} \quad (9.1)$$

The corresponding T_{bub} and T_{dew} of each experiment are listed in Table 9.1.

Here, plotting the void fractions against the relative temperature instead of against the usual homogeneous void fraction (Kawahara et al, 2002; Serizawa et al, 2002; Yue et al, 2008; de Loos et al, 2010) or vapour quality (Revellin et al, 2006; Agostini et al,

2008) allowed a clearer analysis of the results. Let's note that, since some of the two-phase flows of the present study were obtained below the bubble temperatures interpolated from literature, the range of T_{rel} goes below the zero-value.

A sharp variation of ε_{hom} in a very narrow range of temperatures above the bubble point, $T_{rel} < 0.1$, can be observed in Figure 9.21 for both sets of fluids and all pressures. This is the result of the sudden decrease in mass fraction of CO_2 in the liquid phase close to the bubble point (Fig. 9.5). As a consequence, the system becomes extremely sensitive to temperature changes within a range of 3 K to 5 K above the bubble point, affecting the two-phase flows transitions (Fig. 9.9) and the hydrodynamics of Taylor flow (see Sect. 9.5) in this region. Above this sensitive region, the evolution of ε_{hom} is much softer and the system becomes much more stable. Obviously, ε_{hom} tends to 0 as temperature approaches the T_{bub} , and to 1 as temperature approaches T_{dew} .

When analysing the results of ε_{exp} , two tendencies can be noticed depending on the flow regime of the experiment. On one hand, Taylor flow (6.89 MPa series in Figure 9.21a, and 6.89 MPa and 7.87 MPa series in Figure 9.21b) quickly reaches high values, $\varepsilon_{exp} > 0.9$, exceeding those of ε_{hom} , and then it stabilises as T_{rel} increases. On the other hand, wavy and annular flows (7.87 MPa and 9.81 MPa series in Figure 9.21a, and 9.81 MPa series in Figure 9.21b), after a region of unstable results near the bubble point, show moderate values, below ε_{hom} , with a gradual increment with T_{rel} . These two trends agree with the idea that, unlike Taylor flow where vapour is surrounded by liquid plugs, in stratified flows such as annular and wavy the vapour phase can flow unhindered and, therefore, slip between both velocities is likely to occur, resulting in lower ε_{exp} values. This explains why as T_{rel} increases and the Taylor flow turns to annular flow at a fixed pressure, ε_{exp} decreases significantly, when it should increase.

The volumetric fraction of CO_2 , $\%v/v_{\text{CO}_2}$, corresponding to the initial volumetric ratio at which both fluids reach the T-junction before their mixing begins, is included in Figure 9.21 with the aim to clarify those cases when ε_{exp} exceeds ε_{hom} . $\%v/v_{\text{CO}_2}$ was obtained in a way similar to ε_{hom} (Eq. (7.16)),

$$\%v/v_{\text{CO}_2} = \frac{1}{1 + (1/v_{\text{CO}_2} - 1)\rho_{\text{CO}_2}/\rho_{alc}} \quad (9.2)$$

Here, ρ_{CO_2} and ρ_{alc} are the densities of the pure fluids at the T-junction conditions. $\%v/v_{\text{CO}_2}$, calculated with Eq. (9.2), is almost constant under all pressure and temperature conditions, with values in the range of 0.977 to 0.991 for CO_2 -EtOH, and of 0.941 to 0.979 for CO_2 -MeOH. It can be observed that $\%v/v_{\text{CO}_2}$ is similar to ε_{exp} of Taylor flows, suggesting the possibility that, in these cases, the flow does not reach VLE conditions inside the visualised area, in particular at low temperatures where the difference between $\%v/v_{\text{CO}_2}$ and the void fraction at VLE conditions, ε_{hom} , is larger. On the other hand, the evolution towards VLE conditions in stratified flows is faster than in Taylor flows, as demonstrated by the lower ε_{exp} obtained in these flow regimes.

In both cases, the values of G_d (Fig. 9.6) were very similar to those of ε_{hom} , and the effect of pressure turned to be negligible on the distribution of ε_{hom} . These similar-

ities and negligible effect of pressure are the result of the similar behaviour of VLE at all pressures, with high vaporization values at almost all T_{rel} , together with moderate differences between $\rho_{l,eq}$ and $\rho_{v,eq}$ due to the high content of CO₂ in the saturated liquid phase, in particular at low T_{rel} . Furthermore, this negligible effect of pressure can be corroborated with the similar results of ε_{exp} at different pressures for the same flow regime (7.87 MPa and 9.81 MPa series in Fig. 9.21a, and 6.89 MPa and 7.87 MPa series in Fig. 9.21b).

ε_{exp} is also compared in Figure 9.21 with the void fraction predicted with the correlation of Xiong and Chung (2007), ε_{xio} . This correlation (Eqs. (9.3) and (9.4)), which is an extended version of the one previously developed by Kawahara and co-workers (Kawahara et al, 2002; Chung and Kawaji, 2004), has been tested in adiabatic systems with square, rectangular and circular microchannels of $d_h \leq 1$ mm. It was developed accounting for different flow regimes, including Taylor, annular and wavy flows.

$$\varepsilon_{xio} = \frac{C' \cdot \varepsilon_{hom}^{0.5}}{1 - (1 - C') \cdot \varepsilon_{hom}^{0.5}} \quad (9.3)$$

$$C' = \frac{0.266}{1 + 13.8 \cdot \exp(-0.00688d_h)} \quad (9.4)$$

It can be observed in Figure 9.21 that ε_{xio} underestimates ε_{exp} , especially for Taylor flows. The most probable reason is the previously mentioned non-instantaneous reaching of VLE void fraction conditions after the T-junction. The qualitative trend of ε_{xio} with T_{rel} is in agreement with the ε_{exp} of annular flows, though.

A considerable amount of studies of adiabatic Taylor-like flows in microchannels (de Loos et al, 2010; Serizawa et al, 2002; Yue et al, 2008) have reported linear relationships of ε_{exp} with ε_{hom} , in agreement with Armand-like correlations (Armand, 1946; Ali et al, 1993). In these correlations, the ratio of ε_{exp} to ε_{hom} was in the order of 0.8. To some extent, the present results in Taylor flow might as well indicate a linear relationship between both void fractions, despite the higher ε_{exp} than ε_{hom} .

9.5 Hydrodynamics of Taylor flow

Segmented flows, including Taylor flow, are among the most interesting flow regimes in multiphase microscale engineering, due to their broad range of applications and to their already identified advantages (Shui et al, 2007b; Günther and Jensen, 2006). Their mechanisms of formation are more complex than those of stratified regimes, and have been extensively studied in microfluidic T-junctions both experimentally (e.g. Thorsen et al, 2001; Guillot and Colin, 2005) and numerically (e.g. Steegmans et al, 2009; Gupta and Kumar, 2009; Liu and Zhang, 2009; de Menech et al, 2008; Garstecki et al, 2006), as well as in other systems such as microflows (e.g. Marre et al, 2009) and solvent-antisolvent systems (e.g. Lee et al, 2008). Besides, three main regimes of formation of bubbles have been identified as squeezing, dripping and jetting (de Menech et al, 2008).

A neat and concise description of these regimes and a complete discussion of previous related works is offered by Steegmans et al (2009). According to the literature, these formation regimes are mainly related to the Capillary number, Ca , of the continuous (liquid) phase. The squeezing regime is characteristic of lower Ca and the jetting regime of higher Ca . Altogether, the characterisation of segmented flows and the identification of their hydrodynamics become challenging tasks of great interest.

Taylor flow has been characterised in the present study, and the resulting average velocities (Sect. 9.5.1), elongation rates, and frequencies of generation (Sect. 9.5.2) of liquid plugs, as well as the jet entrainments (Sect. 9.5.3) are presented here against T_{rel} (Eq. (9.1)), for both sets of fluids and for the different operating pressures. As a consequence of the extremely high ratio of bubbles length to liquid plugs length obtained in some experiments, especially at high temperatures where the length of the bubbles exceeded many times the visualised area in the microscope, the liquid plugs have been considered for the analysis of the hydrodynamics of Taylor flow. Otherwise, characterizing the gas bubbles would have implied important inaccuracies in the results.

The experiments in which Taylor flow was the obtained regime are scarce, in particular for CO₂-EtOH, so are the data points in the next figures. Therefore, the analysis of the results such as identifying the effect of pressure or comparing both sets of fluids, might not be conclusive. The available data, though, allows an approximate and significant characterization of the flows.

9.5.1 Velocity of liquid plugs

The average velocity of the liquid plugs, U_{lp} , in the visualized section of the channel, calculated with equation (8.4), is depicted in Figure 9.22. The effect of increasing the relative temperature in the velocity is evident, with a similar trend for both sets of fluids. In the vicinity of the bubble point temperature, though, U_{lp} is not as dramatically affected by temperature variations as the other hydrodynamic parameters. In general, the velocity is doubled from $T_{rel} \approx 0$ to $T_{rel} \approx 0.75$. Despite the few pressure data available for comparison, no obvious effect of pressure on U_{lp} has been observed. This is rather surprising because remarkably higher velocities were expected with pressure increments, according to increased volumetric flow rates delivered by the syringe pump.

A decrease in the velocity of the fluid-fluid interfaces as they travelled along the channel, was observed. However, this decrease is not studied in detail here, even though it certainly affected the bubbles and liquid plugs downwards the channel.

9.5.2 Elongation rate and frequency of generation of liquid plugs

Together with the continuous decrease of the average velocity of bubbles, a variation in the length of liquid plugs as they travelled along the channel was also observed. This length variation was measured in the form of a dimensionless elongation rate, θ , given in equation (8.6) and plotted in Figure 9.23. The positive values of θ suggest an elongation

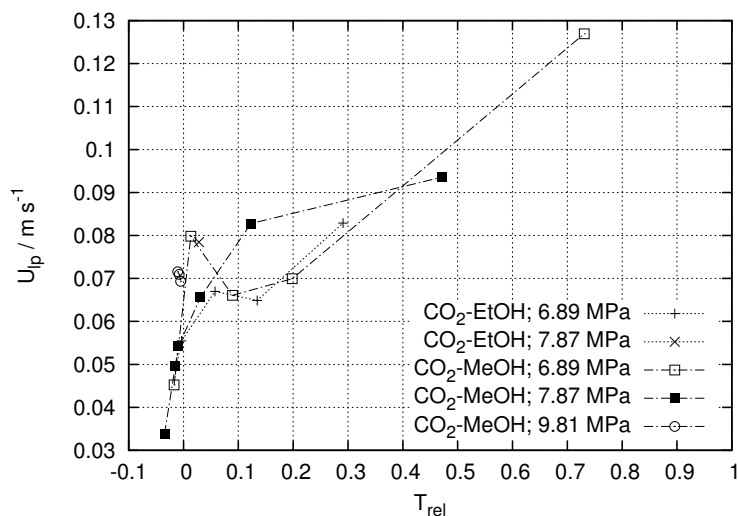


Figure 9.22: Average velocity of liquid plugs, U_{lp} , of Taylor flow for CO_2 -EtOH and CO_2 -MeOH at 6.89 MPa, 7.87 MPa and 9.81 MPa, against the relative temperature, T_{rel} .

of the liquid plugs together with a shrinkage of the bubbles along the channel, under all experimental conditions. It can be seen that all series of experiments experience an initial sharp decrease near the bubble temperature and reach minima at $T_{rel} \approx 0.1$ – 0.2 . Then there is an increase up to values around 0.1.

The length of bubbles depends mainly on the phenomena occurring in the region where both fluids meet, due to the predominance of surface tension (Hessel et al, 2005; van Steijn et al, 2007). Accordingly, given the positive values of θ , the coalescence of bubbles and the bubble-train flow, previously reported in adiabatic (Chen et al, 2002; Dreyfus et al, 2003; Yue et al, 2008) and non-adiabatic (Revellin et al, 2006, 2008) studies, are not expected to occur here downwards the channel.

The elongation of liquid plugs can be explained by two mechanisms. The difference between the volumetric fraction when both fluids join in the T-junction and the void fraction at VLE conditions is especially large at low temperatures (Fig. 9.21). Thus, in that region the prevalent mechanism is the progressive absorption of CO_2 into the liquid phase along the channel to reach VLE compositions. The gap between $\%v/v_{CO_2}$ and ε_{hom} decreases sharply as temperature increases, so does the absorption of CO_2 and the elongation of liquid plugs. This trend is reverted at $T_{rel} > 0.1$ – 0.2 when the previous decrease in absorption of CO_2 is offset by a second mechanism related to the frequency of generation of liquid plugs, f_{lp} . Figure 9.24 shows how f_{lp} experiences a sharp decrease as T_{rel} increases in all series of experiments, with an inflection point in the system behaviour at $T_{rel} \approx 0.1$ – 0.2 , from larger to smoother gradients of f_{lp} . Above that inflection point f_{lp} is small, and there is time enough after a plug for a liquid layer to build up along the channel wall. When the next liquid plug is generated, it gathers

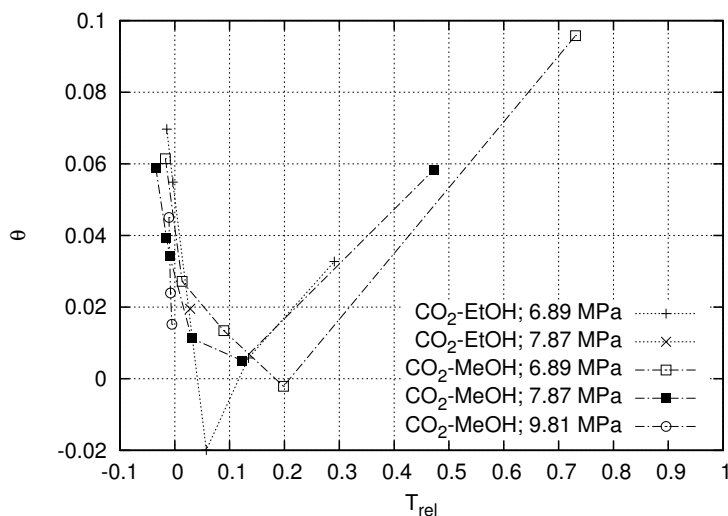


Figure 9.23: Rate of elongation, θ , of liquid plugs of Taylor flow for CO_2 -EtOH and CO_2 -MeOH at 6.89 MPa, 7.87 MPa and 9.81 MPa, against the relative temperature, T_{rel} .

the liquid in the layer as it passes through, progressively increasing its length.

9.5.3 Dimensionless jet entrainment

Most of the Taylor flows obtained in this work clearly showed a jetting regime (Figs. 9.7a–9.7b). Unfortunately, an accurate analysis of the relationship between this regime of formation of bubbles and Ca , previously mentioned in this section, was not possible due to the lack of flow velocity measurements in the T-junction (see Sect. 8.3) and of interface tension data of the CO_2 -MeOH mixture (see Sect. 7.2.4).

Alternatively, the distance between the T-junction and the position where the liquid plugs were generated was measured, and the dimensionless jet entrainment, ι , of Taylor flow was calculated with Eq. (8.8). The results of ι are shown in Figure 9.25. As with the other hydrodynamic parameters, the dependency of ι with pressure is negligible, and the results for both sets of fluids are similar. Very large values of ι and high dependency of temperature are typical at temperatures close to the bubble point, reaching an inflection point at $T_{rel} \approx 0.1$ – 0.2 with minimum values of $\iota \approx 5$. The jet entrainment is then stabilised, with slightly positive gradients of ι with T_{rel} . These long jet entrainments obtained prove the jetting regime of generation of bubbles on most of the present Taylor flows, thus denoting relative importance of viscous and inertial forces. In the vicinity of the inflection region though, the low values of ι might indicate squeezing or dripping regimes. On the other hand, the extremely long values of ι in the vicinity of the bubble point, imply the possibility that some flow regimes might be developed away from the visualization area.

9.5. Hydrodynamics of Taylor flow

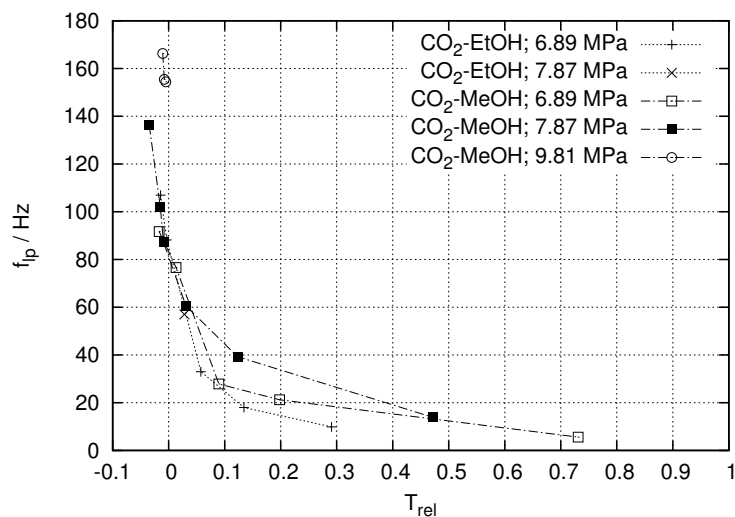


Figure 9.24: Frequency of generation, f_{ip} , of liquid plugs of Taylor flow for CO_2 -EtOH and CO_2 -MeOH at 6.89 MPa, 7.87 MPa and 9.81 MPa, against the relative temperature, T_{rel} .

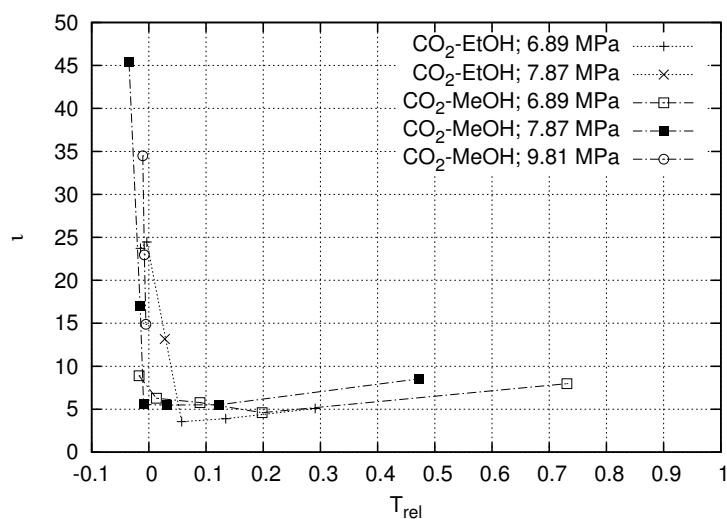


Figure 9.25: Dimensionless jet entrainment, ν , of Taylor flow for CO_2 -EtOH and CO_2 -MeOH at 6.89 MPa, 7.87 MPa and 9.81 MPa, against the relative temperature, T_{rel} .

9.5.4 Conclusions

Overall, from the present analysis the temperature, and by extension the vaporisation conditions of the system (see Sect. 9.4), can be identified as the main agent affecting the hydrodynamics of Taylor flows, with a common inflection point in the behaviour of most of the results at $T_{rel} \approx 0.1-0.2$. On the other hand, both sets of fluids showed very similar hydrodynamics, which is coherent with the resemblance in the phase behaviour of both mixtures, and in the physical and transport properties of both liquid phases (See Figs. 7.4 and 7.7). Finally, the effect of pressure was mostly negligible, and no differences were observed when using CO₂ in gas or supercritical state.

Concluding remarks

Contents

10.1 Overall conclusions	139
10.2 Future directions	141

This final chapter gathers the overall conclusions that can be extracted from the study conducted in the Part II of the thesis (Sect. 10.1), taking into account the main objectives that were proposed initially. Finally, the suggestions for future work directions are listed in Section 10.2.

10.1 Overall conclusions

The behaviour of two-phase flow of miscible fluids in microchannels, with one of the fluids in gas or in supercritical conditions, has been analysed here. Accordingly, two sets of fluids, CO₂-ethanol and CO₂-methanol, which are fully miscible when they are in liquid state, have been experimentally investigated in a non-adiabatic microfluidic T-junction with a semicircular cross-section. Under the pressure, temperature and CO₂ mass fraction conditions considered, the alcohols were in liquid state and the CO₂ was either in liquid, gas or supercritical state. Therefore, their mixtures were in single phase, or in Vapour-Liquid Equilibrium (VLE) with two separated phases. The present work has been presented as a supplement to the usual studies of two-phase flows of immiscible fluids in adiabatic conditions, and of single boiling fluids in non-adiabatic conditions.

The use of Rhodamine B as a fluorescent dye with the mixtures, in order to visualize the two-phase flows in the microscope with a Fluorescence contrast technique, proved to be infeasible. Rhodamine B, initially dissolved in the alcohol, precipitated as soon as it reached contact with CO₂, most probably due to a low solubility of the dye in CO₂. As a consequence, the intensity of fluorescence in the liquid phase was very low, the quality of the recorded images was poor and the identification of the flow regimes was very inaccurate. Also, at moderate-to-high pressure and temperature conditions, the dye experienced a series of phenomena that have been interpreted as the result of its degradation.

Taylor, annular and wavy were the two-phase flow regimes observed, with predominance of annular flow at higher pressures and temperatures, and of Taylor flow at lower

pressures and temperatures. Flow regime maps for both mixtures of fluids were provided. Unlike the usual tendency of representing the maps against the superficial velocities of liquid and vapour phases, here the maps were represented against the pressure and temperature conditions, for the VLE conditions could be properly identified.

Taylor flows showed a jetting regime of generation, given their large dimensionless jet entrainments. Also, a sharp decrease in their frequency of plug generation with relative temperature, resulted in extremely long gas bubbles at the higher temperatures. A continuous elongation of the liquid plugs was obtained throughout all experimental conditions and, therefore, no coalescence of bubbles or bubble-train flow were expected. An inflection point in the behaviour of all these parameters occurred at relative temperatures around 0.1 to 0.2, close to the bubble point temperature, moving from highly pronounced gradients with temperature to smoother gradients, as temperature exceeded the inflection point.

In single phase, the flows were classified into three different groups: standard single-phase flows (liquid-liquid and supercritical-liquid), “pseudo” two-phase flows and local phenomena in the T-junction. Taylor, stratified (smooth) and wavy were the observed “pseudo” two-phase flows, with predominance of stratified flow. The local phenomena were only present at high temperatures, and consisted on a liquid meniscus in the T-junction and boiling, which could be observed together with the meniscus and the “pseudo” wavy flow. Flow regime maps were also provided for these flows, represented against pressure and temperature.

A dynamic phenomenon was found in most of VLE conditions for both sets of fluids, consisting of a continuous accumulation of liquid either in the CO₂ channel before the T-junction or at the CO₂-side wall after the T-junction. The liquid accumulation was found from temperatures slightly above the bubble point until $T \approx 10$ K to 20 K below the dew point. This accumulation periodically blocked the channel and was followed by ejection of several liquid plugs downwards, causing a transient instability that disturbed the whole flow. Four different stages were proposed to constitute the phenomenon. The capillary and wetting effects due to Marangoni stresses generated by local temperature and concentration gradients in the liquid, were analysed and suggested as the most probable causes of the phenomenon. The low values of Capillary and Weber numbers explained why the liquid accumulation was not dragged by the CO₂ stream before blocking the channel and ejecting the liquid plugs.

From the study of two-phase void fractions, extremely high vaporisation values were observed throughout most of the operating conditions, starting around 3 K to 5 K above the bubble point temperature, for both sets of fluids. The homogeneous void fraction quickly reached values of around 0.9 to 0.97 and of 0.8 for CO₂-EtOH and CO₂-MeOH respectively, at relative temperatures below 0.1. The excess of experimental to homogeneous void fraction values with Taylor flows, suggested the possibility that the flow did not reach thermodynamic equilibrium in the visualised area in these cases. This possibility is strengthened by the similar values between the experimental void fraction

and the initial volumetric ratio at which both fluids reach the T-junction, before the mixing begins. However, the qualitative trend of the experimental void fractions agreed with Armand-like correlations in the case of Taylor flow, and with the correlation of [Xiong and Chung \(2007\)](#) in the case of annular and wavy flows.

Overall, in the present work no different two-phase flows than those already reported in the literature were obtained with the CO₂ in supercritical state. From the analysis of the two-phase void fractions and of the hydrodynamics of Taylor-like flows, it can be concluded that pressure and CO₂ state played a minor role in the results. Also, both sets of fluids experienced very similar results, mostly due to the high content of CO₂ in the liquid phase as well as in the gas phase, which balanced the physical and transport properties of both mixtures, CO₂-EtOH and CO₂-MeOH. On the other hand, the system turned to be extremely dependent on temperature, especially at low temperatures, close to the bubble point. Besides, most of the series of results at different pressures and mixtures, based on relative temperature, showed qualitative and quantitative agreement. This makes temperature a determinant condition in the system. The increased dependency on temperature close to the bubble point seems to be caused by the sudden vaporisation rates shown in the VLE in that region, and by the proximity of the pseudocritical point line of CO₂, which results in highly sensitive properties of CO₂ with temperature.

10.2 Future directions

Obviously, as the experimentation and further analysis were underway, new ideas for further work arose. These were extended when the final results were obtained and the objectives of the study were accomplished, especially the main one which was demonstrating the feasibility of two-phase flows with miscible fluids and in supercritical conditions. As a result, a bunch of many possibilities for future work arises now, and few of them are listed hereby.

The first list is related to the experimental facility and the data analysis techniques,

- The current limitations of the setup precluded the control and monitoring of the flow rate and of the feed ratio of fluids, and the monitoring of the pressure in the vicinity of the T-junction. Improving the performance of the experimental setup to avoid these restrictions is suggested. The possible improvements include the following. A secondary syringe pump connected in series with the first one might be a solution for achieving constant fluid flow rate. The control and monitoring of the feed ratio of fluids can be achieved with a control valve and a flow meter in both the CO₂ and the alcohol feed lines. Placing two pressure transducers, one before the chip and the second after the chip, would allow a more accurate estimation of the pressure conditions of the fluids in the T-junction.
- The heating mechanism of the chip was also subjected functional limitations. The

design and fabrication of a new chip with embedded heaters and temperature sensors would result in a higher homogeneity of heat distribution and a more accurate control and monitoring of the temperature of the fluids.

- Replace the present microfluidic chip by another chip with a simpler and shorter channel network. The fluidic resistor might be replaced by a discharge valve after the chip. The accuracy of the measurement of pressure conditions within the channel would be improved.
- Improve the accuracy of the calculation of the experimental void fraction, by adopting any of the available techniques available in the literature. Automate the identification of the fluid-fluid interfaces during Taylor two-phase flows, by using any of the software alternatives for processing image data (they were currently identified manually).

Once the technical limitations are overcome, the following list includes a few number of the possible research directions,

- Replace the T-junction by a straight channel. Several of the present results suggest the possibility that the working mixtures did not reach complete VLE conditions, with both phases saturated, along the visualized channel after the T-junction. This situation can be avoided by allowing both fluids to mix completely before reaching the experimental heated section of the channel. In this way, when the working mixture experiences VLE both separated phases are already saturated.
- Focus on a detailed analysis of the unexpected phenomenon of liquid accumulation experienced in the present work. The scope of the phenomenon should be ascertained, especially the range of conditions where the phenomenon is able to block the channel and generate liquid plugs that disturb the flow. The stages proposed to constitute the phenomenon should also be properly identified and corroborated. Although several causes of the phenomenon have been proposed, and these are coherent, their feasibility has been calculated based on vague assumptions. A more rigorous analysis should be conducted, then. Last but not least, ways to avoid this disturbing accumulation should be found.
- Decrease the CO₂/alcohol feed ratio so the role of the alcohols would be strengthened. In this way, also the vaporisation of the mixtures in VLE as temperature increases would be much softer, thus avoiding the extremely sensitive conditions of the system near the bubble point due to the quick vaporisation. Finally, the tunable properties of supercritical CO₂ would also see their role strengthened and, if the mass fraction of CO₂ was kept at $v_{CO_2} > 0.5$ to 0.6, the pseudocritical point of CO₂ would still be close to the bubble point.
- Change the present working procedure during the experiments, where the temperature was increased a fixed pressure and feed ratio of fluids. The suggestion is to

10.2. Future directions

143

keep the pressure and temperature constant while the feed ratio is changed during the experiments. In this way, the properties of the fluids and the saturated phases in VLE would remain constant in each series of experiments, and the results could be plotted against the usual homogeneous void fraction, the vapour quality or the velocities of the liquid and vapour phases, instead of being plotted against the temperature and pressure.

- Use a different cross-sectional geometry of the channel. Both the more standard circular or rectangular geometries are good candidates.
- Extend the present results with the analysis of two-phase pressure drop along the channel, and of critical heat flux. Pressure drop is commonly addressed in adiabatic and boiling two-phase flow literature, whereas critical heat flux is one of the main concerns of boiling two-phase flow literature.

UNIVERSITAT ROVIRA I VIRGILI

NUMERICAL AND EXPERIMENTAL ANALYSES OF SINGLE AND TWO-PHASE MICROFLUIDIC FLOWS WITH IMPLICATIONS IN MICROREACTORS

Roland Blanch Ojea

DL:T. 149-2012

Part III

Appendices

UNIVERSITAT ROVIRA I VIRGILI

NUMERICAL AND EXPERIMENTAL ANALYSES OF SINGLE AND TWO-PHASE MICROFLUIDIC FLOWS WITH IMPLICATIONS IN MICROREACTORS

Roland Blanch Ojea

DL:T. 149-2012

Vapor-Liquid Equilibrium data from literature

Contents

A.1 VLE data for CO₂-EtOH	147
A.2 VLE data for CO₂-MeOH	152
A.3 Critical locus data for CO₂-EtOH and CO₂-MeOH	155

The present appendix includes the VLE and critical locus data for CO₂-EtOH and for CO₂-MeOH, used in Part II, obtained from different literature sources.

A.1 VLE data for CO₂-EtOH

The following tables contain the VLE data for CO₂-EtOH, including P , x_{eq,CO_2} and y_{eq,CO_2} at different temperatures. Data from [Secuianu et al \(2008\)](#) at 293.15 K, 303.15 K and 353.15 K (Table A.1), from [Tian et al \(2001\)](#) at 353.15 K, 410.15 K and 450.15 K (Table A.2). from [Joung et al \(2001\)](#) at 313.40 K, 322.50 K, 338.80 K and 344.75 K (Table A.3), from [Jennings et al \(1991\)](#) at 325.20 K (Table A.4), from [Suzuki et al \(1990\)](#) at 333.40 K (Table A.5), from [Galicia-Luna et al \(2000\)](#) at 348.40 K and 373.00 K (Table A.6), and from [Mendoza de la Cruz and Galicia-Luna \(1999\)](#) at 391.96 K (Table A.7), were used. The data corresponding to critical conditions of the mixture is properly marked with (^e).

148 **Appendix A. Vapor-Liquid Equilibrium data from literature**

Table A.1: VLE data for CO_2 -EtOH from *Secuianu et al (2008)*

P/MPa	x_{eq,CO_2}	y_{eq,CO_2}	P/MPa	x_{eq,CO_2}	y_{eq,CO_2}
$T = 293.15 \text{ K}$					
0.68	0.0497	0.9879	3.54	0.3062	0.9983
1.67	0.1315	0.9950	4.62	0.4870	0.9978
2.14	0.1692	0.9967	5.15	0.6977	0.9983
2.87	0.2417	0.9978	5.27	0.8071	0.9983
$T = 303.15 \text{ K}$					
0.91	0.0596	0.9870	5.89	0.5628	0.9934
2.03	0.1362	0.9945	6.04	0.5989	0.9927
2.89	0.2014	0.9967	6.49	0.8821	0.9918
4.00	0.2978	0.9960	6.52	0.9125	0.9917
4.90	0.3889	0.9951			
$T = 353.15 \text{ K}$					
0.52	0.0187	0.7819	7.48	0.2948	0.9703
1.45	0.0596	0.8933	7.97	0.3185	0.9704
3.00	0.1096	0.9464	8.53	0.3439	0.9692
4.15	0.1536	0.9604	9.55	0.4077	0.9650
5.27	0.2037	0.9656	10.08	0.4359	0.9610
6.42	0.2471	0.9695	11.08	0.4951	0.9471

Table A.2: VLE data for CO_2 -EtOH from *Tian et al (2001)*

P/MPa	x_{eq,CO_2}	y_{eq,CO_2}	P/MPa	x_{eq,CO_2}	y_{eq,CO_2}
$T = 353.15 \text{ K}$					
12.00	0.5714	0.9510	13.10 ^c	0.8800	0.8800
13.00	0.6956				
$T = 410.15 \text{ K}$					
6.50	0.1721	0.9163	10.20	0.2959	0.8702
8.00	0.2195	0.8932	14.50	0.4983	0.7854
9.50	0.2616	0.8866			
$T = 450.15 \text{ K}$					
4.00	0.0726	0.4777	12.00	0.3256	0.5880
7.00	0.1510	0.5610	12.60	0.3594	0.5901
10.20	0.2469	0.5760			

^c Critical values

Table A.3: VLE data for CO₂-EtOH from Joung et al (2001)

P/MPa	x_{eq,CO_2}	y_{eq,CO_2}	P/MPa	x_{eq,CO_2}	y_{eq,CO_2}
$T = 313.40 \text{ K}$					
0.57	0.0337	0.9614	7.66	0.7619	0.9824
2.59	0.1456	0.9880	7.94	0.9293	0.9799
3.38	0.1937	0.9892	8.04	0.9451	0.9738
4.35	0.2564	0.9903	8.11	0.9568	0.9672
5.44	0.3401	0.9899	8.16 ^c	0.9630	0.9630
7.34	0.6253	0.9849			
$T = 322.50 \text{ K}$					
0.57	0.0302	0.9406	8.46	0.6091	0.9753
2.56	0.1272	0.9804	8.79	0.7056	0.9704
3.81	0.1908	0.9844	8.98	0.7878	0.9645
4.85	0.2514	0.9853	9.14	0.9162	0.9470
5.86	0.3180	0.9855	9.18	0.9192	0.9297
7.74	0.4887	0.9809	9.21 ^c	0.9198	0.9198
$T = 338.80 \text{ K}$					
0.61	0.0269	0.8866	10.39	0.5869	0.9507
2.68	0.1097	0.9630	10.87	0.6691	0.9295
3.68	0.1513	0.9692	11.16	0.7364	0.9030
4.79	0.2005	0.9723	11.17	0.7554	0.8938
6.02	0.2666	0.9733	11.24	0.7756	0.8861
7.92	0.3685	0.9718	11.28	0.8596	0.8713
9.79	0.5154	0.9598	11.31 ^c	0.8601	0.8601
$T = 344.75 \text{ K}$					
0.80	0.0307	0.8727	10.27	0.5024	0.9523
2.83	0.1082	0.9543	11.40	0.6346	0.9252
3.88	0.1492	0.9617	11.63	0.6720	0.9076
6.03	0.2448	0.9678	11.90	0.7734	0.8494
7.06	0.2941	0.9679	11.93	0.8008	0.8068
9.28	0.4253	0.9614	11.97 ^c	0.8020	0.8020

^c Critical values

150 **Appendix A. Vapor-Liquid Equilibrium data from literature**

Table A.4: VLE data for CO_2 -EtOH from *Jennings et al (1991)*

P/MPa	x_{eq,CO_2}	y_{eq,CO_2}	P/MPa	x_{eq,CO_2}	y_{eq,CO_2}
$T = 325.20 \text{ K}$					
6.27	0.3330	0.9870	8.59	0.5680	0.9800
6.90	0.3790	0.9860	8.83	0.6050	0.9760
7.26	0.4110	0.9850	9.20	0.7020	0.9670
7.63	0.4460	0.9840	9.35	0.7750	0.9640
8.36	0.5270	0.9820			

Table A.5: VLE data for CO_2 -EtOH from *Suzuki et al (1990)*

P/MPa	x_{eq,CO_2}	y_{eq,CO_2}	P/MPa	x_{eq,CO_2}	y_{eq,CO_2}
$T = 333.40 \text{ K}$					
0.54	0.0200	0.9050	7.53	0.3720	0.9790
0.99	0.0380	0.9470	9.02	0.4940	0.9720
2.11	0.0880	0.9720	9.95	0.6100	0.9540
3.03	0.1290	0.9780	10.52	0.7260	0.9340
4.04	0.1690	0.9810	10.58	0.7630	0.9230
4.99	0.2170	0.9820	10.65	0.8170	0.9080
6.09	0.2780	0.9810			

Table A.6: VLE data for CO_2 -EtOH from *Galicia-Luna et al (2000)*

P/MPa	x_{eq,CO_2}	y_{eq,CO_2}	P/MPa	x_{eq,CO_2}	y_{eq,CO_2}
$T = 348.40 \text{ K}$					
1.52	0.0576	0.9176	10.61	0.5193	0.9425
3.52	0.1391	0.9606	12.00	0.6718	0.9003
5.52	0.2213	0.9618	12.30	0.7273	0.8851
7.63	0.3285	0.9599	12.46 ^c	0.7980	0.7980
$T = 373.00 \text{ K}$					
2.18	0.0649	0.8827	12.02	0.4790	0.9120
4.22	0.1350	0.9165	12.82	0.5303	0.8980
6.15	0.2054	0.9328	14.11	0.6593	0.8297
9.17	0.3358	0.9161	14.35 ^c	0.7181	0.7181

^c Critical values

Table A.7: *VLE data for CO₂-EtOH from Mendoza de la Cruz and Galicia-Luna (1999)*

P/MPa	x_{eq,CO_2}	y_{eq,CO_2}	P/MPa	x_{eq,CO_2}	y_{eq,CO_2}
$T = 391.96 \text{ K}$					
1.28	0.0284	0.6672	10.32	0.3328	0.8833
3.00	0.0820	0.7934	12.00	0.4148	0.8738
4.62	0.1341	0.8470	14.08	0.5394	0.8312
5.99	0.1798	0.8644	14.60	0.5962	0.8044
7.90	0.2445	0.8738			

A.2 VLE data for CO₂-MeOH

The following tables contain the VLE data for CO₂-MeOH, including P , x_{eq,CO_2} and y_{eq,CO_2} at different temperatures. Data from [Ohgaki and Katayama \(1976\)](#) at 298.15 K and 313.15 K (Table A.8), from [Leu et al \(1991\)](#) at 352.60 K and 394.20 K (Table A.9), from [Bezanehtak et al \(2002\)](#) at 308.15 K (Table A.10), from [Joung et al \(2001\)](#) at 320.15 K, 330.15 K, 335.65 K and 342.80 K (Table A.11), and from [Brunner et al \(1987\)](#) at 298.15 K, 323.15 K, 373.15 K, 423.15 K and 473.15 K (Table A.12), were used. The data corresponding to critical conditions of the mixture is properly marked with (^c).

Table A.8: VLE data for CO₂-MeOH from [Ohgaki and Katayama \(1976\)](#)

P/MPa	x_{eq,CO_2}	y_{eq,CO_2}	P/MPa	x_{eq,CO_2}	y_{eq,CO_2}
$T = 298.15 \text{ K}$					
0.79	0.0596				
$T = 313.15 \text{ K}$					
0.58	0.0285	0.9363	6.27	0.4201	0.9880
1.77	0.1023	0.9774	7.09	0.5429	0.9866
3.00	0.1641	0.9847	7.70	0.6892	0.9840
4.09	0.2339	0.9868	8.06	0.8970	0.9748
5.71	0.3655	0.9882			

Table A.9: VLE data for CO₂-MeOH from [Leu et al \(1991\)](#)

P/MPa	x_{eq,CO_2}	y_{eq,CO_2}	P/MPa	x_{eq,CO_2}	y_{eq,CO_2}
$T = 352.60 \text{ K}$					
0.79	0.0188	0.7543	11.36	0.4228	0.9228
2.16	0.0627	0.8926	12.67	0.5272	0.8874
4.54	0.1417	0.9339	13.47	0.6278	0.8608
7.68	0.2533	0.9423	13.53 ^c	0.6455	0.6455
$T = 394.20 \text{ K}$					
1.06	0.0099	0.3331	13.90	0.3697	0.7886
2.70	0.0435	0.6586	15.31	0.4474	0.7594
3.68	0.0672	0.7452	16.29	0.5479	0.6611
6.00	0.1246	0.8190	16.49 ^c	0.6019	0.6019
10.03	0.2308	0.8409			

^c Critical values

A.2. VLE data for CO₂-MeOH

Table A.10: VLE data for CO₂-MeOH from *Bezanehtak et al (2002)*

P/MPa	x_{eq,CO_2}	y_{eq,CO_2}	P/MPa	x_{eq,CO_2}	y_{eq,CO_2}
$T = 308.15 \text{ K}$					
1.54	0.0903	0.9838	6.63	0.4904	0.9891
2.50	0.1467	0.9863	6.97	0.5798	0.9890
3.55	0.2074	0.9855	7.26	0.7799	0.9828
4.58	0.2742	0.9867	7.43	0.8869	0.9575
5.62	0.3622	0.9890			

Table A.11: VLE data for CO₂-MeOH from *Joung et al (2001)*

P/MPa	x_{eq,CO_2}	y_{eq,CO_2}	P/MPa	x_{eq,CO_2}	y_{eq,CO_2}
$T = 320.15 \text{ K}$					
0.60	0.0326	0.9150	8.62	0.6757	0.9662
2.69	0.1371	0.9717	8.85	0.8053	0.9484
3.70	0.1913	0.9778	8.88	0.8287	0.9441
5.72	0.3166	0.9815	8.93	0.8791	0.9010
6.50	0.3750	0.9804	8.95 ^c	0.8860	0.8860
8.14	0.5505	0.9738			
$T = 330.15 \text{ K}$					
0.78	0.0346	0.8857	9.42	0.5382	0.9584
2.24	0.0960	0.9537	10.22	0.6779	0.9438
3.12	0.1342	0.9610	10.48	0.7401	0.8777
5.17	0.2365	0.9717	10.55	0.7694	0.8619
6.07	0.2845	0.9725	10.57	0.8215	0.8572
8.90	0.4836	0.9647	10.59 ^c	0.8243	0.8243
$T = 335.65 \text{ K}$					
0.84	0.0336	0.8592	10.28	0.5330	0.9466
3.08	0.1208	0.9502	11.15	0.6651	0.8948
4.41	0.1768	0.9620	11.25	0.6762	0.8901
6.52	0.2760	0.9671	11.44	0.7759	0.8250
7.44	0.3247	0.9664	11.45	0.7925	0.8059
9.32	0.4471	0.9583	11.46 ^c	0.7940	0.7940
$T = 342.80 \text{ K}$					
0.67	0.0247	0.7999	11.10	0.5234	0.9312
3.13	0.1145	0.9403	11.64	0.5806	0.9108
4.20	0.1553	0.9510	12.21	0.6719	0.8526
5.23	0.1961	0.9559	12.23	0.6792	0.8498
7.37	0.2909	0.9586	12.37	0.7311	0.8026
8.40	0.3427	0.9574	12.39	0.7603	0.7720
10.41	0.4664	0.9432	12.40 ^c	0.7610	0.7610

^c Critical values

Table A.12: VLE data for CO₂-MeOH from Brunner et al (1987)

P/MPa	x_{eq,CO_2}	y_{eq,CO_2}	P/MPa	x_{eq,CO_2}	y_{eq,CO_2}	P/MPa	x_{eq,CO_2}	y_{eq,CO_2}
$T = 298.15 \text{ K}$								
1.73	0.1214		5.14	0.4729		6.23	0.9693	
1.75	0.1258		5.29	0.4957		5.88		0.9928
2.38	0.1723		5.53	0.5554		5.08		0.9929
3.02	0.2289		5.72	0.6288		3.96		0.9930
3.61	0.2792		5.75	0.6538		2.91		0.9919
4.11	0.3323		5.92	0.8097		1.97		0.9894
4.43	0.3642		5.94	0.8109		0.97		0.9812
4.85	0.4200		6.04	0.9299		0.41		0.9588
$T = 323.15 \text{ K}$								
0.99	0.0413		9.28	0.6581		7.99		0.9758
1.96	0.0946		9.32	0.6950		7.50		0.9765
2.52	0.1197		9.50	0.7293		5.96		0.9809
3.42	0.1632		9.53	0.8172		5.17		0.9796
4.75	0.2368		9.55 ^c	0.8404	0.8404	3.99		0.9792
5.98	0.3045		9.53		0.8606	2.00		0.9676
7.70	0.4344		9.47		0.9460	1.00		0.9412
8.81	0.5529		9.10		0.9628			
9.19	0.6378		8.77		0.9689			
$T = 373.15 \text{ K}$								
2.01	0.0392		15.41	0.6197		12.95		0.8870
3.81	0.0880		15.42	0.6664		11.05		0.9048
4.84	0.1185		15.42 ^c	0.6735	0.6735	10.31		0.9076
5.84	0.1445		15.42		0.6805	8.06		0.9109
8.37	0.2262		15.42		0.6959	6.62		0.9111
9.07	0.2456		15.32		0.7577	3.97		0.8820
11.74	0.3429		15.31		0.7695	2.83		0.8523
12.71	0.3968		14.06		0.8500			
14.75	0.5185		13.44		0.8727			
$T = 423.15 \text{ K}$								
3.67	0.0460		14.80	0.3529		15.60		0.6370
5.89	0.0942		15.13	0.3753		13.93		0.6974
6.95	0.1192		15.97	0.4353		10.79		0.7409
10.45	0.2033		16.08	0.4750		8.64		0.7340
11.62	0.2386		16.13 ^c	0.5178	0.5178	6.33		0.6894
12.80	0.2748		16.06		0.5684	3.81		0.5747
$T = 473.15 \text{ K}$								
7.52	0.0682		12.93 ^c	0.2700	0.2700	7.94		0.3186
10.40	0.1383		12.92		0.2880			
12.80	0.2396		10.98		0.3779			

^c Critical values

A.3 Critical locus data for CO₂-EtOH and CO₂-MeOH

Temperature and pressure data of the critical locus for CO₂-EtOH and for CO₂-MeOH, provided by [Chester \(2004\)](#), is included in Table A.13.

Table A.13: *Critical locus data for CO₂-EtOH and CO₂-MeOH from Chester (2004)*

CO ₂ - EtOH					
<i>T/K</i>	<i>P/MPa</i>	<i>T/K</i>	<i>P/MPa</i>	<i>T/K</i>	<i>P/MPa</i>
304.25	7.39	393.15	15.30	453.15	13.30
323.15	9.60	403.15	15.40	463.15	12.50
343.15	12.10	413.15	15.30	473.15	11.40
363.15	14.00	423.15	15.00	483.15	10.30
373.15	14.70	433.15	14.60	516.15	6.40
383.15	15.10	443.15	14.00		
CO ₂ - MeOH					
<i>T/K</i>	<i>P/MPa</i>	<i>T/K</i>	<i>P/MPa</i>	<i>T/K</i>	<i>P/MPa</i>
304.25	7.39	354.15	14.00	423.15	16.20
321.15	9.50	363.15	14.80	433.15	15.80
323.15	9.80	373.15	15.50	443.15	15.30
333.15	11.40	383.15	16.10	453.15	14.70
343.15	12.70	393.15	16.40	463.15	13.90
344.15	12.80	403.15	16.50	473.15	13.00
353.15	13.90	413.15	16.40	512.75	8.10

UNIVERSITAT ROVIRA I VIRGILI

NUMERICAL AND EXPERIMENTAL ANALYSES OF SINGLE AND TWO-PHASE MICROFLUIDIC FLOWS WITH IMPLICATIONS IN MICROREACTORS

Roland Blanch Ojea

DL:T. 149-2012

APPENDIX B

Velocity of the CO₂ stream in the T-junction

This appendix depicts the development of the equation for the approximate estimation of the velocity of the stream of CO₂ in the T-junction during the experiments (Eq. (8.3)). The development of the equation is based on mass and volumetric flows balance between the syringe pump and the T-junction.

First, let's simplify the flow line between the syringe pump and the T-junction as shown in the scheme of Figure B.1. Five key locations are identified and described in this scheme. Assume that the CO₂ in the sample loop ([2] in the legend) behaves as a plug flow, pumping the alcohol in the same loop ([3] in the legend) without mixing. Assume, also, that all the flow line shown in the scheme is under isobaric conditions.

According to the five key locations identified in Figure B.1, some initial relationships can be formulated:

$$\dot{m} = \dot{V} \cdot \rho \quad (\text{B.1})$$

$$\dot{m}_1 = \dot{m}_2 + \dot{m}_3 \quad (\text{B.2})$$

$$\dot{V}_3 = \dot{V}_4 \quad (\text{B.3})$$

$$\dot{m}_4 = \dot{m}_5 \quad (\text{B.4})$$

$$v_2 = \frac{\dot{m}_2}{\dot{m}_2 + \dot{m}_5} \quad (\text{B.5})$$

$$\dot{V} = A \cdot U \quad (\text{B.6})$$

Now, combining Eqs. (B.1), (B.3) and (B.4), gives,

$$\dot{m}_3 = \frac{\rho_3}{\rho_4} \cdot \dot{m}_5 \quad (\text{B.7})$$

which, combined with Eq. (B.2), gives,

$$\dot{m}_1 = \frac{\rho_3}{\rho_4} \cdot \dot{m}_5 + \dot{m}_2 \quad (\text{B.8})$$

which, combined with Eq. (B.5), gives,

$$\dot{m}_1 = \left[1 + \frac{\rho_3}{\rho_4} \cdot \left(\frac{1}{v_2} - 1 \right) \right] \cdot \dot{m}_2 \quad (\text{B.9})$$

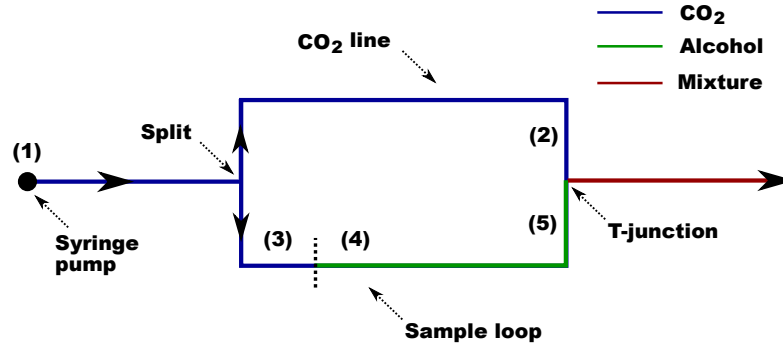


Figure B.1: Simplified sketch of the flow line of the setup, from the syringe pump to the T-junction. Legend: [1] Syringe pump with CO₂ at room temperature; [2] Channel of CO₂ in the T-junction at experimental temperature; [3] Portion of the sample loop filled with CO₂ at room temperature; [4] Portion of the sample loop filled with alcohol at room temperature; [5] Channel of alcohol in the T-junction at experimental temperature. The colours indicate which fluid fills each section: blue for CO₂, green for alcohol, and red for the mixture of CO₂-alcohol.

and finally, combining with Eqs. (B.1) and (B.6), results in,

$$U_2 = \frac{\rho_1}{[1 + \rho_3/\rho_4 \cdot (1/v_2 - 1)] \rho_2} \frac{\dot{V}_1}{A} \quad (\text{B.10})$$

The Equation (B.10), applied to the experimental system working with the corresponding set of fluids, results in the already formulated Equation (8.3):

$$U_{CO_2} = \frac{\rho_{o,CO_2}}{[1 + \rho_{o,CO_2}/\rho_{o,alc} \cdot (1/v_{CO_2} - 1)] \rho_{CO_2}} \frac{\dot{V}_o}{A} \quad (\text{B.11})$$

Nomenclature

Roman Symbols

A	Cross-sectional area of the channel (m^2)
a	Arrhenius pre-exponential factor of reaction ($\text{m}^4 \text{kmol}^{-1} \text{s}^{-1}$)
b	Pixel resolution of images (pixel m^{-1})
C	Molar concentration (kmol m^{-3})
C'	Correlation parameter (-)
c_p	Heat capacity at constant pressure ($\text{J kg}^{-1} \text{K}^{-1}$)
D	Mass binary diffusivity ($\text{m}^2 \text{s}^{-1}$)
d	Diameter (m)
D_{eff}	Mass effective diffusivity ($\text{m}^2 \text{s}^{-1}$)
d_h	Hydraulic diameter of the channel (m)
e_i	Energy flux across the i^{th} surface (W m^{-2})
Ea	Activation energy of reaction (J kmol^{-1})
f	Frequency (Hz)
fr	Camera frame rate (Hz)
g	Gravity constant (m s^{-2})
G_d	Vaporised mass diffusion fraction (-)
G^o	Standard Gibbs free energy (J kg^{-1})
$\Delta\bar{G}^o$	Standard molar Gibbs free energy of reaction (J kmol^{-1})
H	Enthalpy (J kg^{-1})
H	Height (m)
ΔH_{mix}	Enthalpy change of mixing (J kg^{-1})
$\Delta\bar{H}^o$	Standard molar enthalpy of reaction (J kmol^{-1})
$H_{f,\alpha}$	Enthalpy of formation of species α (J kg^{-1})

\mathbf{j}_α	Molecular mass flux vector of species α ($\text{kg m}^{-2} \text{s}^{-1}$)
$j_{\alpha,i}$	Molecular mass flux component of species α in the i^{th} direction ($\text{kg m}^{-2} \text{s}^{-1}$)
k''	Specific rate constant for heterogeneous reaction of order n ($\text{kmol}^{1-n} \text{m}^{3n-2} \text{s}^{-1}$)
$K_{eq,p}$	Pressure equilibrium constant of reaction ($\text{Pa}^{\text{st}_{\text{products}} - \text{st}_{\text{reagents}}}$)
$K_{eq,p}^o$	Standard pressure equilibrium constant of reaction (-)
L	Length (m)
l_i	Direction normal to the i^{th} plane (m)
M	Molecular weight (kg kmol^{-1})
m	Mass (kg)
\dot{m}	Mass flow rate (kg s^{-1})
\bar{M}	Molar mean molecular weight of solution (kg kmol^{-1})
N	Number of chemical species. Number of liquid plugs (-)
\mathbf{n}_α	Combined mass flux vector of species α ($\text{kg m}^{-2} \text{s}^{-1}$)
$n_{\alpha,i}$	Combined mass flux component of species α in the i^{th} direction ($\text{kg m}^{-2} \text{s}^{-1}$)
\tilde{N}	$= 6.02214 \times 10^{26}$. Avogadro's number (molecules kmol^{-1})
P	Pressure (MPa)
p	Pressure (Pa)
p_α	Partial pressure of specie α (Pa)
p^o	$= 1 \text{ bar} \approx 10^5 \text{ Pa}$. Standard pressure (Pa)
Δpx	Pixel distance within an image or between images (pixel)
\mathbf{q}	Heat flux vector (W m^{-2})
q_i	Heat flux component in the i^{th} direction (W m^{-2})
R	Gas constant ($\text{J kg}^{-1} \text{K}^{-1}$)
r	Reaction rate ($\text{kmol m}^{-2} \text{s}^{-1}$)
R^2	Coefficient of determination (-)

Nomenclature

161

S	Entropy ($\text{J kg}^{-1} \text{K}^{-1}$)
Sp	Production source term ($\text{kg m}^{-3} \text{s}^{-1}$)
st	Stoichiometric coefficient (-)
T	Temperature (K)
t	Time (s)
T''	Temperature parameter for transport properties of mixtures (-)
T_{sh}	Temperature parameter for the Shomate equation (-)
U	Velocity. Absolute velocity. Superficial velocity (m s^{-1})
U_a	Actual velocity (m s^{-1})
u, v, w	Velocity components (m s^{-1})
V	Volume (m^3)
\dot{V}	Volumetric flow rate ($\text{m}^3 \text{s}^{-1}$)
\mathbf{v}	Velocity vector (m s^{-1})
v_i	Velocity component in the i^{th} direction (m s^{-1})
W	Width (m)
x	Mole fraction in liquid phase (-)
x, y, z	Cartesian coordinates (m)
y	Mole fraction in vapour phase (-)

Greek Symbols

α	Thermal diffusivity ($\text{m}^2 \text{s}^{-1}$)
χ	Vapour quality (-)
δ_{ij}	Kronecker delta (-)
δ	Unit tensor (-)
δ_i	Unit vector normal to the i^{th} plane (-)
η	Conversion of a chemical specie (-)
γ	Yield of a chemical specie (-)

ι	Dimensionless jet entrainment (-)
κ	Thermal conductivity ($\text{W m}^{-1} \text{K}^{-1}$)
μ	Dynamic viscosity (Pa s)
ν	Kinematic viscosity ($\text{m}^2 \text{s}^{-1}$)
ω	Mass fraction in gas. Mass fraction in vapour phase (-)
Ω_D	Collision integral for mass binary diffusivity (-)
Ω_μ	Collision integral for dynamic viscosity (-)
Φ	Viscous dissipation function (s^{-2})
ϕ	Scalar property (-)
ρ	Density (kg m^{-3})
ϱ	Specific volume ($\text{m}^3 \text{kg}^{-1}$)
σ	Lennard-Jones collision diameter (\AA)
σ	Interface tension (N m^{-1})
τ	Viscous stress tensor (Pa)
Θ	Parameter for transport properties of mixtures (-)
θ	Elongation rate (-)
Υ	Ratio of forward to backward velocities for a reversible reaction (-)
v	Mass fraction in mixture. Mass fraction in liquid phase (-)
ε_{exp}	Experimental void fraction (-)
ε_{hom}	Homogeneous void fraction (-)
ε_{xio}	Correlated void fraction (-)
ξ	Selectivity of a chemical specie (-)

Dimensionless groups

Ar	Arrhenius number
Ca	Capillary number
Co	Confinement number

Cu	Courant number
Da	Second Damköhler number
$Eö$	Eötvös number
Pe_{cell}	Cell Péclet number
Pr	Prandtl number
Re	Reynolds number
Rh	Rh number
Sc	Schmidt number
We	Weber number

Overlines

\sim	Dimensionless
$\hat{}$	Mass partial property

Superscripts

*	Dimensionless
\dagger	Transpose of a tensor
o	Standard conditions

Subscripts

298	Measured at 298 K
alc	Alcohol
α, β, \dots	Chemical species in multicomponent systems
bn	Bubble nose
$bottom$	Bottom side of the chip
bub	Bubble point
bt	Bubble tail
c	Characteristic value
ch	Chip

<i>dew</i>	Dew point
<i>dyn</i>	Dynamic conditions
<i>eq</i>	Equilibrium conditions
<i>fr</i>	Fluidic resistor
<i>hca</i>	Heated or cooled area
<i>i</i>	i^{th} axis direction
<i>if</i>	Fluid-fluid or solid-fluid interface. Direction normal to the interface
<i>in</i>	Inner
<i>inlet</i>	Inlet condition
<i>j</i>	j^{th} axis direction
<i>j</i>	Taylor jet
<i>l</i>	Liquid
<i>lp</i>	Liquid plug
<i>max</i>	Maximum
<i>mc</i>	Main channel
<i>min</i>	Minimum
<i>o</i>	Syringe pump conditions
<i>out</i>	Outer
<i>pc</i>	Pseudocritical
<i>preheated</i>	Preheated
<i>rel</i>	Relative
<i>rg</i>	Reagent of a specific reaction
<i>room</i>	Room conditions
<i>rx</i>	Reaction
<i>s</i>	Solid
<i>stoich</i>	Stoichiometric conditions

<i>top</i>	Top side of the chip
<i>v</i>	Vapour
<i>va</i>	Visualised area
<i>yw</i>	y^{th} direction across the solid wall

Other Symbols

A_{sh}, \dots, H_{sh}	Coefficients for the Shomate equation (-)
\mathfrak{R}	= 8314. Universal gas constant ($\text{J kmol}^{-1} \text{K}^{-1}$)
ε/K	Lennard-Jones intermolecular potential (K)
$\%v/v$	Volumetric fraction (-)

Chemical Formulas

CH_4	Methane
CO_2	Carbon dioxide
CO	Carbon monoxide
H_2	Hydrogen
H_2O_g	Water steam
O_2	Oxygen

Acronyms

2D, 3D	Two-, three-dimensions
CPO	Catalytic partial oxidation of methane
EtOH	Ethanol
MeOH	Methanol
OXI	Oxidation reaction
REF	Reforming reaction
RhB	Rhodamine B
syngas	Synthesis gas
VLE	Vapour-Liquid Equilibrium
WGS	Water-gas shift reaction

UNIVERSITAT ROVIRA I VIRGILI

NUMERICAL AND EXPERIMENTAL ANALYSES OF SINGLE AND TWO-PHASE MICROFLUIDIC FLOWS WITH IMPLICATIONS IN MICROREACTORS

Roland Blanch Ojea

DL:T. 149-2012

Bibliography

- Agostini B, Revellin R, Thome JR (2008) Elongated bubbles in microchannels. Part I: Experimental study and modeling of elongated bubble velocity. *International Journal of Multiphase Flow* 34(6):590–601, DOI (Cited on page(s) 6, 104, 131)
- Akbar MK, Plummer DA, Ghiaasiaan SM (2003) On gas-liquid two-phase flow regimes in microchannels. *International Journal of Multiphase Flow* 29(5):855–865, DOI (Cited on page(s) 5, 6)
- Ali MI, Sadatomi M, Kawaji M (1993) Adiabatic two-phase flow in narrow channels between two flat plates. *The Canadian Journal of Chemical Engineering* 71(5):657–666, DOI (Cited on page(s) 133)
- Ambrosini W (2007) On the analogies in the dynamic behaviour of heated channels with boiling and supercritical fluids. *Nuclear Engineering and Design* 237(11):1164–1174, DOI (Cited on page(s) 121)
- Armand AA (1946) The resistance during the movement of a two-phase system in horizontal pipes. *Izv Vses Teplotekh Inst* 1:16–23, (A.E.R.E. Lib/Trans 828), URL (Cited on page(s) 133)
- Aubin J, Ferrando M, Jiricny V (2010) Current methods for characterising mixing and flow in microchannels. *Chemical Engineering Science* 65(6):2065–2093, DOI (Cited on page(s) 6)
- Barajas AM, Panton RL (1993) The effects of contact angle on two-phase flow in capillary tubes. *International Journal of Multiphase Flow* 19(2):337–346, DOI (Cited on page(s) 117)
- Benito-López F (2007) High pressure: A challenge for lab-on-a-chip technology. PhD thesis, University of Twente, Enschede, The Netherlands, URL (Cited on page(s) 90)
- Bezanehtak K, Combes GB, Dehghani F, Foster NR, Tomasko DL (2002) Vapor-liquid equilibrium for binary systems of carbon dioxide + methanol, hydrogen + methanol, and hydrogen + carbon dioxide at high pressures. *Journal of Chemical & Engineering Data* 47(2):161–168, DOI (Cited on page(s) xxiii, 110, 152, 153)
- Bird RB, Stewart WE, Lightfoot EN (2001) *Transport Phenomena*, 2nd edn. Wiley (Cited on page(s) 18, 19, 20, 22, 24, 28, 50, 76)
- Brauner N, Maron DM (1992) Identification of the range of ‘small diameters’ conduits, regarding two-phase flow pattern transitions. *International Communications in Heat and Mass Transfer* 19(1):29–39, DOI (Cited on page(s) 6)

- Brunner E, Hültenschmidt W, Schlichthärle G (1987) Fluid mixtures at high pressures IV. Isothermal phase equilibria in binary mixtures consisting of (methanol + hydrogen or nitrogen or methane or carbon monoxide or carbon dioxide). *The Journal of Chemical Thermodynamics* 19(3):273–291, DOI (Cited on page(s) xxiii, 110, 152, 154)
- Chehroudi B (2006) Supercritical fluids: Nanotechnology and select emerging applications. *Combustion Science and Technology* 178(1):555–621, DOI (Cited on page(s) 7)
- Chen WL, Twu MC, Pan C (2002) Gas-liquid two-phase flow in micro-channels. *International Journal of Multiphase Flow* 28(7):1235–1247, DOI (Cited on page(s) 81, 135)
- Chen X, Han P (2000) A note on the solution of conjugate heat transfer problems using SIMPLE-like algorithms. *International Journal of Heat and Fluid Flow* 21(4):463–467, DOI (Cited on page(s) 42)
- Cheng L, Ribatski G, Thome JR (2008) Analysis of supercritical CO₂ cooling in macro- and micro-channels. *International Journal of Refrigeration* 31(8):1301–1316, DOI (Cited on page(s) 7, 75)
- Chester TL (2004) Determination of pressure-temperature coordinates of liquid-vapor critical loci by supercritical fluid flow injection analysis. *Journal of Chromatography A* 1037(1-2):393–403, DOI (Cited on page(s) xxiii, 75, 111, 155)
- Chung PMY, Kawaji M (2004) The effect of channel diameter on adiabatic two-phase flow characteristics in microchannels. *International Journal of Multiphase Flow* 30(7-8):735–761, DOI (Cited on page(s) 6, 133)
- Collier JG, Thome JR (1996) *Convective Boiling and Condensation*, 3rd edn. Oxford University Press, USA (Cited on page(s) 75)
- Commenge JM, Falk L, Corriou JP, Matlosz M (2002) Optimal design for flow uniformity in microchannel reactors. *AIChE Journal* 48(2):345–358, DOI (Cited on page(s) 4)
- Cuesta I (1993) *Estudi numèric de fluxos laminars i turbulents en una cavitat cúbica*. PhD thesis, Rovira i Virgili University, Tarragona, Spain, URL (Cited on page(s) 41, 42)
- Damianides CA, Westwater JW (1988) Two-phase flow patterns in a compact heat exchanger and in small tubes. In: *Proceedings of the Second UK National Conference on Heat Transfer*, pp 1257–1268 (Cited on page(s) 117)
- Dang C, Iino K, Hihara E (2008) Study on two-phase flow pattern of supercritical carbon dioxide with entrained PAG-type lubricating oil in a gas cooler. *International Journal of Refrigeration* 31(7):1265–1272, DOI (Cited on page(s) 7)

- Deutschmann O, Tischer S, Kleditzsch S, Janardhanan VM, Correa C, Chatterjee D, Mladenov N, Mihn HD (2007) DETCHEM Software Package, Version 2.0. [URL](#) (Cited on page(s) 20)
- Dickson JL, Gupta G, Horozov TS, Binks BP, Johnston KP (2006) Wetting phenomena at the CO₂/water/glass interface. *Langmuir* 22(5):2161–2170, [DOI](#) (Cited on page(s) 86)
- Dreyfus R, Tabeling P, Willaime H (2003) Ordered and disordered patterns in two-phase flows in microchannels. *Physical Review Letters* 90(14):144505, [DOI](#) (Cited on page(s) 135)
- Ertl G, Knözinger H, Schüth F, Weitkamp J (2008) Handbook of Heterogeneous Catalysis, 8 Volumes, 2nd edn. Wiley-VCH (Cited on page(s) 30)
- Fabregat A (2007) Direct numerical simulation of turbulent dispersion of buoyant plumes in a pressure-driven channel flow. PhD thesis, Rovira i Virgili University, Tarragona, Spain, [URL](#) (Cited on page(s) 42)
- Fedorov AG, Viskanta R (1999) Heat and mass transfer dynamics in the microchannel adsorption reactor. *Microscale Thermophysical Engineering* 3(2):111–139, [DOI](#) (Cited on page(s) 42)
- Felder RM, Rousseau RW (1999) Elementary Principles of Chemical Processes, 3rd edn. Wiley (Cited on page(s) 31, 54)
- Ferziger JH, Perić M (2001) Computational Methods for Fluid Dynamics, 3rd edn. Springer (Cited on page(s) 42, 48, 49)
- Fletcher PDI, Haswell SJ, Pombo-Villar E, Warrington BH, Watts P, Wong SYF, Zhang X (2002) Micro reactors: Principles and applications in organic synthesis. *Tetrahedron* 58(24):4735–4757, [DOI](#) (Cited on page(s) 3)
- Fogler HS (2005) Elements of Chemical Reaction Engineering, 4th edn. Prentice Hall (Cited on page(s) 31, 54)
- Galicia-Luna LA, Ortega-Rodriguez A, Richon D (2000) New apparatus for the fast determination of high-pressure vapor–liquid equilibria of mixtures and of accurate critical pressures. *Journal of Chemical & Engineering Data* 45(2):265–271, [DOI](#) (Cited on page(s) xxiii, 110, 147, 150)
- Garstecki P, Fuerstman MJ, Stone HA, Whitesides GM (2006) Formation of droplets and bubbles in a microfluidic T-junction—scaling and mechanism of break-up. *Lab on a Chip* 6(3):437–446, [DOI](#) (Cited on page(s) 6, 133)
- Gervais T, Jensen KF (2006) Mass transport and surface reactions in microfluidic systems. *Chemical Engineering Science* 61(4):1102–1121, [DOI](#) (Cited on page(s) 5)

- Gosiewski K, Bartmann U, Moszczyński M, Mleczko L (1999) Effect of the intraparticle mass transport limitations on temperature profiles and catalytic performance of the reverse-flow reactor for the partial oxidation of methane to synthesis gas. *Chemical Engineering Science* 54(20):4589–4602, DOI (Cited on page(s) xxiii, 12, 13)
- Grimm M, Mazumder S (2008) Numerical investigation of wall heat conduction effects on catalytic combustion in split and continuous monolith tubes. *Computers & Chemical Engineering* 32(3):552–560, DOI (Cited on page(s) 11)
- Guido S, Preziosi V (2010) Droplet deformation under confined Poiseuille flow. *Advances in Colloid and Interface Science* 161(1-2):89–101, DOI (Cited on page(s) 6)
- Guillot P, Colin A (2005) Stability of parallel flows in a microchannel after a T junction. *Physical Review E - Statistical, Nonlinear, and Soft Matter Physics* 72(6):066301, DOI (Cited on page(s) 6, 133)
- Günther A, Jensen KF (2006) Multiphase microfluidics: From flow characteristics to chemical and materials synthesis. *Lab on a Chip* 6(12):1487–1503, DOI (Cited on page(s) 6, 133)
- Gupta A, Kumar R (2009) Effect of geometry on droplet formation in the squeezing regime in a microfluidic T-junction. *Microfluidics and Nanofluidics* 8(6):799–812, DOI (Cited on page(s) 133)
- Hannemann S, Grunwaldt JD, van Vegten N, Baiker A, Boye P, Schroer CG (2007) Distinct spatial changes of the catalyst structure inside a fixed-bed microreactor during the partial oxidation of methane over Rh/Al₂O₃. *Catalysis Today* 126(1-2):54–63, DOI (Cited on page(s) 14)
- Harlow FH, Welch JE (1965) Numerical calculation of time-dependent viscous incompressible flow of fluid with free surface. *Physics of Fluids* 8(12):2182–2189, DOI (Cited on page(s) 43)
- He M, Kassab AJ, Bishop PJ, Minardi A (1995) An iterative FDM/BEM method for the conjugate heat transfer problem – parallel plate channel with constant outside temperature. *Engineering Analysis with Boundary Elements* 15(1):43–50, DOI (Cited on page(s) 42)
- Hessel V, Angeli P, Gavriilidis A, Löwe H (2005) Gas–liquid and gas–liquid–solid microstructured reactors: Contacting principles and applications. *Industrial & Engineering Chemistry Research* 44(25):9750–9769, DOI (Cited on page(s) 135)
- Hoffman JD, Frankel S (2001) *Numerical Methods for Engineers and Scientists*, 2nd edn. CRC Press (Cited on page(s) 47)

- Hriberšek M, Kuhn G (2000) Conjugate heat transfer by boundary-domain integral method. *Engineering Analysis with Boundary Elements* 24(4):297–305, DOI (Cited on page(s) 42)
- Hwang JJ, Tseng FG, Pan C (2005) Ethanol–CO₂ two-phase flow in diverging and converging microchannels. *International Journal of Multiphase Flow* 31(5):548–570, DOI (Cited on page(s) 7)
- Incropera FP, DeWitt D, Bergman TL, Lavine AS (2006) *Fundamentals of Heat and Mass Transfer*, 6th edn. Wiley (Cited on page(s) 52, 63)
- Jahn R, Šnita D, Kubíček M, Marek M (1997) 3-D modeling of monolith reactors. *Catalysis Today* 38(1):39–46, DOI (Cited on page(s) 43)
- Jennings DW, Lee RJ, Teja AS (1991) Vapor-liquid equilibria in the carbon dioxide + ethanol and carbon dioxide + 1-butanol systems. *Journal of Chemical & Engineering Data* 36(3):303–307, DOI (Cited on page(s) xxiii, 110, 147, 150)
- Jensen KF (2001) Microreaction engineering – is small better? *Chemical Engineering Science* 56(2):293–303, DOI (Cited on page(s) 1)
- Jiménez A (2003) Interacció entre les estructures de flux i el transport de matèria. Aplicació a un doll pla turbulent. PhD thesis, Rovira i Virgili University, Tarragona, Spain, URL (Cited on page(s) 42)
- Joung SN, Yoo CW, Shin HY, Kim SY, Yoo KP, Lee CS, Huh WS (2001) Measurements and correlation of high-pressure VLE of binary CO₂-alcohol systems (methanol, ethanol, 2-methoxyethanol and 2-ethoxyethanol). *Fluid Phase Equilibria* 185(1-2):219–230, DOI (Cited on page(s) xxiii, 110, 147, 149, 152, 153)
- Kaisare NS, Lee JH, Fedorov AG (2005a) Hydrogen generation in a reverse-flow microreactor: 1. Model formulation and scaling. *AIChE Journal* 51(8):2254–2264, DOI (Cited on page(s) xxiii, 5, 12, 13, 14, 52)
- Kaisare NS, Lee JH, Fedorov AG (2005b) Hydrogen generation in a reverse-flow microreactor: 2. Simulation and analysis. *AIChE Journal* 51(8):2265–2272, DOI (Cited on page(s) 5, 12)
- Kaisare NS, Lee JH, Fedorov AG (2005c) Operability analysis and design of a reverse-flow microreactor for hydrogen generation via methane partial oxidation. *Industrial & Engineering Chemistry Research* 44(22):8323–8333, DOI (Cited on page(s) 5, 12)
- Kandlikar SG (2002) Fundamental issues related to flow boiling in minichannels and microchannels. *Experimental Thermal and Fluid Science* 26(2-4):389–407, DOI (Cited on page(s) 5, 121)

- Karniadakis G, Beskok A, Aluru N (2005) *Microflows and Nanoflows: Fundamentals and Simulation*, 1st edn. Springer (Cited on page(s) 1)
- Kawahara A, Chung PMY, Kawaji M (2002) Investigation of two-phase flow pattern, void fraction and pressure drop in a microchannel. *International Journal of Multiphase Flow* 28(9):1411–1435, DOI (Cited on page(s) 6, 131, 133)
- Kays WM, Crawford ME, Weigand B (2004) *Convective Heat and Mass Transfer*, 4th edn. McGraw Hill Higher Education (Cited on page(s) 22, 26)
- Kew PA, Cornwell K (1997) Correlations for the prediction of boiling heat transfer in small-diameter channels. *Applied Thermal Engineering* 17(8-10):705–715, DOI (Cited on page(s) 6, 81)
- Kikas T, Bardenshteyn I, Williamson C, Ejimofor C, Puri P, Fedorov AG (2003) Hydrogen production in a reverse-flow autothermal catalytic microreactor: From evidence of performance enhancement to innovative reactor design. *Industrial & Engineering Chemistry Research* 42(25):6273–6279, DOI (Cited on page(s) 4, 12, 14, 15, 54)
- Kolb G, Hessel V (2004) Micro-structured reactors for gas phase reactions. *Chemical Engineering Journal* 98(1-2):1–38, DOI (Cited on page(s) 3)
- Kritzer P (2004) Corrosion in high-temperature and supercritical water and aqueous solutions: A review. *The Journal of Supercritical Fluids* 29(1-2):1–29, DOI (Cited on page(s) 103)
- Kumar G, Prabhu KN (2007) Review of non-reactive and reactive wetting of liquids on surfaces. *Advances in Colloid and Interface Science* 133(2):61–89, DOI (Cited on page(s) 86)
- Lajeunesse E, Homsy GM (2003) Thermocapillary migration of long bubbles in polygonal tubes. II. Experiments. *Physics of Fluids* 15(2):308–314, DOI (Cited on page(s) 85)
- Lee CY, Lee SY (2008) Influence of surface wettability on transition of two-phase flow pattern in round mini-channels. *International Journal of Multiphase Flow* 34(7):706–711, DOI (Cited on page(s) 82)
- Lee LY, Lim LK, Hua J, Wang CH (2008) Jet breakup and droplet formation in near-critical regime of carbon dioxide-dichloromethane system. *Chemical Engineering Science* 63(13):3366–3378, DOI (Cited on page(s) 133)
- Lemmon EW, Huber ML, McLinden MO (2007) NIST Standard Reference Database 23: Reference fluid thermodynamic and transport properties-REFPROP, Version 8.0. URL (Cited on page(s) 18, 76)

- Leu AD, Chung SYK, Robinson DB (1991) The equilibrium phase properties of (carbon dioxide + methanol). *The Journal of Chemical Thermodynamics* 23(10):979–985, DOI (Cited on page(s) xxiii, 110, 152)
- Levine IN (2008) *Physical Chemistry*, 6th edn. McGraw Hill Higher Education (Cited on page(s) 31)
- Li J, Peterson G (2007) 3-Dimensional numerical optimization of silicon-based high performance parallel microchannel heat sink with liquid flow. *International Journal of Heat and Mass Transfer* 50(15-16):2895–2904, DOI (Cited on page(s) 12)
- Liao SM, Zhao TS (2002) Measurements of heat transfer coefficients from supercritical carbon dioxide flowing in horizontal mini/micro channels. *Journal of Heat Transfer* 124(3):413–420, DOI (Cited on page(s) 75)
- Liu H, Zhang Y (2009) Droplet formation in a T-shaped microfluidic junction. *Journal of Applied Physics* 106(3):034906, DOI (Cited on page(s) 133)
- de Loos SRA, van der Schaaf J, Tiggelaar RM, Nijhuis TA, de Croon MHJM, Schouten JC (2010) Gas–liquid dynamics at low Reynolds numbers in pillared rectangular micro channels. *Microfluidics and Nanofluidics* 9(1):131–144, DOI (Cited on page(s) 6, 131, 133)
- Maranzana G, Perry I, Maillet D (2004) Mini- and micro-channels: Influence of axial conduction in the walls. *International Journal of Heat and Mass Transfer* 47(17-18):3993–4004, DOI (Cited on page(s) 11)
- Marre S, Aymonier C, Subra P, Mignard E (2009) Dripping to jetting transitions observed from supercritical fluid in liquid microflows. *Applied Physics Letters* 95(13):134105, DOI (Cited on page(s) 7, 133)
- Mendoza de la Cruz JL, Galicia-Luna LA (1999) High-pressure vapor–liquid equilibria for the carbon dioxide + ethanol and carbon dioxide + propan-1-ol systems at temperatures from 322.36 K to 391.96 K. *ELDATA: The International Electronic Journal of Physico-Chemical Data* 5:157–164 (Cited on page(s) xxiii, 110, 147, 151)
- de Menech M, Garstecki P, Jousse F, Stone HA (2008) Transition from squeezing to dripping in a microfluidic T-shaped junction. *Journal of Fluid Mechanics* 595:141–161, DOI (Cited on page(s) 133)
- Meng H, Hsiao GC, Yang V, Shuen JS (2005) Transport and dynamics of liquid oxygen droplets in supercritical hydrogen streams. *Journal of Fluid Mechanics* 527:115–139, DOI (Cited on page(s) 126)
- Morini GL (2005) Viscous heating in liquid flows in micro-channels. *International Journal of Heat and Mass Transfer* 48(17):3637–3647, DOI (Cited on page(s) 14)

- Nguyen N, Wereley ST (2002) *Fundamentals and Applications of Microfluidics*, 1st edn. Artech House (Cited on page(s) 1)
- Nguyen NT, Huang X (2005) Thermocapillary effect of a liquid plug in transient temperature fields. *Japanese Journal of Applied Physics* 44:1139–1142, DOI (Cited on page(s) 86)
- NIST (2009) NIST Chemistry WebBook. Visited May 2009, URL (Cited on page(s) 21)
- Ody CP, Baroud CN, de Langre E (2007) Transport of wetting liquid plugs in bifurcating microfluidic channels. *Journal of Colloid and Interface Science* 308(1):231–238, DOI (Cited on page(s) 120)
- Ohgaki K, Katayama T (1976) Isothermal vapor-liquid equilibrium data for binary systems containing carbon dioxide at high pressures: Methanol-carbon dioxide, n-hexane-carbon dioxide, and benzene-carbon dioxide systems. *Journal of Chemical & Engineering Data* 21(1):53–55, DOI (Cited on page(s) xxiii, 110, 152)
- Pallares J, Grau FX, Giralt F (1999) Flow transitions in laminar Rayleigh-Bénard convection in a cubical cavity at moderate Rayleigh numbers. *International Journal of Heat and Mass Transfer* 42(4):753–769, DOI (Cited on page(s) 42)
- Patankar S (1980) *Numerical Heat Transfer and Fluid Flow*, 1st edn. Taylor & Francis (Cited on page(s) 42)
- Quiceno R, Pérez-Ramírez J, Warnatz J, Deutschmann O (2006) Modeling the high-temperature catalytic partial oxidation of methane over platinum gauze: Detailed gas-phase and surface chemistries coupled with 3D flow field simulations. *Applied Catalysis A: General* 303(2):166–176, DOI (Cited on page(s) 4)
- Raja LL, Kee RJ, Deutschmann O, Warnatz J, Schmidt L (2000) A critical evaluation of Navier-Stokes, boundary-layer, and plug-flow models of the flow and chemistry in a catalytic-combustion monolith. *Catalysis Today* 59(1-2):47–60, DOI (Cited on page(s) 5)
- Rasband WS (1997–2011) ImageJ, Version 1.43l. URL (Cited on page(s) 104)
- Revellin R (2005) *Experimental two-phase fluid flow in microchannels*. PhD thesis, EPFL, Lausanne, Switzerland, DOI (Cited on page(s) 83)
- Revellin R, Dupont V, Ursenbacher T, Thome JR, Zun I (2006) Characterization of diabatic two-phase flows in microchannels: Flow parameter results for R-134a in a 0.5 mm channel. *International Journal of Multiphase Flow* 32(7):755–774, DOI (Cited on page(s) 6, 81, 131, 135)

- Revellin R, Agostini B, Thome JR (2008) Elongated bubbles in microchannels. Part II: Experimental study and modeling of bubble collisions. *International Journal of Multiphase Flow* 34(6):602–613, DOI (Cited on page(s) 6, 135)
- Sammarco TS, Burns MA (1999) Thermocapillary pumping of discrete drops in micro-fabricated analysis devices. *AIChE Journal* 45(2):350–366, DOI (Cited on page(s) 86)
- Schneider A, Mantzaras J, Jansohn P (2006) Experimental and numerical investigation of the catalytic partial oxidation of CH₄/O₂ mixtures diluted with H₂O and CO₂ in a short contact time reactor. *Chemical Engineering Science* 61(14):4634–4649, DOI (Cited on page(s) 14, 54, 70)
- Schwiedernoch R, Tischer S, Correa C, Deutschmann O (2003) Experimental and numerical study on the transient behavior of partial oxidation of methane in a catalytic monolith. *Chemical Engineering Science* 58(3-6):633–642, DOI (Cited on page(s) 14, 43, 69)
- Secuianu C, Feroiu V, Geană D (2008) Phase behavior for carbon dioxide + ethanol system: Experimental measurements and modeling with a cubic equation of state. *The Journal of Supercritical Fluids* 47(2):109–116, DOI (Cited on page(s) xxiii, 110, 147, 148)
- Serizawa A, Feng Z, Kawara Z (2002) Two-phase flow in microchannels. *Experimental Thermal and Fluid Science* 26(6-7):703–714, DOI (Cited on page(s) 81, 82, 131, 133)
- Shao N, Gavriilidis A, Angeli P (2009) Flow regimes for adiabatic gas-liquid flow in microchannels. *Chemical Engineering Science* 64(11):2749–2761, DOI (Cited on page(s) 5, 80, 81, 117)
- Shewchuk JR (1994) An introduction to the conjugate gradient method without the agonizing pain. Tech. rep., URL (Cited on page(s) 42)
- Shui L, Eijkel JCT, van den Berg A (2007a) Multiphase flow in micro- and nanochannels. *Sensors and Actuators B: Chemical* 121(1):263–276, DOI (Cited on page(s) 5, 86)
- Shui L, Eijkel JCT, van den Berg A (2007b) Multiphase flow in microfluidic systems – Control and applications of droplets and interfaces. *Advances in Colloid and Interface Science* 133(1):35–49, DOI (Cited on page(s) 5, 133)
- Smith JM, Van Ness HC, Abbott MM (2000) *Introduction to Chemical Engineering Thermodynamics*, 6th edn. McGraw-Hill Education (ISE Editions) (Cited on page(s) 6, 25, 75)
- Squires TM, Quake SR (2005) Microfluidics: Fluid physics at the nanoliter scale. *Reviews of Modern Physics* 77(3):977–1026, DOI (Cited on page(s) 1, 6, 86)

- Srinivasan R, Hsing I, Berger PE, Jensen KF, Firebaugh SL, Schmidt MA, Harold MP, Lerou JJ, Ryley JF (1997) Micromachined reactors for catalytic partial oxidation reactions. *AIChE Journal* 43(11):3059–3069, DOI (Cited on page(s) 14)
- Steggmans MLJ, Schroën CGPH, Boom RM (2009) Generalised insights in droplet formation at T-junctions through statistical analysis. *Chemical Engineering Science* 64(13):3042–3050, DOI (Cited on page(s) 133, 134)
- van Steijn V, Kreutzer MT, Kleijn CR (2007) μ -PIV study of the formation of segmented flow in microfluidic T-junctions. *Chemical Engineering Science* 62(24):7505–7514, DOI (Cited on page(s) 135)
- Stutz MJ, Poulikakos D (2005) Effects of microreactor wall heat conduction on the reforming process of methane. *Chemical Engineering Science* 60(24):6983–6997, DOI (Cited on page(s) 11, 14, 20, 43, 52, 54)
- Sugavanam R, Ortega A, Choi CY (1995) A numerical investigation of conjugate heat transfer from a flush heat source on a conductive board in laminar channel flow. *International Journal of Heat and Mass Transfer* 38(16):2969–2984, DOI (Cited on page(s) 42)
- Sun Y, Shekunov BY (2003) Surface tension of ethanol in supercritical CO₂. *The Journal of Supercritical Fluids* 27(1):73–83, DOI (Cited on page(s) xviii, 80, 81)
- Suzuki K, Sue H, Ito M, Smith RL, Inomata H, Arai K, Saito S (1990) Isothermal vapor-liquid equilibrium data for binary systems at high pressures: Carbon dioxide-methanol, carbon dioxide-ethanol, carbon dioxide-1-propanol, methane-ethanol, methane-1-propanol, ethane-ethanol, and ethane-1-propanol systems. *Journal of Chemical & Engineering Data* 35(1):63–66, DOI (Cited on page(s) xxiii, 110, 147, 150)
- Taylor R, Krishna R (1993) *Multicomponent Mass Transfer*, 1st edn. Wiley series in chemical engineering, Wiley-Interscience (Cited on page(s) 20, 21, 24, 27, 28, 33)
- Thome JR (2006) State-of-the-art overview of boiling and two-phase flows in microchannels. *Heat Transfer Engineering* 27(9):4–19, DOI (Cited on page(s) 5, 121)
- Thorsen T, Roberts RW, Arnold FH, Quake SR (2001) Dynamic pattern formation in a vesicle-generating microfluidic device. *Physical Review Letters* 86(18):4163–4166, DOI (Cited on page(s) 133)
- Tian YL, Han M, Chen L, Feng JJ, Qin Y (2001) Study on vapor-liquid phase equilibria for CO₂-C₂H₅OH system. *Acta Physico - Chimica Sinica* 17(2):155–160, in Chinese, DOI (Cited on page(s) xxiii, 110, 147, 148)

- Tiggelaar RM, Loeters PWH, van Male P, Oosterbroek RE, Gardeniers JGE, de Croon MHJM, Schouten JC, Elwenspoek MC, van den Berg A (2004) Thermal and mechanical analysis of a microreactor for high temperature catalytic gas phase reactions. *Sensors and Actuators, A: Physical* 112(2-3):267–277, DOI (Cited on page(s) 4, 14)
- Tiggelaar RM, Benito-López F, Hermes DC, Rathgen H, Egberink RJM, Mugele FG, Reinhoudt DN, van den Berg A, Verboom W, Gardeniers HJGE (2007) Fabrication, mechanical testing and application of high-pressure glass microreactor chips. *Chemical Engineering Journal* 131(1-3):163–170, DOI (Cited on page(s) 90)
- Tischer S, Deutschmann O (2005) Recent advances in numerical modeling of catalytic monolith reactors. *Catalysis Today* 105(3-4):407–413, DOI (Cited on page(s) 69)
- Tischer S, Correa C, Deutschmann O (2001) Transient three-dimensional simulations of a catalytic combustion monolith using detailed models for heterogeneous and homogeneous reactions and transport phenomena. *Catalysis Today* 69(1-4):57–62, DOI (Cited on page(s) 43)
- Toh KC, Chen XY, Chai JC (2002) Numerical computation of fluid flow and heat transfer in microchannels. *International Journal of Heat and Mass Transfer* 45(26):5133–5141, DOI (Cited on page(s) 42)
- Trachsel F, Tidona B, Desportes S, von Rohr PR (2009) Solid catalyzed hydrogenation in a Si/glass microreactor using supercritical CO₂ as the reaction solvent. *The Journal of Supercritical Fluids* 48(2):146–153, DOI (Cited on page(s) 7)
- Triplett KA, Ghiaasiaan SM, Abdel-Khalik SI, Sadowski DL (1999) Gas-liquid two-phase flow in microchannels Part I: Two-phase flow patterns. *International Journal of Multiphase Flow* 25(3):377–394, DOI (Cited on page(s) 6, 82)
- Valencia L (2006) Estudio numérico y experimental de flujo Rayleigh-Bénard en cavidades cúbicas para régimen transitorio y turbulento. PhD thesis, Rovira i Virgili University, Tarragona, Spain, URL (Cited on page(s) 42)
- Versteeg HK, Malalasekera W (1996) *An Introduction to Computational Fluid Dynamics: The Finite Volume Method Approach*, 1st edn. Prentice Hall (Cited on page(s) 42, 43)
- van der Vorst HA (1992) Bi-CGSTAB: A fast and smoothly converging variant of Bi-CG for the solution of nonsymmetric linear systems. *SIAM Journal on Scientific and Statistical Computing* 13(2):631–644, DOI (Cited on page(s) 42)
- Walter S, Malmberg S, Schmidt B, Liauw MA (2005) Mass transfer limitations in microchannel reactors. *Catalysis Today* 110(1-2):15–25, DOI (Cited on page(s) 3)

- Wanker R, Raupenstrauch H, Staudinger G (2000) A fully distributed model for the simulation of a catalytic combustor. *Chemical Engineering Science* 55(20):4709–4718, DOI (Cited on page(s) 42)
- Weinmueller C, Hotz N, Mueller A, Poulikakos D (2009) On two-phase flow patterns and transition criteria in aqueous methanol and CO₂ mixtures in adiabatic, rectangular microchannels. *International Journal of Multiphase Flow* 35(8):760–772, DOI (Cited on page(s) 7, 99, 100)
- White F (1991) *Viscous Fluid Flow*, 2nd edn. McGraw-Hill Science/Engineering/Math (Cited on page(s) 19)
- Xiong R, Chung JN (2007) An experimental study of the size effect on adiabatic gas-liquid two-phase flow patterns and void fraction in microchannels. *Physics of Fluids* 19(3):033301, DOI (Cited on page(s) xxi, 131, 133, 141)
- Yang CY, Shieh CC (2001) Flow pattern of air-water and two-phase R-134a in small circular tubes. *International Journal of Multiphase Flow* 27(7):1163–1177, DOI (Cited on page(s) 81)
- York APE, Xiao T, Green MLH (2003) Brief overview of the partial oxidation of methane to synthesis gas. *Topics in Catalysis* 22(3):345–358, DOI (Cited on page(s) 4, 12, 14)
- Younes-Metzler O, Svagin J, Jensen S, Christensen CH, Hansen O, Quaade U (2005) Microfabricated high-temperature reactor for catalytic partial oxidation of methane. *Applied Catalysis A: General* 284(1-2):5–10, DOI (Cited on page(s) 4, 14)
- Younis O (2010) Numerical and experimental study of transient laminar natural convection of high Prandtl number fluids in a cubical cavity. PhD thesis, Rovira i Virgili University, Tarragona, Spain, URL (Cited on page(s) 42)
- Yue J, Luo L, Gonthier Y, Chen G, Yuan Q (2008) An experimental investigation of gas-liquid two-phase flow in single microchannel contactors. *Chemical Engineering Science* 63(16):4189–4202, DOI (Cited on page(s) 81, 131, 133, 135)

